2018

Characterizing The Energetic Landscape In Solution Processable Solar Cells Via Frequency-Dependent Impedance Measurements

Eric S. Wong
University of Pennsylvania, wongerics@gmail.com

Recommended Citation

Wong, Eric S., "Characterizing The Energetic Landscape In Solution Processable Solar Cells Via Frequency-Dependent Impedance Measurements" (2018). *Publicly Accessible Penn Dissertations*. 3203.
https://repository.upenn.edu/edissertations/3203

Characterizing The Energetic Landscape In Solution Processable Solar Cells Via Frequency-Dependent Impedance Measurements

Abstract

This thesis presents measurements and analyses aimed at describing charge transport dynamics in quantum dot (QD) photovoltaics (PVs). Due to their solution processability and unique size-dependent optoelectronic properties, ensembles of electronically coupled QDs (QD solids) provide an exciting platform for next generation PV devices. However, the structural disorder associated with the formation of conductive QD solids gives rise to a complicated density of states (DOS) emerging from the distribution of mesoscale charge dynamics occurring in these materials.

I present phenomological models to describe the DOS in the disordered energetic and spatial landscape of QD solids that relies on a suite of frequency-domain measurements known as impedance spectroscopy (IS). Though specific applications of IS such as thermal admittance spectroscopy (TAS) have been applied to the capacitance characteristics of QD solids, a fuller picture of the DOS in these materials is afforded by analysis of the time-scales evident in the full impedance characteristics of QD devices.

I heuristically propose extensions of charge transport models developed for capacitance-voltage (CV) measurements of bulk semiconductors to describe the frequency-dependent capacitance and conductance response of a variety of QD solar cell device architectures. In Chapter 3, I show how TAS and drive level capacitance profiling (DLCP) characterization of a QD Schottky junction is linked to charge hopping processes observed in AC conductance data. This allows me to map the time scales detected in these data to the DOS in the QD solid. I then suggest how the observed DOS translates onto macroscale device properties like the diode current. In Chapter 4, I apply these techniques to a QD heterojunction device. I use forward biased IS characterization to suggest the presence of a defect state at the junction interface, and calculate the associated distribution of carrier lifetimes. In Chapter 5, I attempt to extend this model to a QD p-i-n heterojunction solar cell, and obtain a response consistent with interfacial trapping and carrier transport. Though unambiguous identification of the origin of these responses proves beyond the scope of this thesis, I use illuminated TAS and DLCP measurements to show the presence of an interfacial trap for photogenerated electrons.

Degree Type

Dissertation

Degree Name

Doctor of Philosophy (PhD)

Graduate Group

Physics & Astronomy

First Advisor

Cherie R. Kagan

Subject Categories
Condensed Matter Physics | Nanoscience and Nanotechnology

CHARACTERIZING THE ENERGETIC LANDSCAPE IN SOLUTION PROCESSABLE SOLAR CELLS *VIA* FREQUENCY DEPENDENT IMPEDANCE MEASUREMENTS

Eric S. Wong

A DISSERTATION

in

Physics and Astronomy

Presented to the Faculties of the University of Pennsylvania in Partial Fulfillment of the Requirements for the Degree of Doctor of Philosophy

2018

Supervisor of Dissertation

Dr. Cherie Kagan, Professor of Electrical and Systems Engineering

Graduate Group Chairperson

Dr. Joshua Klein, Professor of Physics

Dissertation Committee:
Dr. Arjun Yodh, Professor of Physics
Dr. Jay Kikkawa, Professor of Physics
Dr. Firooz Aflatouni, Professor of Electrical and Systems Engineering
Dr. Hugh Williams, Professor of Physics

Acknowledgments

> There's nothing more exciting than
> science. You get all the fun of sitting still,
> being quiet, writing down numbers,
> paying attention. Science has it all.
>
> *Principal Seymour Skinner*

No succinct list could ever adequately tally the thanks I owe to everyone who has guided me along personally and professionally as I've toiled away on the work summarized in this weighty tome. That said, I can think of a few folks who have put up with me more than others during the stress of grad school. I would be remiss if I didn't list them here.

My advisor Cherie Kagan deserves particular credit. I consider myself incredibly fortunate to have had the opportunity to work with a scientist (and human!) of your caliber. I would be hard pressed to find another advisor who would simultaneously give me the space and understanding to forge my own intellectual path, while applying appropriate pressure to ensure I thrive. After working in your group, I'm confident I'll have the right tools to study whatever scientific puzzles await me. I am a much deeper thinker for having had you as my teacher. Thank you so much.

My committee also deserves thanks for helping me close this chapter. A special thanks goes to Professor Firooz Aflatouni. Even if you were away on vacation, you always made time for me when I needed advice on understanding an impedance measurement or planning the next steps of my career.

To my past and present colleagues in the Kagan and Murray labs, working at your side has been a pleasure. You are some of the brightest and most motivated people I think I will ever meet. Dr. E.D. Goodwin–you were my first friend in Philadelphia, and are literally providing a roof over my head as I wrap up my time here. I cannot begin to thank you and Danielle enough. Leo Zhao–you met my every request for help and devices with a willing smile and encouragement. Without your effort, none of this would have been possible. Daniel Straus, Dr. David Kim, Dr. Yuming Lai, Professor Aaron Fafarman, Dr. Nicholas Greybush, Dr. Mario Mencagli, Steven Neauhaus–thank you for your guidance, feedback, help, and friendship. To my EFRC colleagues, especially Dr. Joey Luther, Dr. Justin Johnson, and Greg Pach, thank you so much for giving me the courtesy of listening and guiding my work for the past few years. A big thanks goes to Martin Sarott. Sitting together in the library writing these theses together has thankfully humanized this last sprint to the finish.

To my friends outside of the lab, you have made my life unimaginably richer. Cristin, your friendship has been an incredible source of strength for the past six years. A special thanks goes to Dr. Hank Bink and Dr. Steve Gilhool. Our 311 investigations will forever make me laugh. To my Dad Jazz bandmates, I will always smile when I remember the hours of basement practice and walking musical tightropes with with you in front of *literally dozens* of audience members. Amy, the Whislers, Dan, Chip, Rami, Michele, Khilesh, Leigh, Harsha, and others I wish were still with me–sharing my twenties with you has been an absolute blast.

My deepest gratitude is reserved for the people who have somehow tolerated me for 30 years–my family. Some of the happiest times in the past 6 years have been sitting around the dinner table with you all on trips home. Mom and Dad, your continued support and love gives me life (in the obvious literal and more operative figurative sense). I am so grateful for everything you have sacrificed for me. Hopefully, you think it has paid off. Kristen, K2, and Michael–thank you for all the phone calls, the visits, love, and inspiration you continually share with me.

ABSTRACT

CHARACTERIZING THE ENERGETIC LANDSCAPE IN SOLUTION PROCESSABLE SOLAR CELLS *VIA* FREQUENCY DEPENDENT IMPEDANCE MEASUREMENTS

Eric S. Wong

Cherie R. Kagan

This thesis presents measurements and analyses aimed at describing charge transport dynamics in quantum dot (QD) photovoltaics (PVs). Due to their solution processability and unique size-dependent optoelectronic properties, ensembles of electronically coupled QDs (QD solids) provide an exciting platform for next generation PV devices. However, the structural disorder associated with the formation of conductive QD solids gives rise to a complicated density of states (DOS) emerging from the distribution of mesoscale charge dynamics occurring in these materials.

I present phenomological models to describe the DOS in the disordered energetic and spatial landscape of QD solids that relies on a suite of frequency-domain measurements known as impedance spectroscopy (IS). Though specific applications of IS such as thermal admittance spectroscopy (TAS) have been applied to the capacitance characteristics of QD solids, a fuller picture of the DOS in these materials is afforded by analysis of the time-scales evident in the full impedance characteristics of QD devices.

I heuristically propose extensions of charge transport models developed for capacitance-voltage (CV) measurements of bulk semiconductors to describe the frequency-dependent capacitance and conductance response of a variety of QD solar cell device architectures. In Chapter 3, I show how TAS and drive level capacitance profiling (DLCP) characterization of a QD Schottky junction is linked to charge hopping processes observed in AC conductance data. This allows me to map the time scales detected in these data to the DOS in the QD solid. I then suggest how the observed DOS translates onto macroscale device properties like the diode current. In Chapter 4, I apply

these techniques to a QD heterojunction device. I use forward biased IS characterization to suggest the presence of a defect state at the junction interface, and calculate the associated distribution of carrier lifetimes. In Chapter 5, I attempt to extend this model to a QD p-i-n heterojunction solar cell, and obtain a response consistent with interfacial trapping and carrier transport. Though unambiguous identification of the origin of these responses proves beyond the scope of this thesis, I use illuminated TAS and DLCP measurements to suggest the presence of an interfacial trap for photogenerated electrons.

Contents

List of Figures

Chapter 1

Mesoscale Properties of Quantum Dot Solids

1.1 Introduction

Since the introduction of the germanium transistor in 1947, electronic devices based on semiconductors have ushered in the information age. The ability to produce semiconductor crystals (typically made of silicon) with defect levels below one part per billion has enabled high quality electronic materials that are used to make solar panels that deliver $\sim$ 400 GW of solar power worldwide or circuits that compute $\sim$ 3 billion instructions per second in a single modern smart phone. As the demand for ubiquitous electronics increases, research and commercial interest has grown in low-cost, structurally flexible, and large area semiconductor materials to address the modern technological challenges that prohibit the application of traditional crystalline materials, which are typically rigid and expensive to produce for large-area applications.

Solution-processable nanoscale materials, such as organic semiconducting polymers and colloidal quantum dots (QDs), offer an attractive alternative for these emerging applications. These materials may be patterned onto large area, flexible substrates via roll-to-roll processing. Furthermore, their low-temperature syntheses generally avoid costly high-vacuum processing, significantly reducing manufacturing costs. Perhaps most importantly, the precise control offered by the chemical methods used to synthesize these nanoscale materials offers routes for functionalization of individual components, allowing for novel optical, magnetic, and electronic properties.

Despite these advantages, significant challenges are introduced when electronic devices are fabricated from arrays of nanoscale components instead of a single bulk crystal. Many of the requisites for high performance semiconductor electronics, such as precise control over doping and purity levels and high charge carrier mobility, are not met by solution processable components due to the lack of spatial and energetic order in ensembles of nanoscale components. As a result, these materials have yet to be widely adopted as viable next-generation technologies aside from a few niche applications.

This thesis uses QD assemblies as a platform to investigate charge dynamics in the complicated energetic landscape exhibited by solution processable materials. Though exquisite control can be exercised over the optical and electronic properties of QDs, making them attractive materials for electronic and solar applications, ensembles of QDs ('QD solids') lack the structural perfection necessary to match the charge transport properties of bulk crystalline alternatives. The goal of this thesis is to understand how the structural complexity characteristic of QD solids maps onto the ensemble density of states (DOS), and the implications of this energetic and spatial disorder for device-scale electronic properties.

In this chapter, we introduce QDs, including a brief overview of their synthesis and a discussion of their unique size-dependent physical properties (Section 1.2). We then discuss how assemblies of QDs may be made into an electronic device, focusing on PV devices in Section 1.3. In section 1.4, we go on to review the emergent properties of QD solids, and how these properties influence both DC and AC conductivity. At the end of this chapter, we present an outline for the main part of the thesis.

1.2 Colloidal QDs

The chemical synthesis methods used to make colloidal QDs has been the focus of intense research for over two decades. As a result, a broad variety of QD materials can be synthesized, including metal chalcogenides ('E'), metal oxides, and III-V semiconductors such as InP and InAs.[74, 107] Among the most well studied are the lead and cadmium chalcogenides. In this thesis, we study PbS synthesized *via* the hot injection method first introduced for CdSe QDs by Murray, Norris, and Bawendi, which we review briefly here.[108] A reaction flask containing a coordinating solvent and metal precursor (Pb-oleate) is heated to $\sim 300°$ C after which a second chalcogen precursor (bis-trimethylsilylsulfide, $(TMS)_2S$) is injected, resulting in a super-saturated solution of precursors. Small crystallites of PbS begin nucleating, consuming precursors, and the final size of these crystallites is determined by the reaction time and temperature. At the end of the reaction, the QD crystallites undergo Ostwald ripening in which smaller QDs are dissolved and redeposit onto larger crystals.

The reaction solution is washed to remove remaining precursors and growth medium. Washing involves mixing the reaction dispersion with an 'anti-solvent' that is typically miscible with the reaction dispersion and solubilizes the growth solution such that the QDs are removed from solution. The total mixture is then centrifuged to separate the QDs from the solution, after which the excess solution ('supernatant') is discarded. Repeating this procedure many times results in highly mono-disperse QD dispersion in which the size of constituent QDs exhibits a standard deviation of $\sim 5\%$.

1.2.1 Size-Dependent Physical Properties of QDs

QDs are prized for their size-dependent optical and electronic properties which result from the confinement of charge carriers such as electrons, holes, and excitons within a volume smaller than their coherence length. The essential physics of this effect, also known as 'quantum confinement', can be understood by considering the elementary example of the particle in a 1-D infinite square well, in which an electron is confined in the following potential distribution:

$$V(x) = \begin{cases} \infty & \text{if } x < a/2 \text{ or } x > a/2 \\ 0 & \text{if } -a/2 < x < a/2 \end{cases}$$

This potential is illustrated in Figure 1.1A. This simple physical example may be used as a first order approximation to derive the spectra of a single QD with length a. Within the well, the electron feels no binding potential, and the general solution to the 1-D time-independent Schrödinger equation is:

$$\psi(x) = A\mathrm{e}^{ikx} + B\mathrm{e}^{ikx} \tag{1.2.1}$$

where $k_1 = \frac{\sqrt{2mE}}{\hbar}$ and A and B are arbitrary constants. This solution describes free electron plane waves traveling in both the $+x$ and $-x$ directions. These waves combine to form a single standing wave, which we can incorporate into our model by letting $A = B$. The resulting wave may be written:

$$\psi(x) = B(\mathrm{e}^{ikx} + \mathrm{e}^{ikx}) = \frac{B'}{2}(\mathrm{e}^{ikx} + \mathrm{e}^{ikx}) = B'\cos(kx) \tag{1.2.2}$$

Since the coefficients A and B are arbitrary, we may also let $-A = B$, whence we obtain:

$$\psi(x) = A'\sin(kx) + B'\cos(kx) \tag{1.2.3}$$

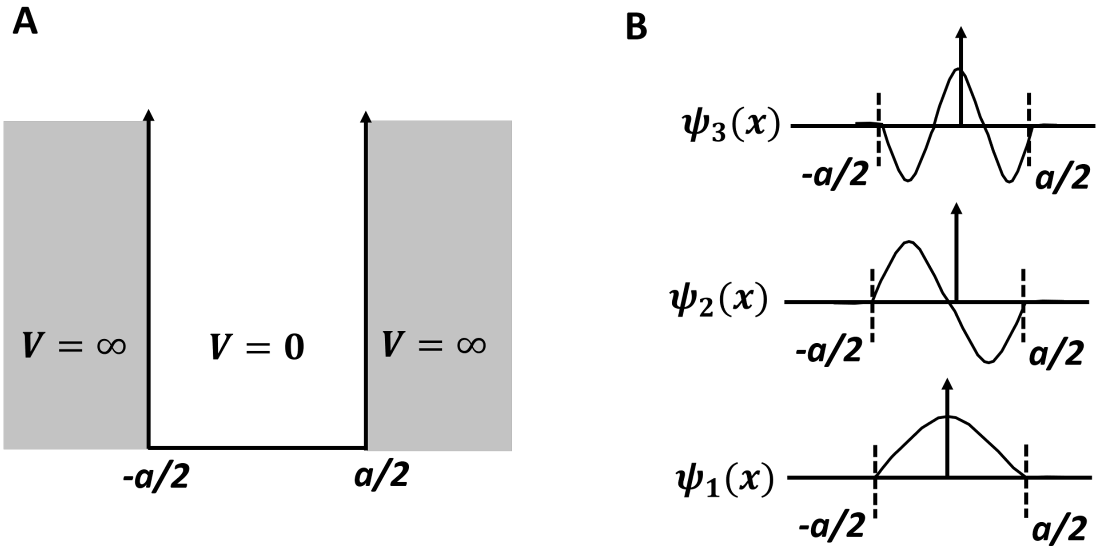

Figure 1.1: (A) Infinite square well potential (B) First three eigenfunctions of the infinite potential well, drawn after [38].

The infinite potential outside the well implies that outside the well, $\psi(x) = 0$. Imposing this boundary condition at both ±$a/2$, we obtain (letting $A', B' \to A, B$):

$$\psi(a/2) = A\text{sin}(\frac{ka}{2}) + B\text{cos}(\frac{ka}{2})$$
$$\psi(-a/2) = -A\text{sin}(\frac{ka}{2}) + B\text{cos}(\frac{ka}{2})$$
$$\implies 2B\text{cos}(\frac{ka}{2}) = 0;$$
$$2A\text{sin}(\frac{ka}{2})$$

We can satisfy these equations by either setting $A = 0$ and $\cos(\frac{k_1 a}{2}) = 0$ or $B = 0$ and $\sin(\frac{k_1 a}{2}) = 0$. Considering the first option, we immediately see that only certain values of k_1 are allowed:

$$\frac{ka}{2} = \frac{\pi}{2}, \frac{3\pi}{2}, \frac{5\pi}{2}, ...$$
$$\implies k_n = \frac{n\pi}{a},\ n = 1, 3, 5...$$

Since k_n can only assume discrete values, E can only assume discrete values:

$$E_n = \frac{\hbar^2 k^2}{2m} = \frac{\pi^2 \hbar^2 n^2}{2m} \tag{1.2.4}$$

The first few eigenfunctions with these energies are diagrammed in Figure 1.1B.

A more accurate 1-D treatment of a single QD uses the finite potential well. Outside the well, $\psi(x)$ is an evanescent wave that decays as $\propto e^{-kx}$ where $k = \frac{\sqrt{2m(V_0 - E)}}{\hbar}$ for a potential height V_0. The eigenfunctions for this potential are plotted in Figure 1.2.

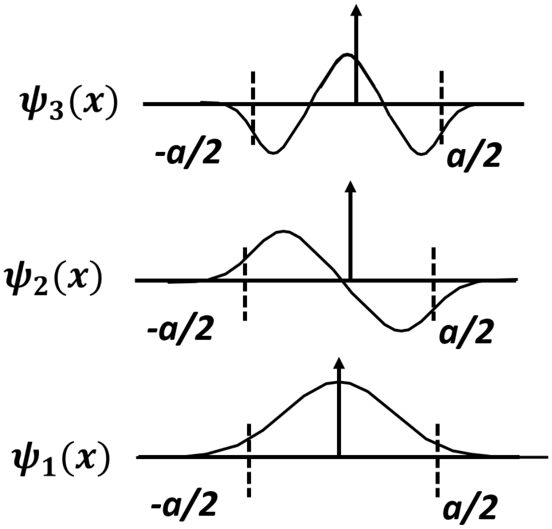

Figure 1.2: Corrections for finite potential depth to eigenfunctions in Figure 1.1B, drawn after [38].

Despite the elementary nature of this example, it communicates the essential physics of quantum confinement. As equation (1.2.4) shows, changing the size of the well a changes the energy spectrum of the well. Analogously, changing the radius of a QD changes its energy spectrum. Quantum confinement in QDs therefore allows for precise control of optoelectronic properties like optical absorption spectra via simple synthetic methods.

1.2.2 QD Assemblies

In QD synthesis, long organic ligands are used to mediate the growth of the QD crystallites. These bulky, carbon-based ligands are insulators. In the language of the preceding section, these ligands introduce a large potential barrier V_0 for charge within the potential well of the QD. As a result, the wavefunction in a QD with native ligands is highly localized.

A conductive QD assembly may therefore be obtained by a decrease in V_0 or in barrier width, requiring removal or exchange of these native ligands for smaller, more compact species. Carrier mobilities in QD assemblies have been shown to systematically vary with ligand length for ligand molecules such as alkanedithiols[91] and short chain acids.[138] As will be discussed in the next section, an increase in carrier mobility μ can be expected for a decrease in the length of the barrier R between QDs as:

$$\mu \propto \exp(-\alpha R) \tag{1.2.5}$$

where α is the decay constant.

The more compact ligands used to exchange native ligands–typically oleic acid (OA)– include small molecules such as hydrazine, amines, or carboxylic acids[91, 78, 76, 97, 83]. Small chain thiols such as 1,2-ethanedithiol (EDT)[97, 76] and 1,4-benzenedithiol[78] have been shown to be effective at exchanging assemblies of PbE QDs. The first QD PV devices [97, 68] and field effect transistors (FETs) [141] were demonstrated using these ligands.

Halide ions ($X^- = Cl^-$, Br^-, I^-) have also been shown to passivate QD surfaces and enhance electronic coupling in QD arrays. Halide ions have the added benefit of being chemically inert to oxidation due to their high electron affinity. Salts with a weak counterion, such as tetrabutylammonium ($TBA^+ X^-$) have been effective at increasing the efficiency of QD PV devices to $\sim 10\%$[32, 27, 62]

Recent studies of the mechanism by which these species displace native ligands have revealed that removal of OA occurs through detachment of oleate from the QD surface.[4] This implies that the the metal atoms on the QD surface to which the OA is bound may also be removed during ligand exchange. Though necessary for electronic coupling, ligand exchange in QD solids may also change the QD surface stoichiometry and inadvertently introduce dangling bonds and other localized electronic traps[46, 60]

Ligand exchange may be accomplished either in solution ('solution-exchange') or after a solution of QDs has been deposited ('solid-state exchange'). For the devices and QD solids studied in this thesis, solid-state exchange procedures that use spincoating are used. As illustrated schematically in Figure 1.3, spincoating involves first depositing a solution of QDs stabilized by native organic ligands dispersed in a non-polar solvent onto a substrate. The spincoater is run, which deposits a thin, dry film of ~ 20 nm of QDs depending on the spin-speed, QD concentration, and solvent drying time. More compact ligands to increase electronic coupling in the QD array are then introduced in the second step. This exchange solution is typically allowed to sit on the substrate for ~ 60 s before being spun dry. In the third step, the QD film is rinsed with non-polar solvent to remove excess compact ligand from the surface. This process is repeated until the desired film thickness is achieved. For FETs, the desired thickness is typically ~ 50 nm, whereas for PV devices, thicker films of $\sim 100 - 200$ nm are required. The charge transport mechanisms exhibited in these QD solids will be discussed in detail in Section (1.4)

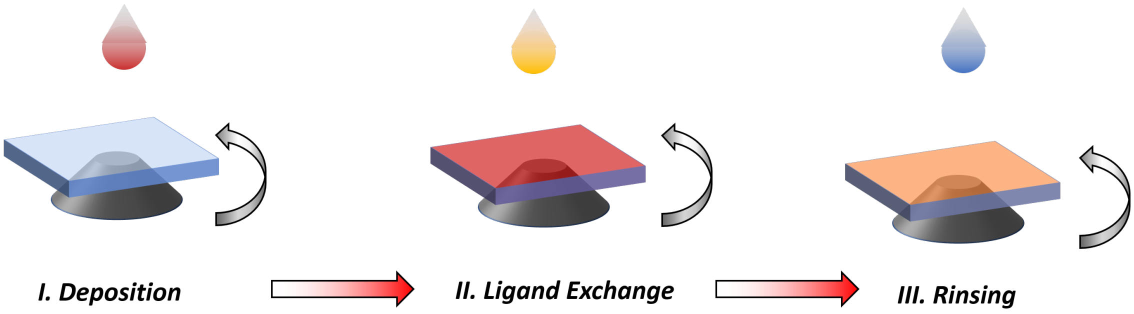

Figure 1.3: Schematic of the spincoating process, showing (I) deposition of NC solution, (II) ligand exchange, and (III) subsequent rinsing in polar solvent.

1.3 JV Characteristics of PV Devices

As mentioned, QD solids offer promising avenues for low cost PV devices. QD PV devices can be constructed in p-n, Schottky, or p-i-n junction architectures. A schematic of a simple p-n junction PV device is provided in Figure 1.4, with a depletion region W that extends over both the n-side with length W_n and the p-side with length W_p. When a positive voltage (forward bias) is applied to the device, the minority carrier densities are changed from their equilibrium concentrations, implying that the product of the carrier concentrations $pn \neq n_i^2$. On the p-side of the junction far from the depletion region, the holes are still in equilibrium with the valence band. Similarly, for $x >> W_n$, the electrons are in equilibrium with the conduction band. As a result, we can define the quasi-Fermi levels E_{Fn} and E_{Fp}:[139]

$$\begin{aligned} E_{Fn} &= E_i + k_B T \ln(\frac{n}{n_i}) \\ E_{Fp} &= E_i - k_B T \ln(\frac{p}{n_i}) \end{aligned} \tag{1.3.1}$$

where k_B is Boltzmann's constant, E_i is the intrinsic energy level of the semiconductor, and n_i is the intrinsic carrier concentration. The pn product is:

$$pn = n_i^2 \exp(\frac{E_{Fn} - E_{Fp}}{k_B T}) \tag{1.3.2}$$

Under forward bias, $E_{Fn} - E_{Fp} > 0$ and thus $pn > n_i^2$. This situation is illustrated schematically in 1.4, which displays the variation in E_{Fn} and E_{Fp} with distance. The hole concentration on the p-side (p_p) drops dramatically across the junction, and equilibrates to the minority hole concentration on the n-side (p_n). The same dynamics are observed across the junction for electrons. An applied electric field $V = \frac{E_{Fn} - E_{Fp}}{q}$ drops across the depletion region which drives charge carrier drift across the junction. This gives rise to an electron current $J_n = \mu_n n \nabla E_{Fn}$ and a hole current $J_p = \mu_p p \nabla E_{Fp}$, where $\mu_{n,p}$ are the electron and hole mobilities, respectively.

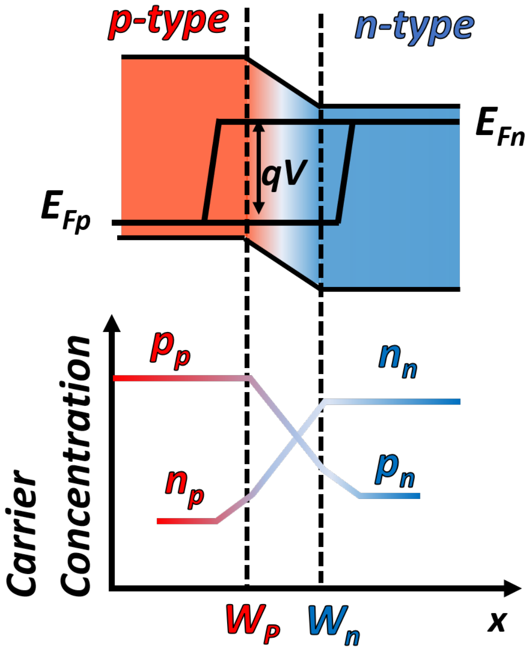

Figure 1.4: (Energy band diagram with quasi Fermi levels E_{Fn} and E_{Fp} and carrier distributions under forward bias, reproduced after [139].

In the dark, the total current density of a PV device device J at voltage V is given by the Shockley diode equation:[139]

$$J = J_p + J_n = J_0[\exp(\frac{qV}{nk_BT}) - 1] \tag{1.3.3}$$

where J_0 is the saturation current density, n is the diode ideality fator, and T is the temperature. J_0 is the saturation current, which ideally depends only on the minority carrier diffusion lengths on each side of the heterojunction:[139]

$$J_0 \equiv \frac{qD_p p_n}{L_p} + \frac{qD_n n_p}{L_n} \tag{1.3.4}$$

where $D_{n,p}$ are the electron and hole diffusivities, respectively, and $L_{n,p}$ are the corresponding carrier diffusion lengths. We note that the physical interpretation of parameters in equation (1.3.3) may not be obvious in systems where the current density exhibits large deviations from the ideal diode equation (equation (1.3.3)).

The low forward bias region ($V \lesssim 0.3$ V) captures the transport physics of the diode device when the injected minority-carrier density on each side of the heterojunction is small compared to the majority carrier concentration. The current density increases exponentially at a rate determiend by n and J_0. In PbS QD PV devices, J_0 ranges from $\sim 10^{-4} - 10^{-7}$ mAcm^{-2} for both Schottky and pn device architectures.[29, 158, 28] The ideality n in a diode has been shown to be linked to the dominant charge recombination mechanism in the PV device. In the ideal case, $n = 1$, charge recombination occurs as excited electrons in the conduction band relax to the valence band. Trap-assisted recombination, which will be discussed in some detail in Section 1.3, is indicated when $n = 2$. We note that n may also describe other non-idealities, such as barrier lowering in Schottky junctions due to large interfacial charge densities.[127]

The same diode equation (1.3.3) governs the current density under illumination, only the photocurrent J_L increases as incident solar radiation excites excess carriers in the device. The total current density is a summation of the dark and illuminated current, and may be written as:

$$J = J_0[\exp(\frac{qV}{k_BT}) - 1] - J_L \tag{1.3.5}$$

The open circuit voltage V_{oc} of the PV device is the maximum attainable voltage in the cell due the difference in E_{Fn} and E_{Fp} under solar irradiation, and therefore describes how much charge may accumulate in the PV device under operating conditions. V_{oc} may be obtained by setting $J = 0$:

$$V_{oc} = \frac{k_BT}{q}\ln(\frac{J_L}{J_0}) \tag{1.3.6}$$

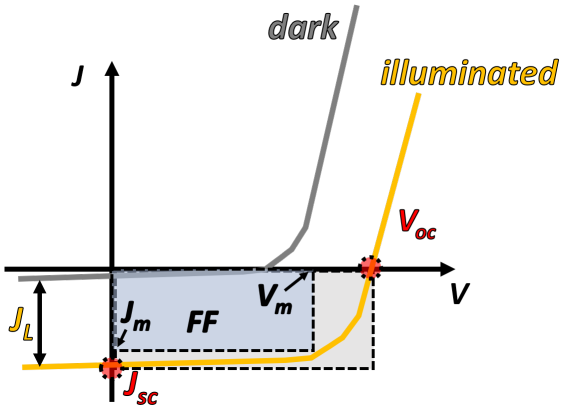

Figure 1.5: JV characteristics of a PV device under illumination with V_{oc} and J_{sc} indicated, along with FF and maximum voltage (V_m) and current (J_m) points.

V_{oc} is marked in Figure 1.5. Along with the illuminated short circuit current J_{sc} it defines the achievable power output P of the PV device. The fill factor (FF) describes the ratio $\frac{P_m}{P}$, where P_m is the ideal power output $P_m = J_m V_m$. The total power conversion efficiency (PCE) η of the device is defined by $\eta = \frac{P_m}{P_{in}}$ where P_{in} is the input power. The current PCE record in QD PVs is $\sim$ 11%.[82, 25]

1.3.1 Recombination Kinetics in Diodes

The excess charge carriers created under solar irradiation imply that $pn > n_i^2$. Equilibrium is restored as these excess carriers are eliminated *via* recombination processes.[139] Recombination encompasses several distinct charge relaxation processes within the semiconductor, including band-to-band electron-hole recombination or trap-assisted recombination in which either an electron or a hole are captured by a discrete energy state within the bandgap.

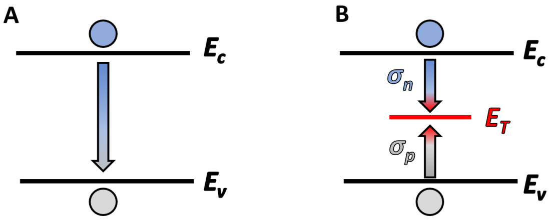

Figure 1.6: (A) Band-band recombination (B) Trap assisted recombination in defect level E_T with electron capture cross section σ_n and hole capture cross section σ_p.

These two processes are diagrammed schematically in Figure 1.6. Figure 1.6A shows band-to-band recombination, in which an electron from the conduction band recombines directly with a hole from the valence band. Band-to-band recombination events encompass a negligible proportion of total recombination processes exhibited in QD solids used for PV devices. Recombination instead is dominated by non-radiative events that take place in a defect DOS N_T that lies within the bandgap and are possibly localized on the surfaces of QDs in the assembly.[139] These processes are known as Shockley-Read-Hall (SRH) recombination, and are depicted schematically in Figure 1.6B. To simplify the picture, we consider the effect of discrete trap levels with an energy E_T inside the bandgap. In general, these defects may be capable of capturing holes or electrons. Assuming they are far enough from the band-edge to be non-degenerate (e.g., for an electron trap of E_T, $E_c - E_T > 3k_BT$), their population may be calculated by using Boltzmann statistics. The net transition rate U may be defined as:[139]

$$U = \frac{\sigma_n \sigma_p v_{th} N_T (pn - n_i^2)}{\sigma_n [n + n_i \exp(\frac{E_t - E_i}{k_B T})] + \sigma_p [p + n_i \exp(\frac{E_i - E_t}{k_B T})]} \tag{1.3.7}$$

where σ_n and σ_p are the electron and hole capture cross sections in units of cm^2 and $v_{th} = \sqrt{\frac{3k_BT}{m}}$ is the root mean square of the velocity of the charge carriers. The terms in the denominator describe the population of each carrier type weighted by the capture cross section for the defect. The numerator is proportional to $pn - n_i^2$, implying that whenever $pn > n_i^2$, $U > 0$ and carriers are eliminated *via* SRH processes. Note that U is maximized with $E_t = E_i$, meaning that for a continuous spectrum of defects throughout the bandgap, those with energies lying close to mid-gap will be the most effective recombination centers. Using this approximation, we can re-write equation (1.3.7) as:

$$U = \frac{\sigma_n \sigma_p v_{th} N_T (pn - n_i^2)}{\sigma_n (n + n_i) + \sigma_p (p + n_i)} \tag{1.3.8}$$

Restricting our focus to the example of low level injection in n-type semiconductors, we can further simplify equation (1.3.8):

$$U = \frac{\sigma_n \sigma_p v_{th} N_T [(p_{n0} + p)n - n_i^2)}{\sigma_n n} \approx \sigma_p v_{th} N_T \Delta p \equiv \frac{\Delta p}{\tau_p} \tag{1.3.9}$$

where the lifetime $\tau_p \equiv \frac{1}{\sigma_p v_{th} N_T}$. Similarly, the electron lifetime in a p-type semiconductor may be defined as $\tau_n = \frac{1}{\sigma_n v_{th} N_T}$. The carrier lifetimes in SRH recombination are thus inversely proportional to trap density N_T.

1.4 Charge Transport in Disorderd QD Arrays

1.4.1 Emergent DOS in Array of Potential Wells and DC Transport

As commented in Section (1.3), the diode equation generally provides adequate phenomological description of macroscopic JV characterisitcs within QD PV devices. However, the microscopic transport physics that gives rise to these ensemble properties is complex. In this section, we discuss the physical models of charge transport in spatially and energetically disordered materials, which rely on quantum mechanical arguments and classical statistical mechanics.

Charge transport across disordered QD arrays may be expected to occur *via* the same conduction mechanisms exhibited by Fermi glasses, a broad class of non-crystalline materials that lack long range spatial order[105]. Much like in crystalline materials, solutions of the Schrödinger equation in these non-crystalline media give rise to a DOS $N(E)$ defined as the number of eigenstates in a unit volume for the electron with a given spin and energy between E and $E + dE$ to occupy. The total number of electrons within the energy range E and $E + dE$ is still given by the

Fermi function $f(E)$.

As first shown by Anderson, Fermi glasses differ from crystalline solids in that the structural disorder of in a Fermi glass yields solutions to the Schrödinger equation that are localized in space.[5] To see this, consider a series of regularly spaced potential wells which produces a narrow band of levels $N(E)$, as depicted in Figure 1.7A. Assume that the wells be far apart enough such that the overlap of the wavefunctions on individual wells ϕ_r is small. Let n denote the n-th well and R_n the n-th lattice site. The Bloch wavefunction ψ_k for an electron in this potential array is:

$$\psi_k(x, y, z) = \sum_n \exp(ik \cdot R_n)\phi(r - R_n) \tag{1.4.1}$$

Take ϕ to be a spherically symmetric (s) wavefunction. If w_0 is the energy of a single well, the energy for the electron in the lattice in Figure 1.7A is:

$$E = w_0 + w_k \tag{1.4.2}$$

where $w_k = -2I(\cos(k_x a) + \cos(k_y a) + \cos(k_z a))$. I is the transfer integral that describes the overlap of single well wavefunctions ϕ between two adjacent sites, defined in the radial coordinate $r = \sqrt{x^2 + y^2 = z^2}$ as:[105]

$$I = \langle \phi^*(r - R_n)|H|\phi(r - R_{n+1}\rangle \tag{1.4.3}$$

Here, H is the Hamiltonian, and, in general, I may be written as $I_0\exp(-\alpha R)$ as in the case for the exponential decay of a wavefucntion outside of the simple, isolated potential well of QD.[160] $\alpha = \frac{\sqrt{2mw_0}}{\hbar}$ is defined so that $\exp(-\alpha R)$ is the rate at which the wavefunction falls off with distance. The effective mass at the bottom of the band in this formulation is $m^* = \frac{\hbar}{2Ia^2}$ and the bandwidth of the extended state transport levels in $N(E)$ is written $B = 2zI$, implying that as the wavefunction overlap between adjacent sites increases, the bandwidth available for charge transport across the crystal increases.

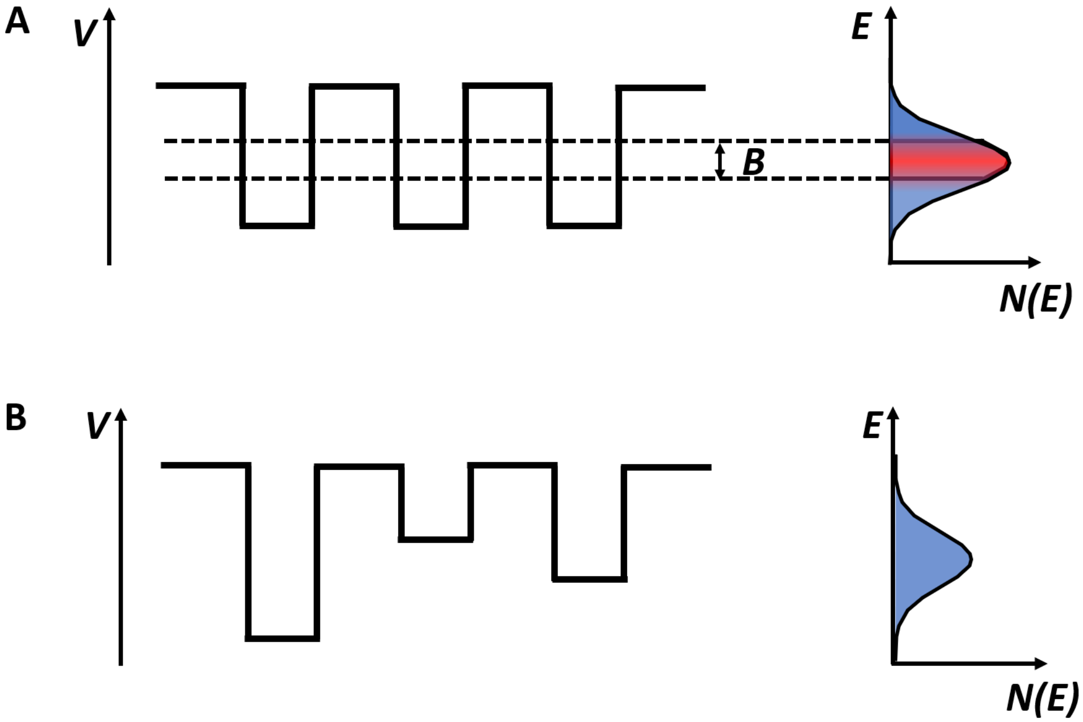

Figure 1.7: (A) Crystalline array of wells with potential V_0 that give rise to a band of extended states with bandwidth B inside $N(E)$. (B) Disorder introduced into array by adding a random potential with variance $\frac{1}{2}V_0$ giving rise to an $N(E)$ characterized by strong localization. Adapted from Ref [105].

Now consider the case where the array of potentials becomes non-periodic, either by random fluctuations in well separation a or by the addition of a random potential $\frac{1}{2}V$ to each well (Figure 1.7B). Anderson originally supposed the perturbation potential V assumes values at $\pm V_0$ so that the spread of energies is V_0;[5] however, other distributions, such as the Gaussian, can be considered as well.[105]

Considering only the second form (energetic disorder), Mott and Massey used the Born approximation to calculate the mean free path L of an electron in a disordered energetic landscape:[106]

$$\frac{1}{L} = \frac{2\pi}{\hbar}\frac{1}{2}(\frac{1}{2}V_0)^2 a^3 \frac{N(E)}{u} \tag{1.4.4}$$

where $\frac{1}{2}V_0$ is the variance of the potential fluctuation and E and u are the energy and carrier velocity defined at E_F. Assuming the 3D Fermi surface is spherical and that $N(E)$ may be written as a function of the free electron energy $E = \frac{\hbar^2 k^2}{2m}$, Mott goes on to show that equation (1.4.4) may be simplified to a simple constant:

$$\frac{a}{L} = \frac{1}{32\pi}(\frac{V_0}{I})^2 \tag{1.4.5}$$

In any solid material, Ioffe and Regel have shown that L may not exceed the lattice spacing in any diffusive transport process.[105] Stated another way, this fundamental limit implies that the shortest mean free path for any charge transport process occurs when the wavefunction loses phase coherence as it travels from site to site. With this criterion, the wavefunction ψ in the random potential lattice of Figure 1.7B becomes:[105]

$$\psi_k(r) = \sum_n A_n \phi(r - R_n) \tag{1.4.6}$$

where A_n has random phases and amplitudes, as depicted in Figure 1.8A. Non-localized transport in a non-crystalline potential landscape may then be defined as when $L \approx a$. From equation (1.4.5), the potential barrier V_0 can then be written:

$$\frac{V_0}{I} = \sqrt{32\pi} \approx 10 \tag{1.4.7}$$

For randomly close packed lattices with a coordination number $z = 6$, this becomes:[105]

$$\frac{V_0}{B} \approx 0.83 \tag{1.4.8}$$

implying that the variation in the potential distribution is directly proportional to the bandwidth B that characterizes $N(E)$. If the bandwidth (or wavefunction overlap I) is high, extended state conduction mechanisms may occur for larger variation in the energetic landscape. For a smaller B or I, the allowed range of V_0 that can give rise to coherent charge transport across multiple wells is smaller. For negligible B or I, all wavefunctions are localized, and a broad Gaussian distribution of $N(E)$ can be expected (Figure 1.7B).[105]

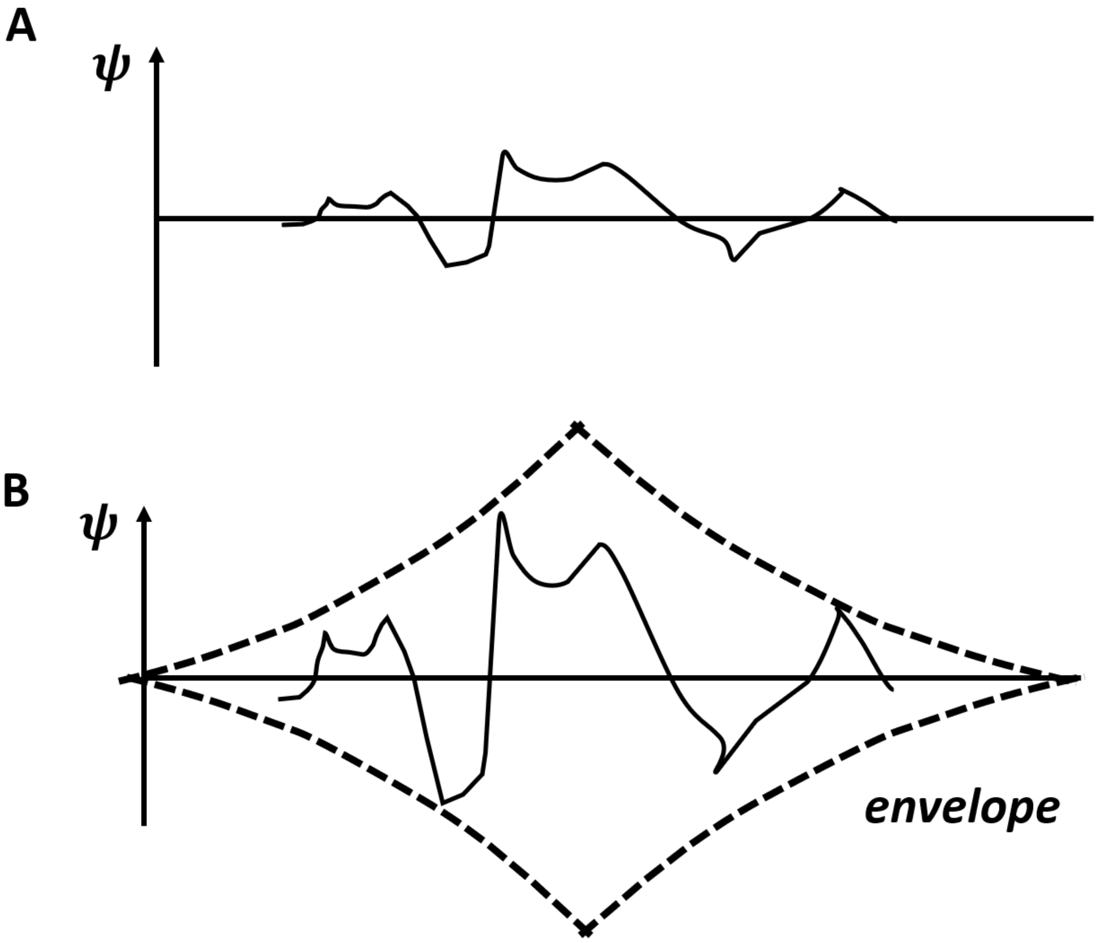

Figure 1.8: Form of the ψ in the Anderson model for (A) extended state conduction where $L \approx a$ and (B) localized conduction. Adapted from Ref [105].

Similarly, for large disorder V_0, all wavefunctions become localized, and equation (1.4.6) takes on an exponential decay term:

$$\psi_k(r) = \sum_n A_n \phi(r - R_n) \exp(-\alpha R) \tag{1.4.9}$$

The wavefunction described by equation (1.4.9) is depicted schematically in 1.8B.

Charge motion in strongly localized states is characterized by overcoming the energy barrier $\Delta E = E_{n+1} - E_n$ between the n-th site and the adjacent $n + 1$ site. Electron transmission between sites thus requires an electron to 'hop' over ΔE by acquiring (or dissipating) sufficient energy, which is typically acquired thermally. The hopping rate Γ between sites in disordered materials may be written [100]:

$$\Gamma(R, E_A) = \Gamma_0 \text{exp}(-\alpha R - \frac{E_A}{k_B T}) \tag{1.4.10}$$

where α and R take on the definitions given above, k_B is Boltzmann's constant and $E_A = \max(\Delta E, 0)$ is the activation energy of the charge hop given by ΔE for hop upward in energy or 0 for a jump downwards in energy. Equation (1.4.10) defines the Miller-Abrams hopping regime, also known as the nearest neighbor hopping (NNH) regime, in which thermal activation of charge hopping follows a simple Arrhenius law $\Gamma \propto \frac{1}{T}$.

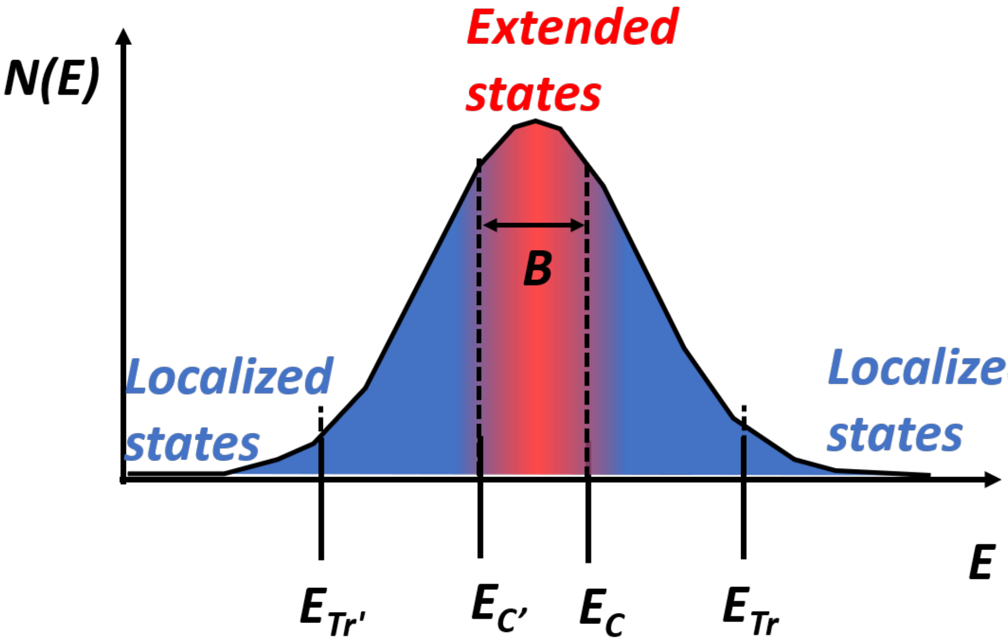

Figure 1.9: $N(E)$ for amorphous bulk materials which exhibit extended and localized states separated by E_C (E_C). The onset of DC conduction occurs at the transport level E_{Tr}.

The DC conductivity in a disordered solid arises from many such charge hops, and therefore follows the same Arrhenius activation law:[105]

$$\sigma(0) = \sigma_0 \exp(-\frac{E_A}{k_B T}) \tag{1.4.11}$$

where σ_0 is a pre-term which may itself be thermally activated.

Since $\sigma(0)$ arises from an ensemble of many charge hopping processes, the value of E_A in equation (1.4.11) depends on the distribution of energy states $N(E)$. An example $N(E)$ for the case in which wavefunction overlap among potential wells creates a band of extended states with bandwidth B (Figure 1.7A) is illustrated in Figure 1.9. Thermally activated hopping transport can occur within the band tails of $N(E)$ (blue region) provided $N(E)$ is sufficiently dense to allow nearest neighbor sites to form a percolation network that extends across the solid.[105, 36] In this case, the energetic onset of hopping conduction is the transport level E_{Tr}, and $E_A = E_{Tr} - E_F$ indicates the energetic barrier charge at the Fermi level must overcome to hop to adjacent sites.

As charge gains sufficient thermal energy to access regions of higher state density in $N(E)$, the conductivity can be expected to increase. In bulk amorphous materials, transport at sufficiently high temperatures may also contain contributions from carriers thermally excited from localized portions of $N(E)$ into extended states at E_C that arises from the overlap of wavefunctions in the potential well. In this case, $E_A = E_C - E_F$.

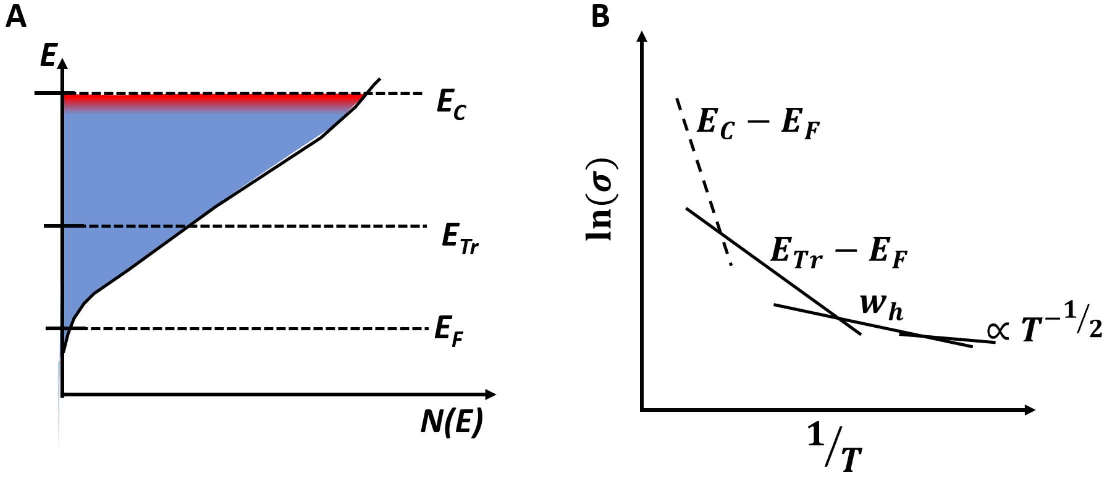

Figure 1.10: (A) $N(E)$ exhibiting broad distribution of transport levels from E_{Tr} to E_C and a finite DOS at E_F, all of which may contribute to charge hopping. (B) Temperature-dependence of the conductivity based on $N(E)$ in (A). Dashed line at $E_C - E_F$ imply that these conduction mechanisms are not typically observed in QD solids. Adapted from Ref[105].

For a finite density of states at the Fermi energy, there will be a contribution of carriers hopping in localized states with energies near E_F, as depicted schematically in Figure 1.10A. This contribution will have a similar temperature-dependence a equation (1.4.11) above:

$$\sigma(0) = \sigma_0 \exp(-\frac{w_h}{k_B T}) \tag{1.4.12}$$

where w_h is the hopping energy and is generally of order $k_B T$.

The form of equation (1.4.10) implies a competition between the term that describes wave-function overlap $\propto \exp(-\alpha R)$ and the thermal activation term $\propto \exp(-\frac{E_A}{k_B T})$. At low enough temperature, the activation term becomes negligible as electrons do not have sufficient energy to hop to the adjacent site. As Mott and Austin first pointed out, charge hopping processes may then occur *via* tunneling transmission between spatially distant sites.[6] In this case, the conductivity can be expected to have a weaker thermal activation:

$$\sigma(0) = \sigma_0 \exp(-\frac{B}{T^{\frac{1}{4}}}) \tag{1.4.13}$$

with $B = 2[\frac{\alpha^3}{k_B N(E_F)}]^{\frac{1}{4}}$.[105] This type of hopping, known as variable range hopping (VRH) can be expected at all temperatures, yet usually does not appreciably contribute to the measured conductivity at high temperature.

Equations (1.4.11), (1.4.12), and (1.4.13) imply that the broad distribution of energy states $N(E)$ in a disordered solid may be interrogated experimentally be determining the temperature dependence of the DC conductivity. This is depicted schematically in Figure 1.10B, which illustrates the temperature dependence of the conductivty expected for $N(E)$ given in 1.10A.

QD solids exhibit all the conduction mechanisms discussed above,[91, 49, 94] with two notable exceptions:

1. Aside from notable examples of local 'mini-band' transport in coupled QD systems that utilize short-chain metal chalcogenide or thiocyanate ligands, [26, 85] extended state conduction at E_C has yet to be widely observed in QD arrays with quantum confined constituent (i.e. non-fused) QDs typically used for PV devices, and

2. Quantum confinement in QD arrays results in a VRH temperature exponent $T^{-\frac{1}{2}}$ for highly doped QDs and $T^{-\frac{1}{/}4}$ for lightly doped QDs due to an appreciable coulomb gap in highly doped QDs [94].

The first exception implies that the DC conductivity at all temperatures in the QDs used for PV applications is governed by NNH. While an extended state band level E_C may be observed via optical absorption, the energy levels associated with typical DC conductivity in QD arrays is known to be smaller than E_C.[18] In QD solids, conduction occurs near the maximum of the $N(E)$, which is made up of localized states. For instance, the onset of DC conductivity in Pb-chalcogenide QD solids treated with hydrazine has been shown to coincide with the band tail level E_{Tr} marked schematically in Figure 1.10A.[77] The second exception implies that VRH conduction can be expected to exhibit a temperature exponent that depends on the specific form of $N(E)$.[94, 57, 130] Despite these discrepancies, experimental interrogation of the DC conductivity

$\sigma(0)$ can be an extremely useful tool for determining $N(E)$ in QD solids.

1.4.2 AC Conductance in Disordered Materials

QD solids, like amorphous semiconductors, conducting polymers, organic semiconductors, and other disordered solids exhibit characteristic frequency dispersion in their conductivity.[36] At low ω, these materials display a constant total conductivity σ' that becomes strongly frequency-dependent at high ω, as exhibited in Figure 1.11A. Early attempts to measure the AC conduction mechanisms in amorphous semiconductors adopted an approximate power law for the AC conductivity

$$\sigma'(\omega) \propto \omega^s \tag{1.4.14}$$

where the exponent $s \approx 0.8$ for a wide range of amorphous semiconductors.[105] As discussed in the preceding section, Mott and Austin developed a pair approximation model invoking quantum mechanical tunneling between pairs of impurities to interpret this phenomena, in which s was assumed to be derived from a random distribution of tunneling distances.[6]. Extensions to the pair approximation model attempt to explain the smooth transition to frequency-independent conductivity at low frequency by adding a term $\sigma(0)$ due to DC conduction:

$$\sigma'(\omega) = \sigma(0) + \sigma(\omega) \tag{1.4.15}$$

The $\sigma(0)$ term is assumed to capture transport in extended states at the band edge. As a result, this model fails to adequately describe the constant conductivity at low ω for semiconductors where hopping is known to dominate DC conduction.[95]

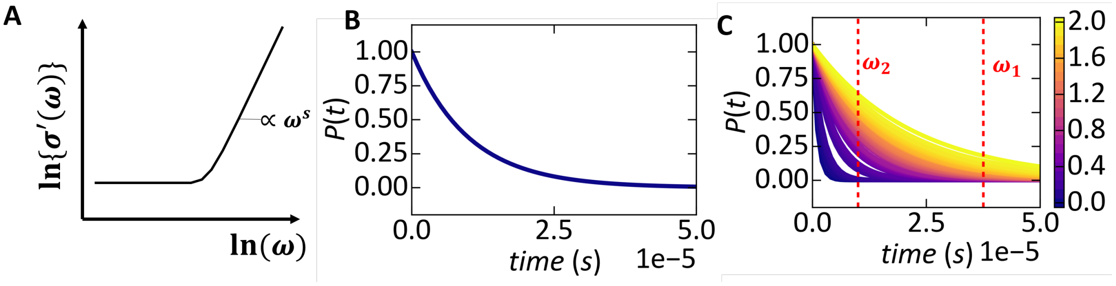

Figure 1.11: (A) Schematic of frequency dispersion in $\sigma(\omega)$ observed in a typical AC conductance measurement. (B) Probability $P(t)$ for a charge to remain at a given site in a solid with a single time constant $\tau = 10^5$ s^{-1}. (C) Distribution of $P(t)$ resulting from a broad Gaussian distribution $n(\tau)$ centered at $\tau_0 = 10^{-5}$ s^{-1}, with color bar indicating value of $\frac{\tau}{\tau_0}$. Test interrogation frequencies $\omega_1 = 2.67 \times 10^{-4}$ s^{-1} and $\omega_2 = 1.0 \times 10^5$ s^{-1} are indicated by dashed red lines.

More recent developments relying on continuous time random walks (CTRW) have posited that the that the probability of a charge hop P is constant in time so that $P(t + \Delta t) = P(t) = P_0 \exp(-\frac{t}{\tau})$, where τ is a characteristic relaxation time for the charge hop. The probability for a charge to occupy a given site therefore decreases exponentially.[36] This is illustrated in Figure 1.11B, which plots the $P(t)$ for a single charge at a given site within the semiconductor for $\tau = 10^{-5}$ s.

In amorphous semiconductors, τ itself is characterized by a distribution $n(\tau)$ resulting from the structural and energetic disorder in the material.[41] Figure 1.11C exhibits $P(t)$ for a range of τ values drawn randomly from a broad Gaussian distribution centered at $\tau_0 = 10^{-5}$ s. As the value of τ increases (yellow lines), the decay of $P(t)$ slows, indicating that the charge is more likely to remain at its initial location. Conversely, for small τ (purple lines), $P(t)$ decays faster and the charge hops to the next available site quickly.

Measurements of $\sigma'(\omega)$ at a given test frequency $\omega_t = \frac{1}{\tau_t}$ act as an experimental limit for the interrogation of these charge hops. All hops with a time constant $\tau < \tau_t$ will be recorded by a measurement made at ω_t. Figure 1.11C exhibits the time limits interrogated by test frequencies

$\omega_1 = 2.67 \times 10^4$ Hz and $\omega_2 = 1 \times 10^5$ Hz (dashed red lines). Measurements made at ω_1 will be able to probe a broader set of charge hops, whereas hops associated with larger τ are invisible to ω_2. As a result, we expect differences in the total conductivity as the applied frequency of the measurement changes.

The observed frequency dispersion in $\sigma'(\omega)$ is therefore a result of the distribution of τ.[36] Amorphous materials generally exhibit a very broad $n(\tau)$, since the number of available paths for charge hopping and the distribution of activation energies for these processes scale with the structural and energetic disorder in the material. To obtain the total conductivity $\sigma'(\omega)$, we can integrate the product of $n(\tau)$ with a Drude-type conductivity expression:[105, 41]

$$\sigma'(\omega) \propto \int_0^\infty n(\tau)\frac{\omega^2\tau}{1+\omega^2\tau^2}d\tau \tag{1.4.16}$$

Obtaining the approximately linear dispersion relation $\omega = \omega^s$, $s \approx 0.8$ displayed in Figure 1.11A requires $n(\tau) \propto \tau^{-1}$. [41] Assuming this value, we obtain:

$$\sigma'(\omega) \propto \int_0^\infty \frac{\omega d(\omega\tau)}{1+\omega^2\tau^2} \propto \omega \tag{1.4.17}$$

The required form of $n(\tau)$ implies that τ itself is an exponential function. For hopping conduction in amorphous semiconductors, τ is assumed to be exponentially dependent on the energy barrier E separating two charge sites.[41, 36] Large hopping times are associated with overcoming large energetic barriers, whereas smaller hopping times result from barriers easily surmounted by the charge. τ is therefore given by:[41]

$$\tau = \tau_C \exp(\frac{E}{k_B T}) \tag{1.4.18}$$

where τ_C is a constant characteristic relaxation time.

Equation (1.4.18) is of fundamental importance for interpreting AC conductivity data, as it implies that the distribution of relaxation times $n(\tau)$ acts as a reporter for the density of states $N(E)$ available for charge hopping in an amorphous semiconductor. Energetically distant sites from a charge's initial position are associated with longer $\tau = \frac{1}{\omega}$, whereas sites much closer in energy that are available for charge hops have a much smaller τ (longer ω). This illustrated schematically in Figure 1.12B for the specific case of a broad Gaussian $N(E)$ centered at E_F (Figure 1.12A). Charge hops to sites around E_F require small energies and thus τ is small. The shape of $N(E)$ implies that $n(\tau)$ in this region should be large. Hops further away in energy correspond to the tail of $N(E)$, implying that $n(\tau)$ at large τ is much smaller. The corresponding distribution of hop frequencies $n(\omega)$ can be made by inverting the abcissa of $n(\tau)$ vs. τ. Equation (1.4.18) allows us to reconstruct the Gaussian DOS in Figure 1.12A. Different distributions of $N(E)$ should give analogously different distributions in $n(\tau)$ and result in slightly different frequency-dispersion in $\sigma'(\omega)$.

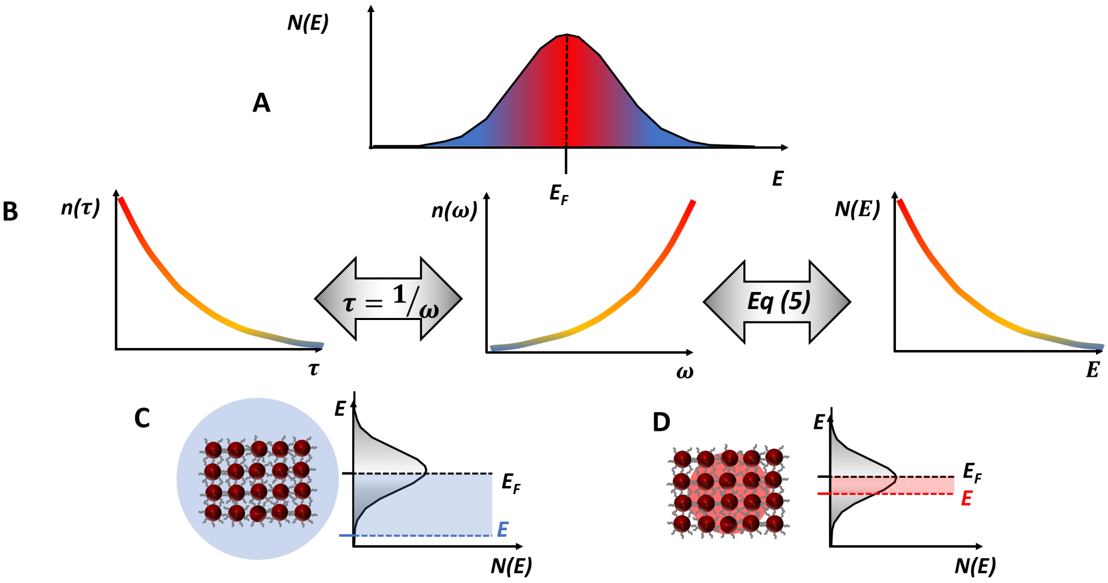

Figure 1.12: (A) Gaussian $N(E)$ in an amorphous semiconductor give rise to (B) $n(\tau)$ and $n(\omega)$ swept out by measurement. These distributions may be converted into an picture of $N(E)$ *via* equation (1.4.18). (C) Spatial and energetic radius probed by low measurement energies E_ω. (D) Spatial and energetic radius probed by high measurement energies E_ω.

The availability of greater portions of $N(E)$ for charge hopping at low applied frequency implies that larger volumes of the amorphous semiconductor may be probed in measurements of $\sigma'(\omega)$. This is illustrated in Figure 1.12C, which shows a measurement radius that includes an entire array of sites (schematically illustrated as a QD array). The energetic difference from E_F is also highlighted. At sufficiently low applied frequencies, a nearly infinite percolation path in the material is formed, allowing charge to hop across the entire array of sites. The constant $\sigma'(\omega)$ at low frequency (Figure 1.11A) is therefore an indication that the DC limit of the hopping conductivity is reached.[36] In general, the inclusion of all parts of $N(E)$ implies that the DC hopping conductivity is dominated by overcoming the energetic barriers in the solid to form a continual percolation path.

At higher frequencies, smaller energetic distances from E_F are available for charge to hop into. This results in a narrowing of the hopping radius available for each electron, as illustrated in Figure 1.12D. As a result, transport is dominated by hopping in finite clusters where the energetic barrier for a hop is low. The pronounced enhancement in $\sigma'(\omega)$ as frequency increases is thus a result of more hops occurring in energetic and spatial regions with large jump probability.[36]

CTRW models are thus able to explain the approximate power law (1.4.14) in terms of a distribution of relaxation times which is intimately related to $N(E)$ and thus to the disorder in the material. Depending on the specific model invoked, the exponent s is interpreted differently, but generally is related to the energetic barrier between hopping sites. Among the most widely accepted models is the random free energy barrier model, which assumes a distribution of energy barriers and an exponent s given by:[36]

$$s = 1 - \frac{T}{T_0} \tag{1.4.19}$$

where $k_B T_0 = \frac{1}{2} E_A$, characterizes the activation energy of DC conduction.

Despite their differences, these models allow for the inclusion of loss peaks in $\sigma'(\omega)$ at low and high frequency. Loss peaks occur at applied frequencies $\omega_0 = \frac{1}{\tau_0}$ that are resonant with the charge hopping time τ.[111] These peaks therefore indicate sub-regions of favorable charge hopping paths, which may be super-imposed on the broad distributions of $n(\tau)$ [41]. This is illustrated schematically in Figure 1.13A. A Gaussian $N(E)$ with a shoulder due to a sub-distribution of states centered around energy E_T gives rise to a corresponding small peak in $n(\tau)$. Experimentally, the convolution of these two regions of high $N(E)$ may be probed with the use of equation (1.4.18) (Figure 1.13B). In dielectric spectroscopy of high mobility semiconductors such as CIGS, these loss peaks indicate SRH recombination between band-edge states and localized defect state.[150, 112] This will be discussed in Chapter 2. In low mobility, disordered materials, these features in $N(E)$ indicate states important for forming percolation pathways for DC transport.[36]

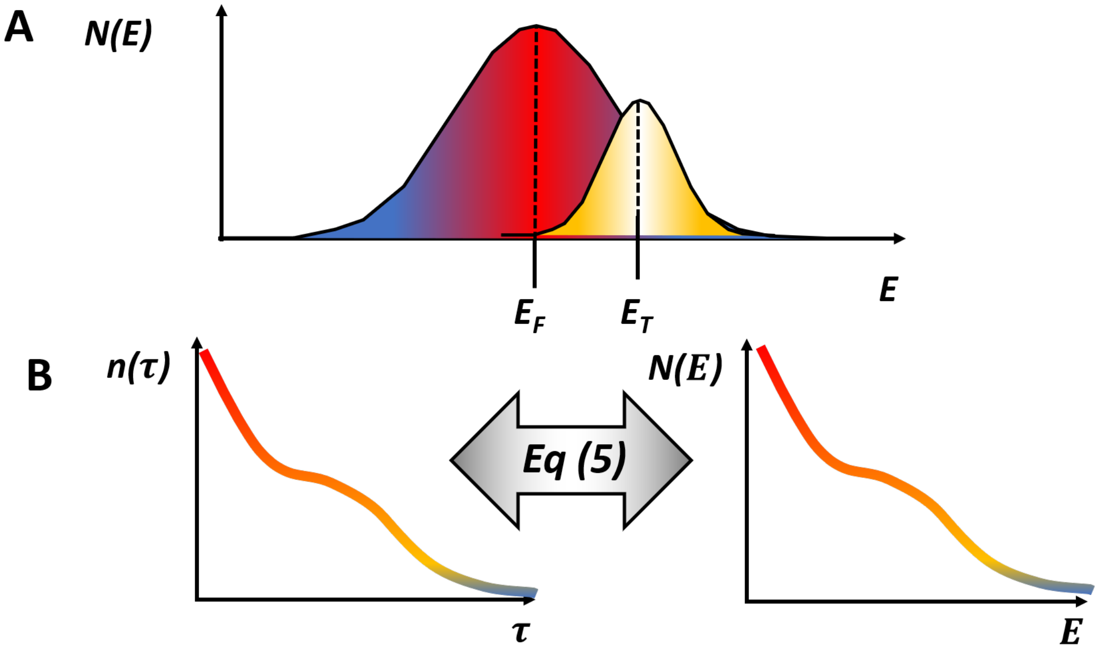

Figure 1.13: (A) Gaussian $N(E)$ with small shoulder due to a sub DOS centered at E_T which gives rise to (B) a corresponding peak in $n(\tau)$. The sub-peak may be experimentally resolved with the aid of equation (1.4.18).

1.5 Thesis Outline

This thesis uses AC and DC techniques to characterize the distribution of energy states in QD solids in functional device geometries. In Chapter 2, we describe in detail the physical models used to interpret frequency-domain measurements in terms of charge dynamics in semiconductors. We then discuss the particulars of the thermal admittance spectroscopy (TAS), drive level capacitance spectroscopy (DLCP), and impedance spectroscopy (IS), which we use to characterize the time constant dispersion resulting from charge recombination and transport in fully functional QD PVs. In Chapter 3, we apply these techniques to a Schottky junction PV device. The simplicity of this single carrier device structure allows us to build a full picture of ensemble charge dynamics from a combination of temperature- and frequency-dependent conductance and capacitance measurements. Chapter 4 details the application of these techniques to PbS QD heterojunction PV devices. Using IS and TAS, we show how interfacial defects provide effective centers for both electron and hole recombination, limiting V_{oc}. In Chapter 5, we apply these techniques to p-i-n device architectures with a halide-capped PbS QD absorber layer. Though the complexity of this device structure limits the firm conclusions that can be drawn, we posit the presence of two electron transport barriers within the device, and use illumination in TAS and DLCP to corroborate the presence of a recombination center for photogenerated charge.

Chapter 2

Frequency Domain Characterization of the Density of States in Disordered Materials

2.1 Introduction

As discussed in Chapter 1, the energetic and spatial disorder inherent in QD solids results in a range of carrier transport phenomena. To a good approximation, these transport processes may be modeled by considering charge hopping over a distribution of energy barriers. We further discussed how these energetic scales translate into spatial lengths and a broad distribution of characteristic charge hopping times.

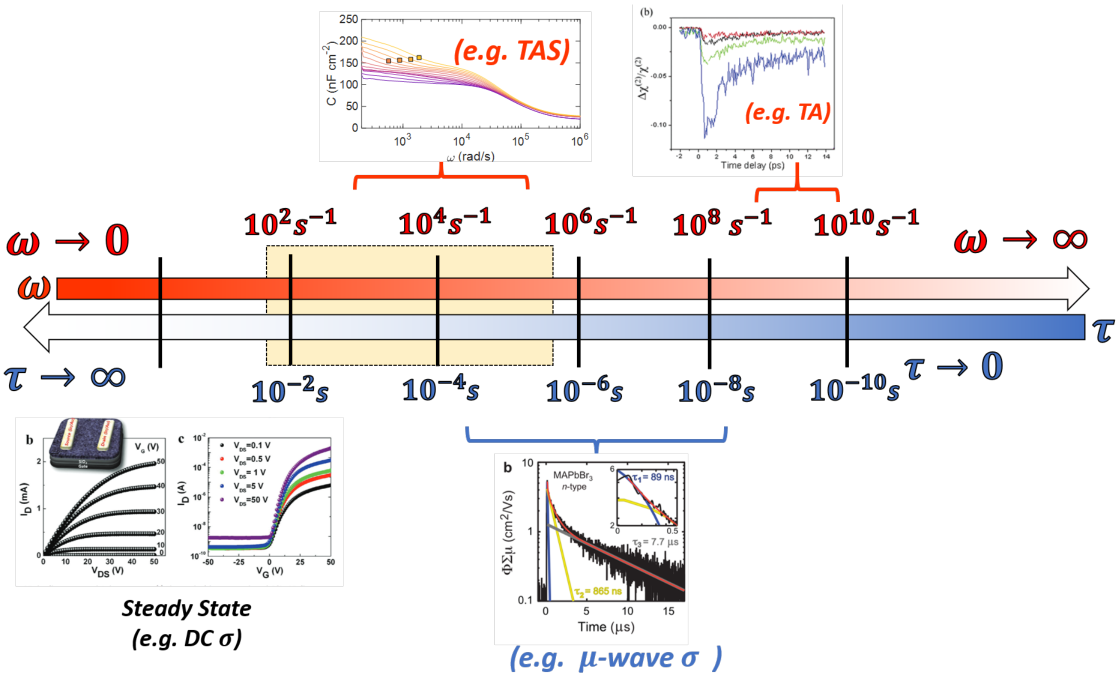

Figure 2.1: Characteristic time and frequency scales associated with charge transport measurements. Credit to references [26, 40, 67].

In this chapter, we discuss spectroscopic techniques that access different regions of the time domain *via* the application of an AC bias with frequency ω. The AC frequencies used in these techniques allow for the experimental interrogation of sub-domains of charge dynamics. Figure 2.1 exhibits a few examples of the spectroscopic techniques used to interrogate charge dynamics in solution processable materials like QD solids, along with the time and frequency scales involved with the measurement. At the highest frequencies and shortest time scales, measurements such as transient absorption (TA) have been used to probe carrier dynamics in QDs within 10^{-12} s after optical excitation.[99, 67] Microwave conductivity measurements have also been applied to QD solids[137, 116, 47] and perovskite materials[40] to probe charge diffusion lengths on time scales of $\sim 10^{-6} - 10^{-9}$ s. At $\omega = 0$ ($\tau = \frac{1}{\omega} \to \infty$), DC conductivity measurements are used to probe charge transport in QD solids in the steady state[26, 85, 159, 49, 91, 117, 115]

The main frequency-domain technique used in this thesis is impedance spectroscopy (IS), which probes timescales between $\sim 10^{-2} - 10^{-6}$ s ($\omega \approx 10^2 - 10^7$ rad/s). Because IS techniques probe an intermediate time scale between the steady state limit and higher frequency measurements such as microwave conductivity, it provides crucial information that bridges the physical models of charge dynamics at the DC limit and within individual QDs. This implies that IS is capable of probing mesoscopic scales involving both entire QD solids and small clusters of QDs.

In the next section, we discuss the physical models that underlie IS in semiconductor materials by discussing the capacitance-voltage (CV) measurement. We then go over the salient details needed to understand the IS technique. Afterward, we examine thermal admittance spectroscopy (TAS) and drive level capacitance profiling (DLCP), two important IS techniques used to study majority carrier charge dynamics in metal semiconductor and pn junctions under reverse bias. Finally, we discuss the instrumentation used to make these measurements.

2.2 Capacitance-Voltage

Though IS is a powerful experimental technique capable of providing useful information on charge relaxation processes in complex systems, the interpretation of IS spectra is not unambiguous. In semiconductors, the theory of the frequency- and voltage-dependence of the capacitance in a diode device can be used to guide interpretation of IS spectra. At an ideal semiconductor-metal junction, the depletion region behaves in many respects like a parallel plate capacitor. Using this model as a basis, measurements of the junction capacitance at zero or reverse bias can be used to gain information about barrier height and energy levels within the semiconductor.

An ideal n-type Schottky contact is depicted in Figure 2.2A, with the corresponding charge density profile in Figure 2.2B [127]. Under zeros bias, the bands assume the form of the solid lines; as reverse bias V_R is applied, electrons shift further away from the interface and the depletion region width increases from w to $w + \Delta w$. The bands shift and assume the form of the dashed lines. The change in the depletion region charge density gives rise to a change in capacitance. The application of V_R may also give rise to a reverse bias current. To aid in the analysis of the charge dynamics under reverse bias, an equivalent circuit of the junction can be used which consists of a parallel conductance (specified by resistance R) and capacitor C, as depicted in Figure 2.2C.

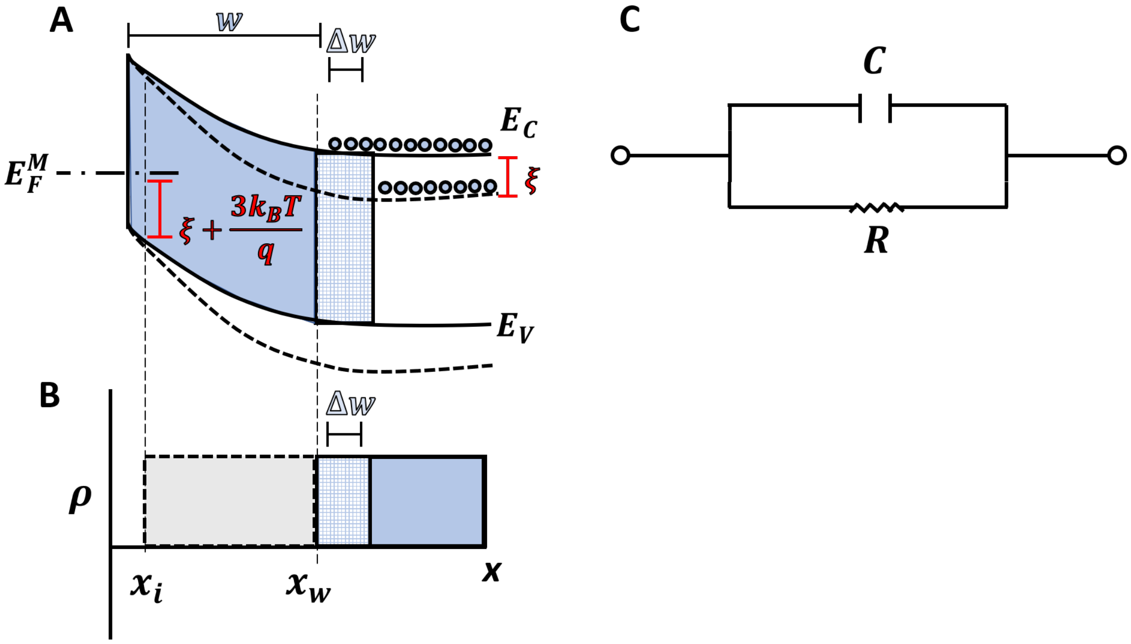

Figure 2.2: (A) Schematic of Schottky barrier under reverse bias. Band positions under applied bias V_R are shown with solid line, and shift in band bending induced by applied AC signal depicted by dashed line. Reproduced from Reference [127]. (B) Charge density n due to mobile charge carriers outside depletion region (blue) [127] with ionized depletion density in in gray. (C) General equivalent circuit describing junction charge dynamics.

When the applied bias changes with the application of V_R, the resulting current contains two contributions:

- a displacement current $J_d = \varepsilon_S \frac{\partial \mathcal{E}}{\partial t}$, where $\mathcal{E}$ is the value of the electric field in the depletion region
- a conduction current J_c that itself is made up of two components:

- a drift and diffusion current J_{c1} resulting from electrons injected over the barrier and into the semiconductor
- a current J_{c2} that charges (or discharges) regions of the semiconductor where the depletion region charge density changes as bias is applied.

If the bias V_R modulates sinusoidally with time, J_{c1} will always be in phase with V_R, and is thus responsible for the parallel conductance in the equivalent circuit of Figure 2.2C. The components J_{c2} and J_d are in phase-quadrature with V_R. Since they are 90^{o} out of phase with the input signal, these currents make up the parallel capacitance in Figure 2.2C.

We will now describe how the capacitance changes with V_R in the ideal situation depicted in the band diagram of Figure 2.2A and charge density profile in Figure 2.2B. For $x > x_i$, $E_F^m - E_{V(x_i)} > \xi + \frac{3k_BT}{q}$, where E_F^m is the Fermi level of the metal and ξ is the energy difference between E_F^m and the bottom of E_V. As a result, though there may be a significant concentration of minority carrier holes at the interface due to the band offset, the density of holes in the bulk remains negligible. For $x < x_w$, $E_C(x_w) - E_C(\infty) > \frac{3k_BT}{q}$, and the mobile electron density between x_w and the interface is tiny. As a result, for $x_i < x < x_w$, the total charge density is given by the charge of ionized donors within the depletion region (gray box) and is independent of time. As reverse bias increases (decreases), electrons leave (enter) the depletion region from the bulk of the semiconductor. In this scenario, $J_{c2} = 0$ in the region between x_i and x_w, and J_d is the only part of the capacitance.

Between x_i and x_w (depicted in Figure 2.2A,B), the capacitance is $J_d = \varepsilon_S \frac{\partial \mathcal{E}}{\partial t} = C \frac{dV_R}{dt}$. Since $\mathcal{E}$ is a function of V_R, we can write, generally, $\frac{\partial \mathcal{E}}{\partial t} = \frac{\partial \mathcal{E}}{\partial V_R} \times \frac{dV_R}{dt}$, and obtain:

$$C = \varepsilon_s \frac{\partial \mathcal{E}}{\partial V_R} \tag{2.2.1}$$

$\mathcal{E}$ is evaluated between x_i and x_w where the total charge density is independent of time, allowing us to calculate $\mathcal{E}$ by applying Gauss's theorem to a surface bounded by one plane in the region $x_i < x < x_w$ and another plane far into the bulk of the semiconductor where the bands are flat. Varying the bias changes the depletion width and thus also modulates the charge enclosed by this surface. The resulting change in charge density is given by the change in donor charge density Q_d, such that $\varepsilon_s \Delta \mathcal{E} = \Delta Q_d$. Thus, from (2.2.1), we obtain:

$$C = \frac{\partial Q}{\partial V_R} \tag{2.2.2}$$

This result implies that the capacitance can be calculated by considering only the charge due to uncompensated donors within the depletion region. Assuming that the effects of holes at the interface can be neglected, the electric field at the barrier can be expressed as:

$$\mathcal{E}^2 = \frac{2q}{\varepsilon_s}[N_D(V_d - \frac{k_BT}{q}) + \frac{k_BTN_D}{q}\exp(\frac{-qV_d}{k_BT})] \tag{2.2.3}$$

where $V_d = V_{bi} + V_R$ is the diffusion voltage corresponding to the sum of the reverse bias voltage V_R and the built in voltage of the barrier V_{bi}, and N_D is the density of ionized donors. For $qV_d > 3k_BT$, the last term is zero and we obtain:

$$\mathcal{E}^2 = \frac{2q}{\varepsilon_s}[N_D(V_d - \frac{k_BT}{q})] \tag{2.2.4}$$

and thus $Q_d = \varepsilon_s \mathcal{E} = (2q\varepsilon_s N_D)^{\frac{1}{2}}(V_d - \frac{k_BT}{q})^{\frac{1}{2}}$. We can now solve for the differential junction capacitance $C = \frac{\partial Q_d}{\partial V_r} = \frac{\partial Q_d}{\partial V_d}$, obtaining:

$$C = (\frac{q\varepsilon_s N_D}{2})^{\frac{1}{2}}(V_d - \frac{k_BT}{q})^{-\frac{1}{2}} \tag{2.2.5}$$

Equation (2.2.5) implies that a graph of C^{-2} vs. V_R should give a straight line with slope $\frac{2}{q\varepsilon_s N_D}$ and intercept $V_{bi} + \frac{k_BT}{q}$. The same result can also be derived starting from the depletion approximation, which assumes that N_D decays to zero at the edge of the depletion region ($x = w$).

This simple analysis serves as the basis for traditional capacitance-voltage (CV) experiments in which a small AC perturbation of amplitude δV is super-imposed onto V_R. The resulting capacitance is measured as V_R is varied. However, in obtaining this result, we explicitly assumed that charge accumulates only at the edge of the depletion region. In non-ideal semiconductor junctions, in which defects at the interface and within the depletion region can trap charge, more detailed models are needed to account for the charging of these states in response to the change in bias.

2.2.1 Effect of Defects on Capacitance Response

Both interfacial and depletion-region defects alter the voltage-dependence of the charge within the semiconductor-metal junction. The capacitance of these non-idealities is in series or parallel with the capacitance of the depletion region, depending on the density and nature of the defects.[127] Since the depletion capacitance is non-linear with respect to voltage, the resulting total capacitance can be rather complicated.

Consider the effect of an interfacial defect layer with denisty D_S and sufficient thickness such that the population of interface states is determined by electron exchange with the E_c and E_v in the semiconductor, implying that the interface layer provides an effective pathway for SRH recombination. The interface states introduce a capacitance $C_S = qD_S$ in parallel with the depletion capacitance C_D, resulting in the equivalent circuit depicted in Figure 2.3A. The resistor R_S is the SRH recombination resistance that gives rise to the recombination current. If R_S is large, recombination is less likely to occur and the capacitance C_S charges slowly. For small values of R_S, recombination occurs more readily and thus C_S fills quickly. The series connection of R_S and C_S gives rise to the SRH time constant $\tau_S = C_S R_S$.

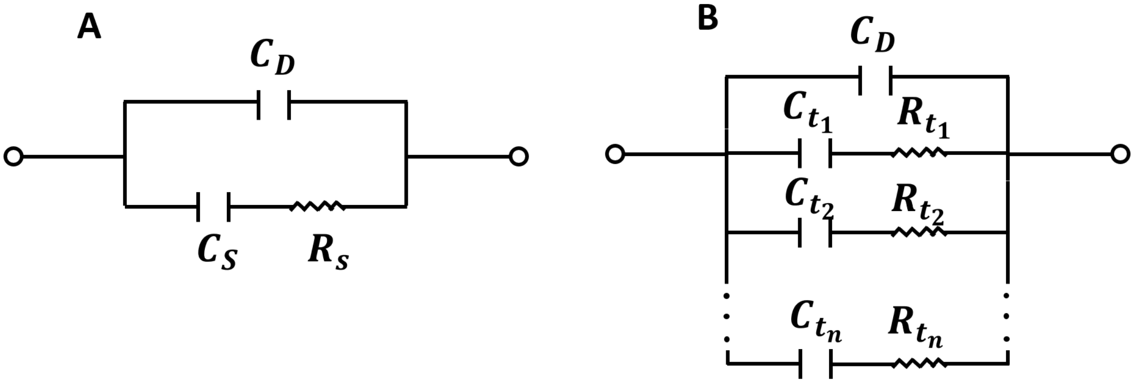

Figure 2.3: (A) Addition of interface capacitance to equivalent circuit (parallel conductance not shown) (B) Equivalent circuit network for multiple trapping level, after reference [63].

As first proposed by Sah and coworkers[128] and later summarized by Jansen, et. al.[63], multiple trapping levels can be modeled with the equivalent circuit depicted in Figure 2.3B. We will now solve for the total impedance of the network in Figure 2.3B. For a given RC branch i, the impedance Z_i is:

$$Z_i = R_i + \frac{1}{j\omega C_i} = \frac{1 + j\omega C_i R_i}{j\omega C_i} = \frac{1 + j\omega\tau_i}{j\omega C_i} \tag{2.2.6}$$

The corresponding admittance $Y_i = \frac{1}{Z_i} = \frac{j\omega C_i}{1+j\omega\tau_i}$. To simplify our analysis, we will work with admittance instead of impedance, since admittances in parallel add in series. The total admittance Y_t is thus:

$$Y_t = j\omega C_d + \frac{j\omega C_1}{1 + j\omega\tau_1} + \frac{j\omega C_2}{1 + j\omega\tau_2} + ... = j\omega C_d + \sum_i^n \frac{j\omega C_i}{1 + j\omega\tau_i} \tag{2.2.7}$$

Ensuring that the denominators are real, we obtain our result:

$$\begin{aligned} Y_t = j\omega C_d + \frac{\omega^2 C_1\tau_1 + j\omega C_1}{1 + \omega^2\tau_1^2} + \frac{\omega^2 C_2\tau_2 + j\omega C_2}{1 + \omega^2\tau_2^2} + ... \\ = j\omega C_d + \sum_i^n \frac{\omega^2 C_i\tau_i + j\omega C_i}{1 + \omega^2\tau_i^2} \end{aligned} \tag{2.2.8}$$

The conductance, G is the real part of Y_t:

$$G = \frac{\omega^2 C_1\tau_1}{1 + \omega^2\tau_1^2} + \frac{\omega^2 C_2\tau_2}{1 + \omega^2\tau_2^2} + ... = \sum_i^n \frac{\omega^2 C_i\tau_i}{1 + \omega^2\tau_i^2} \tag{2.2.9}$$

The capacitance of the network, C, is given by the imaginary part of Y_t divided by the frequency:

$$C = C_d + \frac{C_1}{1+\omega^2\tau_1^2} + \frac{C_2}{1+\omega^2\tau_2^2} + ... = C_d + \sum_i^n \frac{C_i}{1+\omega^2\tau_i^2} \tag{2.2.10}$$

Thus, G contains information about the branches of the equivalent circuit due to traps, whereas C contains these terms in addition to the effect of the depletion capacitance C_d. Referring to the equivalent circuit for the ideal junction in Figure 2.2C, the conductance G corresponds to the out-of phase components J_d and J_{c2} of the total junction conductance.

Equations (2.2.9) and (2.2.10) imply that information about trapping levels within the junction can be obtained by generalizing the simple CV analysis that culminates in equation (2.2.5) and measuring the total admittance of the junction as a function of frequency. The response of each branch is determined by the time constant τ_i: for $\omega < \tau_i$, the branch can respond and serve as an effective SRH recombination center, whereas for $\omega > \tau_i$, the branch ceases responding and the overall measured value of G (or C) decreases. Typically, these measurements are made by LCR meters that assume the simple equivalent circuit in Figure 2.4A. In this geometry, the measured capacitance C' corresponds to the capacitance terms in equation (2.2.10), whereas $R' = \frac{1}{G'}$ gives the terms in (2.2.9). As pointed out by Nicollian and Goetzberger,[112, 111] the conductance contains information on defect levels, whereas the capacitance branch summarizes both defect capacitance and depletion region capacitance. A plot of a simulated $\frac{G}{\omega}$ measurement containing 2 trap levels based on the equivalent circuit in Figure 2.4B is provided in Figure 2.4C, and exhibits two peaks for a deep trap (responsive at low ω) and a shallower trap (responsive at higher ω).

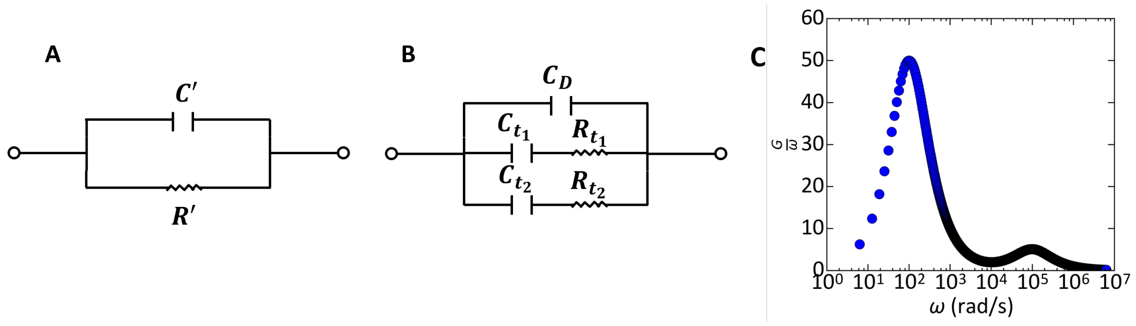

Figure 2.4: (A) Equivalent circuit assumed by LCR measurement meters. (B) Equivalent circuit representing 2 defect levels t_1 and t_2 simulated in (C) corresponding $\frac{G}{\omega}$ spectra showing 2 loss peaks corresponding to t_1 and t_2.

2.3 Impedance Spectroscopy

IS generalizes the capacitance analysis in Section (2.2) and applies the equivalent circuit formalism developed for CV to a diverse array of materials systems, including Schottky junctions,[63] biological tissues,[56, 30, 14] and electrochemical systems.[119, 110, 98, 13] IS measures macroscopic quantities such as current I (or current density J) and potential V that represent the spatial and temporal average of many microscopic events, and attempts to map them onto a consistent physical picture of system-scale properties such as diffusivity and relaxation constants.

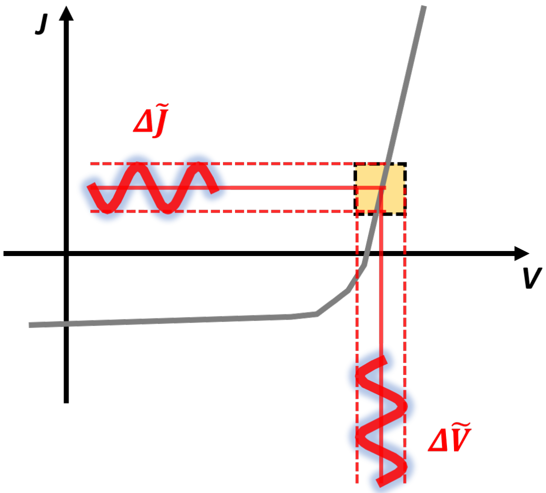

Figure 2.5: Schematic illustrating operating principle of IS in semiconductor devices, wherein frequency domain measurements allow for the interrogation of charge dynamics at a specific operating point in the JV characteristics.

This can be most easily visualized for a semiconductor system *via* the schematic in Figure 2.5 which depicts the diffusion of electrons as described by the Shockley diode equation (equation 1.3.3). In bulk-crystalline semiconductor systems in which individual charge dynamics occur in band states, JV parameters may be readily linked to models of electron transport through the solid. In disordered semiconductors where the DC transport is governed by hopping, the steady state limit gives only a partial physical picture of the charge dynamics. IS adds frequency-dependence to the macroscopic measurement of J, which significantly expands the information that may be extracted from a measurement. Sweeping the frequency at a given operating point along the diode curve in Figure 2.5 allows one to interrogate different sub-domains of the charge relaxation times that contribute to the measured J at that voltage. This also allows one to probe the different energetic states responsible for the transport current.

Instead of measuring the total impedance, IS measures changes in current density $\Delta\widetilde{J}$ due to the application of a time varying voltage $\Delta\widetilde{V}$. The response can be expressed as a frequency-dependent impedance $Z(\omega) = \frac{\Delta\widetilde{V}}{\Delta\widetilde{J}} = Z_r(\omega) + iZ_i(\omega)$, where the real ($Z_r$) and imaginary ($Z_i$) components of the total impedance correspond to currents in and 90 ° out of phase with the input voltage $\Delta\widetilde{V}$ respectively. Following the discussion in section 2.2, this corresponds to a resistance and a capacitance, which can be modeled using series and parallel connections of resistors and capacitors in circuits similar to those used in CV analysis. IS further extends these circuits to include phenomenological elements such as the Warburg impedance, which models the mass transfer in electrochemical systems[119] and electron diffusion in semiconductors[9, 11]

Graphical methods provide the first step towards interpreting IS data in terms of a physically valid model. Phase-angle, Bode-plots, and plots of $Z_r(\omega)$ vs. ω and $-Z_i(\omega)$ vs. ω are commonly used to visualize the output of an IS experiment.[119, 118] The information in these plots is typically condensed into a complex-plane impedance (Nyquist) plot $-Z_i$ vs. Z_r, in which the frequency scale is implicit and runs from the right side of the plot to the left side. The shape of the points in the complex-plane hints at possible mechanisms giving rise to the spectrum; for example, a perfect semi-circle of points indicates that the impedance response results from a single process with one activation energy.[118] An example of a Nyquist plot is shown in grey Figure 2.6A, which corresponds to the simple parallel equivalent circuit in Figure 2.6B.

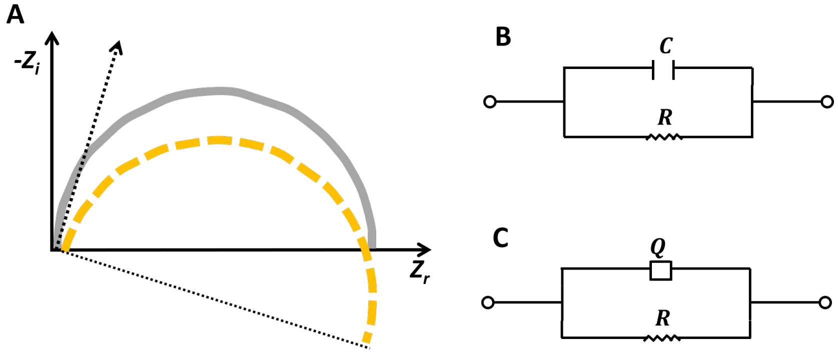

Figure 2.6: (A). Impedance arcs indicating charge relaxation that may be described by RQ circuit with $\alpha = 1$ (grey arc) and $\alpha < 1$ (dashed yellow arc). Reproduced from reference [20]. (B) Equivalent RC circuit for grey arc (C) Equivalent RQ circuit for yellow arc.

In QD solids and other materials that exhibit significant time constant dispersion, the assumption that each physical process has a single-valued time constant is not valid. The impedance response of these systems may be modeled *via* the use of a constant phase element (CPE), which assumes a specific distribution of time constants in the system. CPE models generalize impedance response of a pure capacitor, and the impedance due to a CPE may be written:[119, 118]

$$Z(\omega)_{CPE} = \frac{1}{(i\omega)^{\alpha} Q} \tag{2.3.1}$$

where Q is the CPE coefficient and α parameterizes how imperfect the capacitor is. For $\alpha = 1$, equation (2.3.1) describes an ideal capacitor, and the expected impedance response given by the grey line in Figure 2.6A. For $\alpha < 1$, the capacitor is imperfect, which corresponds to a depression of the semicircle due to a lower phase angle, as depicted by the yellow dashed line in Figure 2.6A. This impedance response may be modeled by the RQ circuit in Figure 2.6B.

IS thus provides a means of quantifying the deviations from ideality due to a distribution of charge relaxation times. $G(\tau)$, the distribution function of τ, is assumed to be a normal distribution of $\ln(\frac{\tau}{\tau_C})$:[119, 20]

$$\tau G(\tau) = \frac{2\sin(\alpha\pi)}{\exp[(1-\alpha)\frac{\tau}{\tau_0}] + \exp[-(1-\alpha)\frac{\tau}{\tau_0}] - 2\cos(\alpha\pi)} \tag{2.3.2}$$

From equation (1.4.18), $\ln(\frac{\tau}{\tau_0}0 \propto E$, so equation (2.3.2) reflects that the distribution of available energy states for electron occupation $N(E)$ is itself a Gaussian.

2.4 Thermal Admittance Spectroscopy

Thermal admittance spectroscopy (TAS) is a powerful device-level spectroscopy technique that characterizes the distribution of defect states by observing how the junction capacitance of a pn or metal-semiconductor junction changes with the frequency of an applied AC perturbation. Unlike traditional CV profiling, TAS is able to interrogate a broad distribution of states by continuously varying the frequency of the applied perturbation. The ability of TAS to probe manifolds of states in a pn junction is particularly useful for polycrstalline films,[150, 39, 61, 90, 89, 88] organic semiconductors,[75, 22, 12] and QD solids[16, 15, 66] in which energetic and spatial disorder give rise to broad distributions of states in the bandgap that can act as effective recombination centers and low mobility transport states.

The small AC signals used in TAS affect both free carriers and trapped carriers. The response of these respective carrier populations to an applied AC perturbation can be written:

$$n = n^{=} + \widetilde{n}e^{i\omega t} \qquad p = p^{=} + \widetilde{p}e^{i\omega t} \qquad n_T = n_T^{=} + \widetilde{n_T}e^{i\omega t} \tag{2.4.1}$$

where $n^{=}$ corresponds to the steady state population of electrons and $\widetilde{n}$ corresponds to the electrons moving with the AC oscillation. This same formulation is applied to both the hole population, p, and the population of trapped electrons, n_T. The change in occupation of defect states is $\frac{dn_T}{dT} = i\omega\widetilde{n}_t e^{i\omega t}$.

In general, the changes in the occupation of these defects can be written as a sum of electron and hole carrier populations in equation (2.4.1) weighted by the respective capture coefficients of electrons or holes, $\beta_{n,p}$. Walter and colleagues have shown that the AC component of defect occupation may be written as:[150]

$$\widetilde{n_T} = \frac{1}{i\omega + \omega_0}[\beta_n\widetilde{n} - f(E)(\beta_n\widetilde{n} + \beta_p\widetilde{p})]N_T \tag{2.4.2}$$

where $f(E)$ is the Fermi function and ω_0 is defined as:

$$\omega_0 = \beta_n n^{=}(1 + e^{-\frac{E_F - E}{k_B T}}) + \beta_p p^{=}(1 + e^{-\frac{E - E_F}{k_B T}}) \tag{2.4.3}$$

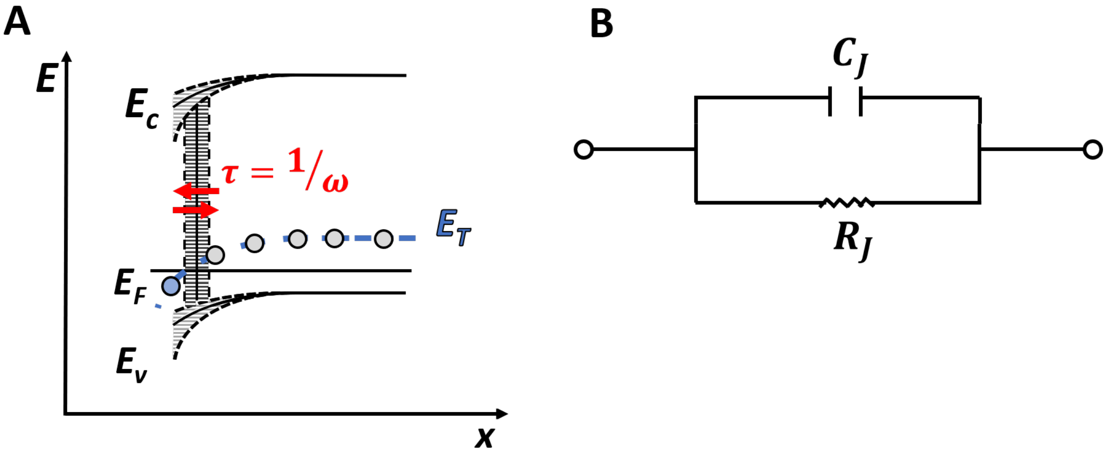

Figure 2.7: (A) Schematic of exchange between holes at E_F exchanging with a bulk defect E_T within the depletion region with a time constant τ determined by the AC signal. (B) Schematic of junction equivalent circuit.

An analogous expression to equation (2.4.2) can be written for the current of holes flowing into defect states. TAS considers these currents under bias conditions in which majority carriers from both the p and the n side of the junction are injected into the depletion region under an applied AC bias, and subsequently captured and re-emitted from defects, as depicted in Figure 2.7 for a one-sided junction with a depletion capacitance. A simple equivalent circuit model of the junction admittance is also included, consisting of a capacitor C_j and a resistor R_j in parallel. As discussed in section 2.2, the junction capacitance is the imaginary part of the current divided by the external AC frequency. Only the defect density $\widetilde{n_t}$ will posses an imaginary part, since the free carrier densities should be in phase with any applied perturbation. The total capacitance due to the charging and discharging of a single defect state n_t at energy E is:

$$C' = \frac{q}{V_{AC}} \frac{\omega_1}{\omega^2 + \omega_0^2} [\beta_n \widetilde{n} + f(E)(\beta_n \widetilde{n} + \beta_p \widetilde{p})] N_T \tag{2.4.4}$$

where V_{AC} is the amplitude of the applied AC signal and ω_1 describes the re-emission of captured charge out of defects.[150] By inspection of equations (2.4.4) and (2.4.2), the last bracketed term is $\widetilde{n}_t$.

The capacitance of a single defect is therefore proportional to the occupation of the defect modified by its ability to respond to the frequency ω. This suggests 2 separate regimes:[75]

1. For $\omega < \omega_0$, the occupation can follow the AC perturbation and thus contributes to the junction capacitance by charging and discharging.
2. For $\omega > \omega_0$, the occupation of the defect cannot follow the oscillation and will not contribute.

The regime in which $\omega = \omega_0$ thus represents a critical frequency above which the occupied defect state will not contribute to the capacitance.

Each occupied defect level will contribute to the junction capacitance with a frequency dependence given by equation (2.4.4). In order to determine the efficiency of an ensemble of defects to contribute to the total junction capacitance, C_{tot}, equation (2.4.4) must be integrated in energy and space. The explicit energy dependence of ω_0, ω_1, and $f(E)$ will weight the resulting integration towards E_F.[150, 17] As a result, the integration of equation (2.4.4) over all energies will be sharply peaked around E_F, yielding:

$$C'' = \int_{-\infty}^{\infty} C' dE = q^2 \frac{v_p}{V_{AC}} N_t(E_F) \tag{2.4.5}$$

where v_p stands for the small potential that arises from the incremental change in the hole Fermi-level in response to V_{AC}. This implies that the TAS measurement is sensitive primarily to the charging and discharging of defect states at the point where the trap band E_T crosses E_F, as depicted in the cartoon in Figure 2.8. Note that if E_T never crosses E_F, states at E_T cannot be probed by TAS.

Equation (2.4.3) allows us to define an energetic window E_ω centered around E_F in which TAS may detect defects:

$$\begin{aligned}\omega = \omega_0 &= 2\beta_p N_v e^{-\frac{E\omega}{k_B T}} \\ &= 2\nu_0 e^{-\frac{E\omega}{k_B T}} \\ \implies E_\omega &= k_B T ln(\frac{2\nu_0}{\omega})\end{aligned} \tag{2.4.6}$$

where we have introduced the thermal emission pre-factor $\nu_0 = \beta_p N_v$, commonly known as the attempt-to-escape frequency. E_ω represents the limiting energy of a TAS measurement. Defects at energies greater than E_ω cannot be detected *via* TAS. This limiting energy, along with the spatial limitation discussed above, is depicted schematically in Figure 2.8.

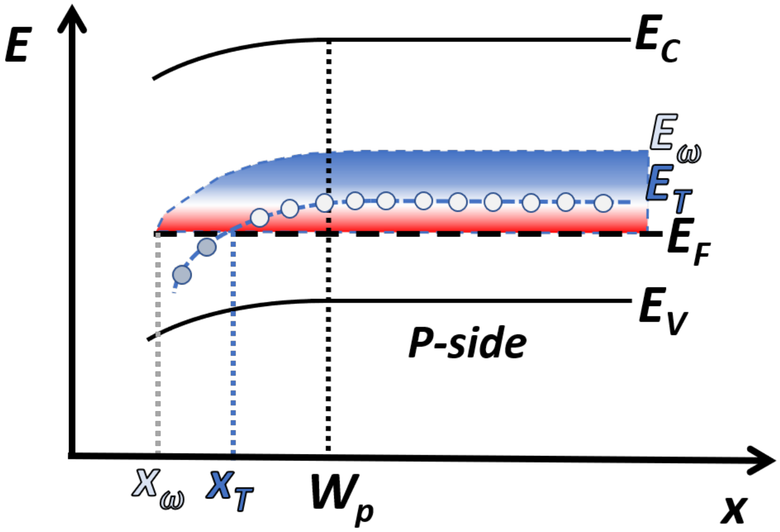

Figure 2.8: Schematic illustrating energetic range E_F to $E_F + E_\omega$ and spatial range x_T to W_P probed by TAS measurement on one-sided pn junction.

C_{tot} can then be derived by integrating equation (2.4.5) from E_F to E_ω. From Figure 2.8, this operation is akin to integrating in space from $< x >$ to the edge of the depletion region in the bulk of the p-type semiconductor, W_p. The total capacitance is:

$$C_{tot} = -\frac{q}{V_{AC}} \int_{E_F}^{E_\omega} v_p(x(E)) N_T(E) \frac{W}{qV_{bi}} dE \tag{2.4.7}$$

where V_{bi} is the built-in potential of the junction. The constant terms in the integral act on the total density of trap states N_T and ensure that integration is performed on occupied states. Upon integration, the total defect distribution N_T can be calculated as:

$$\begin{aligned} N_T(E_\omega) &= \frac{V_{bi}}{qW}\frac{dC}{dE_\omega}\frac{dE_\omega}{d\omega} \\ &= \frac{V_{bi}}{W[qV_{bi}-(E_F-E_\omega)]}\frac{dC}{d\omega}\frac{\omega}{k_BT} \end{aligned} \tag{2.4.8}$$

where the bending of the bands in the depletion region is taken into account in the last step by assuming the shift in the bands towards the junction can be approximated by the linear drop of the applied bias: $V_{bi} = V_{AC}\frac{W-x}{W}$

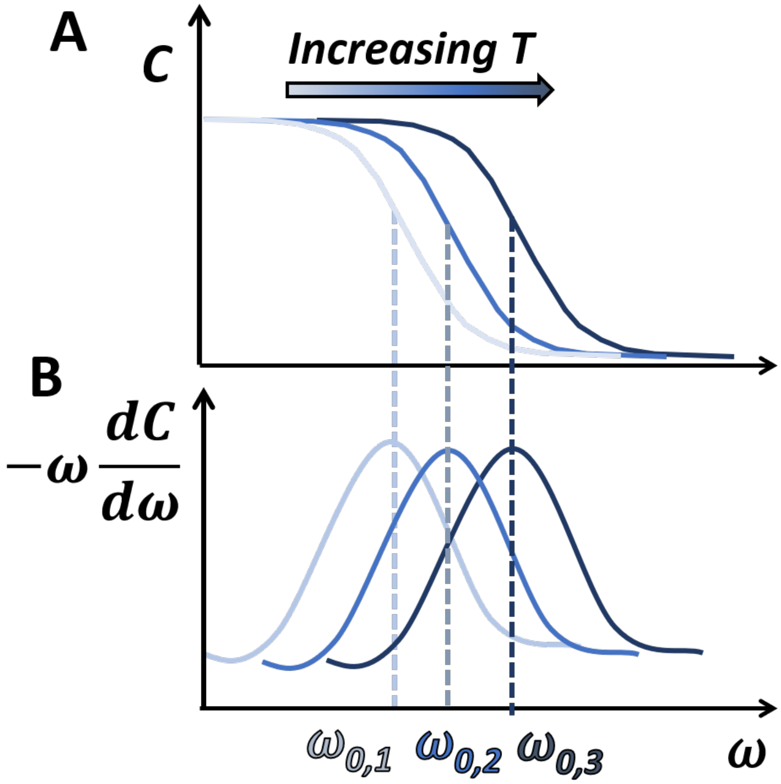

Figure 2.9: Cartoon illustrating temperature-induced shifts to (A) capacitance-frequency and (B) peaks in $-\omega\frac{dC}{d\omega}$..

By determining how the differential capacitance $\omega\frac{dC}{d\omega}$ evolves with frequency, the total defect distribution can be calculated according to equation (2.4.8). The relation in equation (2.4.6) also implies that the energetic depth E_T of the defect can be obtained. At the resonance frequency $\omega = \omega_0$, the differential capacitance $-\omega\frac{dC}{d\omega}$ will be at a maximum since the junction capacitance C decreases rapidly as the charges in occupied defect states stop responding. This scenario is depicted in Figure 2.9. If the temperature is then increased, a different resonance condition $\omega_{0,2}$ will appear as a maximum in the differential spectra. By observing multiple resonances as the temperature changes, both the E_T and $\nu 0$ can be determined in an Arrhenius plot:

$$\omega_0 = 2\nu_0 e^{-\frac{E_T}{k_B T}} \implies ln(\omega_0) = ln(2\nu_0) - \frac{E_T}{k_B T} \tag{2.4.9}$$

The slope of the Arrhenius plot gives E_T, while the intercept of the plot gives ν_0. These parameters are then folded into the calculation of the N_T in equation (2.4.2) in both the $\frac{dC}{d\omega}$ term and the E_ω term in the denominator.

Though the above analysis has been used to interpret thermal admittance spectra obtained from QD devices, the assumption that carriers diffuse sufficiently fast prior to trapping and after subsequent de-trapping so that ω_0 depends only on the emission rate of charge out of traps e_p may not be met in QD assemblies and other low mobility semiconductors.[125, 151] In these materials, the small mobility μ of charge carriers implies that the transport times of diffusion $\tau_{diff} \propto \frac{1}{\mu}$ and drift $\tau_{drift} \propto \frac{1}{\mu}$ cannot be ignored with respect to the frequencies used in TAS. As a result, the dielectric loss peaks in the differential capacitance plot reflect the dielectric relaxation frequency $\omega_0 = e_p(T) + \frac{1}{\tau_{diff}} + \frac{1}{\tau_{drift}}$.[125]. The physical implications of this subtlety will be discussed at length in Chapter 3.

2.5 Drive Level Capacitance Profiling

Drive level capacitance profiling (DLCP) is a dynamic junction capacitance technique that, like TAS, measures the junction capacitance as a function of applied AC frequency. Unlike the small AC signals used in TAS, DLCP utilizes a range of large AC amplitudes to generate a spatial profile of the density akin to traditional CV techniques. The dynamic nature of the applied bias in DLCP means that the charge density data obtained by DLCP is not greatly confounded by the presence of interface states, which can undermine the interpretation of conventional CV measurements.[33]

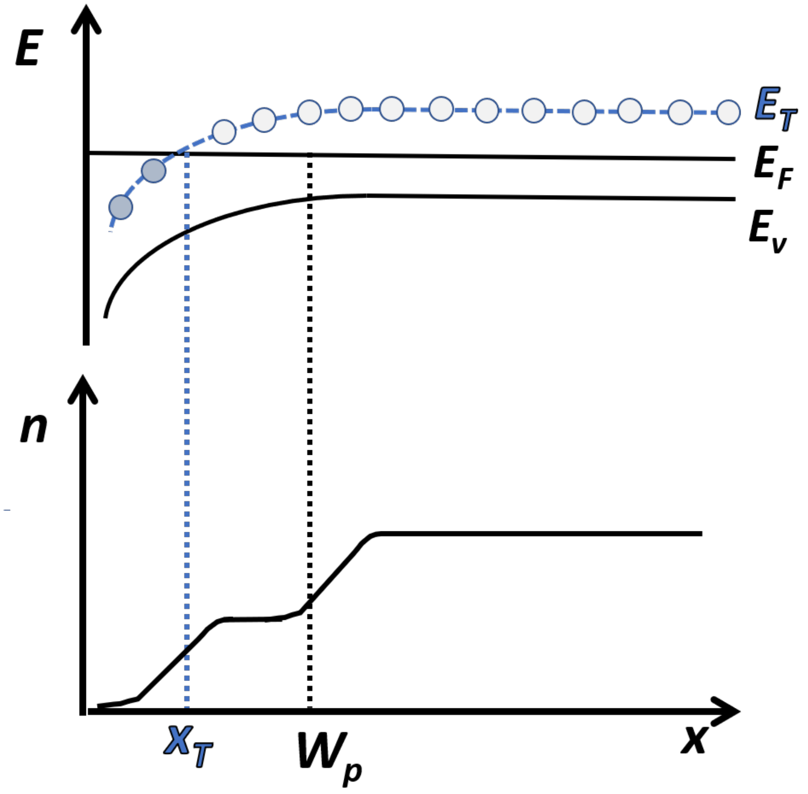

Figure 2.10: (A) Band diagram showing crossing between E_F and E_T resulting in (B) corresponding charge density profile, showing significant charge density at x_T as well as W_p.

The shortcomings of CV to probe charge densities in polycrystalline or amorphous materials is illustrated schematically in Figure 2.10, which depicts an energetically continuous bulk trap band E_T crossing E_F at a position x_T from the junction on the p-side of a p-n junction. To first approximation, the response of the junction capacitance to an applied bias can be written as parallel plate capacitance:[52]

$$C = \frac{\varepsilon A}{< x >} \tag{2.5.1}$$

where ε is the semiconductor dielectric, A is the device area, and $< x >$ is treated generally as the first moment of the charge response:

$$< x >= \frac{\int_0^\infty x\delta\rho(x)dx}{\int_0^\infty \delta\rho(x)dx} \tag{2.5.2}$$

where x is the distance from the barrier and $\rho(x)$ is the differential charge density induced in the semiconductor due to the applied bias. In Figure 2.10B, the junction contains a significant charge density within the depletion region at x_T. As a result, a CV measurement applied to this junction at low frequencies will induce a response at x_T in addition to W, and $< x >$ will be shifted from the edge of the depletion region. As a result, standard CV profiling analysis, which explicitly assumes that free charge is built up at the edge of the depletion region, will yield an inaccurate carrier profile result skewed towards the barrier.

DLCP presents an alternative method by which to profile the charge density in bulk states. By modulating the amplitude of the AC perturbation in addition to the frequency and DC bias, DLCP is able to parse the contributions to the junction capacitance due to defects and those from free carriers. The use of large AC biases implies that the charge response cannot be assumed to be linear; instead, the capacitance due to the dynamic voltage can be written as a power series:[52]

$$C = \frac{dQ}{dV} = C_0 + C_1 dV + C_2(dV)^2 + ... \tag{2.5.3}$$

The higher order terms contain information specifically about the defect response depicted in Figure 2.10. By shifting the frequency of the AC perturbation, different energies within the bandgap can be probed. The energetic range probed by an AC perturbation in a DLCP measurement is again given by equation (2.4.6).

The mechanism of the DLCP measurement for a given E_ω is shown in Figure 2.11 for SRH recombination due to depletion region defect states. Figure 2.11A depicts a trap band in the p-type part of a p-n junction crossing E_F at a spatial location x_T within the depletion region (x_w). The corresponding charge density diagram is shown in Figure 2.11B, with a contribution due to the trapped charge overlaid onto the charge density resulting from free carriers with density N_A.

Upon application of a small reverse bias δV, the bands shift as shown in Figure 2.11C provided the applied frequency $\omega < \omega_0$, and the resulting charge density diagram is shown in Figure 2.11D. The difference between the two charge density diagrams, shown in Figure 2.11E, is the total change in the depletion region charge distribution measured by DLCP in response to an applied voltage $\delta V = V_{RMS}$ and, in general, contains contributions from both N_A and trapped carriers (n_t).

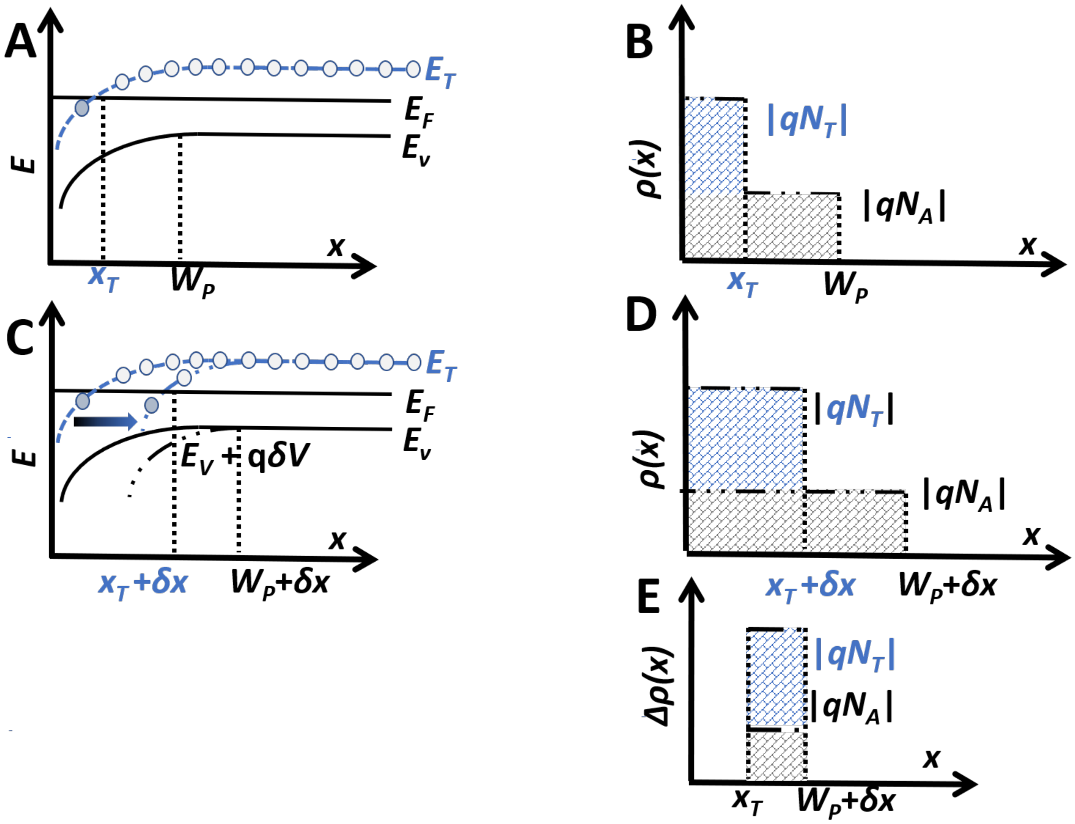

Figure 2.11: (A) Band diagram of p-type semiconductor with a bulk trap E_T crossing E_F at a distance x_T within a junction of depletion width extending to W_p. (B) Approximation of charge density of ionized acceptor density in traps (blue) and in depletion region (gray). (C) Application of a bias perturbation δV shifts the bands down by a corresponding amount $q\delta V$ and extends the depletion region δx. (D) Charge density within junction during application of perturbation. (E) Difference in charge density distributions in (B) and (D).

Figure 2.10E highlights that DLCP is a technique that is primarily sensitive to bulk states where E_T crosses E_F. At high ω DLCP gives an estimate of the charge density around E_F, as explained in equation (2.4.6). Typically, the values obtained at high frequency are interpreted as ionized acceptor concentrations, and thus estimate the free carrier density in the bulk.[52]

To perform a DLCP measurement, frequencies in discrete steps are applied to the device junction, and the capacitance response to the AC signal is measured at various AC amplitudes V_{RMS}. A variable DC bias is simultaneously applied to the sample so that the device is kept under a constant maximum reverse bias $|V_{max}| = |V_{RMS} + V_{DC}|$ for a given measurement. The DC bias ensures that the band bending is held constant throughout the measurement, and only dynamic changes in majority occupation due to the applied AC signal are measured as V_{RMS} changes, as described in DLCP work on polycrystalline semiconductors.[52]

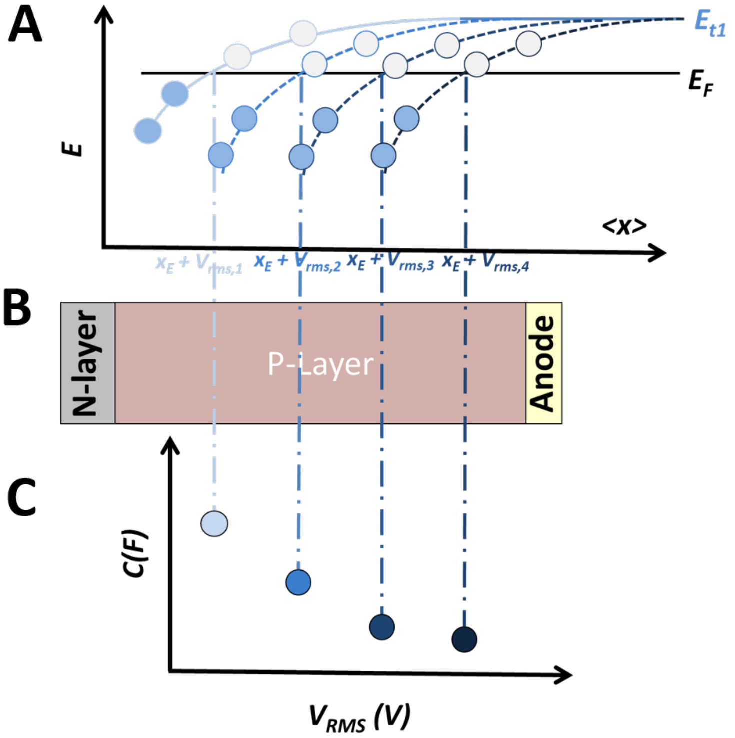

Figure 2.12: (A) Band diagram showing crossing of E_F and trap band E_{t1} at various total applied DLCP voltages $V_{rms,1-4}$. (B) Spatial crossing point $x_E + V_{RMS}$ schematically diagrammed within the device (C) Schematic of C vs. V_{RMS}, showing non-linear decay of C as spatial location of capacitance response extends further from junction.

Figure 2.12 presents a cartoon of how an increase in applied AC amplitude V_{RMS} shifts the crossing point of E_F and a discrete trap state E_T progressively further from the junction. Since the total band bending in a given DLCP scan remains constant (e.g. V_{max} remains constant), the application of V_{RMS} only affects the sub-population concentration of carriers that can respond to the applied frequency. The resulting capacitance, drawn schematically in Figure 2.12C, exhibits a nonlinear decrease, which follows the general form given by equation 2.5.3). The coefficients C_0, C_1, and C_2 may be extracted by fitting the capacitance data, and the resulting drive level density can then be calculated as:[52]

$$N_{DL} \equiv -\frac{C_0^3}{2q\varepsilon\varepsilon_0 A^2 C_1} = \frac{|\rho|}{q} \tag{2.5.4}$$

where A is the area of the device and ε is the dielectric constant of the material. Specifically, ρ is a measure of the charge occupancy of the DOS $N(E)$ at a given ω. A distance profile can be generated by plotting N_{DL} against the distance $< x >$.

2.6 Instrumentation

The IS, TAS, and DLCP measurements on QD diodes presented in this thesis are achieved using a custom set-up that mates frequency-dependent impedance characterization with simultaneous DC transport measurements. These measurements are performed within a cryogenic vacuum probestation to allow for temperature-dependent interrogation of transport and recombination phenomena with the QD device. The total set-up is represented schematically in Figure 2.13, discussed in detail below.

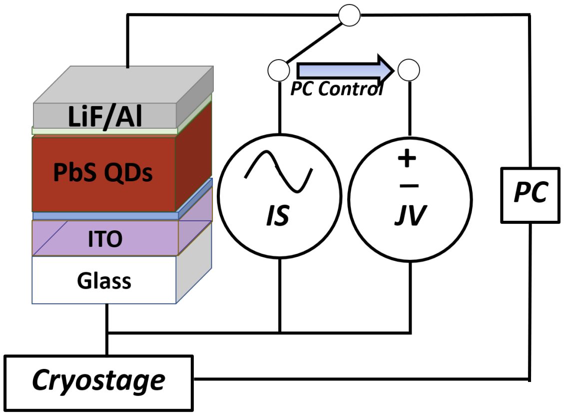

Figure 2.13: Schematic of setup used to collect dark IS data. The IS setu-up consists of an HP-4192A impedance analyzer and the JV setup consists of an Agilent 4156C parameter analyzer.

2.6.1 Cryostage

Electrical characterization is performed within a LakeShore Cryotronics CPX-VF cryogenic probestation, capable of reaching high vacuum levels of $\sim 1 \times 10^{-6}$ torr and temperatures from $T = 4 - 350$ K. The probestation allows for temperature control over heating elements embedded in three separate heating stages and a superconducting magnet located within the chamber. The magnet itself is not used in the electronic measurements discussed in this thesis. Control over these heating elements is achieved using LakeShore model 332 and model 340 temperature controllers with 2 inputs each. The model 340 contains an additional sensor input. The temperature controllers are wired as follows:

- Model 340
    - Loop 1 senses the temperature of the sample stage via a Cernox resistance temperature detector (RTD) that uses a vendor supplied calibration curve (X40711) to output the correct temperature. Heat is supplied via a 50 W resistive heater
    - Loop 2 senses the temperature of the magnet stage via a Cernox RTD with a second vendor-suppied calibration curve (X50126). Heat is supplied via a 100 W resistive heater
    - Sensor 3 reads the temperature of the probe arm via a platinum resistive heater (PT-100). This temperature cannot be directly manipulated
- Model 332
    - Loop 1 uses a Si diode (DT-470) to sense the temperature at the radiation shield, which can be subsequently controlled with a 100 W heater
    - Sensor 2 uses the a second Si diode (DT-470) to sense the temperature at another point on the radiation shield. The temperature at this location is controlled by an analog

voltage output by the 332 to an external amplifier (LakeShore model 142B), which controls the current through a second 100 W heater.

To cool the system, liquid N_2 is introduced into the coldhead of the cryostat *via* a vacuum transfer line. An Edwards nEXPT turbopumping station, consisting of an nEXT85 turbomolecular pump and a nXDS scroll pump, is used to pump the system to pressures of $\sim 1 \times 10^{-6}$ torr.

2.6.2 Electrical Measurements

Variable temperature TAS, DLCP, AC conductance, and JV measurements can be performed within the vacuum probestation discussed above. Two probe admittance and JV measurements are carried out using a Hewlett Packard HP4192A impedance analyzer and an Agilent 4156C parameter analyzer, respectively. A computer-controlled relay switch is used to toggle between AC impedance measurements and DC JV characterization at each temperature or time-step as depicted in the schematic in Figure 2.13. For TAS measurements, the capacitance response of a solar cell device to small (10-100) mV AC perturbation is collected for 200 frequencies that are equally logarithmically spaced from 20 Hz to 1.3 MHz at DC biases of 0, -100, and -200 mV. IS data is collected at large forward biases of 400, 500, and 600 mV. The same DC and AC biases are applied for AC conductivity measurements. DLCP measurements are performed immediately afterward using the same setup, with AC signals at frequencies of 100 Hz - 500 kHz, and maximum applied biases $V_{max} = V_{RMS} + V_{DC}$ from -50 mV to -300 mV in small ($\sim$ 50) mV steps. To obtain the non-linear capacitance response, V_{RMS} was varied from 10 mV - 300 mV, and V_{DC} is automatically modulated to keep V_{max} constant using custom LabView software.

2.7 Conclusion

This chapter has summarized the frequency-domain characterization techniques used to characterize the charge transport dynamics in QD solar cell devices featured in Chapters 3, 4, and 5. Section

(2.2) discussed the physical models to describe the frequency dependence of the capacitance-voltage characteristics in bulk semiconductors. Section (2.3 extended these physical models used to describe the total electronic impedance of a macroscopioc system in terms of micrososcopic parameters. Sections (2.4) and (2.5) describe the 0 and reverse applications of IS, commonly known as TAS and DLCP, to study majority carrier dynamics within semiconductor junctions. Finally, section (2.6 describes the physical instrumentation used to make these measurements.

Chapter 3

In-Situ Characterization of the Density of States in QD Schottky Junction Photovoltaic Devices

3.1 Introduction

Organic semiconductors,[146, 87, 50] lead halide perovskites,[155, 113, 132] and quantum dot (QD) solids[69, 140, 62] have attracted considerable attention in the last decade as demand grows for solution processable materials that enable flexible, low-cost, large-area photovoltaic (PV) devices. Like their bulk semiconductor counterparts, the carrier mobility and lifetime that define the power conversion efficiency (PCE) of these emerging PV platforms are governed by the density of states $N(E)$ available for charge occupation. $N(E)$ in bulk single- or poly-crystalline semiconductors is characterized by extended states at the conduction or valence band edge, with mid-gap trap states created by atomic defects within and at the surface of crystalline grains. In contrast, the greater structural and energetic disorder in amorphous and many solution-processable semiconductors leads to a more dispersive $N(E)$ with localized states that tail into the bandgap.[49, 94, 91, 159, 72, 105] Despite this significant difference in $N(E)$, efforts to characterize trap states that limit the carrier mobility-lifetime product in low mobility PV materials often rely on the same techniques developed for higher mobility bulk crystalline materials.

Impedance spectroscopy (IS) is one of the most widely used techniques to characterize electronic defects in PV devices. IS is a suite of frequency domain measurements that link macroscopic current density-voltage (JV) characteristics to microscopic transport dynamics within a semiconductor device.[119] The time-varying AC biases used in IS studies of semiconductors are typically applied with frequencies $\omega = 10^2 - 10^6$ rad/s, allowing for the interrogation of charge dynamics characterized by relaxation times $\tau = \frac{1}{\omega} = 10^{-6} - 10^{-2}$ s. The interrogation of these time scales enables the investigation of charge dynamics between states separated by an energy barrier ΔE:[41]

$$\tau = \tau_0 \exp(\frac{\Delta E}{k_B T}) \tag{3.1.1}$$

where τ_0 is a characteristic relaxation time. Thermal admittance spectroscopy (TAS) is a specific variant of IS that decouples the capacitance contribution of trapped charge from the depletion capacitance of a PV device at zero or reverse bias by measuring the frequency- and temperature-dependent junction capacitance response. TAS is commonly used to probe carrier recombination through discrete defect levels, and in addition to PV devices containing Cu(In,Ga)Se_2 (CIGS) thin film materials for which the method was initially developed[150, 39, 61], TAS has been applied to PV devices made of CdTe,[90, 89, 88] amorphous silicon,[53] organic semiconductors,[75, 22, 12] lead halide perovskites,[35, 65] and QD solids.[16, 15, 66] In bulk crystalline materials, these relaxation times are typically associated with Shockley-Read-Hall (SRH) recombination through traps with energy E_T such that $\Delta E = E_C - E_T$ or $E_T - E_V$ and $\tau_0 = \frac{1}{\nu_0}$ where 'the attempt to escape frequency' $\nu_0 = \beta_p v_{th}$ is the frequency with which a charge in a defect state with capture cross section β_p and thermal velocity v_{th} attempts to escape into the band.[150, 90, 39] In disordered materials, low charge carrier mobility associated with hopping in localized energy states implies that a broader range of both charge transport and recombination phenomena may be probed by IS.[125, 129, 151]

Recent experimental studies[125, 90] and PV capacitance simulations[151, 156] have pointed out that low carrier mobilities in materials such as QD solids or organic semiconductors can complicate standard TAS analysis, leading to the mis-identification of hopping transport signatures as evidence of discrete defect levels. More extensive characterization of hopping transport in low mobility materials has been provided by IS studies of AC conduction in disordered dielectric materials such as conductive glasses[148] and electronic polymers.[42] The structural and energetic disorder that characterizes these materials can be correlated to a relaxation time that corresponds to the hopping time τ *via* the random free energy barrier model (RFEB). The RFEB model assumes charge carrier hopping is subject to spatially random energetic barriers, and has been shown to describe the frequency-dependence of Miller-Abrams or nearest neighbor hopping (NNH) transport.[36] As depicted in Figure 3.1A, the model assumes transport over larger distances (blue circle) involves more site-to-site hops and is thus more likely to require a carrier to surmount a large energy barrier, limiting the response to lower frequencies (longer times). By contrast, closer hops are more likely to involve smaller energetic barriers and can be probed with higher applied frequencies. The distribution of energy barriers in a low mobility semiconductor such as a QD solid can be thus be probed by frequency-dependent conductivity measurements and analyzed *via* equation (3.1.1), where ΔE now represents the difference between the majority carrier band edge and localized energy states at a characteristic transport energy E_{Tr} such that $\Delta E = E_C - E_{Tr}$ or $E_{Tr} - E_V$.[41, 36, 77]

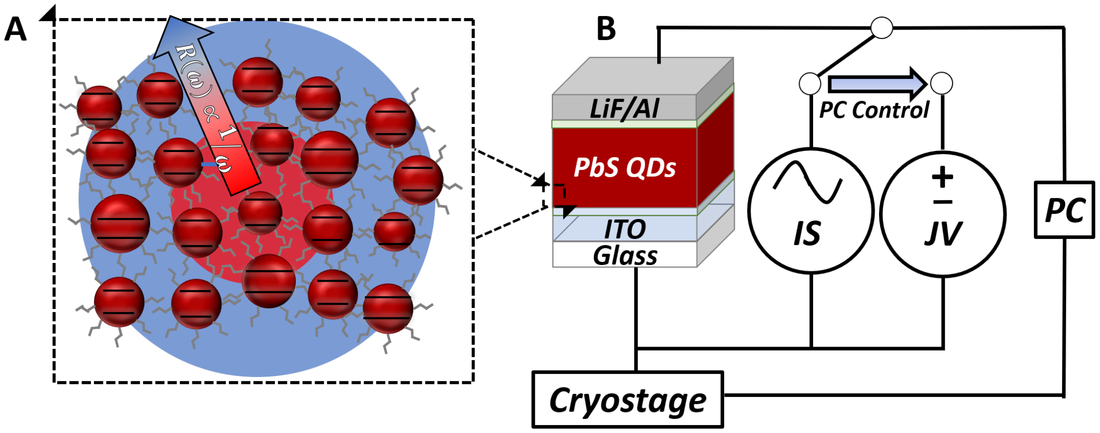

Figure 3.1: Schematic of (A) a disordered QD array, with varying conduction and valence band states (black lines), capped by short organic ligands integrated in (B) a Schottky junction PV device. Devices are mounted in a cryostat and probed in an AC and DC electronic measurement apparatus. In (A), the red circle shows the radius of charge hopping in the QD array under low frequency conditions and the blue circle shows the radius of charge hops in high frequency conditions.

Here, we correlate the thermal admittance spectra of a PV device with an active layer of 1,2 ethanedithiol (EDT)-capped PbS QDs with temperature-dependent AC and DC conductivity measurements (Figure 3.1). PbS QD devices offer a model system for studying the contribution of hopping transport in IS measurements since QD solids are known to exhibit limited carrier mobilities $\sim 10^{-4} - 10^{-3}$ cm^2(Vs)$^{-1}$[160, 1, 157, 136] yet have been optimized to achieve ∼ 11% power conversion efficiency (PCE).[25, 82] We show that the spectroscopic signatures detected in our TAS data arise from hopping conduction and not from trap kinetics. We use TAS measurements to identify the energy of states through which charges hop, and in combination with drive level capacitance profiling (DLCP), we quantify the occupation of these states, showing that hopping transport occurs in a broad tail of states extending from the valence band (E_V) to a transport level E_{Tr} below the band edge. By relating these measurements to optical absorption and JV data, we show how the frequency dispersion exhibited by charge hopping processes may be mapped onto the energetic landscape in QD solids, and examine the implications of charge hopping dynamics for PV device performance. Using this physical picture, we are able to deduce the effect of O_2 on $N(E)$ in our devices by observing the evolution of the admittance response under high vacuum.

3.2 Optical Absorption and JV

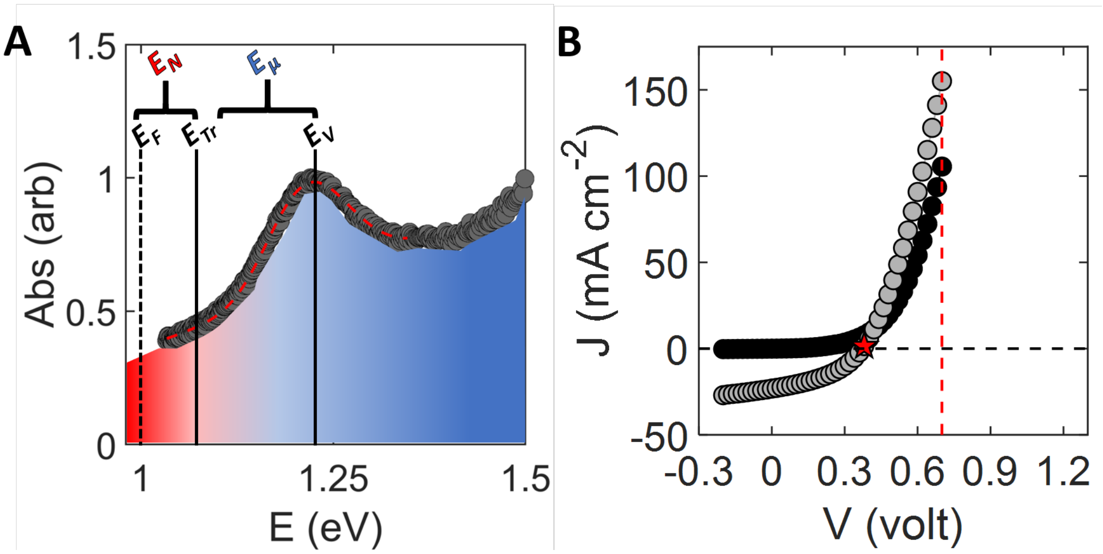

Figure 3.2: (A) Normalized absorption spectrum for an EDT-capped PbS QD film (gray circles) with fit of the low-energy side of the absorption spectrum to a Gaussian distribution (dashed red line). Positions of E_F, E_{Tr}, and E_V and energy differences E_N and E_μ highlighted schematically. (B) Dark (black) and illuminated (gray) JV curve for PbS QD PV device device, with red star indicating $V_{oc} = 0.37$ V.

QD PV devices are fabricated by spincoating 3 nm diameter, oleic acid capped, PbS QDs, synthesized according to literature methods, onto ITO/glass substrates. The native oleic acid ligands are exchanged by depositing a solution of the EDT ligand in acentonitrile onto the film for 30 s. The film is then rinsed with fresh acetonitrile to remove excess ligand. This process is repeated to deposit 5 layers of EDT-capped PbS QDs to yield a $\sim$ 90 nm film. The device is capped with a LiF/Al top contact as depicted in Figure 3.1. The normalized optical absorption spectrum of an EDT-exchanged PbS QD film at energies near the first exciton peak is shown in Figure 3.2A. An exponentially modified Gaussian distribution is fit to the peak, from which we deduce an optical bandgap $E_G = 1.22 \pm 0.01$ eV given by the peak of the distribution and a total width in first absorption energy given by $\sim 3\sigma_{var} \approx 0.15$ eV where $\sigma_{var} = 0.051 \pm 0.002$ eV is the variance of the Gaussian fit. The width of the first exciton peak has been previously shown to parameterize the inhomogeneous distribution of electronic states in the QD film and therefore provides a measure of the width of the density of valence band states N_V.[153]

Figure 3.2B displays the dark and illuminated JV characteristics of the completed PV device. Under AM 1.5G illumination, the device exhibits an open circuit voltage (V_{oc}) of $\sim$ 0.37 V and a PCE of $\eta = 3.7\%$, in good agreement with PCE figures previously obtained for PbS QD Schottky PV devices.[145, 123] Since the maximum theoretical observed V_{oc} of our Schottky cell $V_{oc,max} \approx \frac{E_G}{2} = 0.61$ eV[97], our data indicate a V_{oc} deficit of $\sim$ 0.24 eV, which may either result from defects within the PbS QD layer.[15, 28] or pinning of E_F at the interface. [37, 58, 73, 92, 93]

3.3 TAS Measurements

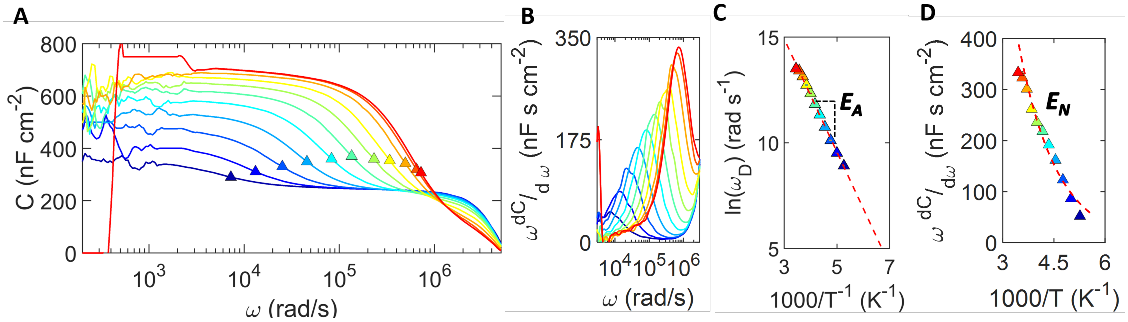

Figure 3.3: (A) TAS spectrum of a PbS-EDT QD PV device measured from $T = 190-290$ K. Resonant frequencies (triangles) determined from (B) the derivative plot. Temperature-dependence of (C) the frequency $\omega_0 = \omega_D$ of the capacitance derivative fit to an Arrhenius function to yield activation energy E_A, and of the (D) amplitude of the capacitance derivative with fit to a Fermi-function to yield the activation of the carrier density E_N, respectively.

To understand the mechanism behind V_{oc} losses in our QD PV devices, we perform TAS measurements by mounting the devices in a cryostat kept under vacuum ($\sim 10^{-4}$ torr) and measuring the frequency-dependent capacitance response to 20 mV AC signals at 0 V DC bias from $T = 190-290$ K. The capacitance displayed in Figure 3.3A shows a large plateau at low frequencies followed by a temperature dependent decay to $\sim$ 300 nFcm^{-2} at high frequency. The low ω plateau reflects charge dynamics within the PbS QD Schottky junction. For sufficiently low temperature or high ω, the charge can no longer respond to the applied AC signal. As a result, the measured capacitance decays to the capacitance of the depletion width, C_D, at high ω. For $\omega >\sim 2 \times 10^6$ rad/s, a second capacitance drop off can be observed in the TAS data due to parasitic series resistance effects reported in both experiment and simulation.[75]

The high and low ω regions in Figure 3.3A are separated by the resonance frequency ω_0. Experimentally, ω_0 is obtained from loss peaks in a plot of the frequency-scaled derivative $-\omega\frac{dC}{d\omega}$ vs. ω, provided in Figure 3.3B. The peaks in Figure 3.3B display a temperature-dependent shift in ω_0

and increase in amplitude. The thermal activation of ω_0 in higher-mobility thin film semiconductors for which TAS was developed is related to SRH recombination through a predominant trap with energy E_T. However, in low mobility semiconductors, the assumption that carriers diffuse sufficiently fast prior to trapping and after subsequent de-trapping so that ω_0 depends only on the charge emission rate e_p from a trap may not be met.[125, 151] In these materials, the low mobility μ of charge carriers implies that the transport times of diffusion $\tau_{diff} \propto \frac{1}{\mu}$ and drift $\tau_{drift} \propto \frac{1}{\mu}$ cannot be ignored at the frequencies applied in the TAS measurement. As a result, the dielectric loss peaks measured in plots of the differential capacitance occur at $\omega_0 = e_p(T)+\frac{1}{\tau_{diff}}+\frac{1}{\tau_{drift}}$.[125, 151]. Carriers can thus follow the AC signal up to a limiting frequency given by ω_D, the dielectric relaxation frequency, which approximates the carrier travel time $\frac{1}{\tau_{diff}} + \frac{1}{\tau_{drift}}$.[125] Since ω_D is the frequency associated with transport time, it depends on the conductivity $\sigma = q\mu N_A$ of charge carriers in the semiconductor according to:[90, 151]

$$\omega_D = \frac{\sigma}{\varepsilon_0 \varepsilon_s} \frac{w}{d} \tag{3.3.1}$$

where w is the depletion width, d is the film thickness, and ε_s is the dielectric constant. Room temperature electrical characterization of FETs made of 3 nm PbS QDs capped with EDT, provided in Appendix A.1, give a mobility $\mu \approx 1 \times 10^{-4}$ cm^2(Vs)$^{-1}$, consistent with literature reports.[64]. Assuming that $\varepsilon = 11.5$ (Appendix A.2), the EDT-capped PbS QD active layer is fully depleted such that $\frac{w}{d} = 1$[16, 133] and $N_A \approx 10^{17}$ cm^{-3},[133] we obtain $\omega_D \approx 1.6 \times 10^6$ rad/s. At $T = 290$ K, we measure $\omega_0 = 8.8 \times 10^5$ rad/s. Similar ω_0 frequencies are observed in EDT-capped PbS QD/Au junction devices (Appendix A.2), providing evidence that the loss peaks in Figure 3.3B results from majority carrier mobility freeze out and not charge trapping in the depletion region of the device.

Within the temperature range of our TAS measurement, hopping transport in QD solids follows Arrhenius behavior consistent with NNH, implying the thermal activation of σ is given by:[91, 105, 71]

$$\sigma = \sigma_0 \exp(-\frac{\Delta E_A}{k_B T}). \tag{3.3.2}$$

where σ_0 is a pre-factor that may depend on temperature and E_A is the activation energy of the conductivity. Combining (3.3.1) and (3.3.2) gives a thermally activated expression for the dielectric relaxation peak:

$$\omega_D = \frac{\sigma_0}{\varepsilon_0 \varepsilon_s} \frac{w}{d} \exp(-\frac{E_A}{k_B T}) \tag{3.3.3}$$

E_A can therefore be determined by applying a linear fit to $\ln(\omega_D)$ vs. $\frac{1}{T}$, shown in Figure 3.3C. The slope of the fit yields $E_A = 0.230 \pm 0.001$ eV, where the error reported is obtained from the fit.

The growth in amplitude of the differential capacitance in Figure 3.3B has been previously ascribed to a 'de-tuning' energy that corresponds to the thermal activation energy of the carrier density $E_N = E_{Tr} - E_F$ where E_{Tr} is the predominant hopping level above E_F as depicted in Figure 3.2A.[16, 15] A Fermi fit to $\omega \frac{dC}{d\omega}|_{\omega=\omega_0}$ vs. T is provided in Figure 3.3D, allowing us to estimate that $E_N = 0.08 \pm 0.01$ eV. Since $\sigma \propto n\mu$, where n is the carrier density, the thermal activation of the conductivity E_A similarly contains contributions from E_{Tr} and the activation energy of the mobility E_μ.[105, 125] We obtain $E_\mu = E_A - E_N = 0.15 \pm 0.01$ eV, in excellent agreement with the band tail width deduced from the absorption spectrum.

3.4 $\frac{G_p}{\omega}$ Measurements

The energetic landscape probed by TAS measurements may also be visualized by plotting the frequency-normalized conductance $\frac{G_p}{\omega}$[150, 127]. In analogy with plots of $-\omega \frac{dC}{d\omega}$, the frequency-dependence of $\frac{G_p}{\omega}$ directly probes the loss tangent ($\tan(\delta)$) in metal-semiconductor junctions.[111] At low ω, charge in the semiconductor may follow the AC signal resulting in no energy loss and small values of $\frac{G_p}{\omega}$. As ω increases, $\frac{G_p}{\omega}$ increases since the phase lag between the carrier response and the AC signal produces energy loss. $\frac{G_p}{\omega}$ continues to increase with ω until it reaches a peak at the resonance frequency ω_0. As ω increases further and larger portions of $N(E)$ cease responding to ω, the energy loss drops and $\frac{G_p}{\omega} \rightarrow 0$.

Figure 3.4 shows $\frac{G_p}{\omega}$ vs. ω at 0 bias from $T = 220 - 290$ K, calculated from normalizing the real part of the admittance response to the applied frequency of the measurement. The data show 2 peaks–a large feature at $\omega \lesssim 10^3$ rad/s and a set of smaller features at $\omega \approx 10^5$ rad/s. As temperature increases, the amplitude of the high ω features grows from low shoulders into a distinct set of peaks. The two different relaxation processes in Figure 3.4A may be interpreted using an equivalent circuit model containing two RC branches (Figure 3.4B). Similar equivalent circuit models have been used to model charge emission from deep states in n-GaAs Schottky junctions[63] and CIGS thin film PV devices.[124] Fits to the two peaks are obtained using the equivalent circuit in Figure 3.4B, for which we have derived the following conductance-frequency relations:

$$G = \frac{\omega^2 C_{t_1} \tau_{t_1}}{1 + \omega^2 \tau_{t_1}^2} + \frac{\omega^2 C_{t_2} \tau_{t_2}}{1 + \omega^2 \tau_{t_2}^2} \tag{3.4.1}$$

Similarly, the capacitance of the equivalent circuit is given by:

$$C = C_d + \frac{C_{t_1}}{1 + \omega^2 \tau_{t_1}^2} + \frac{C_{t_2}}{1 + \omega^2 \tau_{t_2}^2} \tag{3.4.2}$$

where $\tau_{t_1}\,(\tau_{t_2}) = \frac{1}{\omega_0}$ is the time constant associated with the low (high) peaks. The form of equation (3.4.1) reflects that the capacitance due to frequency-dependent charge dynamics is in parallel with the depletion capacitance, whereas the conductance branch of the equivalent circuit is primarily sensitive to charge dynamics outside the depletion region of the PV device. As a result, $\frac{G_p}{\omega}$ is more sensitive to interfacial recombination.[112]

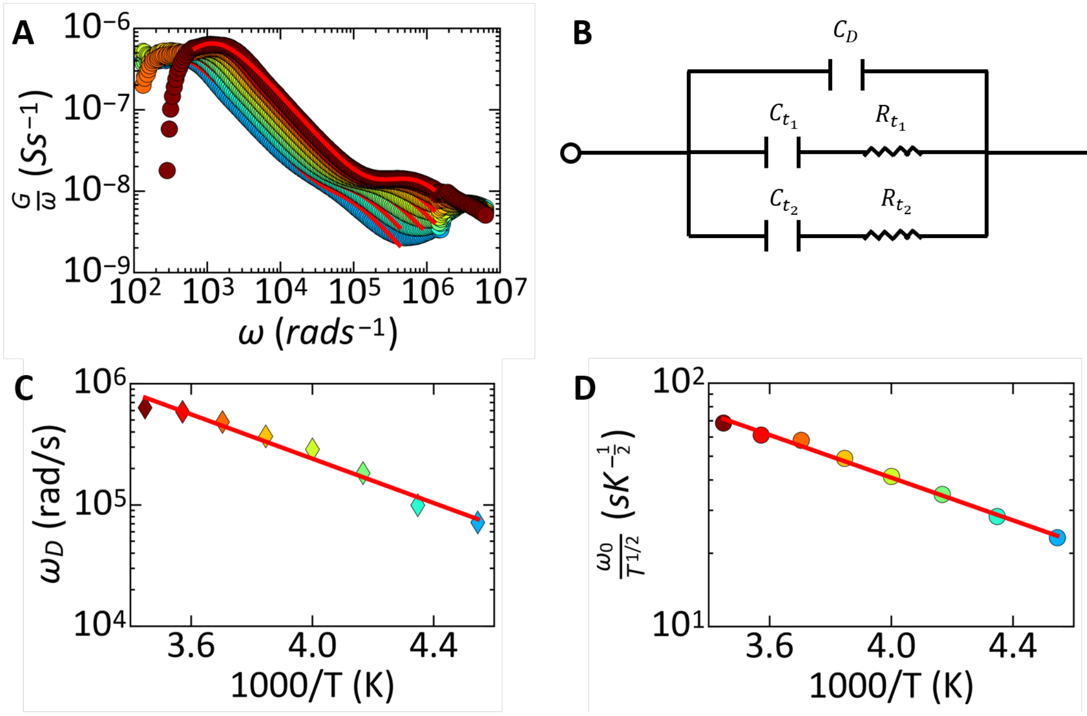

Figure 3.4: (A) $\frac{G_p}{\omega}$ vs. ω for $T = 220-290$K, with fits (red line) generated from (B) an equivalent circuit model of the PV device. The model includes contributions from interface states with capacitance C_{t_1} and recombination resistance R_{t_1} and transport charge dynamics with capacitance C_{t_2} and R_{t_2}. (C) Arrenhius fit to $\ln(\omega_D)$ vs. $\frac{1}{T}$ for high frequency peaks, giving thermal activation energy E_A. (D) Arrhenius fit to $\ln(\omega T^{-\frac{1}{2}})$ vs. $\frac{1}{T}$, giving thermal activation energy E_N.

The fits displayed in Figure 3.4A indicate that the proposed equivalent circuit provides an excellent model for interpreting the loss peaks in $\frac{G_p}{\omega}$. The extracted peak positions of the high ω feature give similar resonant frequencies observed in Figure 3.3B. We therefore infer that the high ω features in Figure 3.4A are due to dielectric relaxation and thus $\omega_0 = \omega_D$. An Arrhenius plot of ω_D vs. $\frac{1}{T}$ provided in Figure 3.4C yields $E_A = 0.181 \pm 0.026$ eV.

The pronounced low ω peaks in $\frac{G_p}{\omega}$ appear to have no explicit counterparts in the capacitance-frequency data exhibited in Figures 3.3A,B. Re-writing equation (3.1.1) in terms of $\omega = \frac{1}{\tau}$ yields the following expression for the resonant frequency of charge emission out of defects:

$$\omega_0 = 2\beta_p N_v \exp(-\frac{\Delta E}{k_B T}) \tag{3.4.3}$$

In bulk materials, the pre-factor $\beta_p N_V$ is usually written as the product of $\nu_{00}T^2$, where ν_{00} is the reduced attempt to escape frequency and the T^2-dependence comes from both $v_{th} \propto T^{1/2}$ and $N_V \propto T^{3/2}$.[150, 111] In QDs, however, N_V is temperature independent, so we may write equation (3.4.3) as:

$$\omega_0 = 2\nu_{00}T^{1/2} \exp(-\frac{\Delta E}{k_B T}) \tag{3.4.4}$$

In Figure 3.4D, we present Arrhenius fits of (3.4.4) to ω_0 of the low frequency peaks in Figure 3.4A. The slope of the fit indicates $\Delta E = 0.086 \pm 0.023$ eV, in excellent agreement with E_N inferred from the capacitance data.

The fits in Figure 3.4A allow us to extract the capacitance $C_{t_{1,2}} = qN_{t_{1,2}}(E)$ for both the interface state peaks and the dielectric relaxation peaks.[127] Since $\tau_t = R_t C_t$, we may also extract a characteristic resistance R_t for both sets of these features. In traditional SRH analysis, R_t is interpreted as a resistance to recombination–low values of R_t indicate that charge may flow into the state E_t *via* fast recombination processes.[119] By analogy, R_t for the dielectric freeze out peak corresponds to the relative probability of a charge hopping into the DOS at the mobility edge E_V. Large values of R_t imply that charge hopping at E_V is less likely than smaller values of R_t.

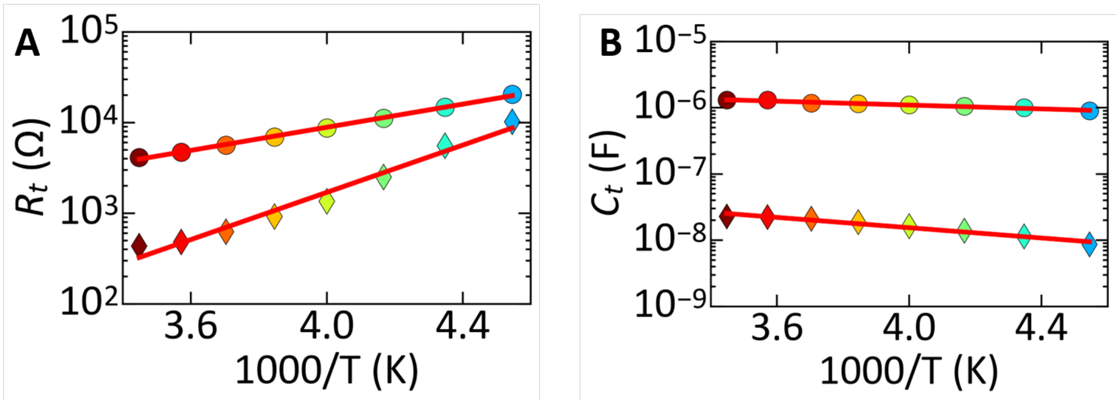

Figure 3.5: Extracted (A) R_t and (B) C_t for low (circles) and high frequency peaks (diamonds) from $T = 220 - 290$K from fits in Figure 3.4A.

The temperature-dependence of R_t and C_t for both ω_D and the low frequency feature is plotted in Figure 3.5A-B. The low frequency charge dynamics are associated with higher resistance (circles) than the freeze out feature, and changes only by a factor of ~ 2 across the temperatures probed in the experiment. By contrast, R_{t_2} associated with ω_D (diamonds) decreases over an order of magnitude from $T = 220 - 290$K. As a result, we conclude that charge capture by states that give rise to the low frequency peaks is less likely than occupation of the transport states responsible for dielectric relaxation. From Arrhenius fits to both sets of data, we obtain an activation energy of the resistance $E_{A_1} = 0.126 \pm 0.025$ eV for the low frequency feature and $E_{A_2} = 0.258 \pm 0.025$ eV for the dielectric freeze out peaks. We note the excellent agreement between the activation energy of the resistance for states associated with freeze-out and E_{A_2} of ω_D obtained in Figure 3.3C. These data therefore reflect that the temperature-dependent charge dynamics in the QD PV device probed at frequencies $\sim 10^4 - 10^6$ rad/s are dominated by thermally activated hopping between transport states responsible for dielectric relaxation.

The origin of the relative importance of these states to dielectric loss can be seen in the temperature-dependence of the capacitance C_t of the QD PV device in Figure 3.5B. The capacitance of the low frequency peaks (C_{t_1}, circles) is almost constant and ~ 2 orders of magnitude larger than C_{t_2}, the capacitance due to dielectric relaxation. As a result, we infer that the occupation of charge states responsible for the low frequency peaks undergo little increase in occupation over the temperature range of the experiment. By contrast, the capacitance of states responsible for dielectric relaxation (diamonds) continually increases with temperature, as expected for hopping conductivity of thermally activated carrier densities.[105] An Arrhenius fit to C_{t_1} indicates $E_A = 0.029$ eV. The activation energy of C_{t_2} for the higher frequency feature we ascribe to transport states yields 0.077 eV, implying that ~ 2.7 times more energy is needed to access the density of states responsible for this spectral feature. The ratio of these two energies is comparable to the factor of ~ 2.9 between E_N and E_A determined in Section 3.3. We also note the agreement between the activation energy of the capacitance of the transport states and the carrier activation calculated in Figure 3.3D, which further match the activation energy of charge emission of the low frequency charge relaxation feature states calculated from the fit in 3.4D. The agreement of these energies suggests that charge relaxation probed at low frequency provides carriers for transport throughout the QD film. We hypothesize that these low ω features may result from interfacial states, since states localized at the interface are obscured in the capacitance-frequency spectra due to the contribution of C_D.

3.5 AC Conductivity Measurements

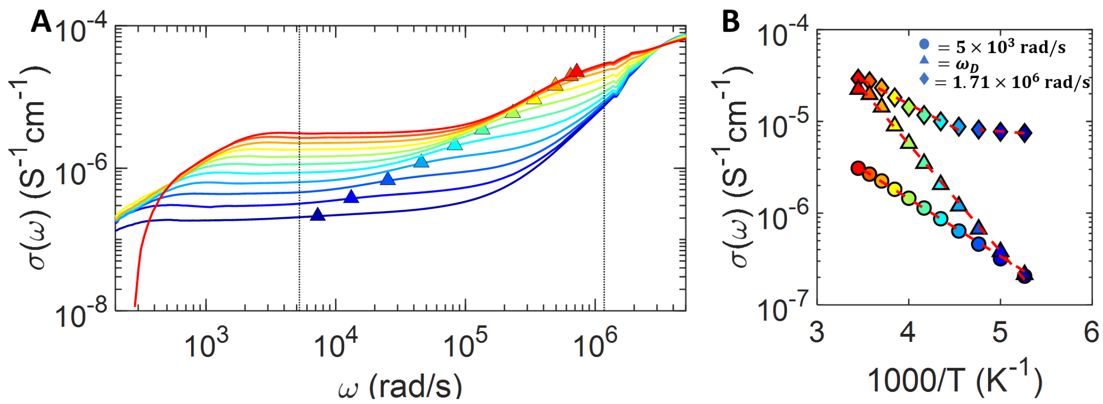

Figure 3.6: (A) Log-log plot of $\sigma'(\omega)$ vs. ω. (B) $\sigma'(\omega)$ vs. $\frac{1}{T}$ with Arrhenius fits (dashed red lines) for $\omega_{mf} = 5 \times 10^3$ (circles), $\omega = \omega_D$ (triangles), and $\omega_{hf} \approx 1.2 \times 10^6$ rad/s (diamonds), yielding activation energies corresponding to E_μ, $E_F - E_V$, and E_{Tr}, respectively.

The frequency-dependent total conductivity $\sigma'(\omega)$ (Figure 3.6A), calculated from normalizing the real part of the admittance response to the area of our PV devices, is simultaneously collected as a function of temperature as a part of our TAS experiments. For $\omega \lesssim 10^3$ rad/s, $\sigma'(\omega)$ at all temperatures exhibits a pronounced low frequency roll off due to loss peaks at these frequencies that we ascribe to thermal activation of the carrier density (see Section 3.4). Between $10^3 \lesssim \omega \lesssim 10^5$ rad/s, $\sigma'(\omega)$ exhibits only slight frequency dispersion for $T < 230$ K and almost no dispersion at higher T. This mid-frequency plateau in $\sigma'(\omega)$ occurs over the same frequency range as the capacitance plateau in Figure 3.3A, indicating that this feature corresponds to frequencies at which charge can follow the applied AC signal. From equation (3.1.1), low measurement frequencies allow for the experimental interrogation of longer hopping times and large energy excursions to states further away from E_F. According to the RFEB model, the availability of greater portions of $N(E)$ for charge hopping at low measurement frequency implies that larger volumes of the QD film may be probed in measurements of $\sigma'(\omega)$ (Figure 3.1A).[36] The low frequency $\sigma'(\omega)$ data thus reflect the dispersion-less DC limit of the hopping conductivity $\sigma'(0)$ in which charge may hop along a percolation path that stretches across the QD film.[105, 36, 41]

The activation energy of $\sigma'(\omega)$ in the mid-frequency regime can be obtained by considering the temperature dependence of conductivity at a single test frequency $\omega_{mf} = 5 \times 10^3$ rad/s, as indicated in Figure 3.6A. An Arrhenius fit to $\sigma'(\omega_{mf})$ vs. $\frac{1}{T}$ from $T = 190 - 290$ K, provided in Figure 3.6B (circles), yields an activation energy $E_A = 0.124 \pm 0.01$ eV, in agreement the activation energy of the mobility $E_\mu = 0.15$ eV calculated from the energy levels probed in TAS measurements. The consistency of these results suggests that the largest energetic barrier that must be surmounted for continuous charge hopping throughout the QD film at these applied frequencies involves a transition between states at E_{Tr} and those E_V.

Figure 3.6A also highlights the loss peaks at ω_0 (triangles) detected in TAS, which span the frequency range of the measurement. The Arrhenius fit to $\sigma'(\omega_0)$ in Figure 3.6B yields $E_A = 0.23 \pm 0.01$ eV, indicating that thermal activation of ω_0 in Figure 3.3D exactly follows the thermal activation of $\sigma'(\omega_0)$ as indicated by (3.3.3). The agreement between the capacitance and conductance measurements provide further evidence that the resonant frequency detected in TAS corresponds to the dielectric freeze out frequency ω_D. The activation energy $E_A = 0.23$ eV observed in these measurements likely correspond to the difference between E_F and E_V,[150] implying that the effective bandgap of our QD PV device is less than the $\frac{E_G}{2}$ expected in an ideal Schottky junction device. We therefore expect the V_{oc} of our PV device to be constrained by the observed Fermi level, and calculate a maximum achievable V_{oc} of $\frac{E_G}{2} - (E_F - E_V) = 0.61 - 0.23 = 0.38$ eV[28], in excellent agreement with the observed V_{oc}.

At higher frequencies, $\sigma'(\omega)$ exhibits a large, temperature-dependent enhancement in Figure 3.6A. This increase occurs roughly where the capacitance drops to a minimum in Figure 3.3A, suggesting that $\omega > \omega_D$ and charge can no longer follow the applied signal. At these high frequencies (low τ), equation (3.1.1) dictates that only small energetic barriers are interrogated such that only charge hops to states near E_F may be resolved by the measurement. Similar high-frequency enhancements to the AC conductivity of dielectric materials have been shown to result from charge hopping hopping back and forth within finite regions where charge hopping is more probable due to low internal energetic barriers.[36] From the drift velocity $v_d = \frac{\tau}{L} = \mu\mathcal{E}$, we can estimate the AC drift length L of a charge through a single cluster at a given frequency $\omega = \frac{1}{\tau}$. For $\mu = 1.2 \times 10^{-4}$ cm^2(Vs)$^{-1}$ at 300 K (Appendix A.1) and an AC amplitude of 20 mV, we calculate $L \approx 9$ nm for $\omega = 2 \times 10^6$ rad/s, indicating that high frequency AC conductivity measurements probe clusters containing a small number of dots. The use of the DC mobility in this calculation implies that the calculated L serves as a limit of the cluster length. As frequency increases, the cluster length decreases, and we estimate that the cluster length drops below the 3 nm single QD diameter at $\sim 5 \times 10^6$ rad/s using the DC mobility.

As in the case with the low frequency conductivity, the activation energy of the high frequency conductivity can be calculated by considering the temperature-dependence of $\sigma'(\omega)$ at a test frequency $\omega_{hf} = 1.71 \times 10^6$ rad/s. Since $\omega_{hf} > \omega_D$, hopping from states at E_F to those near E_V is forbidden. Two different activation energies are apparent in Figure 3.6B (diamonds): a small activation energy on the order of the thermal energy from $T = 190 - 220$ K ($E_A \approx 0.015$ eV), and a larger activation energy $E_A = 0.10 \pm 0.025$ eV from $T = 230 - 290$ K. The activation energy of the low temperature portion of the data is consistent with the nearest neighbor hopping energy obtained from FET measurements of EDT-capped Pb-chalcogenide QDs, suggesting that only charge hops within single QDs or across QD pairs are allowed at these temperatures and frequencies.[117, 71] At higher temperatures, $\sigma'(\omega_{hf})$ exhibits stark thermal activation indicating that the the clusters interrogated contain several QDs, consistent with our calculation of the AC drift length L above. The larger thermal activation required for hopping among clusters of QDs suggests that these clusters exhibit a broader site-to-site energy dispersion than the shorter range hops among pairs of QDs or within single QDs. The extracted activation energy for charge hopping within these clusters is in agreement with the thermal activation of the carrier density E_N obtained from capacitance measurements in Figure 3.3. The consistency of these energies implies that the most probable energetic transitions in the QD film at these frequencies are those involving charge hops from states at E_F to states in the band tail at E_{Tr}.

3.6 DLCP Measurements

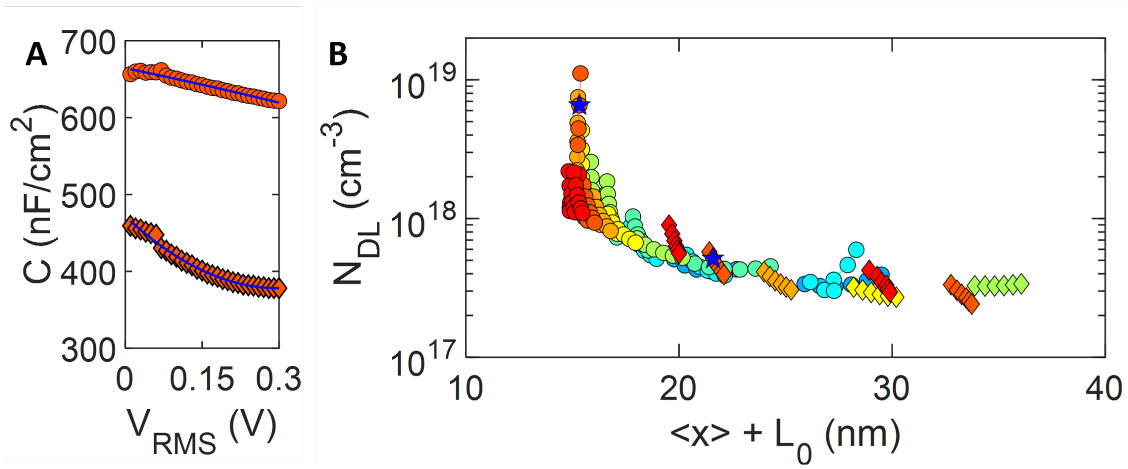

Figure 3.7: (A) C vs. V_{RMS} for $\omega = 6.28 \times 10^3$ rad/s (circles) and 6.28×10^5 rad/s with accompanying non-linear fits (blue line). (B) Profile of drive level densities obtained *via* DLCP from $T = 220290$ K with example N_{DL} values from (A) highlighted (blue stars).

The occupation of the energy levels detected in TAS and temperature-dependent AC conductivity may be quantified with the aid of temperature-dependent DLCP. DLCP measurements of the PbS QD device were obtained in parallel with the TAS and conductance measurements by measuring the non-linear capacitance response of the device to large AC perturbations (V_{RMS}) applied at a given frequency ω against a total reverse bias $V_{max} = |V_{RMS} + V_{DC}|$. V_{max} is held constant for a given DLCP measurement, implying changes in V_{RMS} must be compensated by a variable DC bias V_{DC}.[52] Figure 3.7A shows example data for $T = 280$K, $V_{max} = -100mV$, and $\omega = 2\pi f = 6.28 \times 10^3$ rad/s (circles) and $\omega = 3.14 \times 10^5$ rad/s (diamonds). As described in Appendix A.4, the coefficients of cubic fits to these data can be used to calculate the drive level carrier density

N_{DL}, defined as:[52]

$$N_{DL} = p + \int_{E_F}^{E_F+E_\omega} N(E,x)dE \tag{3.6.1}$$

Here, p is the density of free carriers in the VB provided by ionized acceptors N_A^-. The integration in energy performed over the $N(E)$ implies that N_{DL} may be interpreted as the concentration of occupied states (measured in cm^{-3}) at a given spatial location x. The integral is bounded by E_F and $E_F + E_\omega$, where E_ω is a limiting energy separating states that may respond to the AC signal from unresponsive states.[150, 54] E_ω may be written:

$$E_\omega = k_B T \ln(\frac{\nu}{\omega}) \tag{3.6.2}$$

In the case of charge emission out of a defect state governed by Shockley-Read-Hall (SRH) kinetics, $\nu = \nu_0$, the attempt-to-escape frequency from equation (3.4.4). Equation (3.1.1) allows us to define an analogous limiting energy for the case of charge hopping in a disordered QD array if $\nu \rightarrow \frac{1}{\tau_c}$. In this interpretation, hops requiring a charge carrier to surmount larger energetic barriers become forbidden as frequency increases, resulting in a decrease E_ω and a smaller capacitance response, as reflected in Figure 3.7A.

Fits to DLCP data are also used to find the mean spatial location $< x >$ of the charge density that can respond to the AC signal. $< x >$ may be calculated by assuming that the junction capacitance C probed by the DLCP measurement at $V_{RMS} = 0$ (y-intercept of Figure 3.7A) may be written as:[53, 52]

$$C = \frac{A\varepsilon\varepsilon_0}{L_0 + < x >} \tag{3.6.3}$$

where A is the device area and $L_0 = (\frac{\varepsilon\varepsilon_0 k_B T}{q^2 N_{DL}})^{\frac{1}{2}}$ is the Debye screening length of the charge density that can respond to the measurement.[122] In DLCP measurements of defects in CIGS thin film devices, $< x >$ can vary hundreds of nm as the application of V_{RMS} alters the junction band bending, allowing for N_{DL} to be profiled far into the depletion region.[52, 39] By contrast, L_0 only slightly contributes to the profile distance; for instance, given $N_{DL} \approx 10^{17}$ cm^{-3} and $T = 300$ K, $L_0 \approx 15$ nm for $\varepsilon \approx 10$. Since the measurement is not sensitive to variation in charge density below the Debye length, L_0 provides a lower bound to the spatial resolution of DLCP.[52]

The fits to the the low frequency data in Figure 3.7A yield the highlighted value of N_{DL} (blue star) ~ 15 nm from the junction as displayed in the distance profile in Figure 3.7B. DLCP data obtained from $T \sim 260 - 290$ K and $\omega \lesssim 10^4$ give similar values of $< x >$, revealing a large charge density $\sim 10^{18} - 10^{19}$ cm^{-3} 15 nm from the interface. Fits to the high frequency data in Figure 3.7A yield a charge response at slightly larger distances (blue star) $< x > \approx 24$ nm. At higher applied ω and V_{max}, the charge response is centered even further away from the junction. For instance, at $T = 280$, $\omega = 6.28 \times 10^5$ rad/s, and $V_{max} = -300$ mV, the charge response is located ~ 38 nm from the junction.

As discussed in Appendix A.4, the variation in $L_0 + < x >$ in Figure 3.7B that results from increases in frequency is much larger than the variation due to increases in V_{max}. The observed variation in the profile distance due to V_{max} is also smaller than the shifts in the depletion region expected from the application of V_{max}. We therefore conclude that the spatial variation in N_{DL} exhibited in Figure 3.7B results from changes in L_0. The trends in Figure 3.7B can be explained by a growth in L_0 resulting from decreases in E_ω and thus the interrogation of smaller ranges of $N(E)$ as frequency increases (equation (3.6.2). At $T = 280$ K, E_ω shrinks $\sim 20\%$ as ω increases from 3.14×10^3 rad/s to 6.28×10^5 rad/s, assuming $\frac{1}{\tau_0} >> \omega$. Over the same frequency range, $L_0(T = 280\,\mathrm{K})$ increases $\sim 30\%$ given the N_{DL} values obtained in the measurement, implying that changes in L_0 can account for the change in profile length in Figure 3.7B.

3.7 Density of States

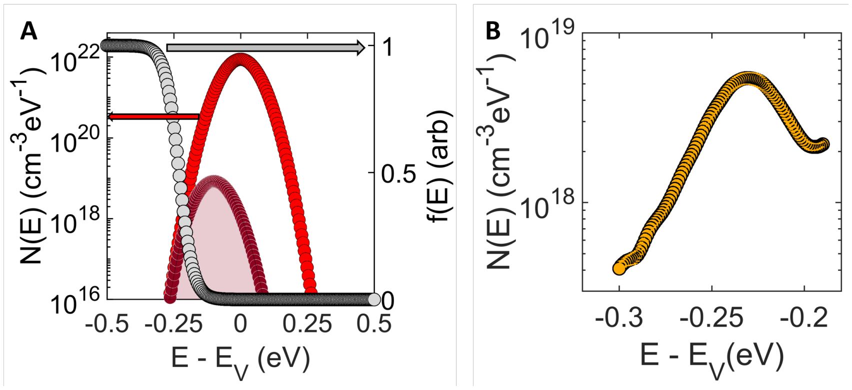

Figure 3.8: (A) Calculated $N(E)$ (red) with Fermi function for $E_F = 0.23$ eV at 300K (gray). Integrating the product of the 2 distributions yields the concentration of carriers p (burgundy) in cm^{-3}. (B) $N(E)$ calculated from normalizing the capacitance derivative from $T = 260290$ K to N_{DL} obtained at $\omega = 6.28 \times 10^5$ rad/s.

The energy levels and carrier densities obtained *via* junction admittance measurements may be clearly visualized by relating them to $N(E)$ of band-edge states probed in optical absorption measurements. To facilitate comparison with our DLCP data, we convert the absorption ordinate of Figure 3.2A into N_V in cm^{-3}eV^{-1} by normalizing the amplitude of a Gaussian distribution centered at $E_G = 1.22$ eV with variance $\sigma_{var} = 0.051$ eV to an amplitude $N_V = \frac{n_V}{E_{QD}}$, where E_{QD} is the single particle energetic linewidth previously measured to be 20 meV.[153] n_V is the spatial concentration of valence band states, and depends on the effective volume of a single QD in the film V_{eff} as $n_V = \frac{8}{V_{eff}}$.[162] As described in Appendix A.5, we calculate $V_{eff} \approx 1.4 \times 10^{-20}$cm^{-3} to obtain $n_V = 1.77 \times 10^{20}$ cm^{-3}. This results in a band-edge density of states $N(E)_V = 8.83 \times 10^{21}$ cm^{-3}eV^{-1}, displayed in bright red in Figure 3.8A.

Figure 3.8A also displays $f(E) = \frac{1}{1+\exp(-\frac{E_F - E}{k_B T})}$ calculated assuming $E_F = 0.23$ eV at room temperature (gray). Integrating the product of $f(E)$ and N_V (Figure 3.8A, burgundy) yields a total carrier concentration $p = 1.05 \times 10^{18}$ cm^{-3}, in reasonable agreement with $N_{DL} \approx 3 \times 10^{18}$ cm^{-3}

obtained by low frequency DLCP at high temperatures (Figure 3.7B) and an order of magnitude larger than N_{DL} closer to E_F in the band tail determined *via* high frequency DLCP.

To corroborate this analysis, we also estimate $N(E_F)$ from the values of N_{DL} deduced from high frequency DLCP measurements. As noted in Appendix A.5, $N(E_F)$ probed in TAS may be calculated *via* normalization of the capacitance derivative in Figure 3.3B by device parameters such as V_{bi}. Instead, we estimate $N(E_F)$ by assuming the capacitance derivatives in Figure 3.3B probe a Gaussian density of states with peak amplitude A and variance σ^*. We can then analytically carry out the integration of the $N(E_F)$ and set it equal to N_{DL} as follows:

$$\begin{aligned} N_{DL} &= \int_{-\infty}^{\infty} A\exp(\frac{(E-E_F)^2}{2\sigma^{*2}}) \\ N_{DL} &= \sqrt{2\pi}A\sigma^* \end{aligned} \tag{3.7.1}$$

The energetic width of the distribution σ^* may be estimated by converting the frequency abscissa of Figure 3.3B to an energy scale *via* equation (3.1.1). Since both σ^* and N_{DL} are known, we can then calculate the total amplitude A and therefore $N(E)_V$.

The result of this calculation is presented in Figure 3.8B for $\omega = 10^5$ rad/s and averaged over $T = 260-290$ K. These values were chosen since the high frequency N_{DL}, which reflects the charge carrier density close to E_F, exhibits a smaller variance at higher temperatures. At $E = E_F = 0.23$ eV, we obtain a total peak density $N(E_F) = 5.4 \times 10^{18}$ cm^{-3}eV^{-1}. Though this value is ~ 1 order of magnitude larger than $N(E_F) = 4 \times 10^{17}$ cm^{-3}eV^{-1} predicted by optical absorption in Figure 3.8A, we note that integration of $N(E_F)$ in Figure 3.8B gives a carrier density $p = 2.96 \times 10^{17}$ cm^{-3}eV, while integration of $N(E)$ in Figure 3.8A obtained by optical absorbance over the same energetic range gives $p = 1.29 \times 10^{17}$ cm^{-3}. The discrepancy in $N(E_F)$ between these methods may result from additional contributions to the capacitance measured in DLCP from $T = 260 - 290$ K at $\omega = 10^5$ that are not observable in the derivatives of the TAS capacitance over the same temperature range, which are centered around slightly higher frequencies $\omega_0 = 3 \times 10^5 - 8 \times 105$ rad/s. This additional contributions may make shape of $N(E_F)$ determined by DLCP and TAS broader than $N(E)$ deduced *via* optical absorption.

3.8 Temperature-Dependent JV Characteristics

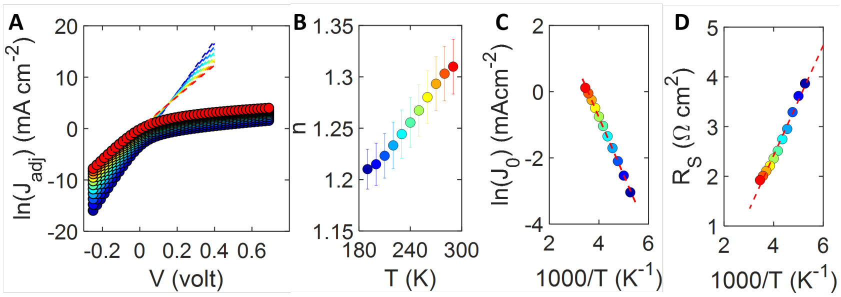

Figure 3.9: (A) Logarithmic plot of J_{adj} vs. V with linear fit to low voltage characteristics yielding the ideality n. (B) n vs. T. (C) Logarithmic plot of $\ln(J_0)$ vs. $^{1000}/_T$ with Arrhenius fit (dashed red line) giving E_μ. (D) Temperature-dependence of R_s with Arrhenius fit (dashed red line) yielding activation energy E_{R_s}.

Temperature-dependent JV characteristics of the PbS QD PV device were obtained in parallel with the frequency-dependent characterization as indicated in Figure 3.1B. A general diode equation for the current density J in a Schottky junction may be written:[127]

$$J = J_0 \exp(\frac{qV}{nk_BT})[1 - \exp(-\frac{qV}{k_BT})] \tag{3.8.1}$$

where J_0 is the reverse saturation current density and n is the ideality factor. Writing the diode equation in this form allows for the ideality factor to capture recombination in the depletion region and the bias-dependent lowering of the barrier height ϕ barrier due to the accumulation of charge at the interface such that $n = 1 - \frac{\partial\phi}{\partial V}$.[127] Equation (3.8.1) suggests that n and J_0 may be determined by considering the slope and intercept of a plot of $\ln(\frac{J}{[1-\exp\{-\frac{qV}{k_BT}\}]})$ against V. Fits of (3.8.1) to the dark JV data obtained from our PbS-QD EDT PV device from $T = 190 - 290$ are provided in Figure 3.9A. The diode equation (3.8.1) well describes the data below ~ 0.1 V, above which the series resistance R_S causes a roll off in J. As temperature increases, the slope of the fits in Figure 3.9A decrease. This results in an increase in n from $\sim 1.2 - 1.3$ with temperature (Figure 3.9B). Assuming that charge recombination occurs via by band-to-band or trap recombination mechanisms in the bulk, n assumes a value of 1-2. In semiconductor-metal junctions, charged interfacial layers which pin E_F can dominate bulk charge dynamics. In this case, n is related to the change in barrier height as the interface charge density accumulates with bias: [127]

$$\frac{1}{n} = 1 - [\frac{\partial(\phi_e + \Delta\phi_{b,im})}{\partial V}] \tag{3.8.2}$$

where ϕ_e is the effective barrier height and $\Delta\phi_{b,im}$ is the electrostatic lowering of the barrier due to the charge density at the interface. In an ideal case with no image force lowering due to interfacial charge accumulation, $\frac{\partial(\phi_e+\Delta\phi_{b,im})}{\partial V} = 0$ and thus $n = 1$. Figure 3.9B clearly exhibits temperature-dependent deviations from this ideal case, from which we conclude that the amount of image force lowering increases with temperature. The increase in n with T is consistent with the temperature-dependent increase in charge density observed in the low frequency DLCP data, which grows one order of magnitude from $T = 220 - 290$ K (Appendix A.4).

Charged interfacial at the layers at PbS QD-metal surface have been shown to contribute to anomalous JV characteristics in QD PV devices, and stem from the temperature-dependent hopping mobility $\sim 10^{-3} - 10^{-4}$ cm^2(Vs)$^{-1}$ governing charge transport in the EDT-capped PbS QD layers.[59] The observation that the deviation from $n = 1$ increases with temperature in Figure 3.9C is consistent with barrier lowering at the interface resulting from an increase in interfacial charge density that occurs as the hopping mobility increases with temperature and more charge moves to the interface. Because n is extracted from reverse bias JV data, the barrier at the semiconductor surface is large enough to prohibit the accumulated interfacial charge from injecting into the metal even at room temperature.

In low mobility semiconductors, the saturation current density J_0 is dominated by charge carrier diffusion according to:[127]

$$J_0 = N_v \mathcal{E}_{max} \mu_0 \exp(-\frac{E_\mu}{k_B T})\exp(-\frac{\phi_b}{k_B T}) \tag{3.8.3}$$

where $\mu = \mu_0 \exp(-\frac{E_A}{k_B T})$ is the activated charge carrier mobility, $\mathcal{E}_{max}$ is the value of the electric field at the junction, and ϕ_b is the barrier height at the metal-semiconductor interface. Since N_V in QD films is a constant,[161] the temperature dependence of the prefactor is given by E_μ, and the total activation energy of J_0 is $E_A = E_\mu + \phi_B$. Figure 3.9C displays the temperature-dependence of $\ln(J_0)$ extracted from the fits in Figure 3.9A with an accompanying Arrhenius fit. The slope of the fit indicates $E_A = 0.150 \pm 0.025$ eV. The excellent agreement of E_A with E_μ implies that J_0 contains no dependence on ϕ_B. We hypothesize that the the large interfacial charge density detected in DLCP sufficiently lowers ϕ_B so that the dominant thermal activation in J_0 is derived from μ.

In forward bias, R_S dominates the JV characteristics at $V \gtrsim 0.1$ V. Figure 3.9D displays the Arrhenius plot of R_S from $T = 190 - 290$ K, obtained *via* an analysis of the dark JV curves which minimizes device parasitics (Appendix A.7). The Arrhenius fit yields an activation energy $E_A = 0.095 \pm 0.001$ eV. The agreement with the carrier activation energy E_N indicates that the dominant DC transport mechanism in forward bias is likely hopping through band tail states at E_{Tr}, which form a continuous percolation network for charge to hop throughout the QD film. At applied frequencies $\sim 10^3$ rad/s, this low energy percolation network is broken up, as indicated by the loss peak discussed in Section 3.4. Continuous charge transport through the film then relies on hopping between smaller clusters of QDs that occurs with an inter-cluster hopping energy E_μ. At higher frequencies $\sim 10^6$ rad/s, the inter-cluster hops are frozen out and only the low energy charge hops between E_F and E_{Tr} are allowed within isolated, small islands of QDs.

3.9 Vacuum Admittance Measurements

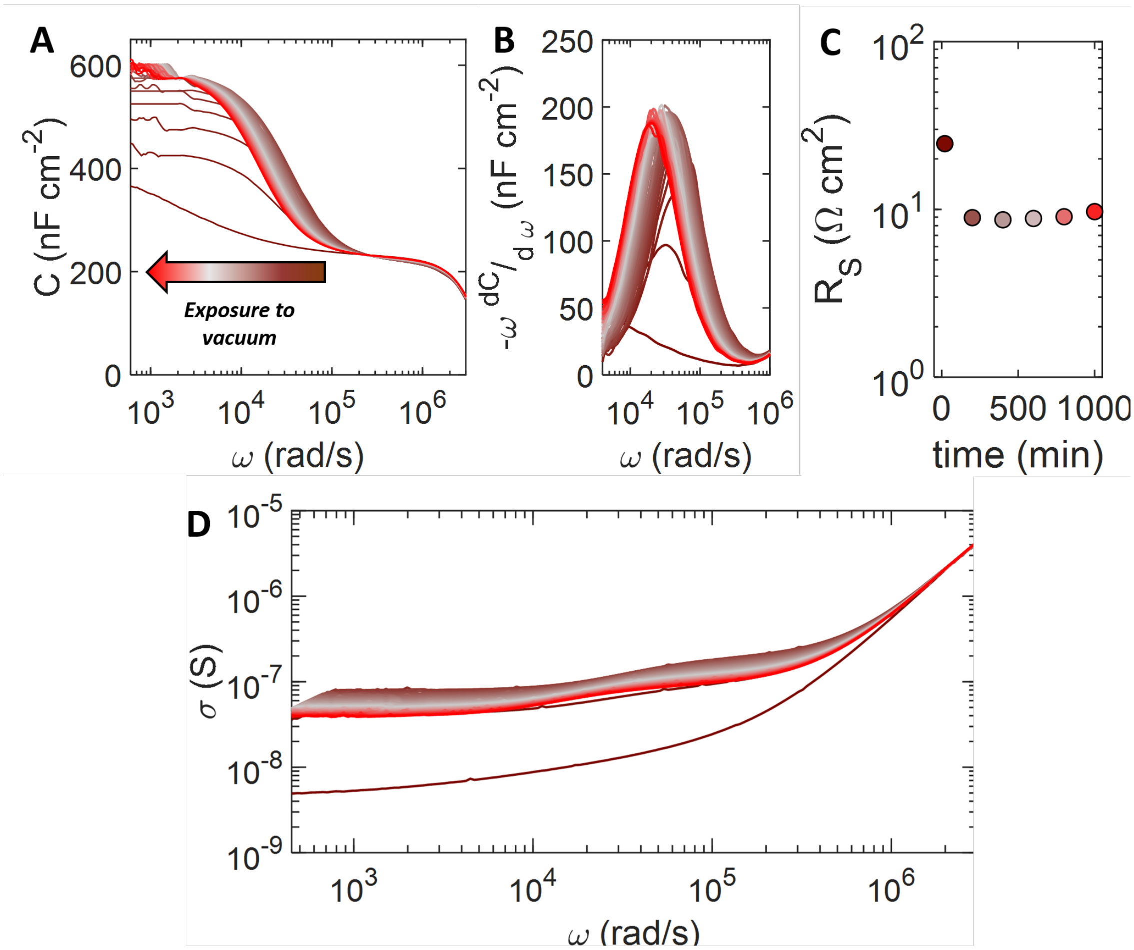

Figure 3.10: Vacuum evolution of (A) C vs. ω, (B) ω_D, (C) R_S and (D) $\sigma(\omega)$ vs. ω.

To confirm the position of E_F with respect to E_V, we use TAS and DLCP to monitor the variation in the room temperature defect capacitance of a second PbS-EDT QD Schottky junction PV device continuously exposed to vacuum at $\sim 10^{-4}$ torr over the course of 17 hours at constant temperature. The well known p-doping effect of molecular oxygen is known to be reversible by desorbing O^2 from the surfaces of both bulk Pb-chalcogenide crystals[102, 101, 51] and Pb-chalcogenide QDs[86] under vacuum. By exposing our PbS QD device to vacuum, we may therefore qualitatively determine how the occupation of $N(E)$ depends on the concentration of oxygen adsorbed to the QD surface. In contrast to the reversible adsorption of atmospheric O_2 to the surface of Pbs QDs, oxidation of the Al top contact occurs quickly and irreversibly.[2, 3] Therefore, we minimize the reduction of the Al Schottky contacts in the presence of ambient O_2 by depositing a thin layer of Au on top of the completed Al contact as has been done in previous studies of the effect of oxygen on PbS QD films.[16]

The time-dependent capacitance in Figure 3.10A shows an initial, rapid rise as adsorbed oxygen is removed under vacuum. While the magnitude of the low frequency capacitance stabilizes within ~ 100 min, continued exposure to vacuum shifts ω_D to lower frequencies, as seen in Figure 3.10B. Commensurate initial drops in R_S (calculated from JV curves available in Appendix A.8) and increases in the low frequency DC conductivity region of $\sigma'(\omega)$ are observed in Figures 3.10C,D. These trends are consistent with an initial increase in charge carrier concentration as oxygen is desorbed from the film, with a subsequent decrease in the conductivity as probed by ω_D. We hypothesize that these two phenomena occur concurrently due to an increase in the population of less mobile states in the PbS QD PV device.

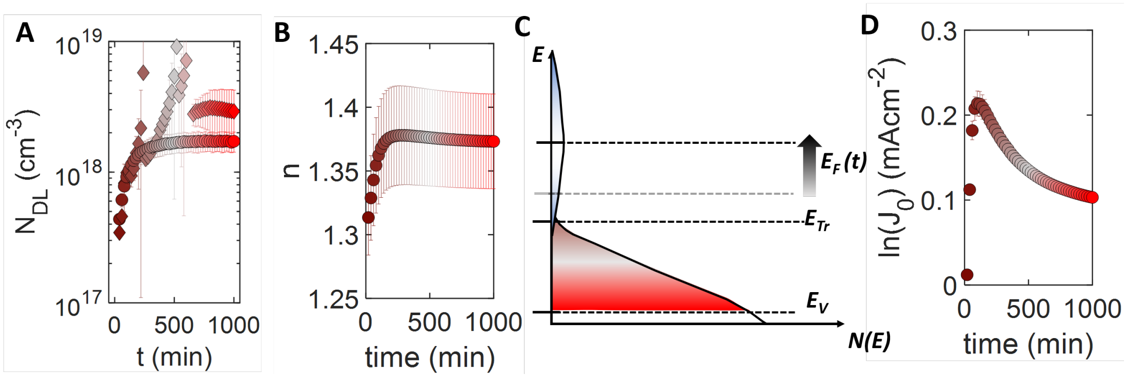

Figure 3.11: Vaccum evolution of (A) N_{DL} measured at $\omega = 3.14 \times 10^3$ rad/s (circles) and $\omega = 4.5 \times 10^4$ rad/s (diamonds), and (B) n. (C) Schematic of upward shift in E_F to pinning level upon initial exposure to vacuum. (D) Vacuum evolution of $\ln(J_0)$

Figure 3.11A exhibits N_{DL} measured as a function of time under vacuum. Like the capacitance in 3.10A, N_{DL} obtained at low ω (circles) exhibits a sharp increase and later stabilization after $t \approx 100$ minutes. At high frequency (diamonds), N_{DL} follows an identical trend within the error of the measurement. We ascribe the large error in the high-frequency N_{DL} to the vacuum-induced shifts in ω_D observable in Figure 3.10A: early in the measurement, ω_D is larger than the frequency used to measure the high frequency values of N_{DL} ($\omega = 4.5\times10^4$ rad/s. At longer vacuum exposure times, ω_D shifts below this frequency. This transition occurs at $\sim$ 550 mins, roughly to where the high frequency N_{DL} values saturate in Figure 3.11A. The consistency between the low and high frequency N_{DL} measurements suggests that the total increase in charge density in the QD PV device may be explained by increases in charge density at energies close to E_F rather than in states associated with high mobility around E_V, which can only be accessed at low frequency.

The evolution of N_{DL} matches the time-dependent behavior of n, exhibited in Figure 3.11B and calculated from JV data provided in Appendix A.8. The agreement between N_{DL} and n indicates that the desorption of oxygen quickly pins E_F which results in a large spike in the interface charge density, as indicated in Figure 3.11C. This interfacial charge density, in turn, lowers the barrier, leading to the quick initial rise in J_0 as the device is exposed to vacuum observed in Figure 3.11D.

Scanning tunneling spectroscopy studies (STS) of FETs made of 5.5 nm PbS QDs capped with EDT have previously measured $E_F \approx 0.1 - 0.2$ eV above E_V [161, 162], corresponding approximately to the position of E_{Tr} measured in our QD device in section 3.3. Desorption of surface O^2 has been previously linked to a decrease in the density of these intra-gap states in both STS studies and density function theory (DFT) calculations of PbS QD films.[161]. We therefore expect that desorption of O_2 in our QD film would lead to a decrease in the density of band tail states $N(E_V)$ and in the occupation of these states. Decreases in n_v would explain the gradual decrease in ω_D and $\sigma'(\omega)$ observed in Figures 3.10 B and C after N_{DL} saturates.

To investigate how n_V changes with vacuum exposure, we perform a series of absorption measurements on a PbS QD film deposited on a sapphire substrate and mounted inside a sealed cryostat. The sample is held at room temperature while the absorbance of the film is measured for $\sim$ 12 hours under continual exposure to vacuum at $\sim 10^{-4}$ torr. Figure 3.12A shows examples of the absorption spectra with Gaussian fits (dashed blue lines) at 8 evenly spaced intervals over the course of the 12 hour measurement (i.e. each example corresponds to an absorption curve measured every $\sim$ 90 min). Using the parameters obtained from the Gaussian fits, Gaussian distributions representing N_V was generated, as depicted in Figure 3.12B.

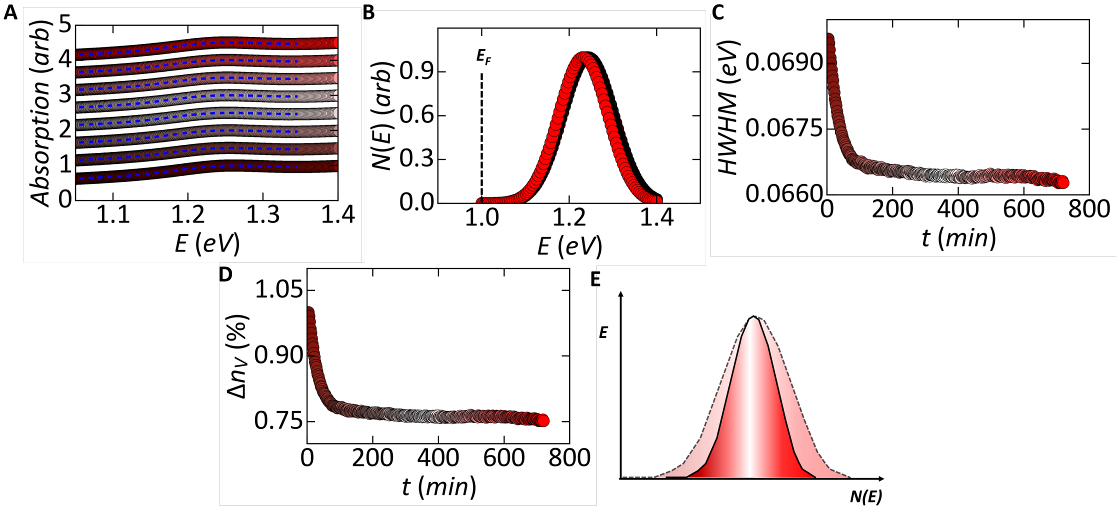

Figure 3.12: (A) Example absorption curves of EDT-capped PbS QDs measured under exposure to vacuum with accompanying Gaussian fits (dashed blue lines). (B) Gaussian distributions calculated from fits to optical absorption spectra in (A), with assumed value of $E_F = E_V - 0.23$ eV drawn in schematically (C) Decrease in long wavelength side of HWHM of Gaussians in (B) as a function of exposure to vacuum. (D) Change in n_V calculated by integrating $f(E_F)$ and N_V distributions pictured in (B). (E) Schematic of decrease in N_V.

The half-width at the half-maximum (HWHM) of the absorption data at long wavelength has been previously reported to be an indicator of the dispersion in N_V due to QD size polydispersity.[153] For this analysis, we use the HWHM to report on the width of the band tail of our PbS QD film. Exposure to vacuum results in a notable decrease in the HWHM on the long wavelength side, as displayed in Figure 3.12C. This shift is generally unobservable in the Gaussian distributions displayed in Figure 3.12B calculated from the fits to the absorption spectra Figure 3.12A due to a $\sim 10meV$ redshift of the absorption peak (displayed in Appendix A.8). Assuming $E_F \approx 1.0eV$, (Figure 3.12B), the decrease in the HWHM leads to a commensurate $\sim 20\%$ decrease in n_V with exposure to vacuum, as shown in Figure 3.12D. We note that the decreases in the HWHM and n_v occur at ~ 100 mins, which matches the time-trends observed in TAS and DLCP.

Though qualitative, this analysis suggests that desorption of oxygen narrows N_V and leads to decreases in n_v, as depicted in Figure 3.12E. The resulting small decrease in n_v may be linked to the corresponding small decreases in $\sigma'(\omega)$ and thus ω_D observed in Figure 3.10B,D. This small decrease can further help explain the decreasing trend in J_0 exhibited in Figure 3.11D, which occurs as n_V decreases and thus less charge is available in the high mobility pathways that dictate the magnitude of J_0. As indicated by the relatively small uptick in R_S observed in 3.10C, the contributions of the decrease in band tail density are likely outweighed by the increase in charge density at E_F due to interface states.

3.10 Conclusion

We have performed systematic IS experiments to give broader context to the the admittance response of a low mobility QD PV device. By correlating TAS measurements with temperature-dependent AC conductance studies, we are able to interpret the primary loss peaks obtained in TAS as the dielectric relaxation frequency ω_D. We suggest that the low conductivities responsible for these features result from the energetic distance between E_F and E_V, which may constrain the V_{oc} of our PbS QD PV device. The AC conductance measurements allow us to correlate the broad distribution of relaxation times to the energetic and spatial structure of the QD film. DLCP measurements allow us to estimate the occupation of $N(E)$ detected in TAS and AC conductance, which is mapped onto absorbance data and temperature-depdendent JV data. Finally, by considering changes in the admittance under vacuum, we are able to hypothesize the effect of O_2 adsorption on the width of N_V observed in capacitance and optical absorption measurements. Most studies that interrogate $N(E)$ in QD solids rely on using gated FET measurements to sweep through the DOS available for charge transport. Frequency-dependent measurements provide an additional tool for interrogating the structure of $N(E)$ in disordered materials like QD solids, where the frequency of the signal acts analogously to the gate bias in more common FET measurements.

3.11 Methods

3.11.1 Materials

Oleic acid (OA, 90%), 1-octadecene (ODE, 90%), lead oxide (PbO, 99.999%), 1,2 EDT($> 98\%$), anhydrous hexane, anhydrous 2- propanol, anhydrous methanol, anhydrous acetonitrile and anhydrous acetone are purchased from Sigma-Aldrich. Bis(trimethylsilyl) sulfide ($(TMS)_2S$, 95%) is purchased from Acros Organics.

3.11.2 Pbs QD Synthesis

PbS QDs are synthesized following literature methods. In brief, a mixture of 0.47 g of PbO, 23 mL of ODE, and 2 mL of OA is degassed at 120 °C for 2h under vacuum. Then 5 mL of 21 μL (TMS)2S/1mL ODE solution is swiftly injected at 100 C with N_2 flowing. The heat is turned off immediately after injection, and the reaction solution is quenched in a water bath. The product is transferred into a glovebox and purified by precipitating four times by acetone, 2-propanol and methanol and finally re-dispersed in octane/hexane (4:1) at 50 mg/mL.

3.11.3 Device Fabrication

All fabrication steps are carried out in air unless otherwise noted. Pre-patterned ITO/glass substrates (Thin Film Devices) are cleaned by sonication in 5% Hellmanex in DI water, pure DI water, and ethanol consecutively, followed by UV-ozone treatment for 30 min. A thin layer of PEDOT:PSS (Clevios) is spin-coated on the ITO/glass substrate at 3000 r.p.m. for 1 min, and annealed at 130 °C for 20 min. PbS QD films are fabricated by building up 5 layers. Each layer is prepared by spin-coating a PbS QD dispersion (50 mg/mL) at 3000 r.p.m for 15 s, applying an 0.02 M EDT ligand solution in acetonitrile to cover the entire film for 30 s, and washing three times with acetonitrile. A 0.8 nm LiF/65 nm Al top contact is deposited through a shadow mask using a thermal evaporator mounted inside a N_2-filled glovebox to define 2×2 mm^2 active device areas.

3.11.4 Room Temperature Characterization

Dark and illuminated JV data are measured using a Keithley 2420 sourcemeter. Current is recorded by sweeping the DC applied voltage from -200 to 700 mV in 20 mV steps. The PV device is illuminated using a solar simulator (Oriel instruments model 96000, Newport Co.). The simulated AM 1.5 light is brought into the glovebox through a liquid light guide feed-through. The intensity at the device is calibrated to be 1 Sun, i.e., 100 mW cm^{-2}, by a Si reference cell and meter from Newport (model 91150). PV devices are illuminated through an aperture of 1.6 mm x 1.6 mm in size, smaller than the active device area.

3.11.5 Variable Temperature Characterization

Variable temperature TAS, $\frac{G_p}{\omega}$, DLCP, AC conductance, and JV measurements are performed within a LakeShore Cryotronics vacuum probestation with a liquid-N_2 cooled sample stage. PbS PV devices are measured from $T = 190 - 310$ K at 10 K intervals. Two probe admittance and JV measurements are carried using a Hewlett Packard HP4192A impedance analyzer and an Agilent 4156C parameter analyzer, respectively. A computer-controlled relay switch is used to toggle between AC impedance measurements and DC JV characterization at each temperature or time-step as depicted in the schematic in Figure 3.1A. For the temperature-dependent measurements, the device is left under vacuum in the dark at room temperature for 1 h, cooled to 150 K, and allowed to thermally equilibrate for 1 h before measurements are started. For TAS measurements, the capacitance response of the PV device to a 20 mV AC perturbation is collected for frequencies ranging from 20 Hz1.3 MHz at a 0 mV DC bias. The same DC and AC biases are applied for AC conductivity measurements and $\frac{G_p}{\omega}$. DLCP measurements are performed immediately afterward using the same setup, with AC signals at frequencies of 1 kHz, 10 kHz, and 100 kHz, and maximum applied biases $V_{max} = V_{RMS} + V_{DC}$ from -50 mV to -300 mV in 50 mV steps. To obtain the non-linear capacitance response, V_{RMS} was varied from 10 mV - 300 mV, and V_{DC} is automatically modulated to keep V_{max} constant using custom LabView software.

JV characterization is performed immediately following capacitance characterization using the same parameters as those used in room temperature measurements.

Chapter 4

Interfacial Defects in Heterojunction Photovoltaic Devices

4.1 Introduction

The gains in efficiency and environmental stability of PbS QD PV devices achieved in the past decade are a result of optimization of the PbS QD absorber layer and the inclusion of n-type metal oxides such as TiO_2 and ZnO to form depleted heterojunction PV devices.[143, 62, 19, 43, 120, 44, 144] The inclusion of these heavily doped oxides in PbS QD PV device architectures is thought to introduce a large depletion region in the PbS QD solid.[120] In these geometries, photogenerated electrons in the PbS QD layer must only diffuse to the edge of the depletion region W before being swept into the n-type material due to the large built-in field (V_{bi}) that drops across the depletion region (Figure 4.1A).[154] Since transport of photoexcited carriers in these heterojunction architectures occurs *via* drift within the depletion region instead of diffusion, these devices are believed to reduce recombination losses arising from the low carrier diffusion lengths in PbS QD solids, resulting in higher V_{oc} and PCE.[120]

The need for large depletion regions within the PbS QD p-type absorber layer imposes strict requirements on the electronic performance of ZnO materials. Adsorption of molecular gases such as O_2 can drastically reduce the electron doping density in ZnO [31, 81], resulting in a substantial depletion width in ZnO, thereby reducing the extent of the depletion width within the PbS QD layer.[154, 135] Detailed EQE studies have shown that these ZnO depletion regions reduce the efficiency by which charge carriers generated within the PbS QD film may be harvested.[154]

Spectroscopic studies have demonstrated a wide range of defect levels near the valence band[121, 79] and below the conduction band in ZnO films.[70, 131, 79, 23, 134, 135] Complicating matters, many of these defects have different oxidation states[142], making a complete chemical description of these defect levels difficult. In PbS QD/ZnO heterojunctions, traps near the ZnO conduction band have been shown to contribute to recombination of electrons in the dark.[135] Efforts to chemically passivate defects in ZnO films *via* incorporation of Mg[58], Cl[25], or Al/Cl [24] have led to some of the highest achievable PCEs achieved by PbS QD PV devices, implying that defects in ZnO films present a large impediment to achieving commercially viable solution processable PV devices.

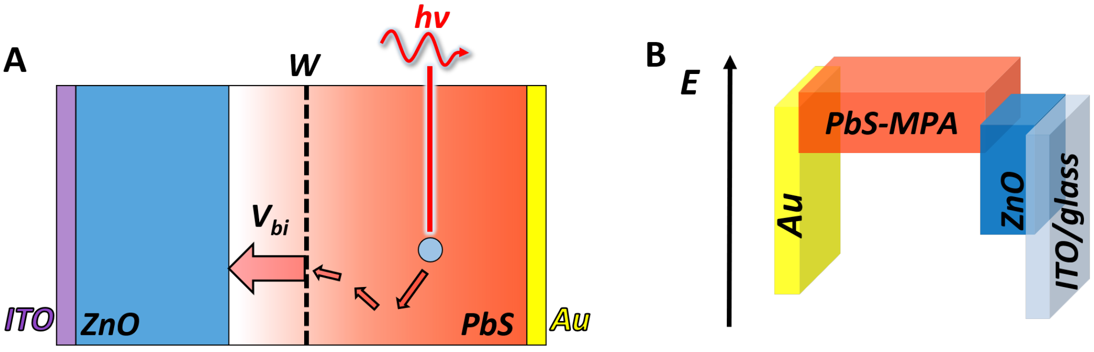

Figure 4.1: (A) Schematic of photogenerated charge diffusing to edge of depletion region W before being swept across the depletion region by V_{bi} into n-type ZnO, where it becomes a majority carrier and may be extracted at the ITO electrode. Adapted from Reference [154]. (B) Device geometry investigated (B) Schematic of PbS QD PV device used to investigated.

In this chapter, we study the frequency-dependent capacitance response of a QD heterojunction PV device with a p-type absorber layer of PbS QDs capped with 3-mercaptopropionic acid (MPA) and an n-type window layer of ZnO (Figure 4.1A). TAS and DLCP experiments on this device exhibit a low-frequency capacitance response that we hypothesize corresponds to a hole trapping level ~ 0.29 eV above the valence band of the MPA-capped PbS QD layer ('PbS-MPA'). Assuming that this spectroscopic signature arises from charge trapping and not limited charge transport as discussed in Chapter 3, we present evidence that this state arises from Fermi level-pinning of at the ZnO/PbS-QD hetero-interface. Frequency-dependent conductance measurements and impedance spectroscopy (IS) performed at open circuit conditions suggest that this interfacial state is similarly capable of trapping electrons in forward bias. We therefore hypothesize that the interfacial defect is also positioned ~ 0.3 eV from the conduction band onset on the ZnO-side of the heterojunction. IS responses corresponding to charge dynamics at this energy exhibit a lifetime of $\sim 10^{-4}$ s, consistent with previous reports of electron capture at ZnO surface [134] and ZnO/PbS QD heterointerfaces.[135]. These IS responses dominate the broad distribution of charge relaxation times for hopping in our PbS QD PV device in forward bias. Though we note that additional analysis is required for unambiguous identification of the origin of the charge response, our preliminary work hypothesizes that this state contributes to the frequency-dependent dynamics of both electrons in the ZnO layer and holes in the PbS QD layer, limiting V_{oc} and thereby constraining the performance of the PV device.

4.2 TAS

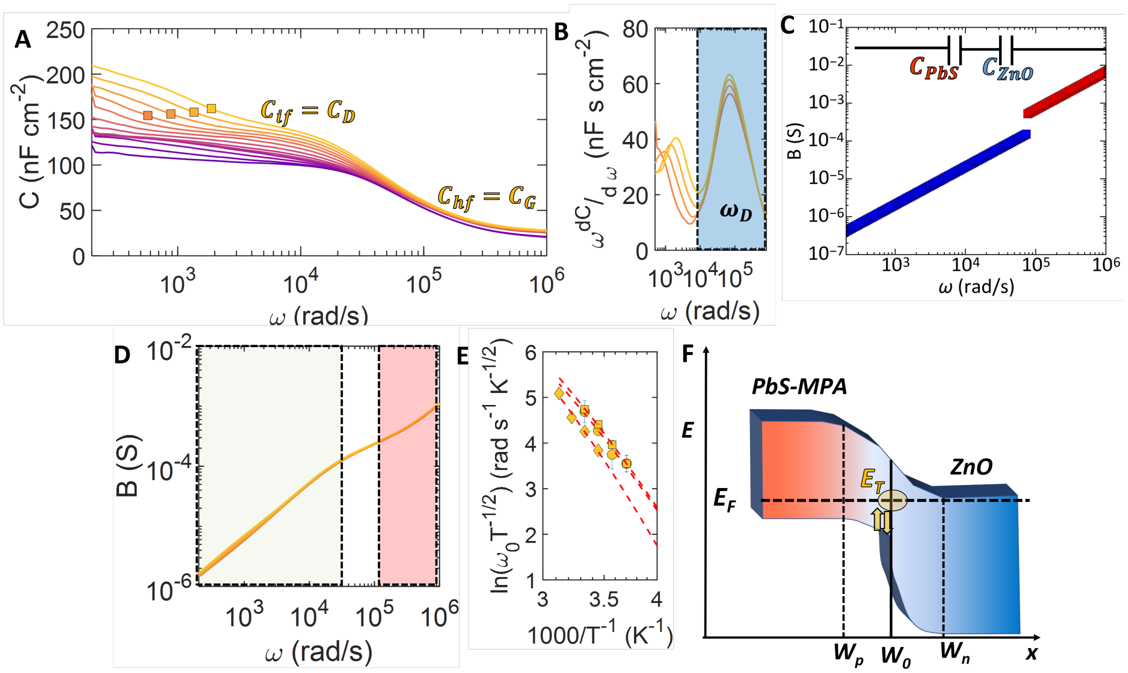

Figure 4.2: (A) C vs. ω obtained 1 day of fabrication (day 1) with highlights indicating ω_0 (squares) and intermediate (C_{if}) and high frequency (C_{hf}) capacitance labeled. (B) $-\omega\frac{dC}{d\omega}$ vs. ω exhibiting loss peaks due to both trapping and ω_D. (C) Calculated frequency-dependent susceptance B derived from series connection (inset) of PbS QD geometric capacitance C_{PbS} (red) and ZnO geometric capacitance C_{ZnO} (blue). (D) Experimentally observed frequency-dependence of B. (E) Arrhenius plot showing activation of ω_0 on day 0 (circles), day 1 (squares), and day 2 (diamonds) with accompanying fits (dashed red lines). (F) Proposed band diagram showing depletion region extending into ZnO layer and charge trap E_T.

A PbS QD PV device is fabricated in air by depositing ZnO nanoparticles (NPs) synthesized according to literature methods [8] onto an ITO/glass substrate *via* spincoating. After mild air-annealing, 3 nm PbS QDs synthesized according to literature methods [163] are spincoated onto the substrate. The native oleic acid ligands in the PbS QD film are exhanged *via* treatment with a solution of MPA in methanol for 30 seconds followed by a methanol rinse to remove excess MOA. 10 layers of PbS QDs are deposited, resulting in a total film thickness ~ 190 nm. The device is capped with MoO_3 and an Au top contact.

Admittance characterization is performed by loading the completed device into a vacuum probestation ($\sim 10^{-4}$ torr) and measuring the frequency-dependent admittance response to 100 mV AC signals at 0, -100, and -200 mV DC bias from $T = 180 - 300$ K. Figure 4.2A shows the frequency dependence of the imaginary part of the response (capacitance) of our PbS-MPA/ZnO PV device, showing two step-like decays due to charge dynamics within the device. The high temperature data exhibits a step-like decay from the low frequency maximum capacitance $C \approx 200$ nFcm^{-2} to a stable intermediate frequency $C_{if} \approx 140$ nFcm^{-2} at $\omega \approx 10^4$ rad/s. A second capacitance step to the high frequency minimum $C_{hf} \approx 30$ nFcm^{-2} occurs at $\omega > 10^5$ rad/s. Unlike the capacitance decrease to C_{if}, the high frequency capacitance decay is largely temperature-independent, indicating that it is not likely related to thermally activated emission from a defect state. Furthermore, as exhibited in Appendix B.1, the high frequency-side of the capacitance step is independent of applied bias, consistent with a decay to C_G, the geometric capacitance of the device.[84]

C_G is attained when the applied measurement frequency exceeds the dielectric relaxation frequency ω_D of charge carriers in the PbS QD PV device active layer. Since no charge carriers are capable of following the applied AC signal at these frequencies, the active layer acts as an insulator. C_G is therefore given by the expression $C_G = \frac{\varepsilon_0 \varepsilon A}{D}$ where A is the device area and D is the total thickness of the layer.[84, 90, 151] The room temperature data in Figure 4.2B show a peak corresponding to dielectric relaxation occurring at $\omega_D \approx 7 \times 10^4$ rad/s (Figure 4.2C). The zero bias AC conductance data provided in Appendix B.2 similarly exhibit a temperature-independent conductivity $\sigma_D \approx 1.1 \times 10^{-7}$ Scm^{-1} at these frequencies, consistent with a small temperature-independent maximum conductivity that limits the frequency-response of the device.

Higher values of ω_D were previously demonstrated for PbS QDs capped with EDT (Chapter

3), even though the mobility of MPA-capped PbS QDs is known to be a factor of ~ 10 larger than EDT-capped PbS QDs.[64]. We hypothesize that the low ω_D value observed results from freeze out of charge carriers on both sides of the PbS/ZnO heterointerface, after which the entire device acts like a dielectric layer since limited conductive pathways exists across the heterointerface. From the value of $C_G \approx 30$ nFcm^{-2} in Figure 4.2A, we estimate the total width W_{ZnO} of the high frequency depletion region within the ZnO layer. Assuming that the high frequency capacitance includes a contribution from 190 nm of completely frozen out PbS-MPA QD film with $\varepsilon = 10$ (measured in Appendix B.3), an additional 38 nm of depletion region within the ZnO is necessary to achieve the observed capacitance at C_G, in excellent agreement with previous estimates of W within ZnO in heterojunctions of ZnO and PbS QDs.[135] The device capacitance at high frequency may therefore be modeled as the series connection of the ZnO and PbS-MPA depletion capacitances, as depicted in the inset of Figure 4.2c. For 190 nm of PbS-MPA, $C_{PbS} \approx 47$ nFcm^{-2}. For a ZnO dielectric constant $\varepsilon = 3.7$,[104] a 38 nm depletion region in the ZnO gives a total depletion capacitance $C_{ZnO} = 84$ nFcm^{-2}. Based on the ratio of the estimated C_{ZnO} to the observed value of C_G, we suggest that the high frequency charge dynamics reflected in the capacitance characteristics may be described by a mixture of $\sim 65\%$ PbS capacitance and $\sim 35\%$ ZnO capacitance. The observed σ_D therefore corresponds to a mixture of the conductivities in both films.

The total imaginary part of the frequency response of the circuit depicted in the inset of Figure 4.2C is given by the susceptance $B = \frac{X}{Z^2}$. Here, $X = \frac{1}{i\omega C}$, where ω is the frequency, X is the reactance, and Z is the total impedance. Though the charge response of the PbS QD layer dominates at high frequencies, as indicated in Figure 4.2C, we expect the geometric contribution of the ZnO layer to exceed that of the PbS layer at mid-frequencies. Figure 4.2D displays the experimentally observed frequency-dependence of B, which increases roughly 3 orders of magnitude across the frequency range interrogated. We note that the observed values of B agree with calculated values presented in Figure 4.2C, indicating that the high frequency capacitance is likely dominated by the PbS QD layer. Though the values of B calculated at lower frequencies in Figure 4.2D are in general agreement with the geometric capacitance of the ZnO layer, small variations in B below $\sim 10^4$ rad/s are readily observable. In contrast to the admittance response analyzed in Chapter 3, DC conductance is not observed in the zero bias frequency-dependent admittance at any frequency (Appendix B.2). Since the admittance response exhibits no signs associated with transport at these frequencies, we hypothesize that these small variations result from a thermally activated capacitance due to charge emission from defect levels. Though definitive identification of the physical origin of these defects is difficult due to the heterojunction structure of the device, we hypothesize that these defect levels are located at the PbS-MPA/ZnO interface since they cannot be accounted for by consideration of the ZnO capacitance alone. We note that the temperature-induced increase in C_D at mid-frequency in Figure 4.2A corresponds to a contraction of the depletion width within the PbS-QD layer as temperature increases, which has been observed in previous capacitance measurements of organic capped PbS QD films [133]. The analysis of the 0-bias admittance that follows assumes that the charge response observed at these frequencies results from trap emission; however, we note that limited carrier mobilities in the PV device may also be responsible for these signals as discussed at lengthin Chapter 3.

Assuming the dropoff in capacitance at low frequency is derived from charge emission from interfacial trap states, the resonant frequency ω_0 can be identified from peaks in a plot of $-\omega\frac{dC}{d\omega}$ vs. ω, provided in Figure 4.2B. Unlike the transport dynamics analyzed in Chapter 3, ω_0 for trap emission is related to the energetic barrier E_T a charge must surmount to be emitted *via*:

$$\omega_0 = \nu_0 \mathrm{exp}(-\frac{E_T}{k_B T}) \tag{4.2.1}$$

where $\nu_0 = 2\sigma_p v_{th} N_V$ is the characteristic frequency with which a charge in a defect state with capture cross section σ_p and thermal velocity v_{th} attempts to escape to the transport level with a density of states N_V.[150] The $T^{\frac{1}{2}}$ temperature-dependence of v_{th} and $T^{-\frac{3}{2}}$ temperature-dependence of N_V are separated from the temperature-independent terms in ν_0, and the attempt frequency is written $\nu_0 = \nu_{00}T^2$.[150, 61, 75, 16, 15, 39, 66] In QD solids, N_V is temperature independent,[161] so we may more accurately write equation (4.2.1) as:

$$\omega_0 = 2\nu_{00}T^{1/2}\exp(-\frac{E_T - E_V}{k_BT}) \tag{4.2.2}$$

Figure 4.2C displays the thermal activation of ω_0 extracted on 3 PbS QD PV devices measured on the day of fabrication ('day 0', circles), 1 day after fabrication, ('day 1', squares), and 2 days after fabrication ('day 2', diamonds) with fits to Arrhenius fits to equation (4.2.2). Day 0 and day 2 data may be found in Appendix B.4. These devices exhibit respective trap depths of $E_{T,0} = 0.27 \pm 0.01$ eV and $E_{T,2} = 0.32 \pm 0.01$ eV, for an average trap depth of $E_T = 0.29 \pm 0.03$ eV. These figures are in excellent agreement with photoluminesnce measurements of defect levels within PbS-MPA QD solids,[21] and we tentatively ascribe E_T as the distance between the trap and E_V of the PbS QD layer. Since TAS is primarily sensitive to energies at which $E_F = E_T$,[17, 150] we note that our preliminary analysis implies that the Fermi level in the the PbS QD layer is ~ 0.3 eV away from E_V. The reduced temperature attempt-frequencies of these defect levels are $\nu_{00} = (2.0 \pm 0.5) \times 10^6$ rad/s K^2 on day 0, $\nu_{00} = (3.0 \pm 0.2) \times 10^6$ rad/s K$^{-1/2}$ on day 1, and $\nu_{00} = (9 \pm 1) \times 10^6$ rad/s K$^{-1/2}$ on day 2, in notable agreement with the attempt-frequencies measured *via* TAS of devices with similarly-sized, organic capped PbS QDs.[16]

The bias-dependent TAS curves presented in Appendix B.1 show that the detected resonant frequencies in the experiment exhibit a marked dependence on the applied reverse DC bias of the TAS measurement. A decrease in ω_0 with increasing reverse bias has been shown to be consistent with E_F pinning at the heterojunction interface.[61, 103] If the detected charge dynamics do correspond to defect levels, the bias-dependence indicates that E_F is likely pinned under DC equilibrium conditions.[61] We note an applied reverse bias would act to increase the ratio $\frac{w}{d}$ of the depletion width w to the total film thickness d. Therefore, an increase in the observed resonant frequency can be expected if $\omega_0 = \omega_D$ based on equations (3.3.3) and (3.3.1), in contrast to the observed bias dependence. These results are in line with X-ray photoelectron spectroscopy (XPS) and ultraviolet photoelectron spectroscopy (UPS) studies of ZnO/PbS QD interfaces, which suggest that the E_F of the QD layer is pinned to E_F in the ZnO.[147, 135] The resulting hypothesized picture of our Pbs-MPA/ZnO junction is provided in Figure 4.2D, which shows an interfacial defect with energy E_T above the valence band of the PbS-MPA layer.

4.3 ZnO Analysis

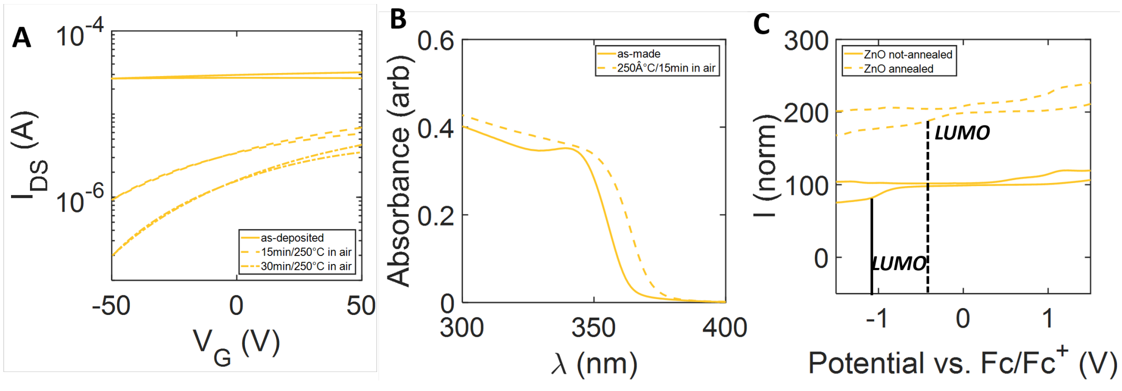

Figure 4.3: (A) FET measurements on pristine and air-annealed ZnO. (B) ZnO absorption spectrum before and after annealing in air. (C) Cyclic voltammetry data for un-annealed ZnO film and ZnO annealed at 250 °C in air, showing a shift in the onset of the LUMO upon air-annealing.

To understand the doping levels in our ZnO films, we fabricate top-contact bottom-gate ZnO field effect transistors (FETS) by depositing ZnO NPs onto n^+ silicon substrates and evaporating gold top contacts onto the film. FET measurements are then performed in a nitrogen glovebox. Pristine ZnO NP films used in PbS QD PV devices are expected to be degenerately n-doped with carrier concentrations $n \sim 10^{20}\text{cm}^{-3}$,[163]; however, lower doping densities have been shown to result from air exposure of ZnO NP films.[154, 81, 31] Figure4.3A exhibits the gate voltage (V_G)-dependent current (I_D) of a ZnO NP FET immediately after deposition (solid line) and after 15 and 25 minutes of annealing in air at 250° C. Initially, the high current levels in the device exhibit no gate modulation across the applied V_G range, consistent with a degenerately-doped n-type ZnO NP film. The mobility μ under these conditions is $\sim 1 \times 10^{-4}$ cm^2(Vs)$^{-1}$. From the value of I_D at

$V_G = 1$ V and the dimensions of our film, we estimate a conductivity $\sigma \approx 0.26$ Scm^{-1}, resulting in a carrier concentration of $n \sim 10^{22}$ cm^{-3}. Upon air exposure, the current levels decrease an order of magnitude, allowing for appreciable n-type gate modulation. A commensurate increase in μ to $\sim 1 \times 10^{-3}$cm^2(Vs)$^{-1}$ is observed, implying the carrier concentration in the film decreases by a factor of ~ 500. Previous reports have suggested that carrier concentrations $\sim 10^{19}$ cm^{-3} can be re-attained in air-exposed ZnO NP films *via* UV illumination.[81, 24]

Figure 4.3B exhibits the absorption spectra of both pristine and air annealed ZnO NP films, allowing us to probe the band-edge $N(E)$ in these materials. Though the ZnO NP film initially exhibits a small quantum confinement peak at ~ 345 nm, mild annealing in air smooths out the absorption peak into a broad, bulk-like shoulder. The absorption also exhibits a significant red-shift to ~ 360 nm, indicating that lower energy photons provide sufficient energy for exciting charge in the valence band of the ZnO NP film across the bandgap. These results are confirmed in cyclic voltammetry (CV) studies of ZnO NP films, provided in Figure 4.3C. These daata were obtained by spincoating ZnO NPs onto a gold substrate and applying a potential between the ZnO NP working electrode and a reference electrode and measuring the amount of current flowing through a third, inert ferrocene counter electrode. When the energy levels in the ZnO NP film coincide with the external potential, current flows in the counter electrode. Since CV is typically used to study molecular and quantum confined systems, the energy levels identified by small peaks in current are commonly interpreted the lowest unoccupied molecular orbital (LUMO) and highest occupied molecular orbital (HOMO). In QD films the HOMO and LUMO levels correspond to the onsets of the valence and conduction bands, respectively. Figure 4.3C shows a pronounced shift in the LUMO upon annealing in air, suggesting that the conduction band onset shifts down towards the valence band. This shift is consistent with the change in the absorption spectra in Figure 4.3B. We hypothesize that these features correspond to a band tail extending toward mid-gap from the ZnO NP conduction band level, in agreement with previous absorption and UPS measurements of ZnO NP films.[58, 25] ZnO band tails are associated with low electron mobility.[58] Under the assumption that the charge dynamics observed at $\omega \lesssim 10^4$ rad/s in Figure 4.2A result from charge trapping on the PbS QD side of the junction, the presence of non-idealities in ZnO suggest that the heterointerface affects both hole and electron dynamics in our PV device.

4.3.1 DLCP and DOS

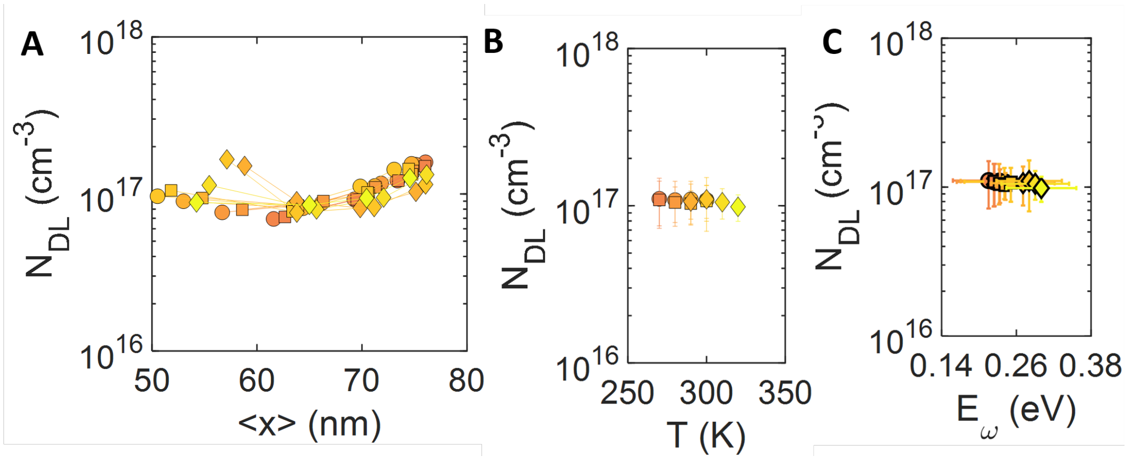

Figure 4.4: (A) Profile of defect densities obtained via DLCP at $\omega = 6.28 \times 10^3$ rad/s on day 0 (circles) and day 1 (squares) from $T = 270-300$ K and on day 2 from $T = 290-320$ K (diamonds). (B) N_{DL} vs. T (C) N_{DL} vs. E_ω

Simultaneous DLCP measurements performed in parallel with TAS allow us to estimate the charge density within the depletion region of the device. Like TAS, DLCP is a dynamic junction capacitance technique that probes the majority carrier occupation of states within the PV device absorber layer by monitoring how the junction capacitance changes with an applied AC signal. As described in detail in Chapters 2 and 3, cubic fits to DLCP capacitance responses allow us to probe the carrier density N_{DL} at a specific location $< x >$ within the junction. N_{DL} is given by:[52]

$$N_{DL} = p + \int_{E_F}^{E_F+E_\omega} N(E,x)dE \tag{4.3.1}$$

where p is the density of free carriers in the VB provided by ionized acceptors N_A^-. In Chapter 3, $N(E)$ was shown to correspond to the broad distribution of valence band staets N_V. In this case, since we hypothesize that the response arises from charge emssion from a defect level, we may write $N(E)$ as the distribution of trap states $N_T(E)$, as in Chapter 2. E_ω in this scenario describes a limiting energy that defines the maximal energetic distance charge at E_F can access, and may be calculated for an arbitrary applied frequency ω as: [150, 54]

$$E_\omega = k_B T \ln(\frac{\nu_0}{\omega}) \tag{4.3.2}$$

In p-type semiconductors, E_ω corresponds to an energetic distance between E_F and the valence band edge.[52] Equations (4.3.1) and (4.3.2) imply that increasing the frequency of the DLCP measurement decreases the energetic width around E_F that can be probed by the DLCP measurement, as discussed in Chapter 3.

Unlike TAS, the AC signal in DLCP measurements are made at a single frequency and use large root mean square (RMS) amplitudes V_{RMS} to induce band-bending at the device heterojunction.[52] These large applied biases shift the band-bending at the junction which changes the width of the depletion region W and thus adjusts the first moment of charge response $< x >$ for charge trapped in the junction. As displayed in Figure 2.10B, $< x >$ can equivalently be thought of as where the trap level E_T crosses E_F. By inducing changes to band bending at the junction, DLCP therefore allows for the spatial profiling of the charge response.

Figure 4.4A shows the charge carrier profile N_{DL} vs. $< x >$ obtained from the capacitance response of the PbS QD PV device on day 0 (circles), 1 (squares), and 2 (diamonds). The values are calculated assuming that $\varepsilon = 10$ for the MPA-capped PbS QD layer, as calculated in Appendix B.3. The raw capacitance transients used to generate these data for day 1 are displayed in Appendix B.6, and show that only data obtained at $\omega = 6.28 \times 10^3$ rad/s show sufficient capacitance modulation to be reliably fit to the cubic response predicted by DLCP. Intuitively this makes sense, given frequencies higher than $\sim 10^4$ rad/s cause carrier freeze out, resulting in a small capacitance response and unphysically high N_{DL} values. The data obtained on all days show a consistent charge response $\sim 1 \times 10^{17}$cm^{-3} centered $\sim 50 - 75$ nm from the junction, indicating that the spatial extent of the depletion region defect response is consistent with W_{PbS} predicted from analysis of the capacitance response in Figure 4.2A. We note that these values were calculated assuming a charge response centered in the PbS QD layer. If we instead assume a charge response containing contributions from ZnO with $\varepsilon = 3.7$, the observed value of $< x >$ would decrease by a factor of ~ 3 based on equation (2.5.1), while N_{DL} would increase by a factor of ~ 3 based on equation (2.5.4).

Using the carrier densities calculated in the former case, we calculate a Debye screening length L_0 for the PbS-MPA QD layer of ~ 5 nm, indicating that the charge response analyzed in DLCP is not limited to the heterointerface. The applied frequency used in this analysis roughly corresponds to the C_D plateau in Figure 4.2A, which gives the capacitance at the edge of the depletion region. We note that the application of lower frequencies in the DLCP measurement would indicate a higher charge density closer to the heterointerface corresponding to the defect at the interface.

Figure 4.4B shows the temperature-dependence of N_{DL}, obtained by averaging the data in Figure 4.4A across the spatial coordinate $< x >$. The variation in density at each temperature point is dominated by the spread in $N_{DL}(< x >)$. We note that the densities at each temperature are the same within error, at $N_{DL} \approx 1 \times 10^{17}$ cm^{-3}, slightly higher than previous estimates of the total carrier density in films of organic-capped PbS QDs of similar size.[133, 149] These carrier densities exhibit little thermal activation at the temperature ranges interrogated, implying that the carrier activation energy E_N discussed in Chapter 3 is small compared to the energy E_ω of the DLCP measurement.

Using equation (4.3.2), the temperature axis in Figure 4.4B may be recast as an energy axis using the values of ν_0 calculated above. Figure 4.4C exhibits the result of the re-scaling, showing that the charge carrier concentration detected in DLCP originates from states $\sim 0.22 - 0.29$ eV away E_F. The error in the energy axis is derived from the error in ν_0, which is $\sim 10\%$.

4.4 Density of States

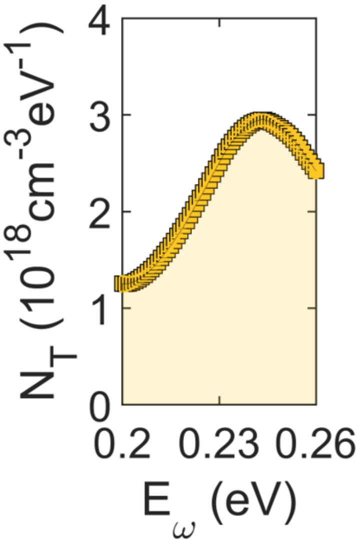

Figure 4.5: N_T on day 1 calculated by direct integration of the capacitance derivative.

.

Assuming that the charge response analyzed in DLCP and TAS results from trap emission and not transport, combining N_{DL} and the energetic scale calculated in TAS allows us to compute the total density of trap states N_T spatially located between the interface and $< x >$ and energetically bounded by E_F and $E_F + E_\omega$. Typically, the value of N_T is obtained via a procedure outlined by Walter, et. al, wherein the N_T is related to the junction capacitance C_{tot} by:[150]

$$C_{tot} = n_T \propto \int_{E_F}^{E_F+E_\omega} N_V(E) \frac{W}{qV_{bi}} dE \tag{4.4.1}$$

Integration of N_T with respect to energy gives the carrier occupation n_T that gives rise to the capacitance response. Considering the linear drop of the applied AC bias due to band bending at the junction, integration of equation (4.4.1) gives:

$$N_T(E_\omega) = \frac{V_{bi}^2}{W[qV_{bi} - (E_{F\infty} - E_\omega)]} \frac{dC}{d\omega} \omega k_B T \tag{4.4.2}$$

where $E_{F\infty}$ is the Fermi level in the bulk. Calculation of N_T *via* equation (4.4.2) requires precise estimates of V_{bi}, which in turn necessitates knowledge of band bending at the junction. In bulk materials, V_{bi} can be estimated by measuring the open circuit (V_{oc}). Obtaining accurate estimates of V_{bi} through measurements of V_{oc} in QD PV devices is considerably more difficult since non-idealities such as Fermi pinning or high defect concentrations can limit charge collection and lead to large deficits in V_{oc}.[28]

In Chapter 3, we used the direct measure of p afforded by DLCP to estimate $N(E_F)$. Here, we analogously estimate N_T by assuming that N_T is Gaussian distributed with a width $\bar{\sigma}$ and height A defined by the amplitude of $\omega\frac{dC}{d\omega}$ obtained in Figure 4.2B. N_T may therefore be written as $N_T = A\text{exp}(\frac{E-E_F}{\bar{\sigma}})$, and can be analytically integrated:

$$\begin{aligned} N_{DL} &= \int_{-\infty}^{\infty} A\text{exp}(\frac{(E-E_F)^2}{2\bar{\sigma}^2}) \\ N_{DL} &= \sqrt{2\pi}A\bar{\sigma} \end{aligned} \tag{4.4.3}$$

For each peak in Figure 4.2B the width in frequency can be converted into an energetic width using equation (4.3.2). Since both $\bar{\sigma}$ and N_{DL} are known, we can also calculate the total amplitude A and therefore N_T.

The result of the integration averaged over temperature is presented in Figure 4.5A for day 1 of the measurement. These values are $\sim 5\times$ larger than the DOS values calculated *via* equation (4.4.2) provided in Appendix B.6, assuming $V_{bi} = 0.9$ eV. We also note that the width of N_T is much smaller than the width of the band tail deduced in Chapter 3. Though this preliminary analysis explicitly assumes that the observed capacitance responses used to calculate the distribution in Figure 4.5A result from charge trapping and de-trapping, we note that if these charge dynamics were instead interpreted as a result of limited carrier mobility in the PbS QD layer as in Chapter 3, these results would be consistent with previous estimates of the relative tail density in PbS-MPA compared to the tail density observed in EDT-capped QDs.[64]

4.5 JV and Conductivity

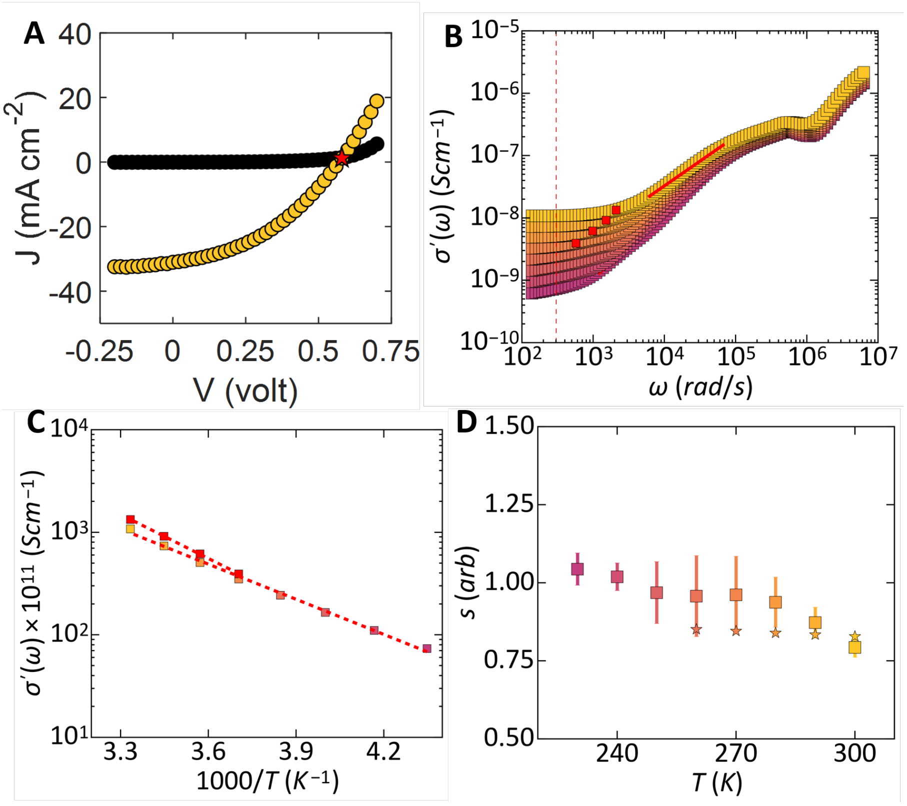

Figure 4.6: ((A) Dark (black) and illuminated (yellow) JV data immediately after fabrication, with observed and theoretical V_{oc} marked with star and dashed line, respectively (B) $\sigma(\omega)$ from $T = 230300$ K, with dashed red line frequency at which the DC conductivity is obtained. (C) DC conductivity vs. $\frac{1000}{T}$ with accompanying Arrhenius fit. (E) Exponent s obtained from linear fit to AC enhanced conductivity region in (B) (squares) and estimated based on equation (4.5.1) (stars).

The predominant recombination mechanisms in our PbS QD PV device device are also reflected the JV characteristics. Figure 4.6A displays the dark and illuminated JV curves of our PbS-MPA device directly after fabrication, measured in an N_2 glovebox. Under AM 1.5G illumination, the device exhibits $V_{oc} = 0.57$ V and a PCE of $\eta = 7.8\%$, consistent with previous reports of PbS-MPA heterojunction devices.[64] Since the maximum theoretical V_{oc} of a pn heterojunction device is given by the bandgap of the PbS QD absorber $E_G = 1.26$ eV,[28] the data indicate a V_{oc} deficit of ~ 0.7 V. In PbS heterojunction devices, the dominant recombination pathway is thought to arise from interfacial mechanisms[37, 58, 73, 92, 93] or from defects in the bulk of the PbS QD absorber.[28]

To investigate the recombination and charge transport dynamics in our device, we analyze the temperature dependence of the AC conductance $\sigma'(\omega)$ at an applied bias $V_A = 600$ mV. Since $V_A \approx V_{oc}$, the charge dynamics probed resemble those at open circuit, and the contributions of majority carrier dynamics probed at zero bias in TAS are dominated by the contributions of minority electrons injected from the ZnO into the PbS QD layer.[10, 45] Figure 4.6B shows $\sigma'(\omega)$ measured from $T = 230 - 300$ K. As discussed in Chapter 3, the dispersion-less conductivity observable at $\omega \lesssim (1-4) \times 10^3$ rad/s indicates the DC limit of the hopping conductivity, $\sigma'(0)$. We note that at room temperature, $\sigma'(0) \approx 10^{-8}$ Scm^{-1}, which is ~ 5 orders of magnitude lower than the conductivity of the air-annelaed ZnO FET device at $V_G = 1$ V.

Figure 4.6C shows the temperature dependence of $\sigma'(0)$ for a fixed frequency $\omega = 2 \times 10^2$ rad/s (purple-yellow squares) and the ω_0 frequencies obtained in 4.2 (red squares). These frequencies are highlighted in Figure 4.6B with a dashed line and red squares, respectively. The fit to $\sigma'(\omega = 2 \times 10^2$ rad/s) yields an activation energy $E_A = 0.23 \pm 0.05$ eV. The high forward bias used to obtain these data imply that this barrier to electron transport precludes majority carrier dynamic and the effect of defects within the depletion region; as a result, we hypothesize that E_A corresponds to the energetic distance between E_F and the ZnO conduction band. The obtained activation energy is in agreement with deep level transient spectroscopy (DLTS) studies of bulk ZnO defect states, which found a range of defects between $0.28 - 0.34$ eV below the ZnO conduction band onset.[131] FET and TAS studies of bulk ZnO films have also detected spectroscopic signatures of an electron trap ~ 0.3 eV below E_C.[70, 23] In the random free-energy barrier (RFEB) model used to explain the AC conductivity of materials dominated by charge hopping, the energy barriers to conductivity in a spatially and energetically disordered material are defined by a broad distribution.[36] Because DC conductivity necessitates charge percolation through the entire sample, the activation energy of $\sigma'(0)$ is dominated by the largest energy barrier charge must surmount as it travels, suggesting that electron hopping under open circuit conditions in our PV device requires thermal activation over a 0.23 eV barrier. Similar energetic barriers have been detected at PbS QD/ZnO heterojunction interfaces *via* time resolved XPS.[135]

The Arrhenius fit to $\sigma'(\omega_0)$ in Figure 4.6C yields an activation energy $E_A = 0.28 \pm 0.03$ eV. While ω_0 was derived the from zero bias admittance response in which DC transport was not observed, we note the agreement between the $E_A = 0.28$ eV and $E_T = 0.29$ eV obtained in Section 4.3. Despite the fact that charge dynamics in the depletion region at zero bias cannot, in general, be expected dominate charge dynamics at high forward bias, we note that the consistency between these two results implies that we cannot definitively rule out the possibility that the charge dynamics responsible for ω_0 observed in Figure 4.2 do not arise from the limited charge carrier mobility in our PV device.

Figure 4.6B displays a steady rise in $\sigma'(\omega)$ after a temperature-dependent inflection frequency ($\omega \approx (1-4) \times 10^3$ rad/s at room temperature). As discussed in Chapter 3, the enhancement to $\sigma'(\omega)$ occurs as the increase in frequency prohibits charge hops with large time constants $\tau = \frac{1}{\omega}$ associated with large energy barriers. Shorter range hops with higher jump probability allowed at high frequencies enhance $\sigma'(\omega)$.[36] The hopping times resulting from this distribution of energy barriers gives rise to the universal power-law for AC conductivity $\sigma'(\omega) \propto \omega^s$ described in Chapter 3. In the RFEB model, s parameterizes the distribution of τ in the energy landscape of the material. Since $\omega\tau \to \infty$ as the energetic barriers to charge hopping become large, $s \to 1$. A similar effect is expected in the limit that $T \to 0$. As a result, s may be written:[36]

$$\begin{gathered} s = 1 - \frac{T}{T_0} \\ T_0 = \frac{E_A}{2k_B} = \frac{E_T}{2k_B} \end{gathered} \tag{4.5.1}$$

The temperature-dependence of the s exponent obtained from fits to the high frequency region in Figure 4.6B are presented in Figure 4.6D, along with the 1σ error bars derived from the fits. Over the temperature range of the experiment, s decreases slightly within error, indicating that the energy barrier to charge hopping decreases as temperature increases. Estimates of s based on equation (4.5.1) and $E_A = 0.3$ eV are also provided in Figure 4.6D (stars), and describe the data within error. The agreement suggests that dark charge hopping at open circuit in our PbS QD PV device are dominated by electron dynamics which may be localized at the ZnO/PbS-MPA interface. These dynamics are dominated by the highest energy barrier electrons must surmount as they travel from the ZnO to the Au anode. Similar conclusions were reached in studies that incorporate Mg dopants to limit the trap density within the ZnO depletion region.[58]

4.6 Impedance Spectroscopy

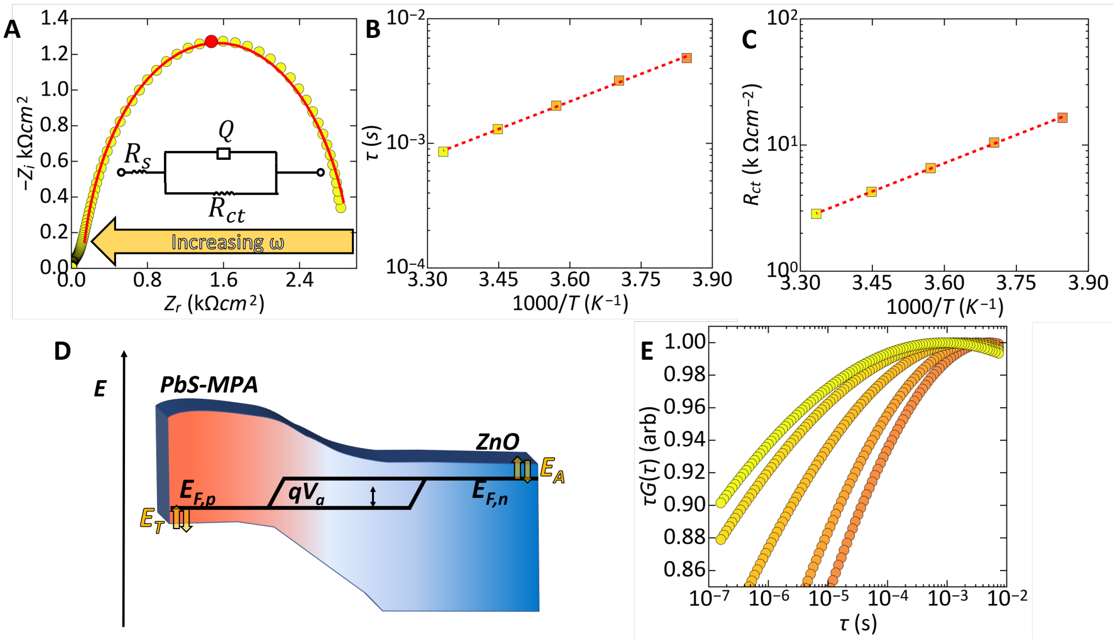

Figure 4.7: (A) Example fit of RQ CPE equivalent circuit to IS data obtained at $T = 300K$ and 600 mV applied bias. (B) Thermal activation of lifetime τ with Arrhenius fit (dashed red line). (C) Thermal activation of R_{ct} with Arrhenius fit (dashed red line). (D) Proposed energy band diagram at V_{oc} showing interfacial electron trap responsible for charge dynamics. (D) Log-normal distribution of time constants $\tau G(\tau)$ detected by IS.

The charge hopping distributions parmeterized by s can be directly visualized *via* analysis of the real (Z_r) and imaginary (Z_i) parts of the frequency-dependent impedance response of the PV device. The total impedance $Z = Z_r + Z_i$ generalizes the concept of a DC resistance for charge flow in a sample due to an oscillating AC bias. Electron dynamics in phase with the measurement give rise to the DC resistance $R = Z_r$. Dynamics in phase quadrature with the signal give rise to a capacitance C that make up the imaginary component Z_i. Analysis of the frequency-dependence of $Z_i(\omega)$ and $Z_r(\omega)$ allows us to obtain a snapshot of charge processes in the PbS QD PV device as different hopping regimes are accessed by the applied frequency.

An example complex plane plot $-Z_i$ vs. Z_r at $V_A = 600$ mV for our PbS QD PV device is provided in Figure 4.7A. The impedance data are obtained by calculating the frequency dependence Z_r and Z_i from the measured admittance response. In this representation, an implicit frequency scale runs from right to left as indicated. The impedance is dominated by a major arc characteristic of the parallel connection of a charge accumulation capacitance C and a charge transfer resistance R_{ct}.[119, 10, 45] These arcs provide essential information on carrier dynamics at the applied bias of the measurement V_A. C is generally interpreted as a chemical capacitance resulting from shifts in E_F due to injected minority carriers. In IS studies of SRH recombination in bulk systems, low R_{ct} values are characteristic of effective recombination centers. As discussed in Chapter 3, R_{ct} for charge dynamics arising from transport corresponds to a probability that a charge hops into the DOS responsible for charge transport.

The values of R_{ct}, C, and the lifetime $\tau = RC$ can be extracted from the impedance arc in 4.7A by fitting the data to an equivalent RC circuit model.[119, 10] The time constant dispersion in our PbS QD PV device resulting from the broad distribution of hopping times implies that the arc in Figure 4.7A reflects an analogously broad distribution of charge relaxation times instead of a single RC response. As a result, we model the arc by incorporating a constant phase element (CPE), Q, which has the following impedance:[20, 109, 119]

$$Z(\omega) = \frac{1}{(i\omega)^{\alpha} Q} \tag{4.6.1}$$

where i is the imaginary unit, Q is the CPE coefficient related to the capacitance, and α is the modified phase angle of the CPE impedance due to the time constant dispersion. For $\alpha = 1$, the phase angle of the impedance is 90°, and equation (4.6.1) reduces to the impedance for a capacitor.[20, 118] The total impedance described by the parallel RQ circuit becomes:

$$Z(\omega) = R_S + \frac{R_{ct}}{1 + (i\omega)^{\alpha} Q R_{ct}} \tag{4.6.2}$$

where R_s is the resistance of a resistor in series with the RQ circuit. The data in 4.7A (red) have been fit to equation (4.6.2), resulting in room temperature values $R_{ct} = 2.8$ kΩcm^{-2}, $Q = 5.1 \times 10^{-4}$

kΩcm^{-2}s$^{\alpha}$ and $\alpha = 0.92$. From the value of Q and α, the effective capacitance C_{eff} be calculated as $C_{eff} = Q(\frac{1}{R_{ct}} + \frac{1}{R_s})^{\frac{\alpha}{1-\alpha}}$, and thus τ can be determined as:[56, 20]

$$\tau = (QR_{ct})^{\frac{1}{\alpha}}. \tag{4.6.3}$$

The data in 4.7A correspond to $\tau = 8.5 \times 10^{-4}$s, in excellent agreement with previous estimates of the dark carrier lifetime in air-annealed ZnO films [134] and in ZnO-PbS heterojunctions due to interfacial trapping [135] measured by XPS.

Fits to impedance arcs observed from $T = 230 - 300$ K (provided in Appendix B.9) allow us to measure the temperature dependence of τ, exhibited in Figure 4.7B. An Arrhenius fit to the data gives the activation energy $E_A = 0.29 \pm 0.02$ eV, in excellent agreement with the low frequency $\sigma'(\omega)$ data in Figure 4.6B. As exhibited in Figure 4.7C, R_{ct} is observed to decrease with temperature with the same thermal activation energy ($E_A = 0.30 \pm 0.01$ eV), indicating that charge dynamics in these levels becomes more likely as temperature increases. Based on the agreement between the thermal activation of R_{ct} and τ, we conclude that charge dynamics in the ZnO show little dependence on the thermal activation of carriers in the temperature range of the experiment, in agreement with the lack of an observable capacitance de-tuning in Figure 4.2C and in contrast with the charge dynamics studied in Chapter 3. We hypothesize that the consistency of these activation energies suggests that charge accumulation at open circuit is dominated by electron hopping from the ZnO to the PbS QD layer over an energy barrier given by E_A. As a result, we expect that this state limits the ability of the PbS QD PV device to store charge under illumination.

The proposed band diagram at V_A is presented in Figure 4.7D. Application of forward bias induces splitting of the quasi-Fermi levels on both sides of the junction. The zero bias TAS measurements discussed above were interpreted assuming that the hole quasi-Fermi level E_{Fp} is situated a distance $E_T \approx 0.29$ eV from the valence band edge in the PbS-MPA layer. The forward-biased AC conductance and IS measurements suggest an electron barrier $E_A \approx 0.3$ eV from the conduction band onset in the ZnO. As a result, we hypothesize that the max achievable V_{oc} is limited to $\frac{E_G}{/}q - 0.29 - 0.3 = 0.67$, in reasonable agreement with the V_{oc} observed in Figure 4.6A.

The fits to $-Z_i$ vs. Z_r further allow us to estimate that α increases slightly from $0.86-0.92$ over temperature range of the experiment, implying that as temperature increases, dynamics at E_A becomes the dominant hopping pathway in the PbS QD PV device.[135] IS allows us to explicitly visualize the specific distribution of relaxation times $G(\tau)$ that gives rise to the dispersion observed in the impedance response of our QD PV device, written as:[20, 119]

$$\tau G(\tau) = \frac{2\sin(\alpha\pi)}{\exp[(1-\alpha)\frac{\tau}{\tau_0}] + \exp[-(1-\alpha)\frac{\tau}{\tau_0}] - 2\cos(\alpha\pi)} \tag{4.6.4}$$

where τ_0 is the characteristic time constant. As discussed in Chapter 2, this distribution is a result of the Gaussian distribution of available energy states for electron occupation. Figure 4.7E shows the distribution of relaxation times calculated *via* equation (4.6.4) from $T = 230-290$ K for values of τ probed over the frequencies used in the IS measurement. As temperature increases, the peak of $\tau G(\tau)$ shifts towards $\sim 10^{-4}$ s, indicating that the time constant distribution is heavily weighted towards the large energetic barrier observed in IS and AC conductance. In addition, the distributions also exhibit significant broadening on the low τ side. In organic capped PbS QDs of similar size, the charge transport lifetime has been estimated to be $\tau \sim 2 \times 10^{-6}$ s,[133], close to the limit in the tail of the calculated distribution. We speculate that these shifts are consistent with contributions to the transport processes in the PV device from charge dynamics within the PbS QD layer.

4.7 Conclusion

We have demonstrated a systematic study of the charge dynamics at a PbS QD-ZnO heterojuntion interface in a completed PV device geometry From TAS measurements, we hypothesize that E_F is located about 0.29 eV from the valence band of the PbS-MPA QD film. We speculate that E_F is partially pinned in a defect state which may be localized at the interface. DLCP measurements allow us to estimate the total charge density within the depletion region. Though the depletion region drops across both the PbS QD and ZnO layer, we conjecture that the $N(E)$ probed in TAS corresponds to a discrete defect on the PbS QD side of the junction, with a total DOS of $\sim 3\times10^{18}$ cm^{-3}eV^{-1}. At open circuit conditions, our preliminary analysis indicates AC conductance and IS measurements are characterized by charge dynamics with activation energy $E_A \sim 0.3$ eV from the conduction band onset in the ZnO. These charge processes dominate the broad distribution of electron hopping times in the PV device.

We note that shallow defects in ZnO bulk films have been experimentally related to zinc inerstitials, [79, 96] suggesting that the Zn-rich NC synthesis used to make the ZnO films may inherently produce defects in the ZnO nanoparticles used to fabricate our device. Our results suggest that charge dynamics within PbS QD heterojunction PV devices may be dominated by the ZnO/PbS QD heterojunction interface. However, we note that throughout the analysis of the admittance response at zero bias, we assumed that the charge response was due to defects at the PbS QD interface. Given the current data, we cannot unambiguously rule out the influence of frequency-limited transport dynamics in the zero-bias admittance response of our PbS QD PV device.

4.8 Methods

4.8.1 Materials

Oleic acid (OA, 90%), 1-octadecene (ODE, 90%), lead oxide (PbO, 99.999%), cadmium chloride ($CdCl_2$, 99.99%), oleylamine (70%), 3-mercaptopropionic acid (MPA, 99%), Tetrabutylammonium iodide, zinc acetate dehydrate (98%), (3-mercaptopropyl)- trimethoxysilane (MPTS, 95%), anhydrous hexane, anhydrous 2- propanol, anhydrous methanol, anhydrous toluene, anhydrous acetonitrile and anhydrous acetone are purchased from Sigma-Aldrich. Bis(trimethylsilyl) sulfide ((TMS)2S, 95%) is purchased from Acros. Tetradecylphosphonic acid (TDPA, 98%) and molybdenum oxide (MoO3, 99.9995%) are purchased from Alfa Aesar. Potassium hydroxide (KOH, 85%) is purchased from Fisher.

4.8.2 QD Synthesis

PbS QDs are synthesized as reported previously[163]. In brief, a mixture of 0.47 g of PbO, 23 mL of ODE, and 2 mL of OA is degassed at 120 C for 2 h under vacuum. Then 5 mL of 21 μL (TMS)2S/1 mL ODE solution is injected at 100 C with N_2 flowing. The heat is turned off immediately after injection, and when the reaction solution is cooled to 70 C, a pre-dried $CdCl_2$ solution (0.3 g of $CdCl_2$ and 0.033 g of TDPA in 5 mL of oleylamine) is added. After 5 min, the reaction is further quenched in a water bath. The product is transferred into the glovebox and purified by washing four times with acetone, 2-propanol, and methanol and finally re-dispersed in octane/ hexane (4:1) at 50 mg/mL.

4.8.3 Device fabrication

All the fabrication steps are carried out in air unless otherwise noted. Prepatterned ITO/glass substrates (Thin Film Devices) are cleaned by sonication in 5% Hellmanex in DI water, pure DI water, and ethanol consecutively, followed by UV ozone treatment for 30 min. The cleaned substrates are soaked in MPTS (5% in toluene) for 10 h before use. The ZnO NPs are synthesized according to a literature recipe [8]. The ZnO NP film is fabricated by spin casting ZnO NPs (100 mg/mL) at 1500 r.p.m., and annealed in air at 250 C for 20 min. On top of the ZnO NP layer, the PbS QD solution (50 mg/mL) is spin cast at 3000 r.p.m for 30 s, followed by MPA (1% vol) solid-state ligand exchange for 30 s or 3 s, respectively, with three rounds of methanol washing. 10 layers of PbS QD film are deposited. To finish the device, 12 nm of MoO3 and 65 nm of Au are thermally evaporated on the PbS QD film through a shadow mask inside a glovebox, which defines a 2 mm by 2 mm device active area.

4.8.4 Room Temperature Characterization

Dark and illuminated JV data are measured using a Keithley 2420 sourcemeter. Current is recorded by sweeping the DC applied voltage from -200 to 700 mV in 20 mV steps. The PV device is illuminated using a solar simulator (Oriel instruments model 96000, Newport Co.). The simulated AM 1.5 light is brought into the glovebox through a liquid light guide feed-through. The illumination intensity at the device is calibrated to be 1 Sun, i.e., 100 mW cm^{-2}, by a Si reference cell and meter from Newport (model 91150). PV devices are illuminated through an aperture of 1.6 mm x 1.6 mm in size, smaller than the active device area.

4.8.5 Variable Temperature Characterization

Variable temperature TAS, DLCP, AC conductance, and JV measurements are performed within a LakeShore Cryotronics vacuum probestation with a liquid-N2 cooled sample stage. PbS PV devices are measured from $T = 190$ to 310 K at 10 K intervals. Two probe admittance and JV measurements are carried using a Hewlett Packard HP4192A impedance analyzer and an Agilent 4156C parameter analyzer, respectively. A computer-controlled relay switch is used to toggle between AC impedance measurements and DC JV characterization at each temperature or time-step as depicted in the schematic in Figure 4.1A. For the temperature-dependent measurements, the device is left under vacuum in the dark at room temperature for 1 h, cooled to 180 K, and allowed to thermally equilibrate for 1 h before measurements are started. For TAS measurements, the capacitance response of the PV device to a 100 mV AC perturbation is collected for frequencies ranging from 20 Hz1.3 MHz at a 0 mV DC bias. The same DC and AC biases are applied for AC conductivity measurements. IS measurements are obtained at the same frequency range and AC bias at an applied DC forward bias $V_A = 600$ mV. DLCP measurements are performed immediately afterward using the same setup, with AC signals at frequencies of 1 kHz, 10 kHz, and 100 kHz, and maximum applied biases $V_{max} = V_{RMS} + V_{DC}$ from -50 mV to -300 mV in 50 mV steps.

To obtain the non-linear capacitance response, V_{RMS} was varied from 10 mV - 300 mV, and V_{DC} is automatically modulated to keep V_{max} constant using custom LabView software.

Chapter 5

Charge Dynamics in Halide-Capped PbS QD PV devices with Multiple Interfaces

5.1 Introduction

Recent gains in QD PV devices have largely been driven by the exploration of a prodigious library of ligand capping chemistries. The changes to the surface dipole moments induced by these ligands allow for the tuning of the conduction and valence band onsets, [80, 18] which in turn provide a basis for optimizing the band alignment in completed QD PV devices.[27] Many of the most efficient PbS QD PV devices demonstrated contain halide (Cl^-, Br^-, I^-) treated PbS-QD layers,[160, 32, 27, 7, 62, 165] which exhibit record carrier diffusion lengths of 20-80 nm[133, 164] and mobilities $\mu \sim 10^{-3} - 10^{-2}$ $cm^2(Vs)^{-1}$.[136, 114] Halide treatments have also been shown to impart environmental stability to PbS QD solids,[32] and the efficiency of devices with active layers of PbS QDs capped with I^- ions have been shown to improve upon storage in atmosphere.[27]

Despite the benefits afforded by halide treatments, the underlying charge dynamics physics in these devices remains unclear. For instance, though halide-treated PbS QDs are thought to be n-type upon fabrication,[18] exposure to air imparts increasing p-type character to the transport characteristics.[152] As a result, the ZnO/PbS-TBAI interface in these PV devices has been reported to be both an n-i heterojunction[27] and an n-n isotpye heterojunction.[126] Furthermore, halide-treated PbS QD PV devices are known to exhibit a smaller V_{oc} than devices made of organic-capped PbS QD layers. Though the exact mechanism of these losses is not yet understood, they have been heuristically linked to recombination pathways in the QD layers.[28]

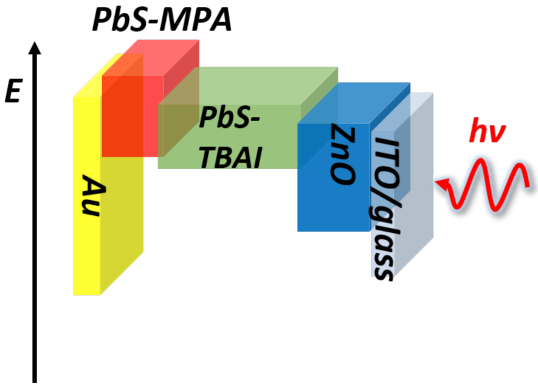

Figure 5.1: (Structure of PbS QD PV device device studied, with illumination direction highlighted

In this chapter, we use study the frequency-dependent charge response of a PbS QD heterojunction PV device with a graded absorber made up of 2 PbS QD layers. The first layer consists of PbS QDs capped with 3-mercaptopropionic acid (MPA), the second of PbS treated with tetrabutyl-ammoinium iodiode (TBAI). As in Chapter 4, an n-type window layer of ZnO completes the device, exhibited in Figure 5.1. The presence of two interfaces between three materials makes unambiguous physical identification of the physical origin of the charge response difficult. However, using a suite of frequency-dependent techniques, we hypothesize a phenomenological model for electron transport with the TBAI-capped PbS QD ('PbS-TBAI') layer and at the PbS-TBAI/ZnO interface. TAS and DLCP show a charge response we suggest is the result an electron trapping level on the PbS-QD side of the junction with an activation energy of ~ 0.39 eV. After sufficient oxidation of the film, the electron concentration within the PbS-TBAI layer decreases, and the charge response of the ZnO and PbS QD layers become difficult to disentangle. Under these conditions, we observe a charge response at ~ 0.3 eV, which we suggest corresponds to pinning at the ZnO/PbS-TBAI heterointerface. We note that other explanations, such as transport limited carrier response, may also be responsible for these signals. *Via* AC conductance and IS measurements, we propose that the observed states at zero bias affect electron transport under applied forward bias. IS analysis provides allows us to deuce time-scales of the charge dynamics within these layers, allowing us to make preliminary correlations bween these energy levels and electron transport and trapping mechanisms in forward bias. Finally, illuminated TAS and DLCP measurements imply that the charge response probed may be an effective recombination center for photogenerated charge.

5.2 Results

5.2.1 TAS

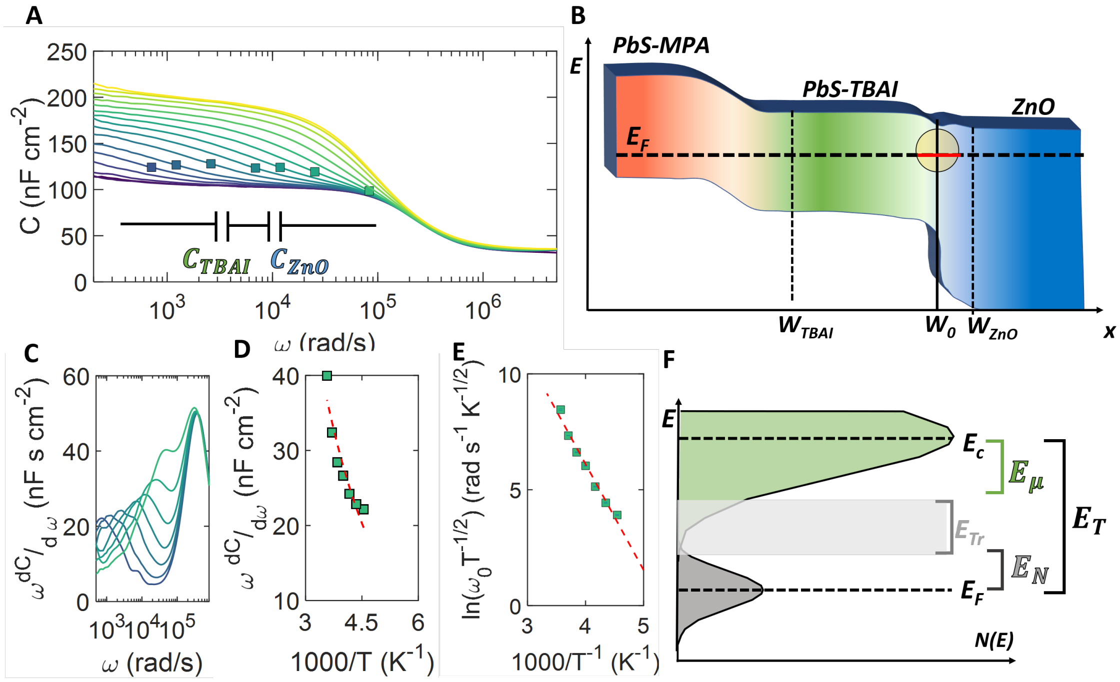

Figure 5.2: (A) (A) C vs. ω 1 day after fabrication (day 1) with highlights (squares) indicating ω_0. Inset: series capacitor model used to analyze data. (B) Proposed band structure and junction measured. (C) $-\frac{dC}{d\omega}$ showing de-tuning. (D) Fermi fit to detuning energy estimating E_N. (E) $\ln(\omega_0 T^{-1/2})$ vs. $\frac{1}{T}$, with Arrhenius fit giving E_T. (F) Estimated band structure from TAS measurements.

A PbS QD PV device was fabricated in air by depositing ZnO nanoparticles synthesized according to literature methods [8] onto an ITO/glass substrate *via* spincoating. After mild air-annealing, 3 nm diameter PbS QDs synthesized according to literature methods [163] are spincoated onto the substrate. To exchane the native oleic acid ligands, the deposited PbS QD film is then treated with a solution of TBAI in methanol followed by a methanol wash to remove excess ligand. 10 layers of TBAI-treated PbS QDs are deposited, resulting in a total film thickness ~ 180 nm. An additional two layers of PbS-MPA is deposited according to the procedure outlined in Chapter 4. The device is then capped with an Au top contact.

Admittance characterization is performed by loading the completed device into a vacuum probestation ($\sim 10^{-4}$ torr) and measuring the frequency-dependent capacitance response to 100 mV AC signals at 0, -100, and -200 mV DC bias from $T = 180 - 300$ K. Figure 5.2A shows the frequency-dependent capacitance characteristics of a PbS-MPA/PbS-TBAI/ZnO QD PV device one day after fabrication ('day 1'). The spectra exhibit similar behavior to the capacitance spectra exhibited in Chapter 4, showing a temperature-dependent, step-like decrease in capacitance for $\omega \lesssim 10^5$ rad/s to a large plateau followed by a temperature-independent step to a stable capacitance minimum at $\omega > 10^5$ rad/s. Bias-dependent TAS measurements included in Appendix C.2 indicate that while the low frequency capacitance steps exhibit a voltage-dependent emission rate, characteristic of Fermi level pinning,[61, 103] the large temperature-independent step at higher frequency shows no modulation on the high-frequency side, consistent with dielectric freeze out.[84, 151] As in Chapter 4, we ascribe the high frequency capacitance step to dielectric relaxation of charge carriers within the device. We hypothesize that the low frequency capacitance step reflects charge emission a defect level within the depletion region.

In Chapter 4, we showed that analysis of the geometric capacitance C_G can be used to gain insight into the structure of the depletion region at the device heterojunction. In Figure 5.2A, the junction capacitance bottoms out at $C_G \approx 40$ nFcm^{-2}. Assuming that the full 40 nm thickness of the PbS-MPA layer with a dielectric constant $\varepsilon = 10$ and the 180 nm thickness of the PbS-TBAI layer with $\varepsilon = 18$ (measured in Appendix C.1) act as a dielectric layer at the high frequencies where C_G is reached, and that no depletion region drops across the ZnO, the geometric capacitance should be ~ 60 nFcm^{-2}. For $\varepsilon_{ZnO} = 3.7$,[104] the observed value of C_G indicates a depletion region of width ~ 35 nm drops across the ZnO layer, consistent with the ZnO depletion region deduced in Chapter 4, as well as previous reports of depletion regions in PbS QD/ZnO heterojunctions.[135] As in Chapter 4, we infer that this depletion region results from the decrease in electron concentration within the ZnO that occurs upon air exposure of the device.[154, 81, 31]

Recent electron-beam spectroscopy studies on PbS QD PV devices with similar architectures have suggested that PbS-TBAI/ZnO forms an n^{+}-n isotype junction,[126] in agreement with ultraviolet photoelectron spectroscopy studies that have shown that PbS-TBAI QD films are n-type when prepared and stored in an inert environment.[18] In a PbS-TBAI/ZnO isotpye junction, a small depletion region can be expected to drop across the wide-bandgap ZnO, while charges accumulate within the PbS-TBAI layer at the interface.[139] The low doping density in the ZnO window layer in our device implies that the depletion region within the ZnO is larger than in the ideal case where the ZnO is degenerately doped. For the purposes of this analysis, we therefore speculate that the junction capacitance on day 1 is dominated by the n-n isotype junction between the PbS-TBAI and the ZnO, as shown in Figure 5.2B.

Figure 5.2C exhibits the frequency-normalized capacitance derivative $-\omega\frac{dC}{d\omega}$ vs. ω used to find the resonant frequency of the defect state ω_0. As in Chapter 3, the peak-amplitude shows a considerable temperature-dependent amplitude, implying that more charge carriers contribute to the measured capacitance at higher temperatures. We estimate the thermal activation energy E_N of the carrier density by fitting a Fermi function to the peak capacitance amplitude,[15, 17] presented in Figure 5.2D. From the fit, we obtain $E_N = 0.05 \pm 0.03$. The large uncertainty and poor fit to the data indicate that our analysis does not fully capture the thermal activation of carriers.

A fuller picture of the charge dynamics at the interface is afforded by an Arrhenius fit to the resonant frequency, provided in Figure 5.2E. Like in Chapter 4, we hypothesize the observation of a distinct temperature-dependent charge response at frequencies below the capacitance decay to C_G implies that the lower frequency dynamics correspond to charge emission from a discrete defect level E_T. The slope of the fit indicates a total activation energy $E_T = 0.39 \pm 0.01$ and a reduced attempt to escape frequency $\nu_{00} = 1.1 \times 10^{10}$ rad/sK$^{-1/2}$. We note that these values are in excellent agreement with previous TAS characterization of the PbS QDs in n^{+}-ZnO/PbS-

TBAI heterojunction PV devices [66] and TAS studies of similarly-sized organic capped PbS QD solids.[16] Unlike TAS analysis of the simpler device structure studied in Chapter 3, the capacitance measurement cannot disentangle contribution of E_N to E_T and therefore cannot identify a charge transport energy E_{Tr} below the conduction band. We nevertheless expect that E_T indicates the position of E_F below the conduction band edge E_C. These levels are drawn in the schematic in Figure 5.2F.

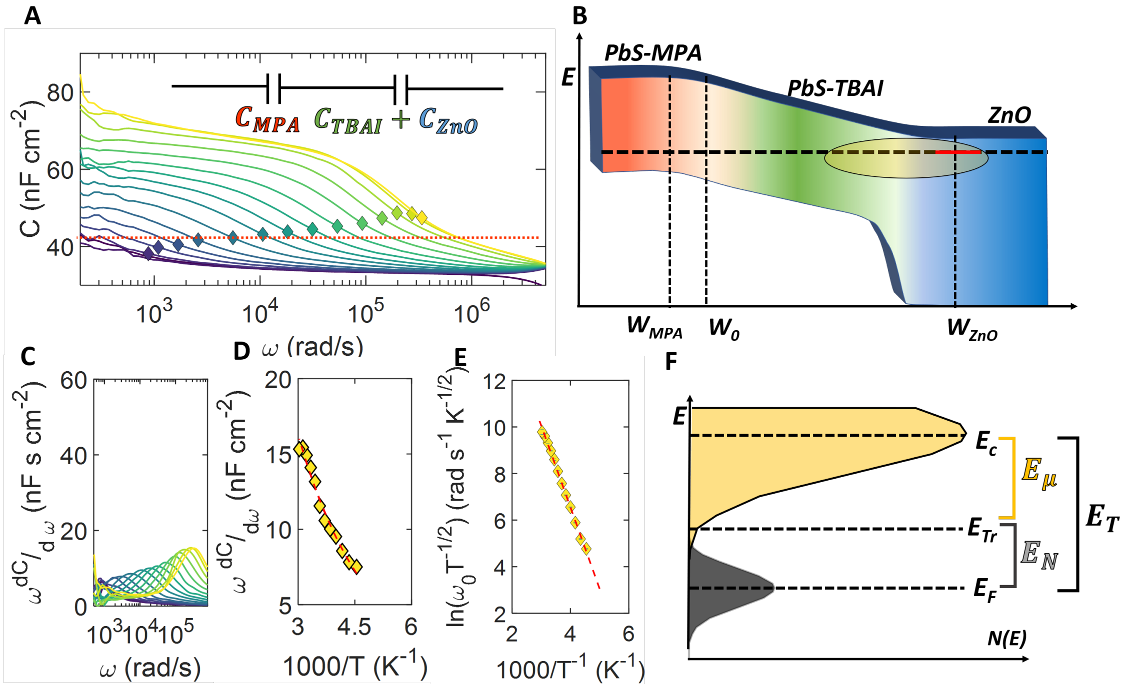

Figure 5.3: (A) C vs. ω 2 days after fabrication (day 2) with highlights (squares) indicating ω_0. Inset: series capacitor model used to analyze data. (B) Proposed band structure and junction measured on day 2. (C) $-\frac{dC}{d\omega}$ vs. ω. (D) Fermi fit to detuning energy giving E_N. (E) $\ln(\omega_0 T^{-1/2})$ vs. $\frac{1}{T}$, with Arrhenius fit giving E_T. (F) Estimated band structure from TAS measurements.

Figure 5.3A exhibits TAS measurements obtained after 2 days of storage in a N_2 glovebox, exhibiting striking differences from the day 1 spectra in Figure 5.2A. Previous reports have suggested that continual air exposure significantly increases device performance in ZnO/PbS-TBAI

PV devices with a similar device architecture.[27] Though the exact mechanism of this improvement has yet to be unequivocally demonstrated, exposure to atmospheric oxygen is known to introduce acceptor levels into PbS bulk[101, 102, 51] and QD films[149, 86], switching the electronic characteristics of as-prepared films from n-type to p-type. As a result, we expect that both PbS-TBAI[152] and PbS-MPA films become more p-type with exposure to air, resulting in an increased p-type doping within the PbS-MPA QD layer and a more intrinsic PbS-TBAI QD layer. We note that an intrinsic PbS-TBAI layer is consistent with the design rationale behind this device architecture.[27] Furthermore, a depleted PbS-TBAI layer is consistent with the decreased total capacitance measured in Figure 5.2A, which reaches a maximum of $\sim$ 75 nFcm^{-2} at low frequencies while achieving the same minimum of $\sim$ 38 nFcm^{-2} at high frequencies observed on day 1.

The decrease from the low frequency capacitance level in Figure 5.3A to that the level in Figure 5.3A may indicate that in addition to the depleted PbS-TBAI and partially depleted ZnO regions, a small depletion region of $W_{MPA} \sim 20$ nm may drop across the PbS-MPA layer, depicted schematically in Figure 5.3B, implying a depletion capacitance $\sim$ 380 nFcm^{-2}. The portion of the n-side of the depletion region in ZnO gives a much smaller depletion capacitance of $\sim$ 90 nFcm^{-2}. Furthermore, assuming electron transport still dominates the charge dynamics within the PbS-TBAI QD layer,[18, 126] which may be reasonable considering the vacuum conditions under which this measurement was performed, the combined capacitance of a fully depleted ZnO and PbS-TBAI layer is $\sim$ 45 nFcm^{-2} (indicated in Figure 5.3A with a dashed red-line). We speculate that the temperature-dependent capacitance decays observed in TAS on day 2 correspond to a mixture of electron dynamics in the ZnO layer, the PbS-TBAI QD layer, and the PbS-MPA QD layer as indicated in the equivalent circuit in the inset of Figure 5.3B. In this model, the decay to C_G at high frequencies occurs as the applied frequency exceeds the temperature-dependent hole conductivity of the PbS-MPA QD layer. We hypothesize that the dashed line in Figure 5.3A may therefore roughly indicate a demarcation level above which charge dynamics are dominated by the

PbS-TBAI/ZnO layer and below which charge response is influenced by PbS-MPA. Differentiation of charge dynamics within the PbS-TBAI and ZnO depletion region is beyond the scope of this discussion, and for the remainder of the analysis of the day 2 data, we assume that the combination of the two layers may be modeled as a homogeneous dielectric material. For a total depletion capacitance of 45nFcm^{-2} and a total thickness of $D_{PbS}+D_{ZnO} = 220$ nm, we obtain an equivalent dielectric constant $\varepsilon = 10.8$

Figure 5.3C shows the capacitance derivative $-omega\frac{dC}{d\omega}$, which exhibits a drastically smaller capacitance de-tuning than the day 1 spectra. A Fermi fit to the capacitance amplitude, provided in Figure 5.3D, shows an excellent fit to the data and yields a carrier activation energy $E_N = 0.046 \pm 0.001$ eV. To determine the activation energy of the resonant frequency, we again assume that the charge response is due to charge emission from a discrete defect level. Though we cannot unambiguously determine if the quantum confined PbS-TBAI QD layer or the more bulk-like annealed ZnO film is responsible for the charge response, the activation energy of ω_0 is calculated by fitting $\ln(\omega_0 T^{-1/2})$ against ω (Figure 5.3D) following equation (4.2.2). The fit yields $E_T = 0.300 \pm 0.002$ eV and a reduced attempt frequency $\nu_{00} = 4.2 \times 10^8$ rad/sK$^{-1/2}$. We note that the observed value of E_T, which is primarily sensitive to E_F following the discussions in Chapters 2 and 4, is consistent with our preliminary estimate of E_F at the ZnO/PbS heterointerface deduced *via* forward biased IS measurements in Chapter 4. This value is also in agreement with previous estimates of defect levels at the ZnO surface detected via TAS[70], deep level transient spectroscopy[131], and FET studies.[23]. However, we note that these data do not unambiguously reflect emission from a discrete trapping level, and that transport-limited charge hopping may also be responsible for the observed response. Assuming the latter to play a role in the dynamics observedin TAS, the implied transport level $E_{Tr} = E_T - E_N = 0.26$ eV (Figure 5.3F) is in excellent agreement with estimates of defect states below the conduction band in PbS-TBAI QD films from sub-bandgap photoluminesnce (PL) measurements. The fact that these PL measurements were made without an interface suggests that if the observed capacitance response results from transport, then E_{Tr} dedued from the data in Figure 5.3 is related to charge dynamics in the the PbS-TBAI QD layer.

5.2.2 DLCP

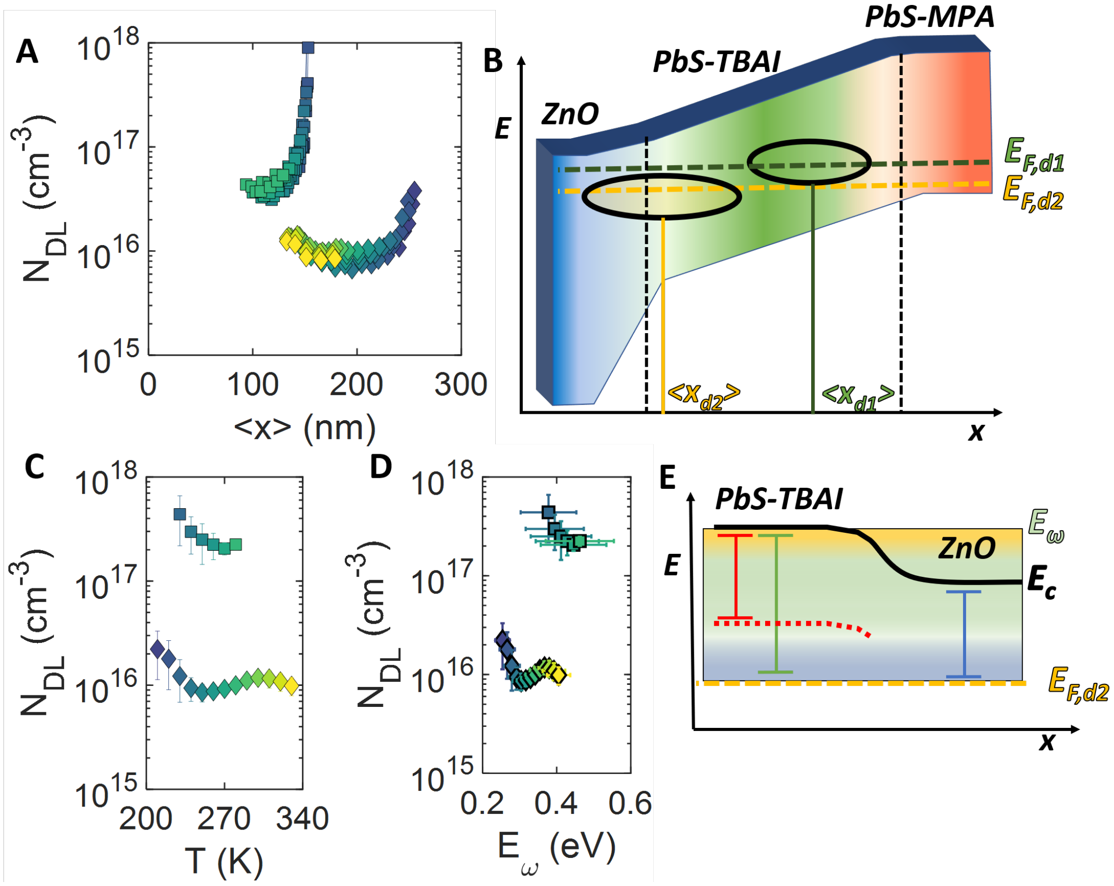

Figure 5.4: (N_{DL} vs. $< x >$ on day 1 (squares) and day 2 (diamonds). (B) Band diagram cartoon showing location of predominant charge responses on day 1 ($< x_{d1} >$) and day 2 ($< x_{d2} >$) along with Fermi levels and junction locations expected on respective days. (C). N_{DL} vs. T for day 1 (squares) and day 2 (diamonds). (D) N_{DL} vs. E_ω on day 1 (squares) and day 2 (diamonds). (E) Band structure used to interpret day 2 N_{DL} vs. E_ω data, showing E_F (yellow), E_{Tr} (red), E_ω (highlights), and positions of E_C in ZnO and PbS-TBAI.

DLCP measurements made in parallel with the TAS measurements allow us to estimate the charge density that gives rise to the response observed in Figures 5.2A and 5.3A. Figure 5.4A shows the charge carrier profile N_{DL} vs. $< x >$ obtained on day 1 (squares) and day 2. (diamonds). The data presented in Figure 5.4A were obtained at measurement frequencies $\omega = 3.14 \times 10^3$ rad/s and calculated assuming that $\varepsilon = 18\varepsilon_0$ on day 1 and $\varepsilon = 10.8\varepsilon_0$ for day 2. On day 1, $N_{DL} \approx 2 \times 10^{17}\text{cm}^{-3}$ in excellent agreement with previous estimates of the carrier density in PbS-TBAI QD solids based on Schottky junction capacitance measurements.[133] By contrast, the day 2 data show a decrease to $N_{DL} \approx 9 \times 10^{15}$ cm^{-3}, indicating a carrier concentration closer to the intrinsic carrier concentration $\sim 10^{14}$ cm^{-3} estimated for PbS QD films.[149] These data indicate that the carrier concentration probed decreases after sufficient air exposure, consistent with our interpretation of the TAS data in Figures 5.2A and 5.3A. Furthermore, $< x >$ increases from ~ 100 nm on day 1 to $\sim 150 - 300$ nm on day 2, consistent with the proposed increase in the extent of the depletion region as the PbS-TBAI layer becomes more intrinsic. We note that since the total width of the PbS-TBAI layer and the ZnO depletion region is ~ 220 nm, $< x >$ values larger than this width can be considered un-physical. We ascribe the ambiguities in the $< x >$-scale to uncertainty in the value of ε. The use of an equivalent dielectric constant in these calculations due to the contributions of both the ZnO and PbS QD layers imply that our profiling analysis is qualitative; however, though the value of ε is not known to high accuracy, the trends in the observed profile distance are physically significant under the assumption that we have identified the charge mechanisms responsible for the response on day 1 and day 2.[52]

In addition to the decrease in carrier concentration from day 1 and day 2 observed in Figure 5.4A, the day 1 depletion width stays constant with temperature, whereas the day 2 depletion width shrinks as temperature increases. Similar temperature-dependent decreases in the depletion width of PbS-TBAI films have been observed in previous capacitance studies and ascribed to carrier activation within the QD solid.[133] The hypothesized trends in the carrier density profile are summarized in Figure 5.4B. In our analysis, the predominant junction on day 1 ('d1') is the

Pbs-TBAI/ZnO interface; as a result, N_{DL} corresponds to a carrier density within the PbS-TBAI QD layer. On day 2 (d2), the PbS QD layers become more p-type. The first moment of charge response detected in DLCP is then centered further from the interface as the PbS-MPA/PbS-TBAI interface becomes the dominant interface in the device.[126]

Figure 5.4C shows exhibits N_{DL} as a function of temperature. Below $T = 280$ K, N_{DL} stabilizes to $\sim 2 \times 10^{17}$ cm^{-3} on day 1 and $\sim 8 \times 10^{15}$ cm^{-3} on day 2. For $T > 280$ K, the day 2 data exhibits a slight increase in density to $\sim 1 \times 10^{16}$ cm^{-3}. Figure 5.4D indicates this increase occurs at an activation energy $E_\omega = E_C - E_F = 0.39$. Since this energy matches the hypothesized energetic distance between E_C and E_F observed in the TAS spectra on day 1, we speculate that the increase in N_{DL} occurs as carriers close to the conduction band in the PbS-TBAI QD layer become responsive to the measurement, as indicated in Figure 5.4E. We note that the observed peak value $\sim 1 \times 10^{16}$ cm$_{-3}$ at this energy is in excellent agreement with the previous estimates of the carrier concentration of ambipolar PbS-TBAI QD films [152].

5.2.3 AC Conductance

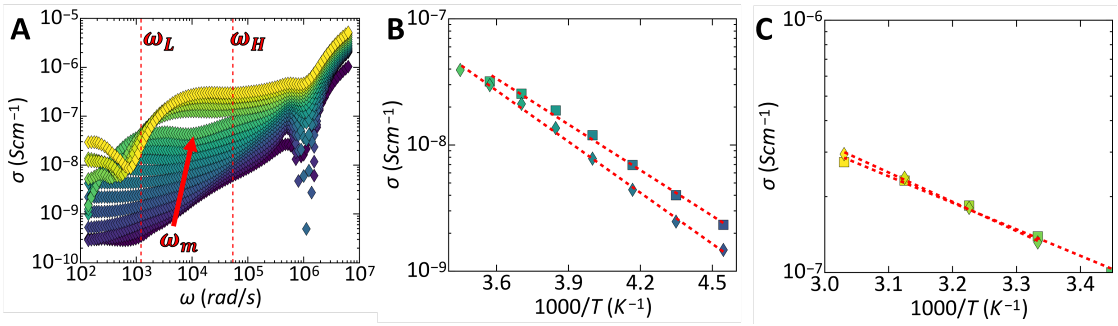

Figure 5.5: (A) $\sigma(\omega)$ obtained at $V_A = 400$ mV on day 2, exhibiting 2 dispersion-less conductance plateaus. Dashed red lines indicate low frequency regime ($\omega_L = 1.2 \times 10^3$ rad/s) and high frequency regime ($\omega_H = 5 \times 10^4$rad/s) used for temperature-dependence analysis. (B) $\sigma(\omega)$ at low temperature, low frequency DC conductance plateau on day 1 (squares) and day 2 (diamonds) with accompanying Arrhenius fits. (C) $\sigma(\omega)$ at high temperature, high frequency DC conductance plateau on day 1 (squares) and day 2 (diamonds) with accompanying Arrhenius fits.

We hypothesize that the presence of two activated processes in the PV device on day 2 is reflected in the frequency-dependence of the AC conductance $\sigma'(\omega)$ displayed in Figure 5.5A. These data are obtained in parallel with the TAS data at $V_A = 400$ mV applied bias. The applied forward bias suggests that the predominant charge dynamics observed in Figure 5.5A are dominated by electron injection from the ZnO into the PbS-QD layers, as discussed in Chapter 4. Two distinct, frequency-independent conductance plateaus are observed in Figure 5.5A. For $T \leq 290$ K, $\sigma'(\omega)$ is flat below a temperature-dependent inflection frequency ω_m ($\approx 10^4$ rad/s at $T = 280$ K, as indicated in Figure 5.5A). For $T > 290K$, this region exhibits a pronounced frequency dispersion, after which the second, higher temperature conductance plateau is observable from $\omega \approx 10^4 - 10^5$ rad/s. As discussed in Chapter 3, dispersion-less plateaus in $\sigma'(\omega)$ vs. ω indicate the formation of a complete percolation network in which charge can hop across the entire device. In this regime, $\sigma'(\omega)$ indicates the DC conductivity limit, and the temperature activation of $\sigma'(\omega)$ is dominated by the largest energy barrier that electrons must hop over as they travel from the ZnO to the Au contact at the back of the device.[36] Interestingly, for $T > 290$ K, the frequencies at which the first conductance plateau appears at low temperatures show no evidence of DC transport. Instead, the data show pronounced frequency dispersion, consistent with dielectric loss due to recombination.[111]

The observation of two distinct DC conductance regimes in Figure 5.5A suggests the presence two different barriers to DC transport in the device on day 2, consistent with the increase in the day 2 N_{DL} observed in Figure 5.4B,C. As exhibited in Appendix C.4, the forward-biased AC conductance data on day 1 also show evidence of two energy barriers to electron transport in the device. To estimate the activation energy E_A associated with these energy barriers, we select two test frequencies: one within the low temperature conductance plateau and one within the high temperature conductance plateau. For the day 2 data exhibited in Figure 5.5A, this corresponds to a low test frequency $\omega_L = 1.2 \times 10^3$ rad/s and a high test frequency $\omega_H = 5 \times 10^4$ rad/s. The day 1 data exhibited in Appendix C.4 are analyzed at $\omega_L = 6.0 \times 10^2$ rad/s and $\omega_H = 1.2 \times 10^4$ rad/s.Figure 5.5B shows the temperature-dependence of the $\sigma'(\omega_L)$ on both day 1 (squares) and day 2 (diamonds). The included Arrhenius fits indicate a day 1 activation energy of low temperature DC conductance $E_A = 0.24 \pm 0.02$ eV, while on day 2, $E_A = 0.27 \pm 0.02$ eV. Similarly, Figure 5.5C displays the temperature-dependence of $\sigma'(\omega_H)$, from which we deduce that the activation energy of the high temperature DC conductance plateau on day 1 is 0.21 ± 0.03 eV whereas $E_A = 0.23 \pm 0.02$ eV on day 2.

5.2.4 Impedance Spectroscopy

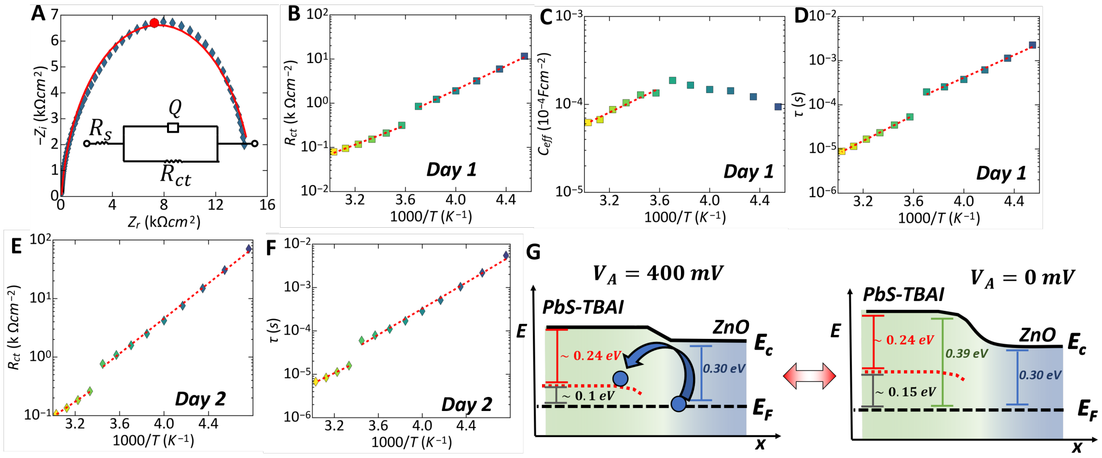

Figure 5.6: (A) Example impedance arc for IS data obtained at T = 230 K with accompanying fit from equivalent RQ circuit (inset). B) R_{ct} extracted from IS fits at different temperatures on day 1 showing 2 different temperature dependences and accompanying Arrhenius fits to low and high temperature regimes (dashed red lines). (B) C_{eff} extracted from IS on day 1 showing high temperature carrier activation with Arrhenius fit (dashed red line). (D) Resulting τ calculated from R_{ct} and Q on day 1 with Arrhenius fits to 2 separate temperature regimes. (E) R_{ct} extracted from IS fits at different temperatures on day 1 showing 2 different temperature trends and accompanying Arrhenius fits to low and high temperature regimes (dashed red lines), with the same thermal activation as (F) τ calculated for day 2 data. (G) Proposed band structures for electron transport at V_A = 400 mV and V_A = 0 mV.

A more complete picture of the charge transport dynamics within the device is afforded by temperature-dependent IS measurements, obtained in parallel with admittance characterization. As in Chapter 4, the frequency-dependence of the real (Z_r) and imaginary (Z_i) parts of the device impedance can be simultaneously analyzed in a complex-plane (Nyquist) plot. Figure 5.6A exhibits an example complex-plane plot of our PV device device obtained on day 2 at T = 240

K. The remainder of the day 2 data is displayed in Appendix C.6, while those for day 1 are featured in Appendix C.5. Though the impedance data is characterized by single RC arc, the broad distribution of charge relaxation times resulting from the spatial and energetic disorder in PbS QD solids results in deviations from the ideal semicircle expected for a single, dominant charge relaxation process. The arc in Figure 5.6A is depressed so that the real axis is larger than the imaginary axis, characteristic of a distribution of time constants that contribute to charge relaxation.[20, 119, 118, 56] As in Chapter 4, we analyze the impedance data with an equivalent circuit that uses a CPE Q in parallel with a charge transfer resistance R_{ct}. These parallel elements are in series with a series resistor R_s. The total impedance described by the parallel RQ circuit is then:

$$Z(\omega) = R_S + \frac{R_{ct}}{1 + (i\omega)^{\alpha} Q R_{ct}} \tag{5.2.1}$$

where Q is the CPE coefficient and α is parameterizes how close to ideal the CPE is. For $\alpha = 1$, $Q \to C$, and the recombination process can be characterized by a single time constant.[20] The values of these circuit elements can be determined by a complex, non-linear least squares regression of both Z_r and Z_i to the impedance given by equation (5.2.1). An example of the fits is provided in Figure 5.6A, yielding $R_{ct} = 7.5$ kΩcm^{-2}, $Q = 1.1 \times 10^{-4}$ s$^{\alpha}$kΩcm^{-2}, $\alpha = 0.93$, and $R_s = 0.05$ kΩcm^{-2}. As in Chapter 4, the calculated values of Q and α allow us to estimate the effective capacitance $C_{eff} = Q(\frac{1}{R_{ct}} + \frac{1}{R_s})^{\frac{\alpha}{1-\alpha}}$. The characteristic time constant τ of the recombination process that gives rise to the impedance arc can thus be determined as:[56, 20]

$$\tau = (Q R_{ct})^{\frac{1}{\alpha}}. \tag{5.2.2}$$

The fit in Figure 5.5A corresponds to $\tau = 5.1 \times 10^{-4}$ s. The highlighted diamond indicates the resonant frequency $\omega_0 = \frac{1}{\tau}$. By repeating this process for impedance data obtained at various temperatures, the activation energy of the recombination process corresponding to the measured impedance arc can be obtained.

Figures 5.6B,C exhibits the temperature-dependence of R_{ct} and C_{eff} deduced from equivalent circuit fits to impedance data measured on day 1 from $T = 210 - 330$ K. The Nyquist plots and accompanying fits are available in Appendix C.6. Both plots show a large discontinuity at $T = 270$ K, consistent with the discontinuous jump exhibited by the day 1 frequency-dependent hopping conductance in Appendix C.4 and by the day 2 data in Figure 5.5A. In Figure 5.6C, C_{eff} exhibits significant thermal activation above $T = 270$ K but an unphysical, negative activation energy below this temperature, consistent with thermal activation of the carrier density at high temperatures. Arrhenius fits to these two regimes are also provided in Figures 5.6B, C. The day 1 activation energy of R_{ct} at low temperature given by the Arrhenius fit in Figure 5.6A is $E_A = 0.3 \pm 0.03$ eV, while in the high temperature regime, $E_A = 0.22 \pm 0.03$ eV. We note that the high temperature E_A is consistent with the activation of the day 1, high temperature conductance data presented in Figure 5.5C. At these temperatures, the activation energy of the carrier density in C_{eff} is calculated to be $E_A = 0.1 \pm 0.02$ eV. These two thermal activation energies combine to give a total high temperature thermal activation energy $E_A = 0.29 \pm 0.01$ eV for the day 1 time constant τ in Figure 5.6D. At low temperatures, the activation energy of τ is dominated by R_{ct} such that $E_A = 0.25 \pm 0.04$ eV. These figures are in excellent agreement with the activation energies of the DC hopping conductivity $\sigma'(\omega)$ once the assumed carrier activation for electrons is added. The day 1 data therefore also suggest the presence of 2 distinct barriers to dark electron transport in our PbS QD device.

The day 2 data, featured in Figure 5.6E,F similarly indicate 2 energy barriers to electron transport. At low temperature, the day2 data exhibit a thermal activation of both τ and R_{ct} at low temperature of $E_A = 0.3 \pm 0.03$ eV, consistent with the activation energy of the day 2 low temperature DC hopping conductance. At higher temperatures, the fit in Figure 5.5B gives $E_A = 0.23 \pm 0.04$ for τ. Again, the obtained activation energy is in agreement with the high temperature DC hopping activation. The observation that E_A for τ matches E_A for R_{ct} suggests that the activation energy of the carrier density in the device (reflected in the temperature-dependence of C_{eff} in Appendix C.7) does not play a role in the charge dynamics probed in forward biased IS and AC conductance on day 2.

The source of the discontinuities in the data is hinted at in the Nyquist plot of the day 2 impedance response at $T = 290$ K, provided in Appendix C.8. The data exhibits a high frequency feature in which Z_i increases nearly linearly with Z_r, distorting the recombination arc. Linear high frequency features in Nyquist plots are characteristic the Warburg impedance, which corresponds to mass transport processes.[119] Warburg impedances have also been used to model electron diffusion in IS studies of semiconductor materials.[9] Recently, heuristic extensions of the Warbug impedance have been formulated to describe anomalous diffusion processes in which carriers hop through structurally disordered media.[11] These carrier diffusion models rely on CPEs to describe the ensemble average transport time that arises as a charge carrier is trapped and subsequently released through a distribution of localized sites. As a result, we hypothesize that the discontinuity in the impedance response above $T = 290$ K on day 2 (and $T = 270K$ on day 1) reflects a transition between the low and high temperature CPEs associate with recombination and transport, respectively.

The physical processes that correspond to the two distinct regimes of charge dynamics in Figure 5.6 are suggested by the values of τ that characterize charge relaxation process at low and high temperatures. In Figures 5.6D,F, the value of the τ ranges from $\sim 10^{-2}$ s at $T = 210$ K at low temperatures to $\sim 8 \times 10^{-5}$ in the high temperature regime. The observed low value time constant matches well with measurements of the dark carrier lifetime in ZnO films annealed in the presence of O_2, which has been estimated to be $\sim 1 - 2 \times 10^4$ s at room temperature *via* XPS studies of ZnO surfaces[134] and ZnO/PbS QD interface.[135] Open circuit voltage decay measurements on PbS QD/ZnO heterojunction PV devices have also observed time constants $\sim 10^{-4}$ s.[34] We note that this figure also matches well with the electron relaxation lifetime analyzed in forward biased impedance data in Chapter 4 which we hypothesized resulted from interfacial ZnO/PbS-MPA states. Based on the similarity between the observed activation energy of τ ($E_A \approx 0.3$ eV) and the activation energy of low temperature DC hopping transport ($E_A \approx 0.27$ eV), we hypothesize that electron dynamics at the interface may present the largest hopping barrier to electrons injected from the ZnO into the PbS QD layer.

At higher temperatures, by contrast, Figures 5.6D,F show that τ extends from $\sim 8 \times 10^{-5}$ s at $T = 280$ K to 7×10^{-6} s at $T = 330$ K on day 1, and $\sim 1.5 \times 10^{-5}$ s at $T = 300K$ down to 7×10^{-6} s at $T = 330$ K on day 2. The observed τ at high temperature is characteristic of electron transport lifetimes in PbS-TBAI QD solids, which has been reported to be $\sim 2 \times 10^{-6}$ s *via* IS[133] and transient photovoltage measurements.[28, 73] As a result, we hypothesize that the carrier lifetime at high temperature likely contains significant contributions from charge dynamics in the PbS-TBAI QD film. The thermal activation of these charge dynamics seems to dominate DC hopping transport at elevated temperatures in Figure 5.5A.

These conclusions are summarized in Figure 5.6G, which shows the proposed band diagram at an applied bias $V_A = 400$ mV. The splitting of the electron and hole quasi-Fermi levels implies that defects at both the PbS-TBAI/ZnO and PbS-TBAI/PbS-MPA both present barriers to charge transport, which give rise to the arcs measured in IS. Since the thermal activation energy of the electron density at high temperatures is measured to be ~ 0.1 eV via IS measurements at 400 mV on day 1, we infer that at zero bias, the thermal activation of this density is $\sim 0.1 + 0.4 \approx 0.14$ V. We note that a carrier thermal activation of ~ 0.14 eV at zero bias implies that any band tail in the PbS-TBAI QD film extends to ~ 0.24 eV, in excellent agreement with the PL interrogation of TBAI-capped QD solids.[28]

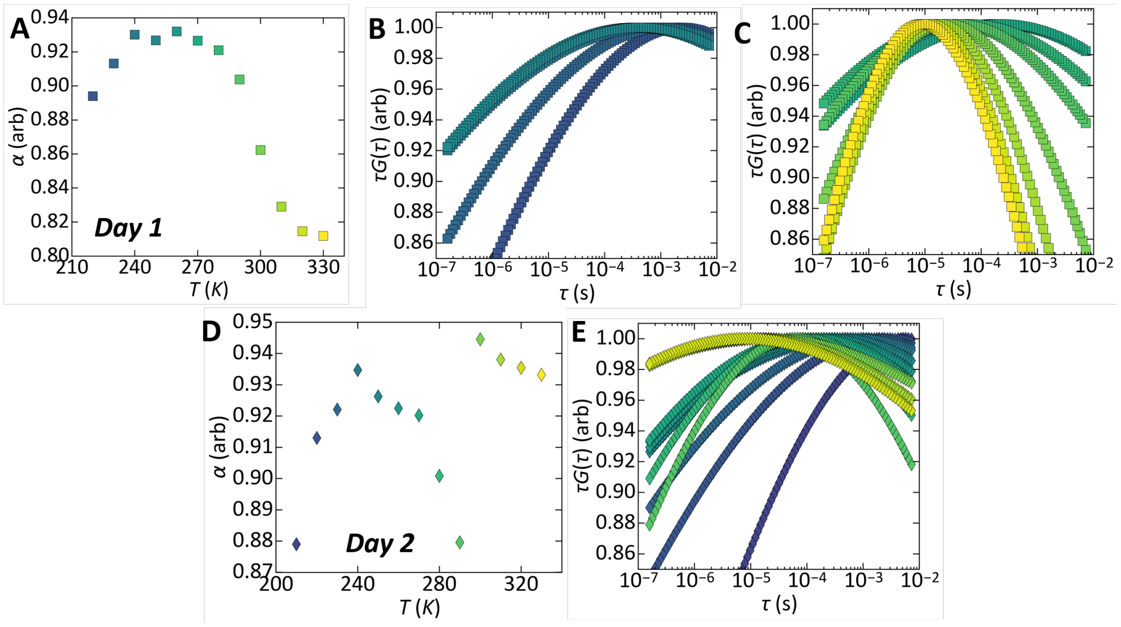

Figure 5.7: (A) α parameter extracted from IS fits on day 2 exhibiting steady decrease at high temperature. (B) Distribution of carrier lifetimes $\tau G(\tau)$ in low temperature regime on day 1. (C) Distribution of carrier lifetimes $\tau G(\tau)$ in high temperature regime on day 1. (D) α parameter extracted from IS fits on day 2 exhibiting discontinuous jump between low and high temperature regimes. (E) Distribution of carrier lifetimes $\tau G(\tau)$ on day 2

Further information about the charge hopping dynamics interrogated by forward biased IS measurements can be obtained by analysis of the temperature dependence of the α parameter extracted from the fits in Figure 5.6, displayed in Figures 5.7A,D. On day 1, α is observed to increase slightly with temperature until $T = 270K$, whereupon it drops about 10% as the high temperature CPE begins to contribute to the impedance of the device. On day 2 (Figure 5.7D), α increases from 0.88 at T = 210 K to 0.94 at T = 240 K, indicating that as temperature increases, the charge dynamics probed in the IS measurement can described by a single relaxation process.[119, 135] As temperature continues to increase to T = 290 K, the competition between the high and low temperature regimes causes α to decrease to 0.88, after which it discontinuously rebounds to 0.95 as the high temperature relaxation process begins to dominate lower temperature dynamics.

As in Chapter 4, the extracted α parameter can be used to estimate the log-normal distribution of time constants $G(\tau)$ assumed to give rise to CPE behavior. For a characteristic time constant τ_0, $G(\tau)$ may be written:[20, 119]

$$\tau G(\tau) = \frac{2\sin(\alpha\pi)}{\exp[(1-\alpha)\frac{\tau}{\tau_0}] + \exp[-(1-\alpha)\frac{\tau}{\tau_0}] - 2\cos(\alpha\pi)} \tag{5.2.3}$$

The distributions on day 1 are plotted in Figure 5.7B,C for the range of τ accessed in our experiment. As temperature increases, the peak of the distribution shifts continuously to lower temperatures, and initially, the short-timescale tail of the distribution is observed to increase in Figure 5.7B. For $T > 270$ K, the width of $\tau G(\tau)$ decreases around $\tau = 10^{-5}$ s, as observed in Figure 5.7C. The observed decrease in the distribution width is consistent with the decreasing contribution of the ZnO/PbS-TBAI interface we hypothesize dominates the charge dynamics probed at these temperatures. The same low temperature increase in the low-timescale tail of $\tau G(\tau)$ is observed in the day 2 data presented in Figure 5.7E. At $T = 270$ a similar decrease in the width of the distribution occurs, followed by a discontinuous broadening of $\tau G(\tau)$ for $T > 290$ K. The peak of this distribution is $\sim 5 \times 10^{-6}$ s but with a large, long-timescale tail extending out to 10^{-2} s. Based on these data, we speculate that on day 2, the highest temperature time constant distributions contain significant contributions from both the PbS-TBAI QD layer, expected to have lower carrier transport times, and the ZnO/PbS-TBAI interface. By contrast, the sharper high temperature distributions observed on day 1 in Figure 5.7C may be related to the clear separation of charge dynamics probed in the day 1 capacitance response in Figure 5.2A. In this scenario, contributions to the observed charge dynamics from processes with large time constants that we tentatively ascribe to the ZnO/PbS-TBAI QD interface in our preliminary analyses may dominate the electron hopping times probed in forward bias. This could explain the narrow time constant distribution in Figure 5.7C. On day 2, by contrast, the intermingling of the PbS QD and

ZnO charge responses may give rise to more facile charge transfer from ZnO band tail states into PbS band tail states, broadening the distribution at the highest temperatures in Figure 5.7E.

5.2.5 IR Illumination

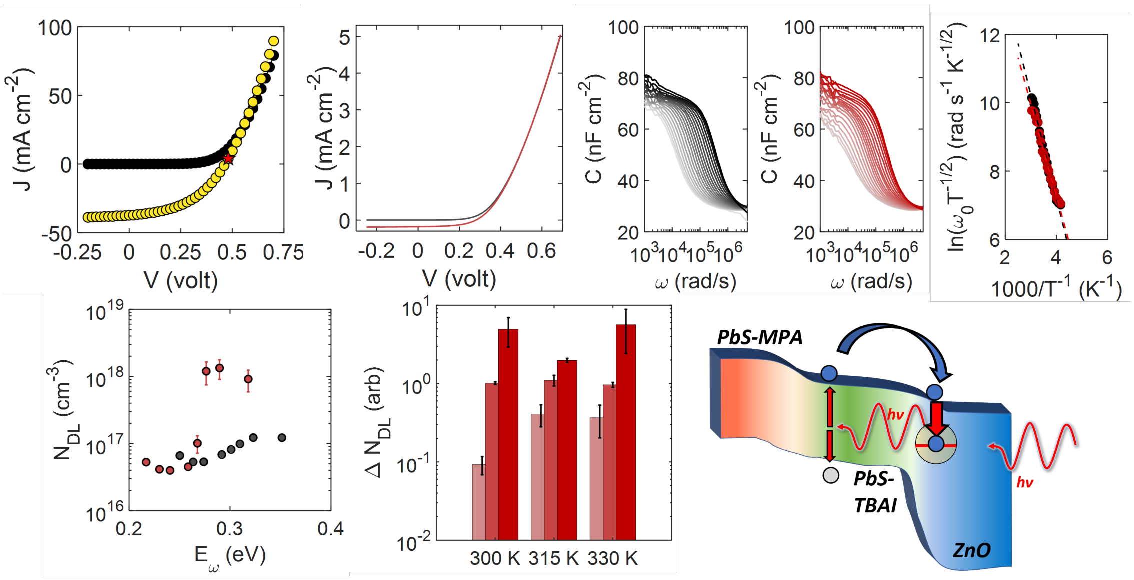

Figure 5.8: (A) JV curves obtained the dark (black) and under AM 1.5G illumination (yellow) in the glovebox immediately after fabrication, with red star indicating V_{oc}. (B) JV data obtained in the dark (black) and under IR illumination with $\lambda = 980$ nm (red) at $T = 300$ K. (C) TAS data obtained in the dark from $T = 240330$ K. (D) TAS data obtained under illumination at $\lambda = 980$ nm. (E) Arrhenius fits to dark and IR-illuminated TAS curve. (F) N_{DL} vs. E_ω in the dark (black) and under illumination (red). (G) Intensity-dependent N_{DL} at various temperatures for illumination powers of 3.8 mWcm^{-2} (i, pink), 4.8 mWcm^{-2} (ii, red), and 5.7 mWcm^{-2} (iii, deep red). (H). Proposed recombination mechanism for photogenerated charge in the PbS layers.

Figure 5.8A shows JV characteristics of the PV device 1 day after fabrication in the dark (black) and under AM 1.5 G illumination (yellow) measured in an inert N_2 glovebox. The dark and illuminated currents are higher than the PbS-MPA/ZnO PV device discussed in Chapter 4, and the PbS-TBAI device exhibits a slightly larger PCE of 8.7% than the device analyzed in Chapter 4. However, the PbS-TBAI device also exhibits a slightly lower $V_{oc} = 0.47$ V compared to $V_{oc} = 0.57$ for the PbS-MPA PV device. Lower V_{oc} parameters are commonly observed in halide-treated PbS QD PV devices compared to their organic-capped counterparts [62, 27, 143]. Though the precise reason for this discrepancy is not well understood, these V_{oc} losses have been heuristically linked to recombination within pathways at the interface [37, 58, 73, 92, 93] and in the bulk of the PbS QD layers.[28]

To clarify the role the distinct charge responses observed *via* IS play in recombination of photogenerated charge, we perform TAS and DLCP experiments on a PbS-EDT/PbS-TBAI/ZnO QD PV device in dark and under illumination. The device was fabricated *via* spincoating methods similar to those used for the PbS-MPA/PbS-TBAI/ZnO device, and measured in the same vacuum sealed probestation. Illumination is provided *via* a 980 nm laser connected to the probestation with an optical fiber. The wavelength of the laser illumination is chosen to match the ~ 1.2 eV bandgap of our PbS QD film. As depicted in Figure 5.1, light enters through the ZnO layer, which exhibits an absorption onset $\sim 350 - 360$ nm according to the spectra presented in Figure 4.3 in Chapter 4. Due to the large ZnO bandgap, we expect that the 980 nm illumination passes through the ZnO layer and is absorbed by the PbS-TBAI QD layer.[27] The illuminated TAS and DLCP measurements are performed in parallel with the dark characterization, such that at each temperature point, dark data is collected and, following a 2 minute waiting period, the illuminated data is collected. After a subsequent 20 minute waiting period, the temperature is increased and the measurement cycle is repeated.

The JV curves of the PbS-EDT/PbS-TBAI/ZnO QD device in the dark (grey) and under 980 nm illumination with a power density of $I = 3.8$ mWcm^{-2} is displayed in Figure 5.8B. Though the current levels are much lower than the PbS-MPA/PbS-TBAI/ZnO device in Figure 5.8A, a weak photocurrent is observed in the cell, indicating excitation of photogenerated carriers within the PV device. Figure 5.8C shows the capacitance-frequency spectra obtained in the dark from

$T = 240 - 330K$, while Figure 5.8D exhibits the illuminated C vs. ω characteristics. The spectra show little observable difference in the inflection frequency ω_0 especially at low temperature. However, the rate of decay of the capacitance-frequency curves at low frequencies is smaller under illumination than in the dark, consistent with an illumination-induced occupancy of a broader range of states which results in a less stark cutoff frequency. This effect is most pronounced at lower temperatures. At higher temperatures, ω_0 decreases slightly under illumination (Appendix C.9), implying that the illuminated charge response at high temperature may be linked to charge occupancy of less mobile charge states due to a low conductivity (assuming ω_0 results from limited carrier conductivity) or a larger energetic distance from the transport band (assuming ω_0 is due to trap emision). Assuming the latter case, we obtain the activation energy of ω_0 in Figure 5.8E by fittingln$(\omega_0 T^{-1/2})$ vs. $\frac{1}{T}$ for both the illuminated and dark data to Arrhenius fits. The fits yield a dark activation energy $E_{T,d} = 0.27 \pm 0.02$ eV and a slightly lower illuminated activation energy $E_{T,i} = 0.23 \pm 0.02$ eV, with respective attempt frequencies of $\nu_{0,d} = (8 \pm 1) \times 10^8$ HzK$^{-1/2}$ and $\nu_{0,i} = (2.2 \pm 0.4) \times 10^8$ HzK$^{-1/2}$. Under the assumption that ω_0 indicates charge emission from a state at E_T, we hypothesize that the decrease in activation energy may correspond to an increase in the quasi-Fermi level under illumination.

The illumination-dependent carrier densities exhibited in Figure 5.8F obtained in parallel DLCP measurements shed more light on the charge carrier dynamics under illumination. The N_{DL} values presented are obtained at test frequencies of 6.28×10^3, $(1.88, 3.14, 4.40, 6.28) \times 10^4$, and $(1.26, 1.88, 3.14) \times 10^5$ rad/s at 300 K. The energy axis E_ω is calculated at $T = 300$ K using these frequency values and equation (4.3.2). In the dark, the carrier density detected at high frequency corresponds to $E_\omega = 0.25$ eV. At this energy, $N_{DL} \approx 6 \times 10^{16}$ cm^{-3}, in good agreement with previous estimates of the dark carrier density in PbS-TBAI QD solids [152] and the dark DLCP measurements on the day 2 PbS-MPA/PbS-TBAI/ZnO PV device measured in 5.2.2. The carrier density in more states which respond at high frequencies is slightly lower under illumination, at $N_{DL} \approx 4 \times 10^{16}$cm^{-3} than in the dark. Interestingly, the slight decrease in N_{DL} in these high frequency-states states under illumination is compensated by a strong increase in N_{DL} observed at lower frequencies. At $E_\omega \approx 0.28 - 0.32$ eV, the illuminated N_{DL} exhibits a large increase to $\sim 10^{18}$ cm^{-3}, compared to a dark $N_{DL} \approx 10^{17}$ cm^{-3} at $E_\omega \approx 0.29 - 0.36$. The energy range at which the increases in N_{DL} under illumination are observed match the energy of the low temperature state characterized by $\tau \sim 10^{-4}$ s, which we tentatively ascribed to the ZnO/PbS-TBAI interface. We hypothesize that this interfacial defect state dominates recombination of photogenerated electrons within the PbS QD layer, in agreement with x-ray photoelectron spectroscopy studies of ZnO-PbS QD heterointerfaces.[135] These results are also consistent with device-level experiments that reduce the ZnO band-tail density *via* inclusion of Mg[58], Cl[25], and Al/Cl [24] dopants, resulting in increases in device performance. As depicted in Figure 5.8G, this phenomena scales with illumination intensity, indicating that the increased carrier density in these states is a direct result of laser illumination.

These results suggest photoexcited electrons within the PbS layer are transported to the ZnO interface with a transit time quicker than the resolution of our frequency-dependent experiment. We hypothesize that charge dynamics are dominated by an interfacial defect state, as depicted in Figure 5.8H. The carrier transport lifetime $\tau \sim 10^{-6}$ s measured in 5.2.4 is the limit of the time resolution of our frequency-dependent measurements; as a result, we note that illumination-induced increases in states with shorter lifetimes are not observable in our measurement. We therefore cannot definitively rule out an illumination-induced increase in the occupation of transport states within the bulk of the PbS-TBAI QD layer. Instead, we can only comment that illumination increases the carrier density in the longer-lifetime state.

5.2.6 Conclusion

We have systematically probed the charge dynamics in a PbS-MPA/PbS-TBAI/ZnO QD PV device. TAS measurements obtained over two days allow us to discern two predominant regimes of charge dynamics–one that we hypothesize may be related to charge dynamics in PbS-TBAI, and one which likely corresponds to charge dynamics within the PbS-TBAI and ZnO layers. DLCP measurements suggest that the differences in carrier profile and density occur as the PbS-TBAI film becomes more intrinsic upon oxidation. Charge dynamics in the PbS-TBAI QD layer then become physically indistinct from the ZnO depletion region. Frequency-dependent AC conductance measurements and detailed IS analysis also reflect the existence of two different energy barriers to transport. The characteristic time scales deduced in the IS analysis are consistent charge dynamics at the ZnO/PbS QD interface and charge transport within the PbS-TBAI QD layer. Finally, preliminary analysis of illumination-dependent TAS and DLCP suggest that the former state acts dominates photogenerated charge dynamics. We note that these results are consistent with the dynamics probed at the ZnO/PbS-MPA interface discussed in Chapter 4 and with recent efforts to optimize the ZnO layer in PbS QD PV devices.[58, 25, 24] Our results suggest that the popular PbS-EDT(PbS-MPA)/PbS-TBAI/ZnO PV device architecture does indeed behave as a p-i-n structure after sufficient oxygen doping, as originally designed.[27] However, though extensive effort has gone into optimization of the the PbS QD layers, defects with the ZnO layer may still dictate cell performance.

5.2.7 Materials

Oleic acid (OA, 90%), 1-octadecene (ODE, 90%), lead oxide (PbO, 99.999%), cadmium chloride ($CdCl_2$, 99.99%), oleylamine (70%), 1,2-Ethanedithiol (EDT, ¿98%), 3-mercaptopropionic acid (MPA, 99%), Tetrabutylammonium iodide (TBAI, 98%), zinc acetate dehydrate (98%), (3-mercaptopropyl)- trimethoxysilane (MPTS, 95%), anhydrous hexane, anhydrous 2- propanol, anhydrous methanol, anhydrous toluene, anhydrous acetonitrile and anhydrous acetone are purchased from Sigma-Aldrich. Bis(trimethylsilyl) sulfide ((TMS)2S, 95%) is purchased from Acros. Tetradecylphosphonic acid (TDPA, 98%) and molybdenum oxide (MoO3, 99.9995%) are purchased from Alfa Aesar. Potassium hydroxide (KOH, 85%) is purchased from Fisher.

5.2.8 QD Synthesis

PbS QDs are synthesized as reported previously[163]. In brief, a mixture of 0.47 g of PbO, 23 mL of ODE, and 2 mL of OA is degassed at 120 C for 2 h under vacuum. Then 5 mL of 21 μL (TMS)2S/1 mL ODE solution is injected at 100 C with N_2 flowing. The heat is turned off immediately after injection, and when the reaction solution is cooled to 70 C, a pre-dried $CdCl_2$ solution (0.3 g of $CdCl_2$ and 0.033 g of TDPA in 5 mL of oleylamine) is added. After 5 min, the reaction is further quenched in a water bath. The product is transferred into the glovebox and purified by washing four times with acetone, 2-propanol, and methanol and finally re-dispersed in octane/ hexane (4:1) at 50 mg/mL.

5.2.9 Device fabrication

All the fabrication steps are carried out in air unless otherwise noted. Prepatterned ITO/glass substrates (Thin Film Devices) are cleaned by sonication in 5% Hellmanex in DI water, pure DI water, and ethanol consecutively, followed by UVozone treatment for 30 min. The cleaned substrates are soaked in MPTS (5% in toluene) for 10 h before use. The ZnO NPs are synthesized according to a literature recipe [8]. The ZnO NP film is fabricated by spin casting ZnO NPs (100 mg/mL) at 1500 r.p.m and annealed in air at 250 C for 20 min. On top of ZnO NP layer, PbS QD solution (50 mg/mL) is spin cast at 3000 r.p.m for 30 s, followed by TBAI (10mg/mL in methanol) solid-state ligand exchange for 30 s or 3 s, respectively, with three rounds of methanol washing. 10 layers of PbS QD films are deposited by sequential deposition. For MPA capped PbS QD layers, a 1% vol MPA in methanol solution is used followed by three methanol rinsing steps. For EDT capped PbS QD layers, EDT in acetonitrile (0.02 M) are used followed by 30 s washing in acetonitrile. Two layers of MPA- (or EDT-) capped PbS QDs are deposited. To finish the device, 12 nm of MoO3 and 65 nm of Au are thermally evaporated on the PbS QD film through a shadow mask inside a glovebox, which defines the active area of the device to be 2 mm by 2 mm.

5.2.10 Room Temperature Characterization

Dark and illuminated JV data are measured using a Keithley 2420 sourcemeter. Current is recorded by sweeping the DC applied voltage from -200 to 700 mV in 20 mV steps. The PV device is illuminated using a solar simulator (Oriel instruments model 96000, Newport Co.). The simulated AM 1.5 light is brought into the glovebox through a liquid light guide feed-through. The illumination intensity at the device is calibrated to be 1 Sun, i.e., 100 mW cm^{-2}, by a Si reference cell and meter from Newport (model 91150). PV devices are illuminated through an aperture of 1.6 mm x 1.6 mm in size, smaller than the active device area.

5.2.11 Variable Temperature Characterization

Variable temperature TAS, DLCP, AC conductance, and JV measurements are performed within a LakeShore Cryotronics vacuum probestation with a liquid-N2 cooled sample stage. PbS PV devices are measured from $T = 190$ to 310 K at 10 K intervals. Two probe admittance and JV measurements are carried using a Hewlett Packard HP4192A impedance analyzer and an Agilent 4156C parameter analyzer, respectively. A computer-controlled relay switch is used to toggle between AC impedance measurements and DC JV characterization at each temperature or time-step as depicted in the schematic in Figure 4.1A. For the temperature-dependent measurements, the device is left under vacuum in the dark at room temperature for 1 h, cooled to 180 K, and allowed to thermally equilibrate for 1 h before measurements are started. For TAS measurements, the capacitance response of the PV device to a 100 mV AC perturbation is collected for frequencies ranging from 20 Hz1.3 MHz at a 0 mV DC bias. The same DC and AC biases are applied for AC conductivity measurements. IS measurements are obtained at the same frequency range and AC bias at an applied DC forward bias $V_A = 400$ mV. DLCP measurements are performed immediately afterward using the same setup, with AC signals at frequencies of 1 kHz, 10 kHz, and 100 kHz, and maximum applied biases $V_{max} = V_{RMS} + V_{DC}$ from -50 mV to -300 mV in 50 mV steps.

To obtain the non-linear capacitance response, V_{RMS} was varied from 10 mV - 300 mV, and V_{DC} is automatically modulated to keep V_{max} constant using custom LabView software.

Appendix A

A.1 FET Measurements

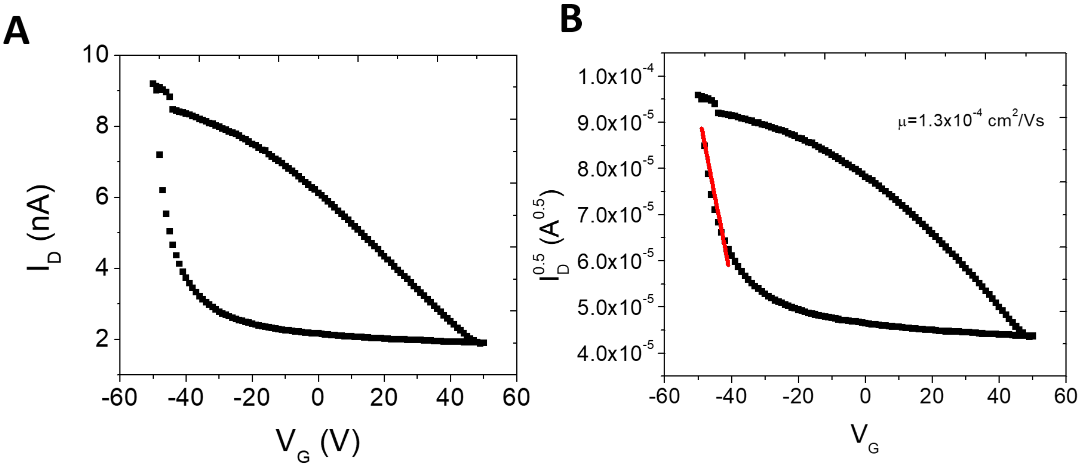

Figure A.1: FET measurements on 3 nm PbS QDs capped with EDT made in the saturation regime. Linear fits to (B) allow us to estimate μ.

Figure A.1 exhibits gated FET measurements on devices made of 3 nm PbS-EDT QDs. Figure A.1A shows the saturation regime response measured at $V_{DS} = 50$ V and. From the fit in Figure A.1, we estimate that $\mu \approx 1.3 \times 10^{-4}$ cm^2(Vs)$^{-1}$.

A.2 Capacitance of PbS-EDT/Au Dielectric Stack

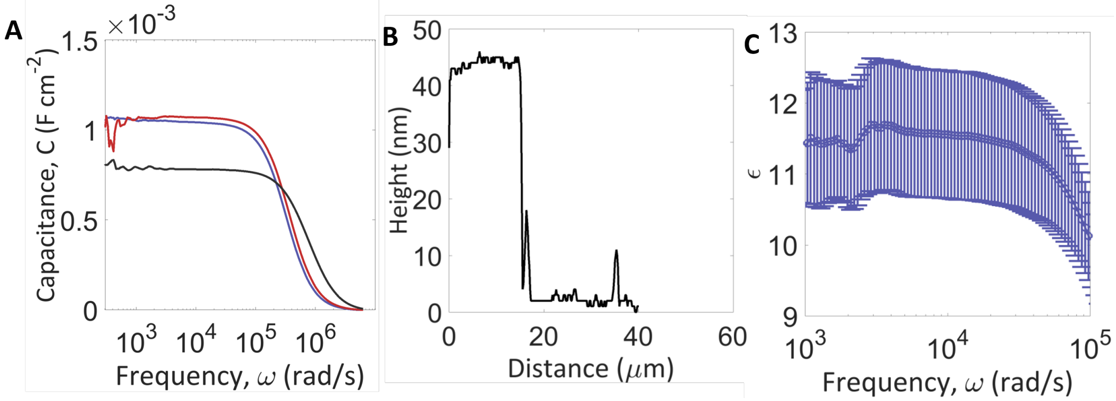

Figure A.2: (A) Capacitance-frequency curves for PbS-EDT dielectric stack with an Au top contact (B) AFM height re-trace of dielectric stack (C) Dielectric constant ε_S as a function of frequency.

Figure A.2 shows the the capacitance of a dielectric stack of a PbS-EDT QD film deposited on a silicon wafer with 250nm SiO_2. To minimize the effect of fringing fields, the SiO_2 was patterned into squares of 8, 6.25, and 4 mm^2 before deposition of the QDs. Four layers of PbS were then deposited onto the substrate via spin-coating following the same exchange procedure followed for the devices, which were subsequently capped with 50mm of thermally evaporated Au for a top contact.

The frequency-dependent capacitance of the resulting films was measured using the same vacuum set-up and HP-4192A impedance analyzer used in the TAS and DLCP measurements, and is displayed in Figure A.2A. Like the capacitance data in Chapter 3, the dielectric stacks studied here show nearly constant capacitance values from $10^2 - 10^5$ rad/s, and exhibit a steep drop-off at afterward. Note that the drop in capacitance occurs at $\omega_0 \approx 6 \times 10^5$ rad/s for 2 measurements, and a at a slightly higher frequency $\omega_0 \approx 1 \times 10^6$ rad/s for the third measurement. The close agreement between ω_0 observed in these Au-PbS junctions, in which no depletion region is expected, and ω_0 observed in the PbS-Al Schottky junction studied in the Chapter 3 implies that

ω_0 is not due to charge dynamics in the depletion region, consistent with the interpretation of ω_0 as the dielectric relaxation frequency ω_D.

We may also use this data to precisely determine the value of ε_S for the PbS-EDT QD film over the operating frequency of the TAS and DLCP measurements. Since we expect contributions of both the SiO_2 substrate and the QD films, we can write the total measured capacitance as a sum of these distinct series capacitances [48]:

$$\frac{1}{C_{tot}} = \frac{1}{C_{sub}} + \frac{1}{C_{QD}} \tag{A.2.1}$$

where C_{tot} is the total measured capacitance, C_{sub} is the capacitance of the substrate, and C_{QD} is the capacitance of the QD film. Since the simple geometry used here is a parallel plate capacitor, the resulting QD film dielectric can be solved for according to:

$$C_{QD} = \frac{\varepsilon_0 \varepsilon_S A}{D} \tag{A.2.2}$$

where ε_0 is the vacuum permittivity, ε_S is the static permittivity of the QD film, A is the device area, and D represents the total thickness of the film.

The film thickness D of the dielectric stacks used in this analysis was characterized by atomic force microscopy (AFM), the results of which are shown in Figure A.2B. The total film height measured was 44nm for 3 layers of PbS-EDT.

Using this film thickness, the QD film permittivities ε_S were then determined and are displayed in Figure AA.2C. The resulting dielectric was calculated to be $\varepsilon_S = 11.5 \pm 0.9$. These results match well literature reports [16].

The same technique is used in Appendices 2 and 3.

A.3 AC Conductance

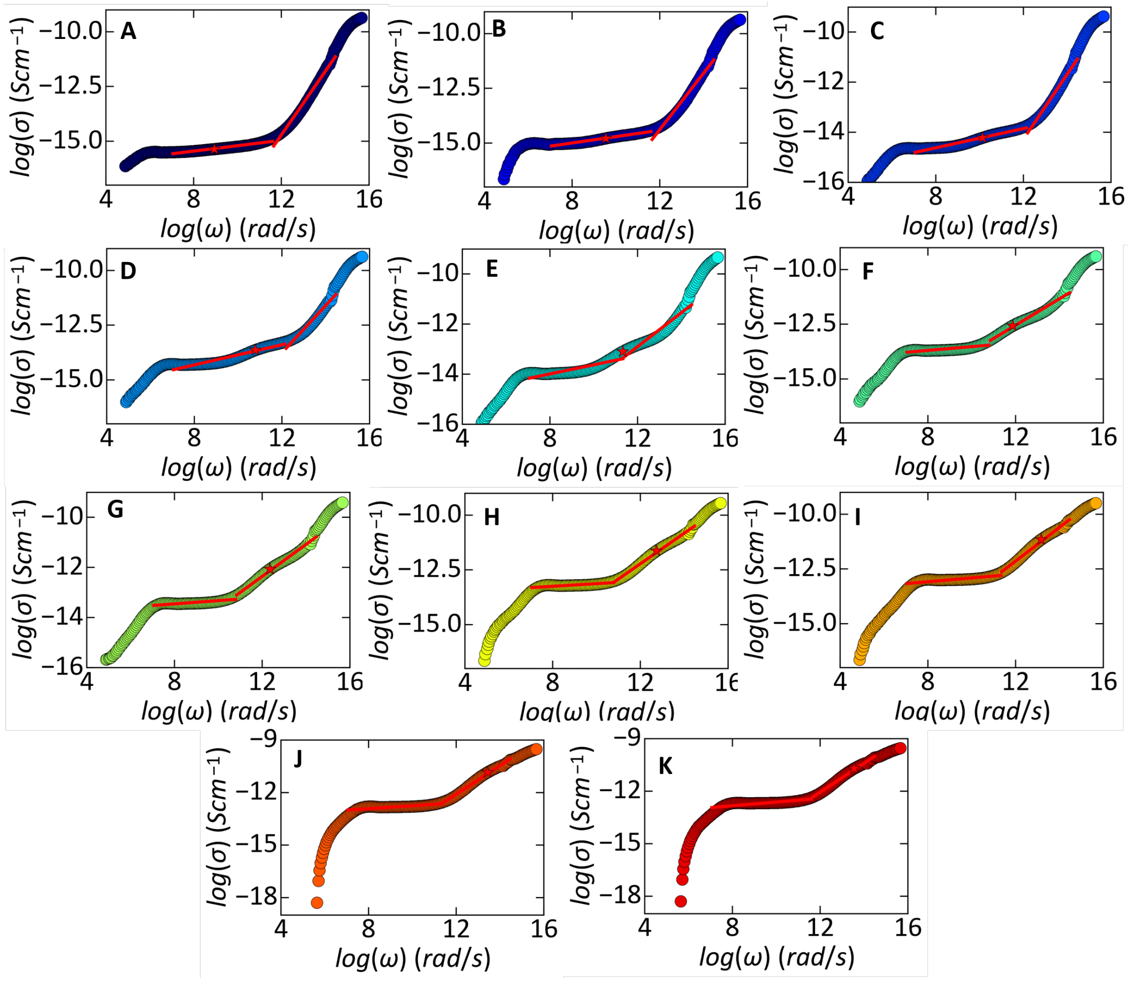

Figure A.3: Fits to $\sigma(\omega)$ in low and high ω regimes at (A) $T = 190$ K, (B) $T = 200$ K, (C) $T = 210$ K, (D) $T = 220$ K, (E) $T = 230$ K, (F) $T = 240$ K, (G) $T = 250$ K, (H) $T = 260$ K, (I) $T = 270$ K, (J) $T = 280$ K, and (K) $T = 290$ K. Fits to high $\ln(\omega)$ give s. Red stars indicate ω_D.

Fits of the $\sigma'(\omega)$ data in Figure 3A of Chapter 3 to equation (1.4.14) at $\omega > \omega_m$ are provided in Figure A.3. The fits yield temperature dependent s values displayed in Figure AA.3. At temperatures below $T = 220$ K, $s > 1$ which is prohibited by the RFB model. However, as observed in Figure 3C of the Chapter 3, high frequency $\sigma'(\omega)$ at this temperature range exhibits little thermal activation, likely indicating that charge hopping between adjacent QDs can no longer occur in this regime. We therefore expect the dominant charge mechanism at these temperatures and frequencies to be significantly enhanced by charge dynamics within a single QD, which may be due to charge motion in extended states within the individual QD bands and not subject to the RFEB model.

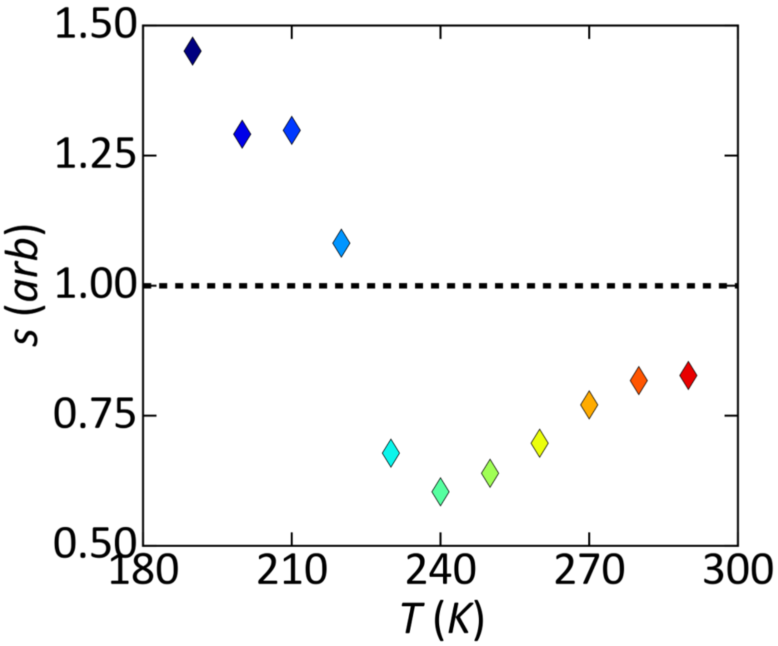

Figure A.4: (A) s vs. T extracted from fits to high frequency regions of $\sigma(\omega)$ in Figure 3A of Chapter 3.

Above these temperatures, $s < 1$, and for $T > 240$ K, s exhibits a steady increase and subsequent roll-off with temperature. At the highest temperatures in the measurement, $s \approx 0.7 - 0.8$, as expected from numerous reported exponents.[55] Inspection of the fits in Figure AA.4 show that the loss peak at ω_D occurs within the range of frequencies fit to equation (1.4.14). The non-linearity of the peak at ω_D can be observed to have a large effect on the fit: at lower temperatures, the feature at ω_D heavily skews the high frequency region of the fit. This effect is mitigated at higher temperatures where ω_D occurs at the end of the frequency domain of the fit. From the high temperature fits, we therefore infer that $s \approx 0.7 - 0.8$, in qualitative accordance with the RFEB model. We note here that broader ranges of applied frequency may be able to discern more quantitatively descriptive structure in $N(E)$.

A.4 DLCP Details

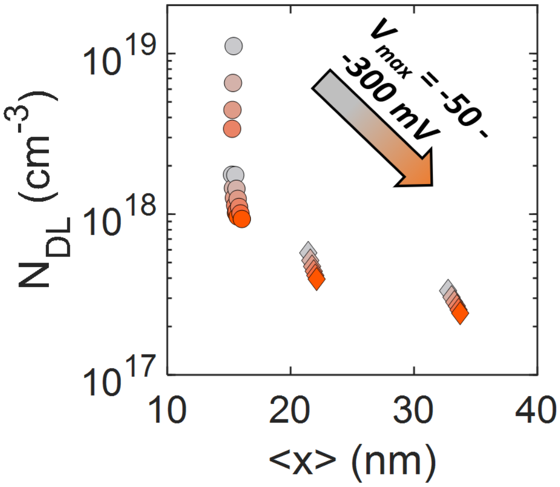

Figure A.5: N_{DL} vs. $< x >$ at $T = 280$ K at all frequencies and biases applied in the measurement

Figure AA.5 shows the distance profile of the capacitance response at $T = 280$ K for all frequencies and biases scanned in the DLCP measurement. As mentioned in Chapter 3, the spatial shift due to frequency far outpaces the change due to the applied reverse bias, indicating that application of reverse bias does little to change the profile distance of the measurement. This implies that changes in the distance profile are dominated by shifts in the Debye screening length L_0, which contains an implicit frequency dependence in the carrier density N_{DL} but no dependence on bias.

The discrepancies between the expected shifts in profile distances due to increases in reverse bias dependence and the observed shifts are more clearly seen in Figure A.6A-B, which plots the expected shift in the depletion width w (lines) given the applied reverse biases V_{max} and the observed shift in the average location of the charge density at low frequencies (circles) and high frequencies (diamonds). In these plots, $w = \sqrt{\frac{2\varepsilon_0\varepsilon(V_{bi}-V)}{qN_{DL}}}$ is calculated assuming the maximum achievable $V_{bi} = \frac{E_G}{2} = 0.6$ and the measured N_{DL} values from $T = 260 - 290$ K. At low applied bias, the low frequency DLCP data in Figure A.6A show reasonable agreement with the expected values. As bias increases, the discrepancy between the observed and expected values increases dramatically. The high frequency DLCP data in Figure A.6A show a similar trend, but larger overall differences between the observed and expected values. The increase in the difference between the data and the expected values with V_{max} is more evidence that band bending induced shifts cannot explain the spatial variation of the data. Since the low mobility of our device prevents the observation of discrete defect levels within the junction, the independence of the profiling depth on V_{max} is not surprising. We note that the lack of band bending is also consistent with the Fermi level pinning exhibited in the JV data.

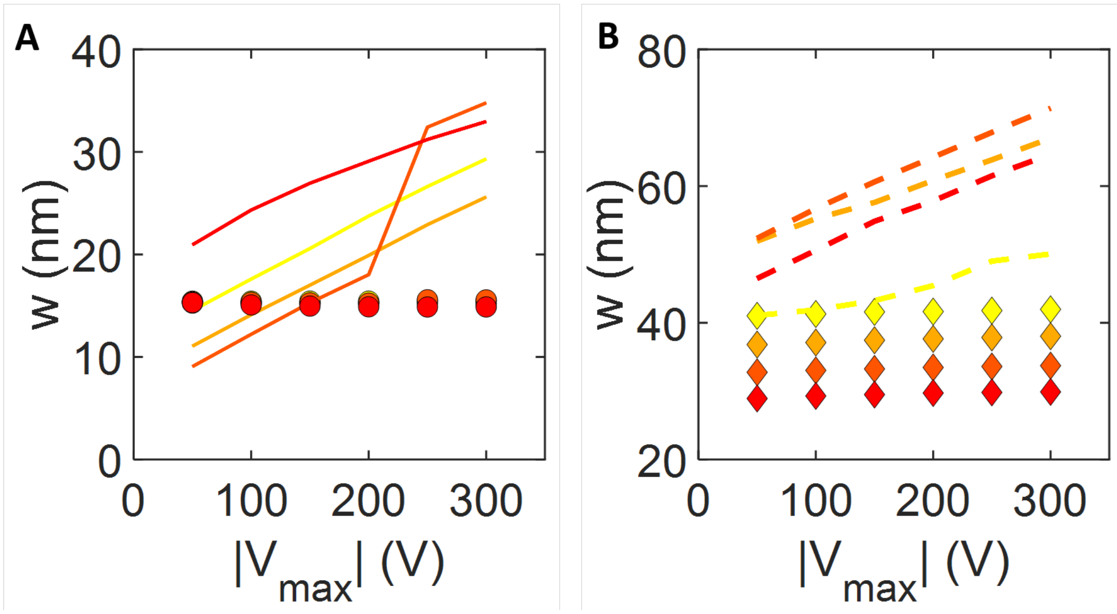

Figure A.6: (A) Depletion width calculated for the carrier densities detected at $T = 260290$ K and applied reverse biases V_{max} of the DLCP measurement at $\omega = 3.14 \times 10^3$ rad/s (lines) and spatial variation of N_{DL} observed in DLCP. (circles) (B) Depletion width calculated for carrier densities and reverse biases over the same range at $\omega = 6.28 \times 10^5$ rad/s (dashed lines) and observed spatial variation of N_{DL} (diamonds).

As described in equation (4) of Chapter 3, the upper energetic limit of a DLCP measurement is given by $E = E_F + E_\omega$, where the limiting energy E_ω is dependent on both T and ω after equation (5) of Chapter 3. We can estimate $E_\omega(T, \omega)$ by measuring $N_{DL}(T)$ at various temperatures and fixed ω and plotting an Arrhenius fit to the data. Figure A.7A-F show fits to the data obtained at each of the discrete frequencies applied in the DLCP measurement. The activation energies extracted from these data are displayed on the ordinate of Figure 3C in Chapter 3. At low ω, charge may follow the AC signal at nearly all temperatures and the resulting capacitance response gives physically meaningful data aside from an outlier at $T = 290$ K that was ignored in the fit. As frequency increases, charge cannot follow at the lowest temperatures in the measurement. As a result, the physically valid range of N_{DL} begins at higher temperatures, and the uncertainty in the extracted activation energy increases.

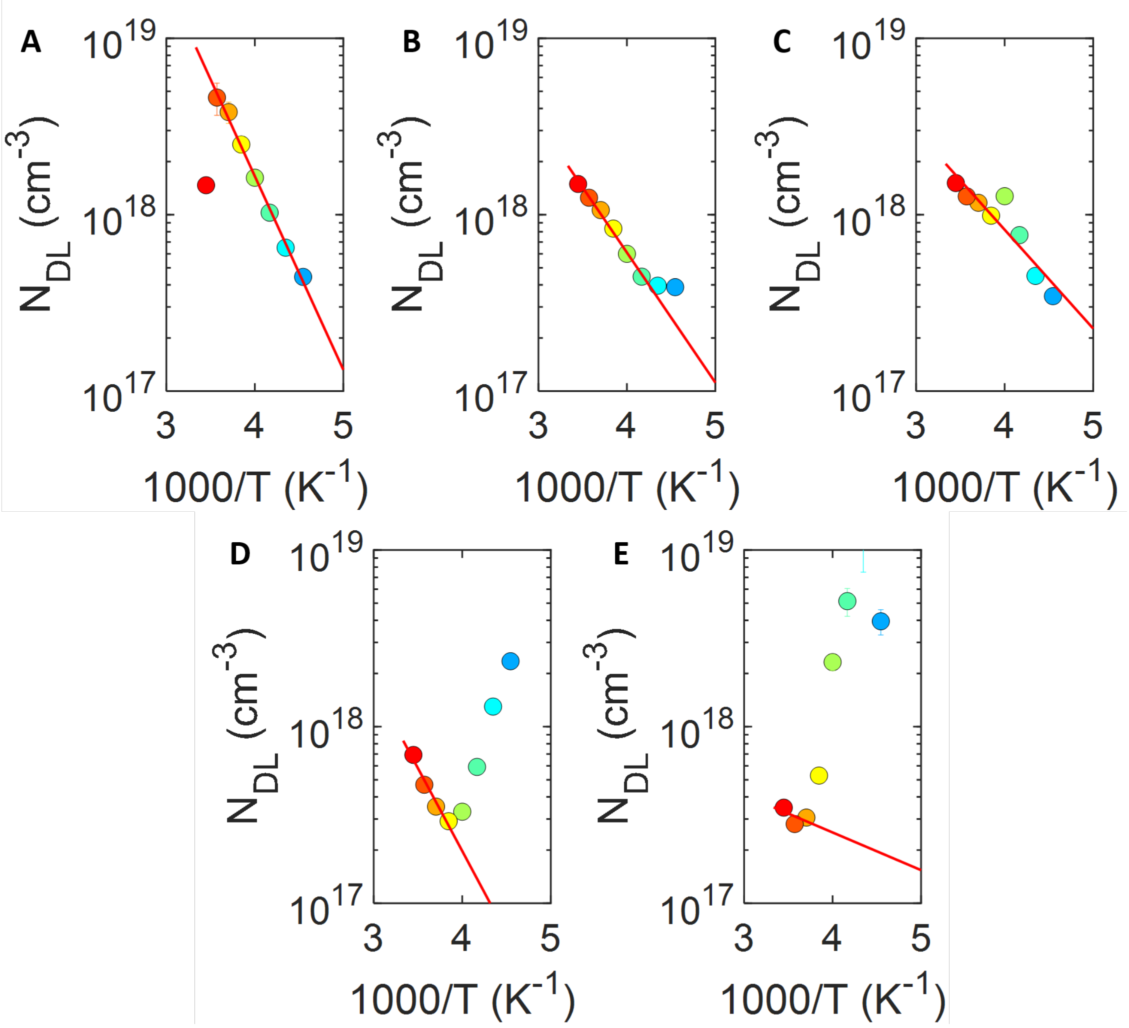

Figure A.7: Thermal activation of N_{DL} obtained at (A) $\omega = 6.28 \times 10^3$ rad/s, (B) $\omega = 3.14 \times 10^4$ rad/s, (C) $\omega = 6.28 \times 10^4$ rad/s, (D) $\omega = 3.14 \times 10^5$ rad/s, and (E) $\omega = 6.28 \times 10^5$ rad/s.

A.5 Optical Absorption Calculations

To determine the total concentration of valence band states n_V in our QD film we first calculate the volume of a single QD $v_{QD} = \frac{4}{3}\pi r_{QD}^3$ for a single QD with radius $r_{QD} = 1.5$ nm. We then calculate the total volume fraction of QDs in the QD film used in the solar cell device. We start by assuming a randomly close packing fraction $\xi \approx 0.64$ of QD-ligand complexes in the film. Since EDT molecules have an average length $r_{QD} \sim 1$ nm[48], the total fraction of the film volume occupied by PbS QDs can be approximated as $\xi' \approx \frac{v_{QD}}{v_{QD+EDT}} \times \xi$, where v_{QD+EDT} is a sphere with radius $r_{EDT} + r_{QD}$. The total number of QDs in the film can thus be calculated as $n_{QD} \approx \frac{\xi'}{v_{QD}} \approx 2.21 \times 10^{19}$ cm^{-3}. Since $n_V = 8 \times n_{QD}$,[161] we obtain $n_V \approx 1.77 \times 10^{20}$ cm^{-3}. This value was used to normalize the $N(E)$ for the absorption analysis in Figure 5 of Chapter 3.

A.6 DLCP $\rightarrow N(E)_V$ Calculation

Typically, the value of $N(E)$ for a trap distribution of states measured by capacitance measurements is obtained via a procedure outlined by Walter, et. al, wherein the total density of states is related to the junction capacitance C_{tot} by:[150]

$$C_{tot} = n_T \propto \int_{E_F}^{E_F+E_\omega} N_V(E) \frac{W}{qV_{bi}} dE \tag{A.6.1}$$

where n_T denotes the occupation of a trap distribution N_T, W is the depletion width and V_{bi} is the built-in voltage. Integration of N_T with respect to energy gives the occupation n_T that gives rise to the capacitance response. Considering the linear drop of the applied AC bias due to band bending at the junction, integration of equation (A.6.1) gives:

$$N_T(E_\omega) = \frac{V_{bi}^2}{W[qV_{bi} - (E_{F\infty} - E_\omega)]} \frac{dC}{d\omega} \omega k_B T \tag{A.6.2}$$

where $E_{F\infty}$ is the Fermi level in the bulk. Calculation of N_V *via* equation (A.6.2) therefore requires precise estimates of V_{bi}, which in turn necessitates knowledge of band bending at the junction. In bulk materials, V_{bi} can be estimated by measuring the open circuit (V_{oc}) of a solar cell device. Obtaining accurate estimates of V_{bi} in QD solar cells is considerably more difficult since high concentrations of defects limit charge collection, leading to large deficits in V_{oc}.[28]

A.7 JV Data

R_s displayed in Figure 6E in Chapter 3 is calculated for high V_D via a procedure to minimize the effects of device parastics outlined by Hegedus and Shafarman [54]. We summarize it briefly here. A standard J-V curve is plotted in Figure A.8A for the PbS QD solar cells as a function of increasing temperature and increasing exposure to vacuum, respectively. From these plots, the conductance $g(v) = \frac{dJ}{dV}$ vs. V in reverse bias is shown in Figure A.7B. These plots allow for the calculation of the shunt conductance G. For an Ohmic G, $g(V)$ will be flat with a reverse bias value of G.

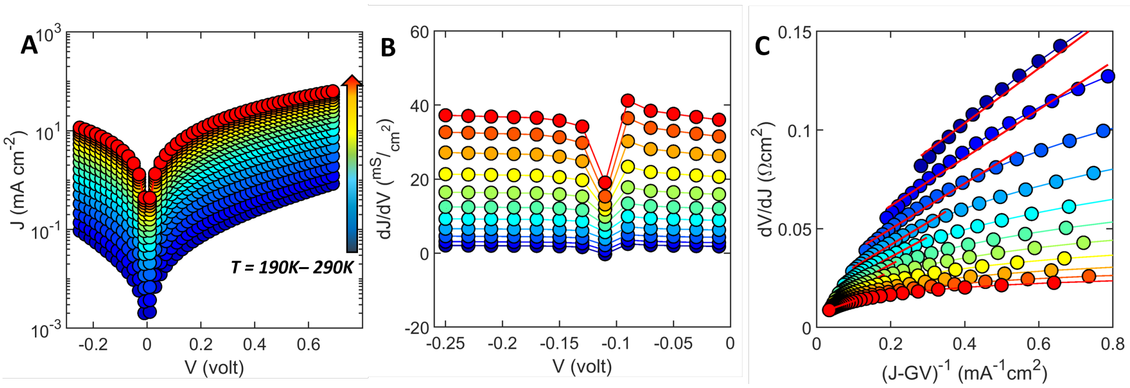

Figure A.8: (A) dark J vs V curves measured as a function of temperature. (B) Shunt $g(V)$ characterization. (C) $\frac{dV}{dJ}$ vs. $J - GV$ with fit used to determine R_s.

The derivative $r(J) = \frac{dV}{dJ} = R_s + \frac{nk_BT}{q}(J - GV)$ is plotted in Figure AA.7C. The intercept of the linear fits to these plots give the series resistance, R_s, shown in the Chapter 3, Figure 6E.

A.8 Vacuum Data

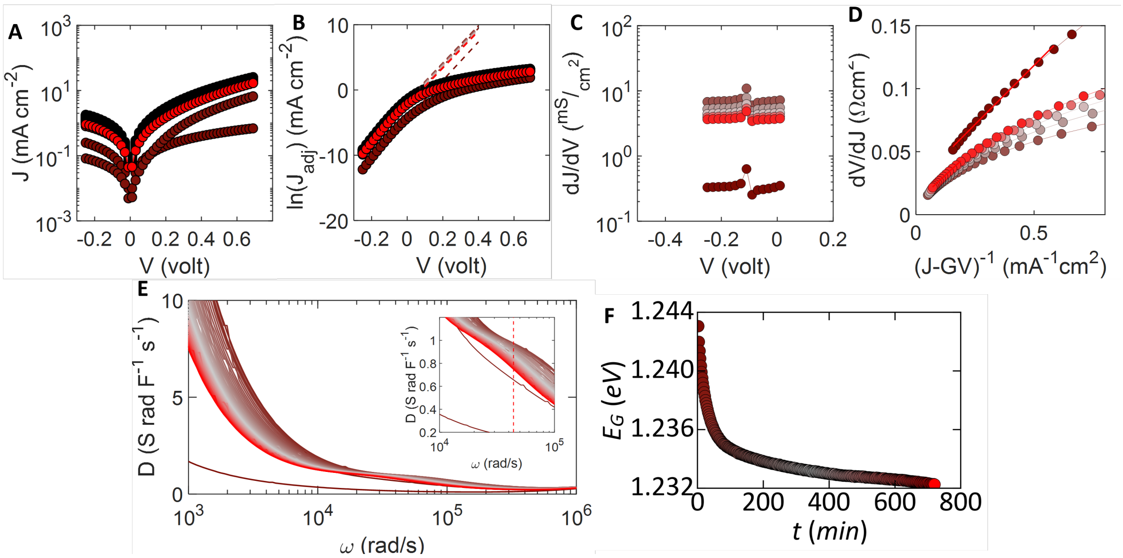

Figure A.9: JV curves taken under continuous exposure to vacuum. (B) J_{adj} calculated for vacuum exposed JV curves. (C) dJ/dV vs. V at evenly spaced intervals of vacuum exposure time (D) dV/dJ vs. $(J - GV)^{-1}$ used to calculate R_S at evenly spaced intervals of vacuum exposure time. (E) Dissipation D vs.ω with inset showing shift in loss peak frequency and ω used to measure high frequency N_{DL} as a function of exposure to vacuum (F) Vacuum-induced redshift in absorption data which obscures direct observation of decrease of long wavelength HWHM

A.9 Full DLCP data

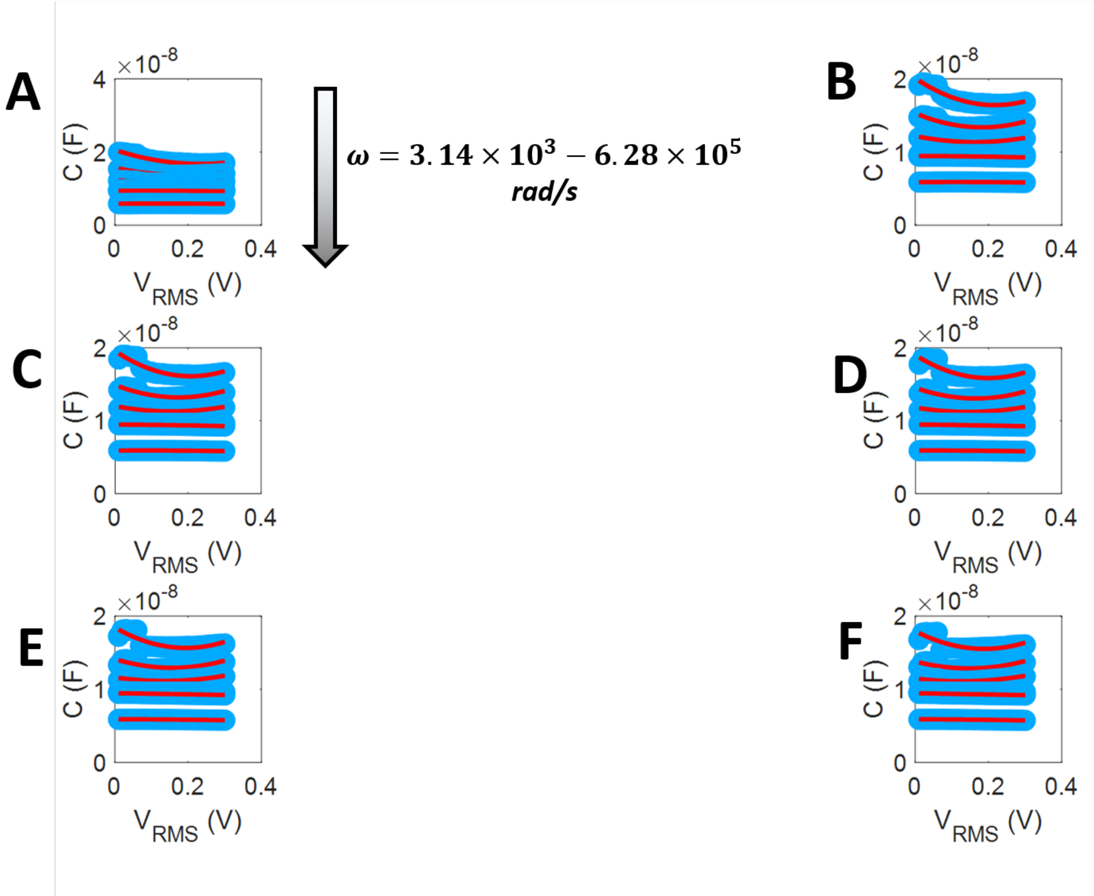

Figure A.10: Raw DLCP data obtained at $T = 220$K and (A) $V_{RMS} = 50$ mV, (B) $V_{RMS} = 100$ mV, (C) $V_{RMS} = 150$ mV, (D) $V_{RMS} = 200$ mV, (E) $V_{RMS} = 250$ mV, and (F) $V_{RMS} = 300$ mV. Frequencies of $\omega = 3.14 \times 10^3$, 6.28×10^3, 3.14×10^4, 6.28×10^4, 3.14×10^6, and 6.28×10^5 rad/s were used to obtain the data at each voltage, as indicated in the figures.

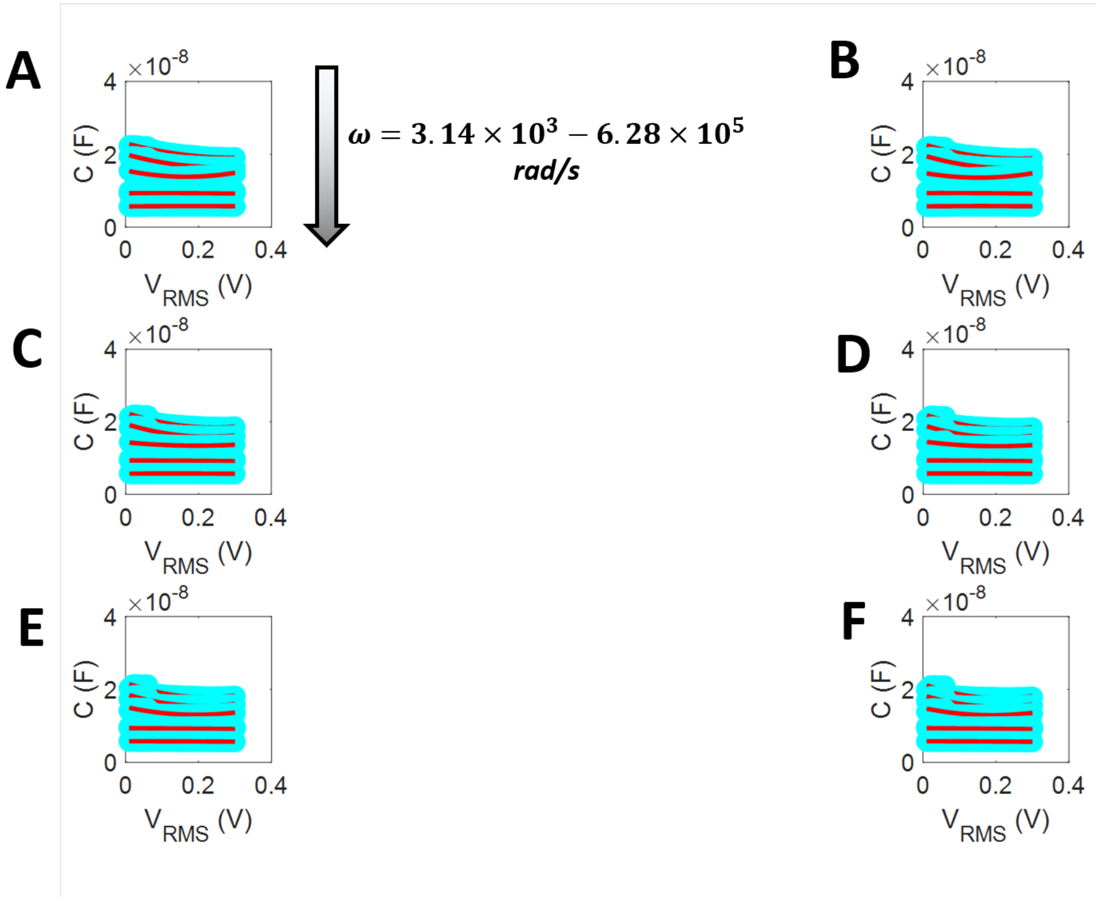

Figure A.11: Raw DLCP data obtained at $T = 230$K and (A) $V_{RMS} = 50$ mV, (B) $V_{RMS} = 100$ mV, (C) $V_{RMS} = 150$ mV, (D) $V_{RMS} = 200$ mV, (E) $V_{RMS} = 250$ mV, and (F) $V_{RMS} = 300$ mV. Frequencies of $\omega = 3.14 \times 10^3$, 6.28×10^3, 3.14×10^4, 6.28×10^4, 3.14×10^6, and 6.28×10^5 rad/s were used to obtain the data at each voltage, as indicated in the figures.

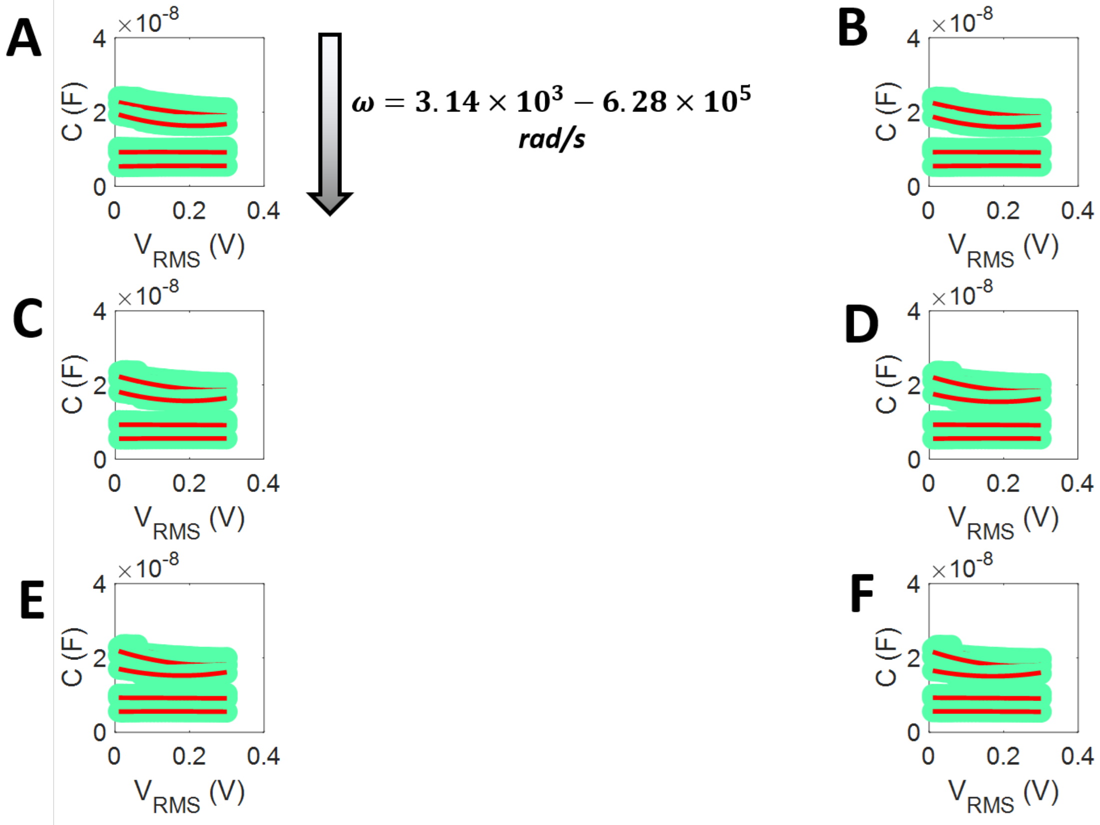

Figure A.12: Raw DLCP data obtained at $T = 240$K and (A) $V_{RMS} = 50$ mV, (B) $V_{RMS} = 100$ mV, (C) $V_{RMS} = 150$ mV, (D) $V_{RMS} = 200$ mV, (E) $V_{RMS} = 250$ mV, and (F) $V_{RMS} = 300$ mV. Frequencies of $\omega = 3.14 \times 10^3$, 6.28×10^3, 3.14×10^4, 6.28×10^4, 3.14×10^6, and 6.28×10^5 rad/s were used to obtain the data at each voltage, as indicated in the figures.

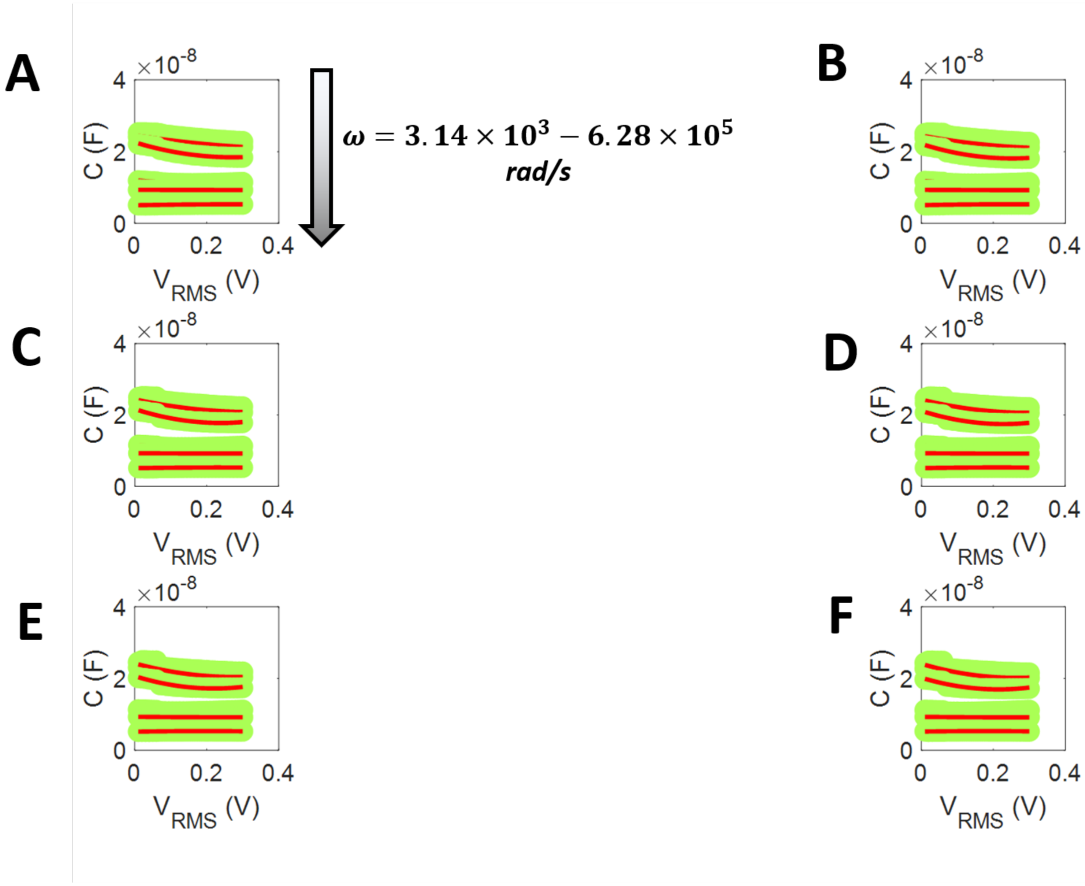

Figure A.13: Raw DLCP data obtained at $T = 250$K and (A) $V_{RMS} = 50$ mV, (B) $V_{RMS} = 100$ mV, (C) $V_{RMS} = 150$ mV, (D) $V_{RMS} = 200$ mV, (E) $V_{RMS} = 250$ mV, and (F) $V_{RMS} = 300$ mV. Frequencies of $\omega = 3.14 \times 10^3$, 6.28×10^3, 3.14×10^4, 6.28×10^4, 3.14×10^6, and 6.28×10^5 rad/s were used to obtain the data at each voltage, as indicated in the figures.

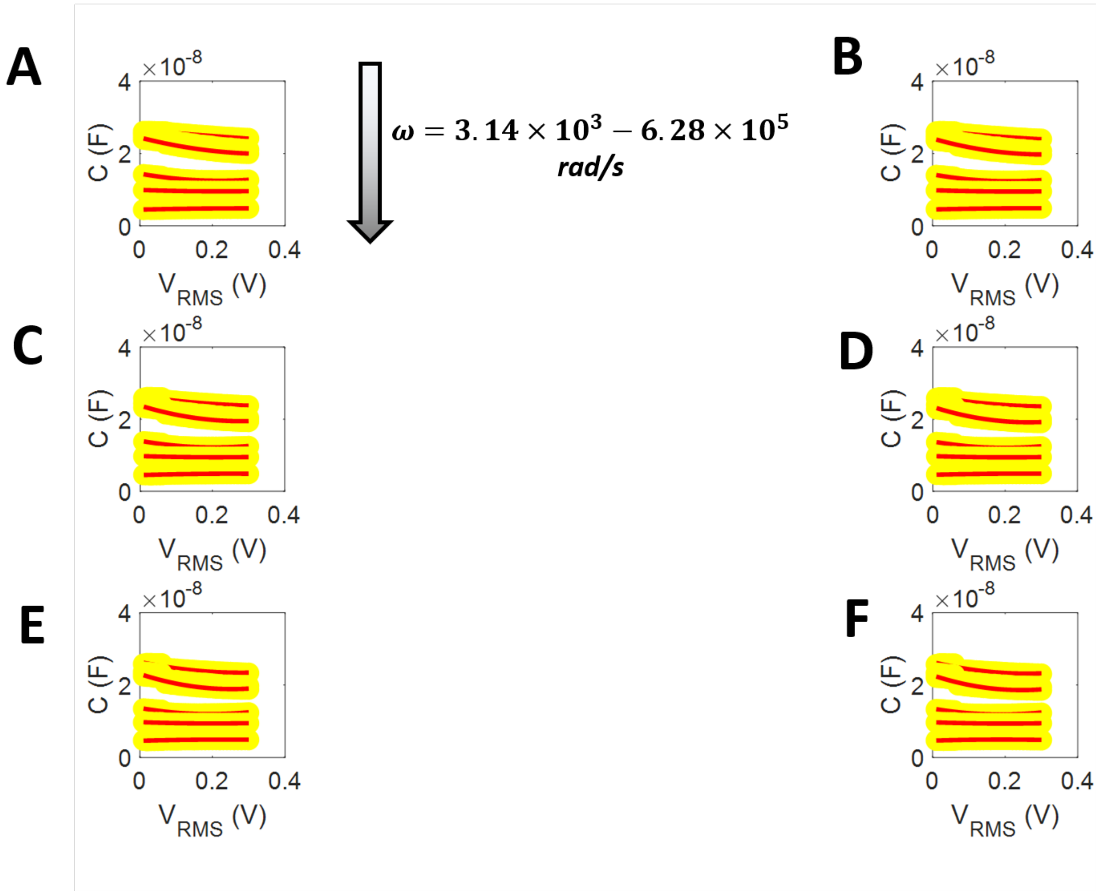

Figure A.14: Raw DLCP data obtained at $T = 260$K and (A) $V_{RMS} = 50$ mV, (B) $V_{RMS} = 100$ mV, (C) $V_{RMS} = 150$ mV, (D) $V_{RMS} = 200$ mV, (E) $V_{RMS} = 250$ mV, and (F) $V_{RMS} = 300$ mV. Frequencies of $\omega = 3.14 \times 10^3$, 6.28×10^3, 3.14×10^4, 6.28×10^4, 3.14×10^6, and 6.28×10^5 rad/s were used to obtain the data at each voltage, as indicated in the figures.

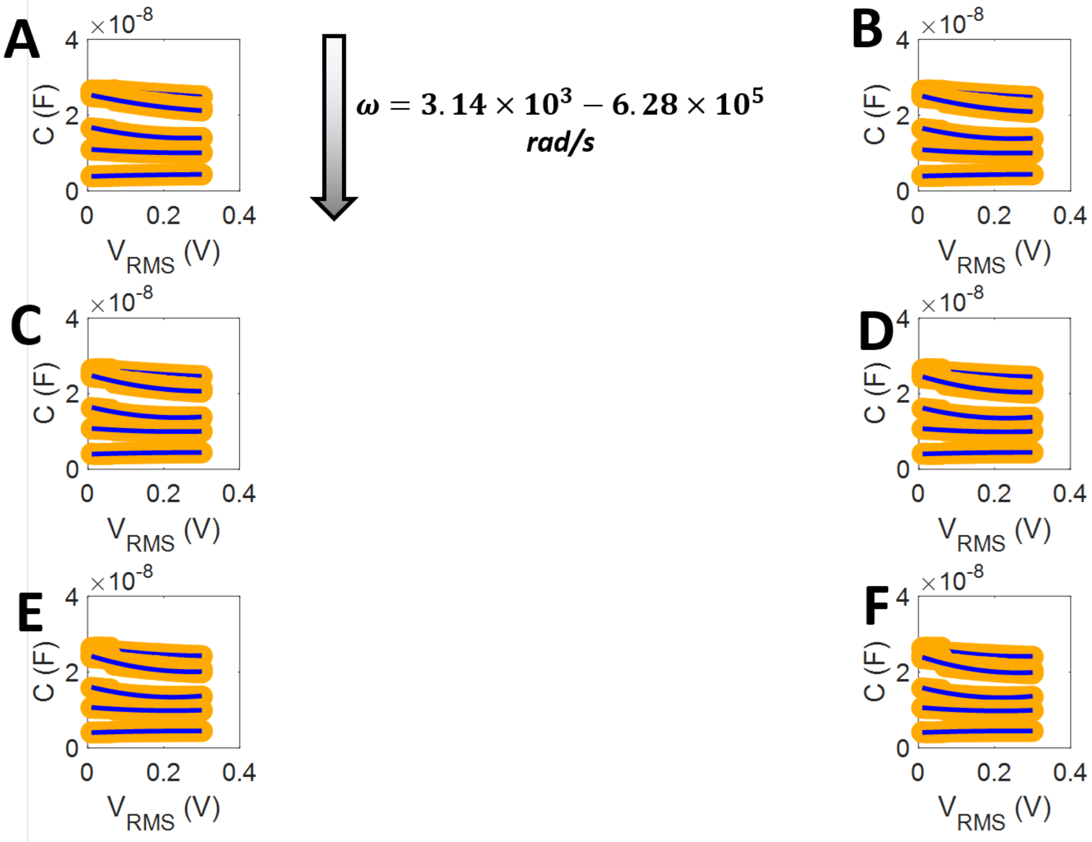

Figure A.15: Raw DLCP data obtained at $T = 270$K and (A) $V_{RMS} = 50$ mV, (B) $V_{RMS} = 100$ mV, (C) $V_{RMS} = 150$ mV, (D) $V_{RMS} = 200$ mV, (E) $V_{RMS} = 250$ mV, and (F) $V_{RMS} = 300$ mV. Frequencies of $\omega = 3.14 \times 10^3$, 6.28×10^3, 3.14×10^4, 6.28×10^4, 3.14×10^6, and 6.28×10^5 rad/s were used to obtain the data at each voltage, as indicated in the figures.

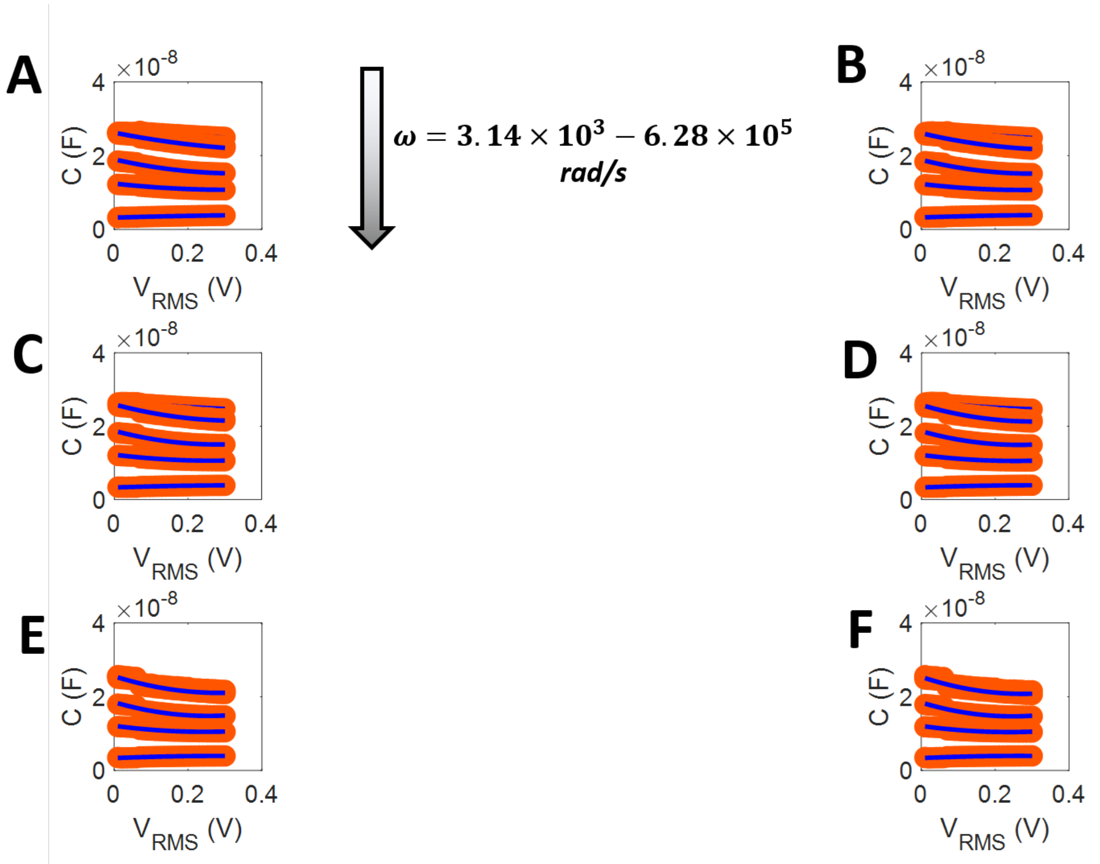

Figure A.16: Raw DLCP data obtained at $T = 280$K and (A) $V_{RMS} = 50$ mV, (B) $V_{RMS} = 100$ mV, (C) $V_{RMS} = 150$ mV, (D) $V_{RMS} = 200$ mV, (E) $V_{RMS} = 250$ mV, and (F) $V_{RMS} = 300$ mV. Frequencies of $\omega = 3.14 \times 10^3$, 6.28×10^3, 3.14×10^4, 6.28×10^4, 3.14×10^6, and 6.28×10^5 rad/s were used to obtain the data at each voltage, as indicated in the figures.

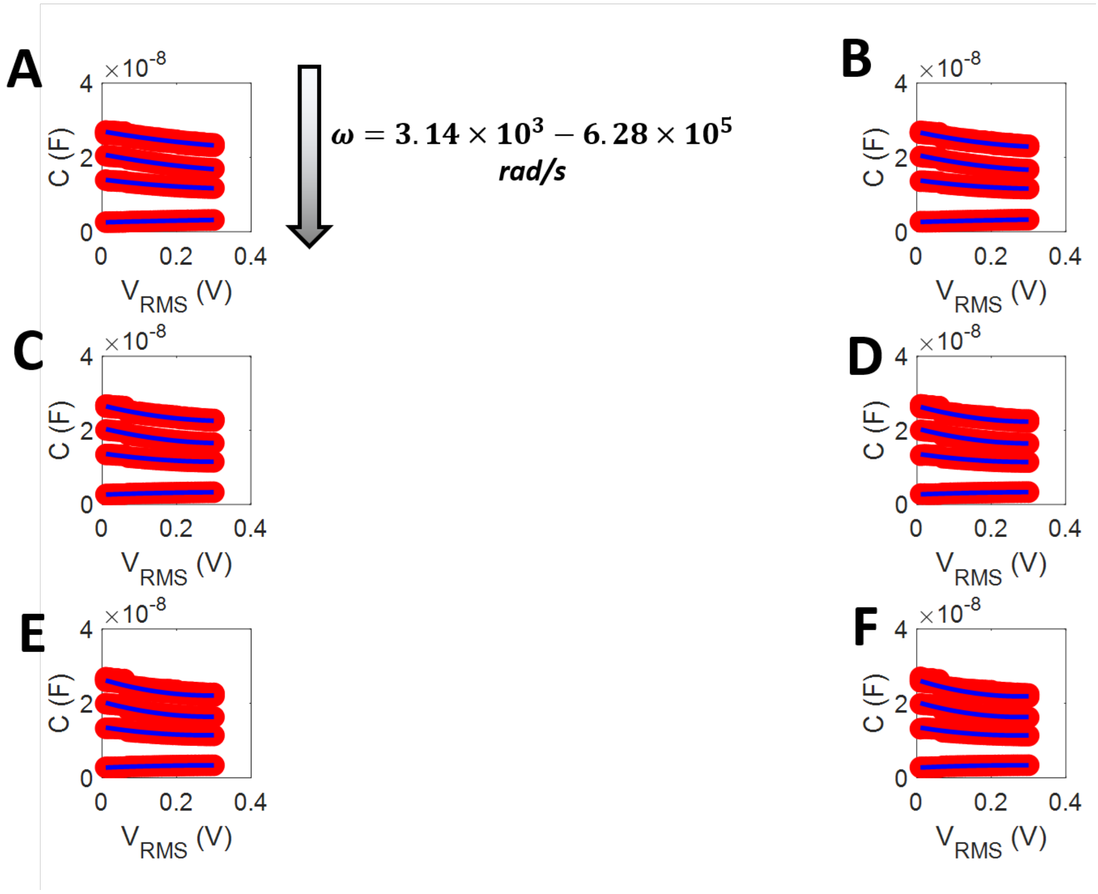

Figure A.17: Raw DLCP data obtained at $T = 290$K and (A) $V_{RMS} = 50$ mV, (B) $V_{RMS} = 100$ mV, (C) $V_{RMS} = 150$ mV, (D) $V_{RMS} = 200$ mV, (E) $V_{RMS} = 250$ mV, and (F) $V_{RMS} = 300$ mV. Frequencies of $\omega = 3.14 \times 10^3$, 6.28×10^3, 3.14×10^4, 6.28×10^4, 3.14×10^6, and 6.28×10^5 rad/s were used to obtain the data at each voltage, as indicated in the figures.

Appendix B

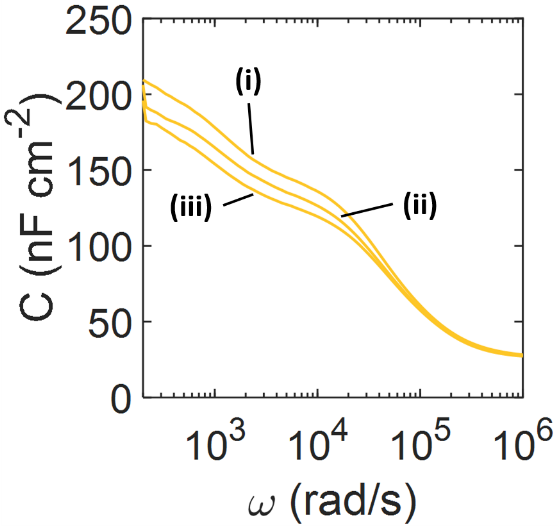

Figure B.1: TAS data obtained at (i) 0mV, (ii) -100 mV, and (iii) -200 mV applied bias.

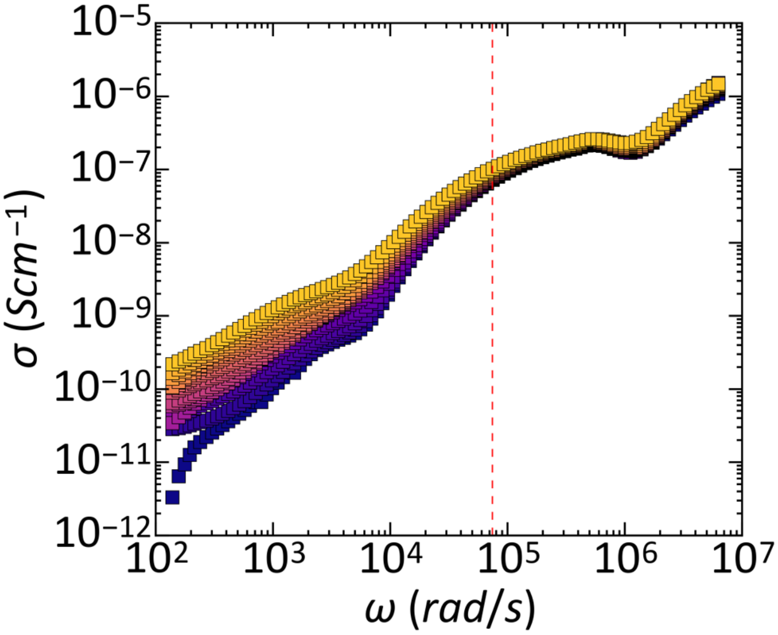

Figure B.2: Frequency-dependent conductance $\sigma(\omega)$ vs. ω at 0 mV on day 1. Dashed red line indicates freeze out frequency.

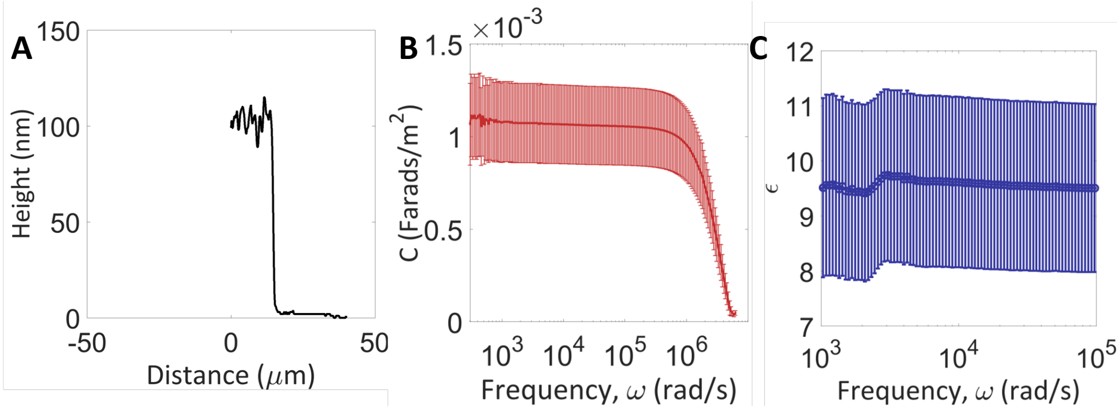

Figure B.3: (A) Film height of ZnO. (B) C vs. ω of dielectric stack of PbS-MPA QD film. (C) Calculated dielectric constant for PbS-QD MPA film.

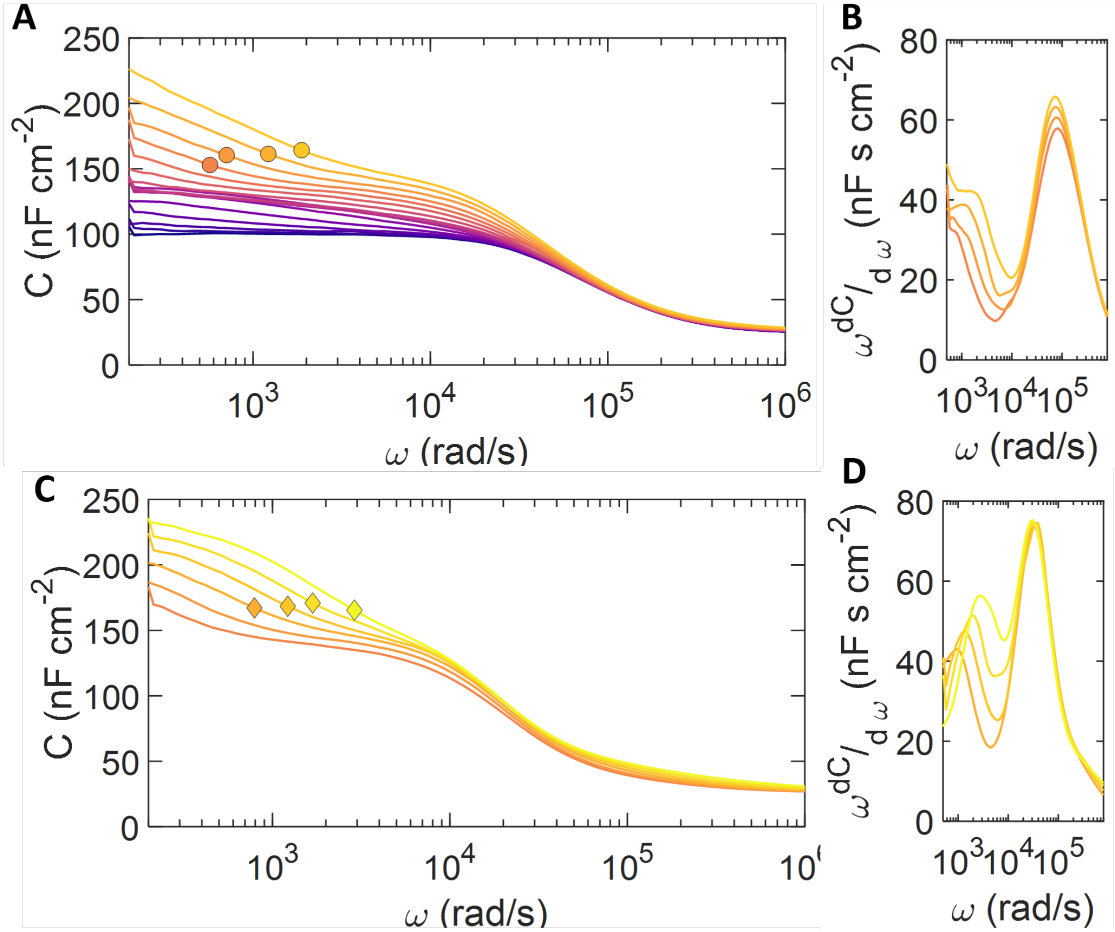

Figure B.4: C vs. ω obtained on day 1 with highlights indicating ω_0 (squares) obtained from (B) $-\omega\frac{dC}{d\omega}$ vs. ω. (C) C vs. ω obtained on day 2 with highlights indicating ω_0 (diamonds) obtained from (D) $-\omega\frac{dC}{d\omega}$ vs. ω.

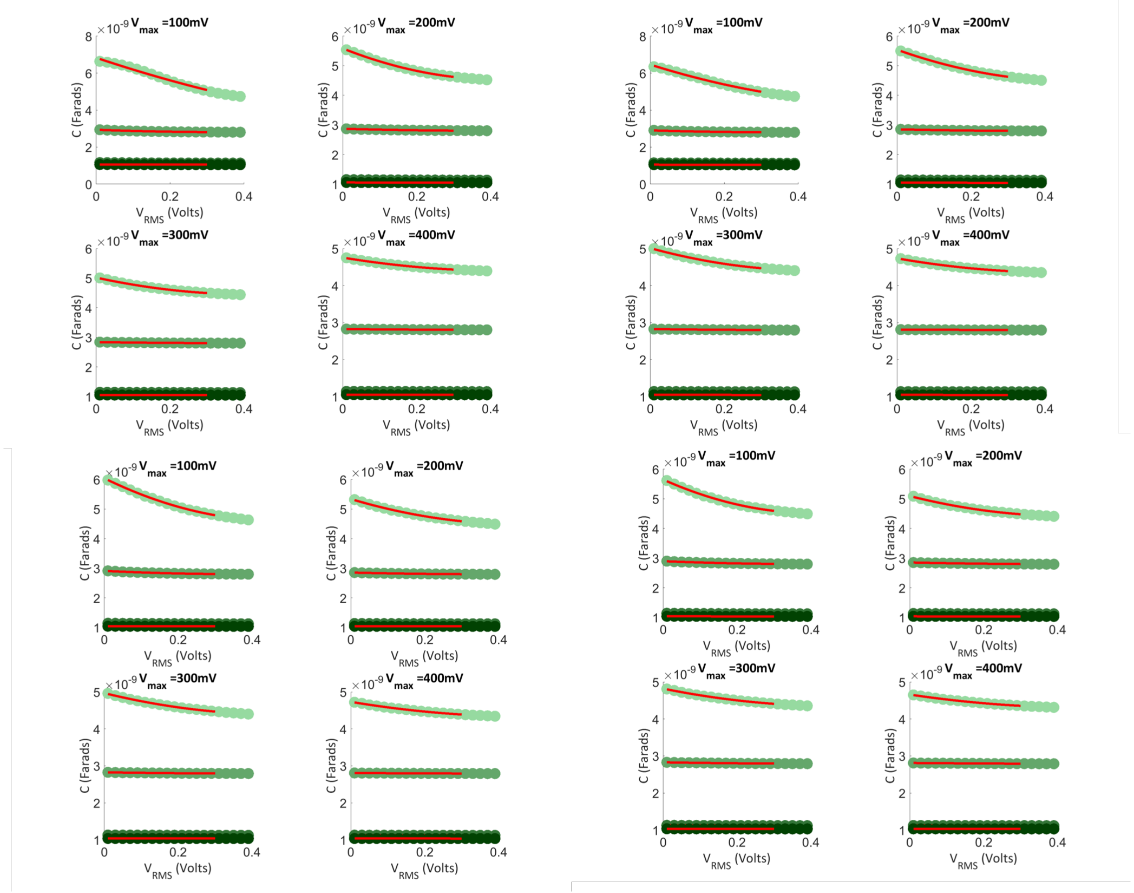

Figure B.5: Appendix 2.5 Raw DLCP C vs. V_{RMS} obtained for day 1 data at (A) T = 270 K, (B) T = 280 K, (C) T = 290 K, and (D) T = 300 K.

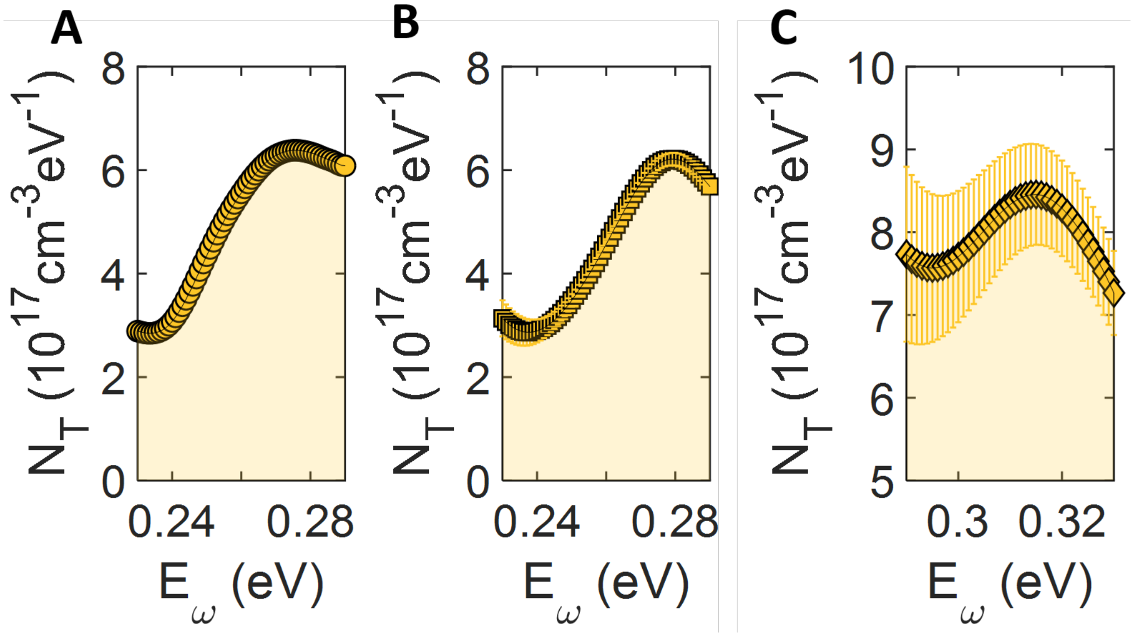

Figure B.6: $N(T)$ determined assuming $V_{bi} = 0.9$ eV and a fully depleted PbS layer on (A) day 0, (B) day 1, and (C) day 2.

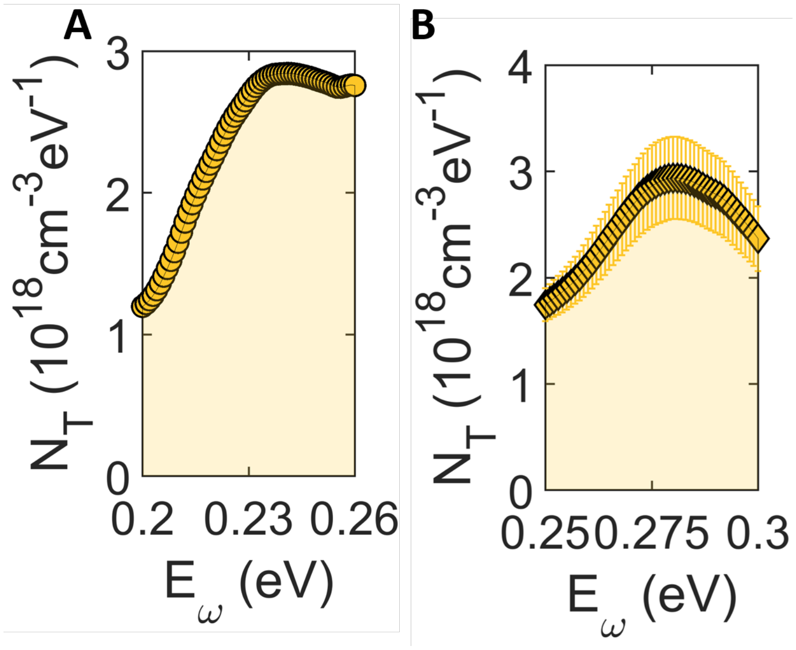

Figure B.7: $N(T)$ determined by direct integration of the capacitance derivatives on (A) day 0 and (B) day 2.

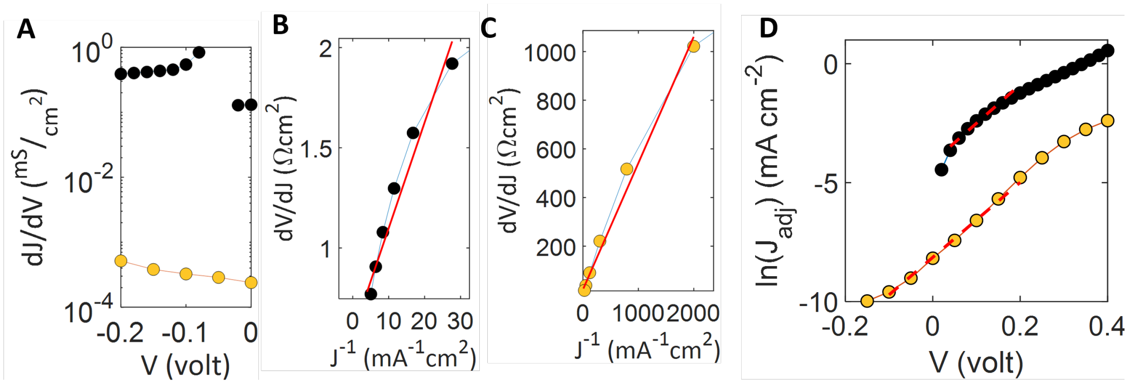

Figure B.8: (A) Shunt $g(V)$ characterization. (B) $\frac{dV}{dJ}$ vs. $J - GV$ with fit used to determine R_s for dark data (C)) $\frac{dV}{dJ}$ vs. $J - GV$ with fit used to determine R_s sample in vaccum (D) Logarithmic plot of J_{adj} vs. V with linear fit to low voltage characteristics yielding J_0 and n.

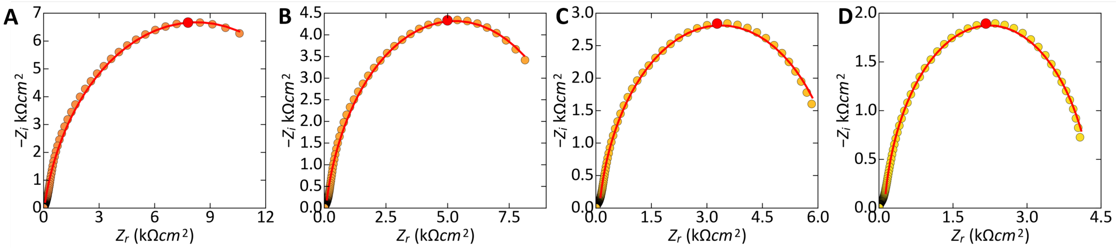

Figure B.9: Fits to IS arcs at $V_A = 600mV$ and (A) T = 260 K, (B) T = 270 K, (C) T = 280 K, and (D) T = 290 K.

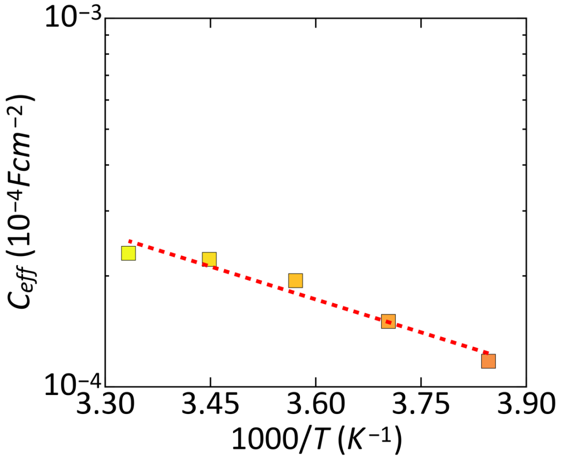

Figure B.10: Thermal activation of effective capacitance C_{eff} with Arrhenius fit (dashed red line).

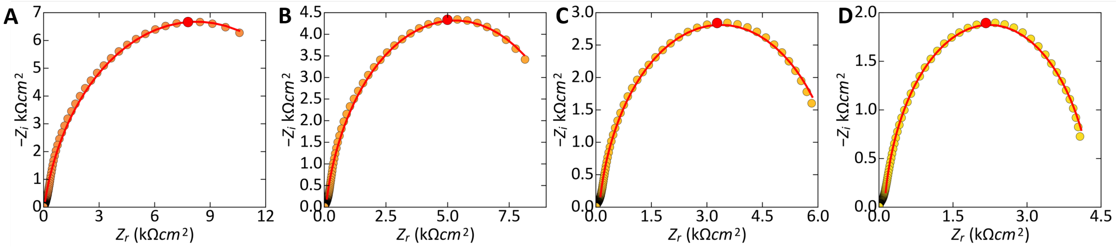

Figure B.11: $\omega\frac{dC}{d\omega}$ vs. ω obtained (A) in the dark from $T = 240 - 330$ K, (B) under 980 nm illumination from $T = 240 - 330$ K, (C) in both dark (grey) and 980 illumination (light red) at $T = 260$ K, and (D) in both dark (black) and under 980 illumination (red) at $T = 325$ K

Appendix C

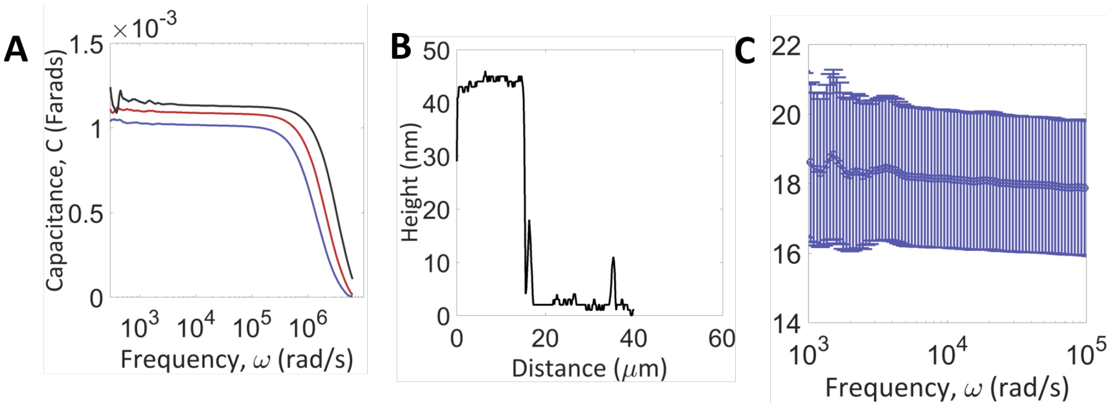

Figure C.1: (A) Capacitance of 3 separate dielectric stacks of SiO_2/PbS-TBAI/Au. (B) AFM height retrace of PbS-TBAI layer used in dielectric stack. (C) Dielectric constant ε for PbS-TBAI

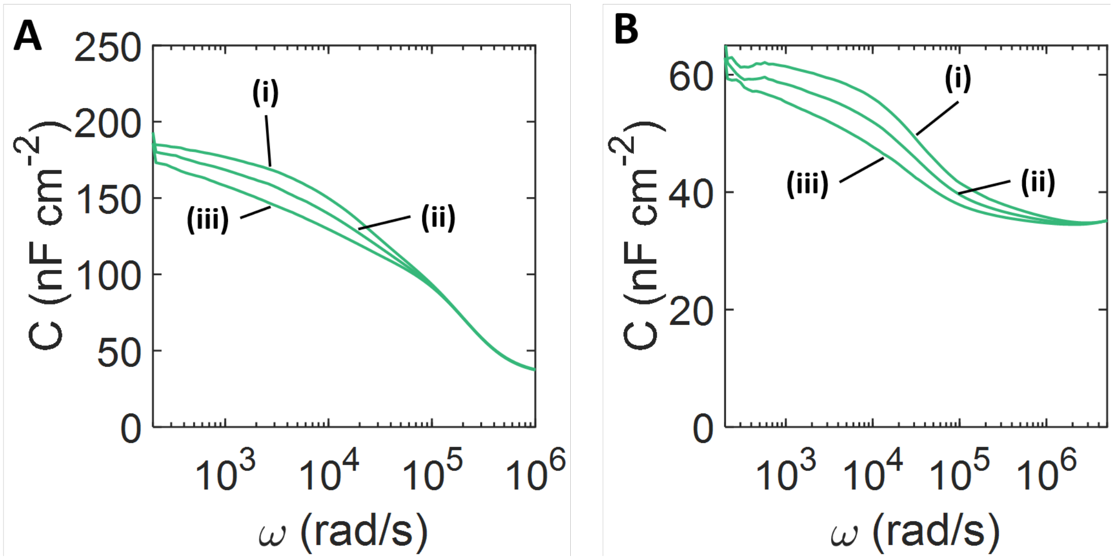

Figure C.2: Voltage-dependent capacitance for PbS-TBAI cell on (A) day 0, showing freeze out at $\omega_D \approx 10^5$, and (B) day 2, showing traces of freeze out at $\omega \approx 3 \times 10^6$ rad/s. The biases used on both days are (i) 0 mV, (ii)- 100 mV and (iii) 200 mV. The bias-dependent emission on both days is consistent with interfacial defect states.

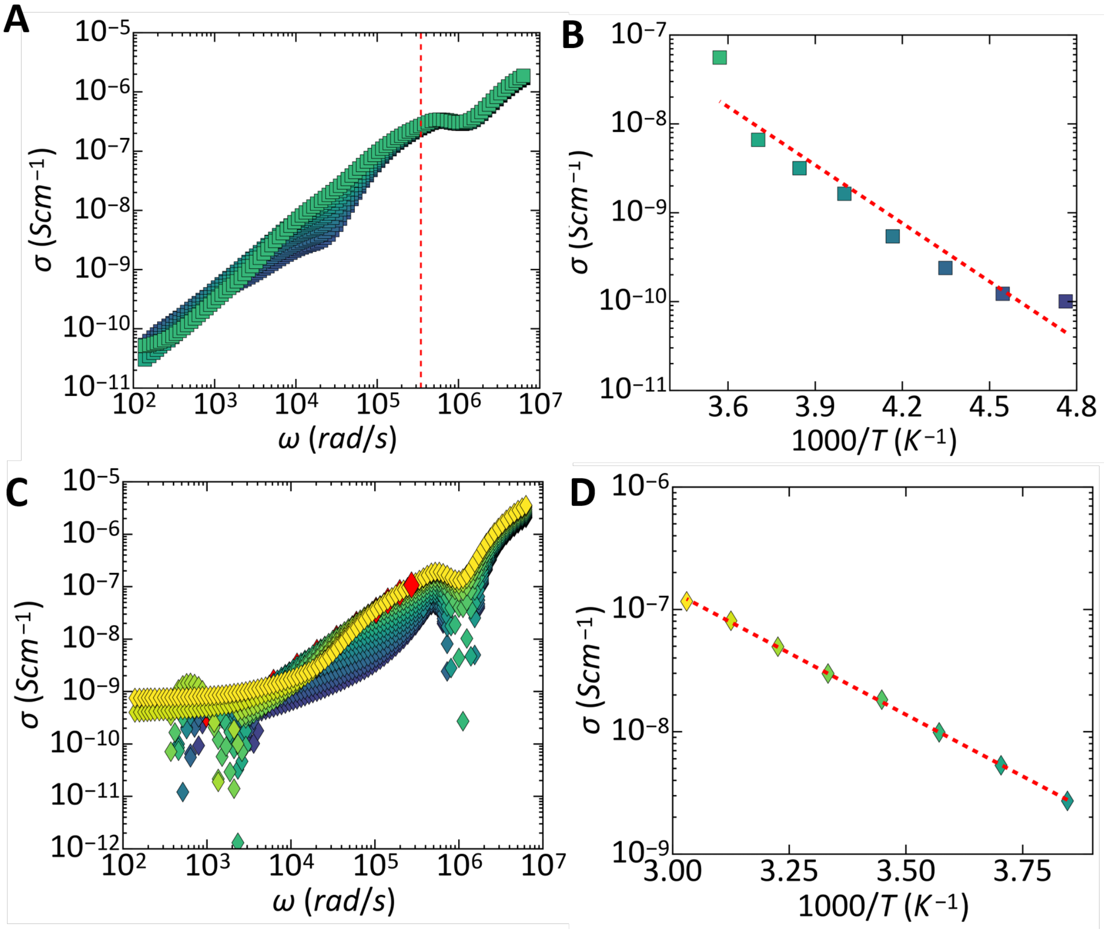

Figure C.3: (A) $\sigma(\omega)$ vs. ω at $V_A = 0$ mV on day 1, with dashed red line indicating ω_D observed in TAS. B) $\sigma(\omega_D)$ vs. ω on day 1 with accompanying Arrhenius fit (dashed red line) giving $E_A = 0.43 \pm 0.03$ eV. (C)) $\sigma(\omega)$ vs. ω at $V_A = 0$ mV on day 2, with red diamonds highlighting ω_0. (C) $\sigma(\omega)$ vs. ω on day 2 with accompanying Arrhenius fit (dashed red line) giving $E_A = 0.40 \pm 0.02$ eV

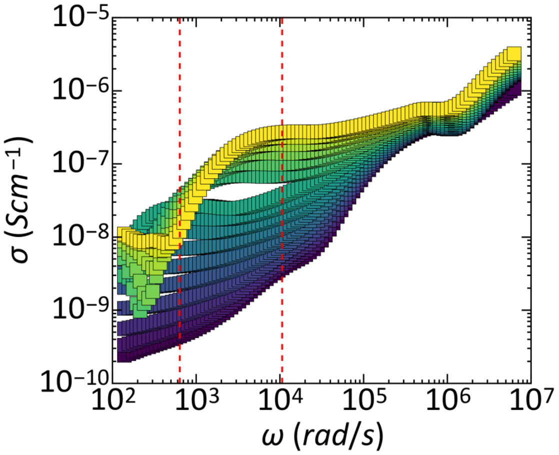

Figure C.4: $\sigma(\omega)$ on day 1, exhibiting 2 dispersion-less conductance plateaus like on day 2. Dashed red lines indicate low test frequency ($\omega_{lf} = 600$ rad/s) and high test frequency ($\omega_{hf} = 1.2 \times 10^4$ rad/s) used in analysis.

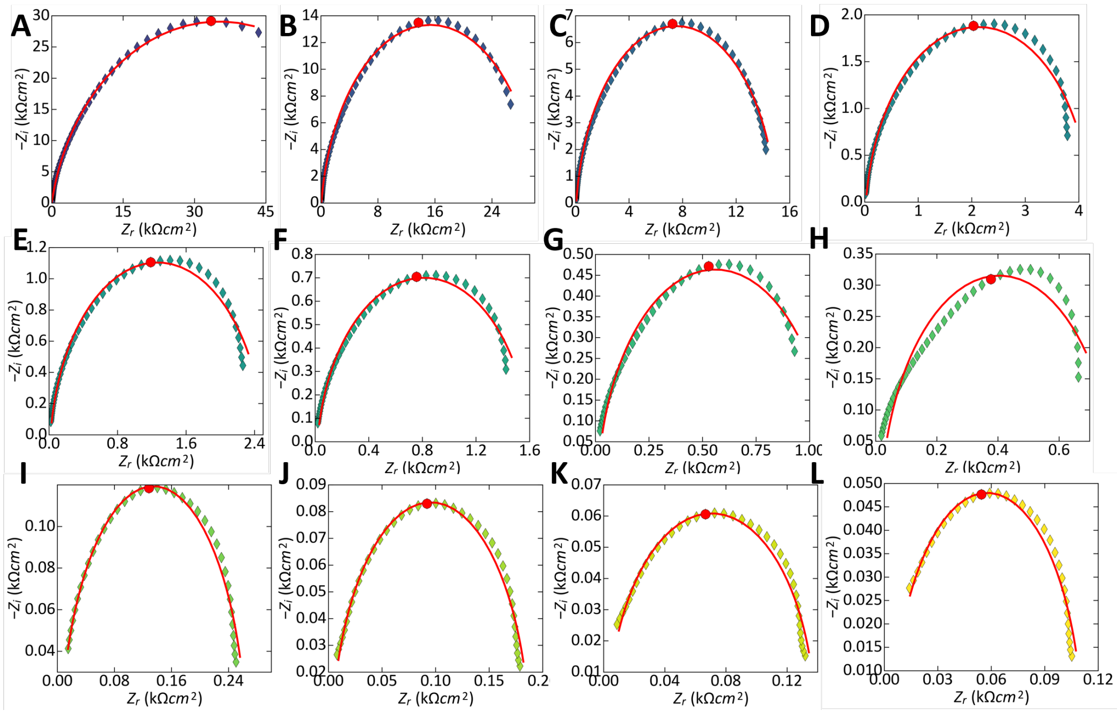

Figure C.5: Appendix 3.5: Impedance arcs and accompanying equivalent circuit fits on day 1 at (A) T = 210 K, (B) T = 220 K, (C) T = 230 K, (D) T = 250 K, (E) T = 260 K, (F) T = 270 K, (G) T = 280 K, (H) T = 290 K, (I) T = 300 K, (J) T = 310 K, (K) T = 320 K, (L) T = 330 K.

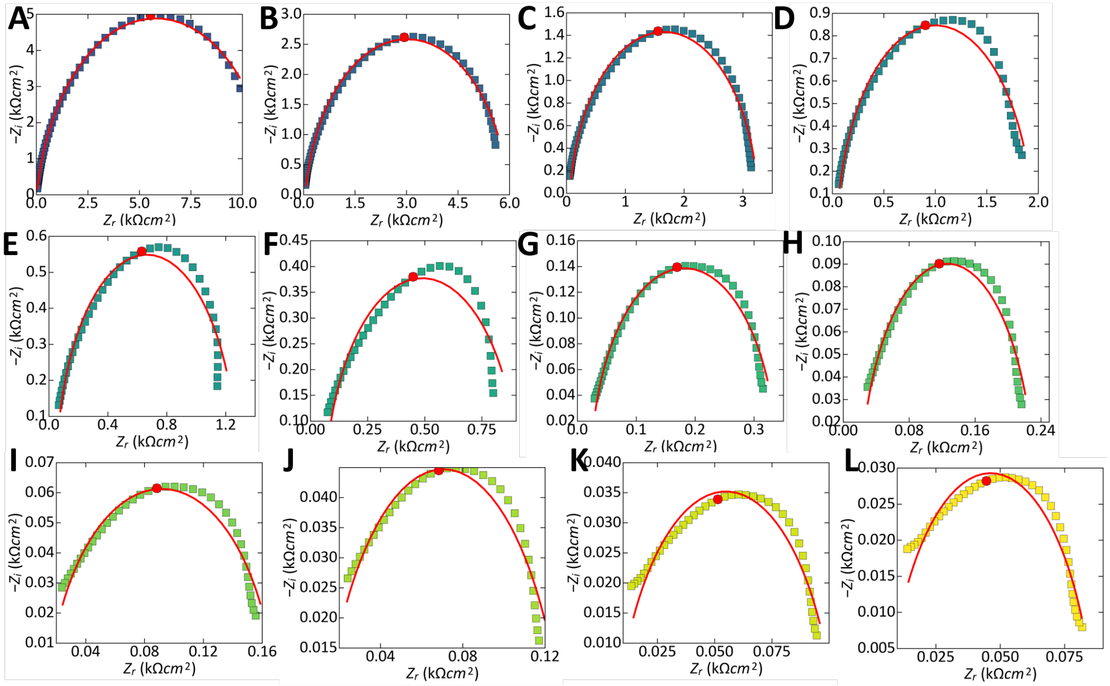

Figure C.6: Impedance arcs and accompanying equivalent circuit fits on day 1 at (A) T = 210 K, (B) T = 220 K, (C) T = 230 K, (D) T = 250 K, (E) T = 260 K, (F) T = 270 K, (G) T = 280 K, (H) T = 290 K, (I) T = 300 K, (J) T = 310 K, (K) T = 320 K, (L) T = 330 K.

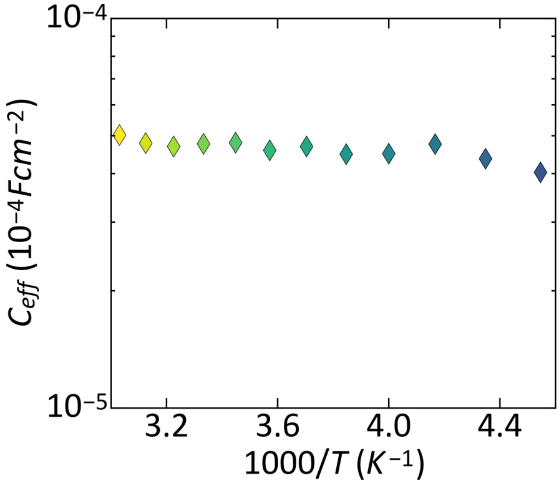

Figure C.7: C_{eff} vs. T extracted from IS fits to the day 2 data.

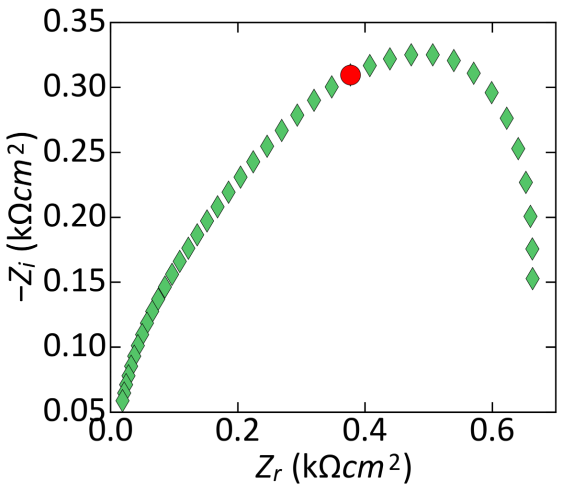

Figure C.8: Impedance arc at $T = 290$ K on day 2 exhibiting distortion due to competition between high and low temperature charge dynamics.

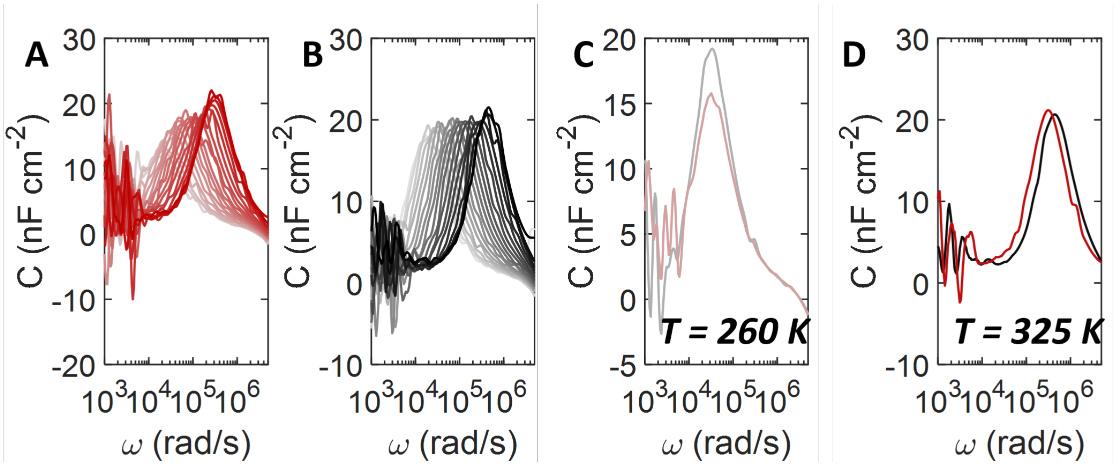

Figure C.9: $\omega\frac{dC}{d\omega}$ vs. ω obtained (A) in the dark from $T = 240 - 330$ K, (B) under 980 nm illumination from $T = 240 - 330$ K, (C) in both dark (grey) and 980 illumination (light red) at $T = 260$ K, and (D) in both dark (black) and under 980 illumination (red) at $T = 325$ K

Bibliography

[1] D. M. Adams, L. Brus, C. E. D. Chidsey, S. Creager, C. Creutz, C. R. Kagan, P. V. Kamat, M. Lieberman, S. Lindsay, R. A. Marcus, R. M. Metzger, M. E. Michel-Beyerle, J. R. Miller, M. D. Newton, D. R. Rolison, O. Sankey, K. S. Schanze, J. Yardley, and X. Zhu. Charge Transfer on the Nanoscale: Current Status. *The Journal of Physical Chemistry B*, 107(28):6668–6697, 2003. 61

[2] V. K. Agarwala and T. Fort. Work function changes during low pressure oxidation of aluminum at room temperature. *Surface Science*, 45(2):470–482, 1974. 84

[3] V. K. Agarwala and T. Fort. Nature of the stable oxide layer formed on an aluminum surface by work function measurements. *Surface Science*, 54(1):60–70, 1976. 84

[4] N. C. Anderson, M. P. Hendricks, J. J. Choi, and J. S. Owen. On the Dynamic Stoichiometry of Metal Chalcogenide Nanocrystals: Spectroscopic Studies of Metal Carboxylate Binding and Displacement. *Journal of the American Chemical Society*, 2:11457–11471, 2013. 7

[5] P. W. Anderson. Absence of diffusion in certain random lattices. *Physical Review*, 109(5):1492–1505, 1958. 15, 16

[6] I. G. Austin and N. F. Mott. Polarons in Crystalline and Non-Crystalline Materials. *Advances in Physics*, 50(7):757–812, nov 1969. 21, 23

[7] W. K. Bae, J. Joo, L. A. Padilha, J. Won, D. C. Lee, Q. Lin, W. K. Koh, H. Luo, V. I. Klimov,

and J. M. Pietryga. Highly effective surface passivation of pbse quantum dots through reaction with molecular chlorine. *Journal of the American Chemical Society*, 134(49):20160–20168, 2012. 119

[8] W. J. E. Beek, M. M. Wienk, M. Kemerink, X. Yang, and R. A. J. Janssen. Hybrid zinc oxide conjugated polymer bulk heterojunction solar cells. *Journal of Physical Chemistry B*, 109(19):9505–9516, 2005. 95, 116, 122, 145

[9] J. Bisquert. Theory of the impedance of electron diffusion and recombination in a thin layer. *Journal of Physical Chemistry B*, 106(2):325–333, 2002. 41, 136

[10] J. Bisquert, F. Fabregat-Santiago, I. Mora-Seró, G. Garcia-Belmonte, and S. Giménez. Electron lifetime in dye-sensitized solar cells: Theory and interpretation of measurements. *Journal of Physical Chemistry C*, 113(40):17278–17290, 2009. 108, 112

[11] J. Bisquert, G. Garcia-Belmonte, and Á. Pitarch. An explanation of anomalous diffusion patterns observed in electroactive materials by impedance methods. *ChemPhysChem*, 4(3):287–292, 2003. 41, 136

[12] P. P. Boix, G. Garcia-Belmonte, U. Muñecas, M. Neophytou, C. Waldauf, and R. Pacios. Determination of gap defect states in organic bulk heterojunction solar cells from capacitance measurements. *Applied Physics Letters*, 95(23), 2009. 43, 59

[13] B. A. Boukamp. A nonlinear least squares fit procedure for analysis of immittancs data of electrochemical systems. *Solid State Ionics*, 20:31–44, 1986. 39

[14] E. Bozler and K. S. Cole. Electric impedance and phase angle of muscle in rigor. *Journal of Cellular and Comparative Physiology*, 6(2):229–241, 1935. 39

[15] D. Bozyigit, W. M. Lin, N. Yazdani, O. Yarema, and V. Wood. A quantitative model for charge carrier transport, trapping and recombination in nanocrystal-based solar cells. *Nature Communications*, 6, 2015. 43, 59, 63, 66, 98, 124

[16] D. Bozyigit, S. Volk, O. Yarema, and V. Wood. Quantification of deep traps in nanocrystal solids, their electronic properties, and their influence on device behavior. *Nano Letters*, 13(11):5284–5288, 2013. 43, 59, 65, 66, 84, 98, 99, 125, 150

[17] D. Bozyigit and V. Wood. Non-Resonant Thermal Admittance Spectroscopy. pages 15–18, 2014. 45, 99, 124

[18] P. R. Brown, D. Kim, R. R. Lunt, N. Zhao, M. G. Bawendi, J. C. Grossman, and V. Bulović. Energy level modification in lead sulfide quantum dot thin films through ligand exchange. *ACS Nano*, 8(6):5863–5872, 2014. 22, 119, 120, 124, 126

[19] P. R. Brown, R. R. Lunt, N. Zhao, T. P. Osedach, D. D. Wanger, L. Y. Chang, M. G. Bawendi, and V. Bulović. Improved current extraction from ZnO/PbS quantum dot heterojunction photovoltaics using a MoO3 interfacial layer. *Nano Letters*, 11(7):2955–2961, 2011. 91

[20] G. J. Brug, A. L. van den Eeden, M. Sluyters-Rehbach, and J. H. Sluyters. The analysis of electrode impedances complicated by the presence of a constant phase element. *Journal of Electroanalytical Chemistry*, 176(1-2):275–295, 1984. xii, 41, 42, 112, 113, 114, 134, 139

[21] G. H. Carey, I. J. Kramer, P. Kanjanaboos, G. Moreno-Bautista, O. Voznyy, L. Rollny, J. A. Tang, S. Hoogland, and E. H. Sargent. Electronically active impurities in colloidal quantum dot solids. *ACS Nano*, 8(11):11763–11769, 2014. 99

[22] J. A. Carr, M. Elshobaki, and S. Chaudhary. Deep defects and the attempt to escape frequency in organic photovoltaic materials. *Applied Physics Letters*, 107(20), 2015. 43, 59

[23] C. Casteleiro, H. Gomes, P. Stallinga, L. Bentes, R. Ayouchi, and R. Schwarz. Study of trap states in zinc oxide (ZnO) thin films for electronic applications. *Journal of Non-Crystalline Solids*, 354(19-25):2519–2522, may 2008. 92, 108, 127

[24] J. Choi, J. W. Jo, F. P. G. de Arquer, Y.-B. Zhao, B. Sun, J. Kim, M.-J. Choi, S.-W. Baek, A. H. Proppe, A. Seifitokaldani, D.-H. Nam, P. Li, O. Ouellette, Y. Kim, O. Voznyy, S. Hoogland, S. O. Kelley, Z.-H. Lu, and E. H. Sargent. Activated Electron-Transport Layers for Infrared Quantum Dot Optoelectronics. *Advanced Materials*, 30(29):1801720, jul 2018. 92, 101, 143, 144

[25] J. Choi, Y. Kim, J. W. Jo, J. Kim, B. Sun, G. Walters, F. P. García de Arquer, R. Quintero-Bermudez, Y. Li, C. S. Tan, L. N. Quan, A. P. T. Kam, S. Hoogland, Z. Lu, O. Voznyy, and E. H. Sargent. Chloride Passivation of ZnO Electrodes Improves Charge Extraction in Colloidal Quantum Dot Photovoltaics. *Advanced Materials*, 29(33), 2017. 12, 61, 92, 101, 143, 144

[26] J. H. Choi, A. T. Fafarman, S. J. Oh, D. K. Ko, D. K. Kim, B. T. Diroll, S. Muramoto, J. G. Gillen, C. B. Murray, and C. R. Kagan. Bandlike transport in strongly coupled and doped quantum dot solids: A route to high-performance thin-film electronics. *Nano Letters*, 12(5):2631–2638, 2012. xi, 22, 31

[27] C.-H. M. Chuang, P. R. Brown, V. Bulović, and M. G. Bawendi. Improved performance and stability in quantumdot solar cells through band alignmentengineering. *Nature Materials*, 13(8):796–801, 2014. 7, 119, 120, 126, 141, 144

[28] C. H. M. Chuang, A. Maurano, R. E. Brandt, G. W. Hwang, J. Jean, T. Buonassisi, V. Bulović, and M. G. Bawendi. Open-circuit voltage deficit, radiative sub-bandgap states, and prospects in quantum dot solar cells. *Nano Letters*, 15(5):3286–3294, 2015. 11, 63, 73, 106, 108, 120, 137, 141, 157

[29] J. P. Clifford, K. W. Johnston, L. Levina, and E. H. Sargent. Schottky barriers to colloidal quantum dot films. *Applied Physics Letters*, 91(25), 2007. 11

[30] K. S. Cole. ELECTRIC PHASE ANGLE OF CELL MEMBRANES. *The Journal of General Physiology*, 15(6):641–649, jul 1932. 39

[31] R. J. Collins and D. G. Thomas. Photoconduction and surface effects with zinc oxide crystals. *Physical Review*, 112(2):388–395, 1958. 92, 100, 124

[32] R. W. Crisp, D. M. Kroupa, A. R. Marshall, E. M. Miller, J. Zhang, M. C. Beard, and J. M. Luther. Metal Halide Solid-State Surface Treatment for High Efficiency PbS and PbSe QD Solar Cells. *Scientific Reports*, 5, 2015. 7, 119

[33] C. R. Crowell and G. I. Roberts. Surface state and interface effects on the capacitance-voltage relationship in Schottky barriers. *Journal of Applied Physics*, 40(9):3726–3730, 1969. 49

[34] C. Ding, Y. Zhang, F. Liu, Y. Kitabatake, S. Hayase, T. Toyoda, R. Wang, K. Yoshino, T. Minemoto, and Q. Shen. Understanding charge transfer and recombination by interface engineering for improving the efficiency of PbS quantum dot solar cells. *Nanoscale Horizons*, 3(4):417–429, 2018. 136

[35] H. S. Duan, H. Zhou, Q. Chen, P. Sun, S. Luo, T. B. Song, B. Bob, and Y. Yang. The identification and characterization of defect states in hybrid organic-inorganic perovskite photovoltaics. *Physical Chemistry Chemical Physics*, 17(1):112–116, 2015. 59

[36] J. C. Dyre. The Random Free-Energy Barrier Model for A.C. Conduction in Disordered Solids. *Journal of Applied Physics*, 64(5):2456–2468, 1988. 20, 23, 24, 25, 27, 28, 60, 72, 73, 74, 109, 132

[37] B. Ehrler, K. P. Musselman, M. L. Böhm, F. S. Morgenstern, Y. Vaynzof, B. J. Walker, J. L. MacManus-Driscoll, and N. C. Greenham. Preventing interfacial recombination in colloidal quantum dot solar cells by doping the metal oxide. *ACS Nano*, 7(5):4210–4220, 2013. 63, 108, 141

[38] R. Eisberg and R. Resnick. *Quantum Physics of Atoms, Molecules, Solids, Nuceli, and Particles*. John Wiley & Sons, second edi edition, 1985. x, 5, 6

[39] T. Eisenbarth, R. Caballero, M. Nichterwitz, C. A. Kaufmann, H. W. Schock, and T. Unold. Characterization of metastabilities in Cu(In,Ga)Se2thin-film solar cells by capacitance and current-voltage spectroscopy. *Journal of Applied Physics*, 110(9), 2011. 43, 59, 76, 98

[40] G. A. Elbaz, D. B. Straus, O. E. Semonin, T. D. Hull, D. W. Paley, P. Kim, J. S. Owen, C. R. Kagan, and X. Roy. Unbalanced Hole and Electron Diffusion in Lead Bromide Perovskites. *Nano Letters*, 17(3):1727–1732, 2017. xi, 31

[41] S. Elliott. A.C. Conduction in Amorphous Chalcogenide and Pnictide Semiconductors. *Advances in Physics*, 36(2):135–217, jan 1987. 24, 25, 27, 59, 60, 73

[42] A. J. Epstein, H. Rommelmann, M. Abkowitz, and H. W. Gibson. Anomalous Frequency-Dependent Conductivity of Polyacetylene. *Physical Review Letters*, 47(21):1549–1553, nov 1981. 60

[43] J. Gao, J. M. Luther, O. E. Semonin, R. J. Ellingson, A. J. Nozik, and M. C. Beard. Quantum dot size dependent J - V characteristics in heterojunction ZnO/PbS quantum dot solar cells. *Nano Letters*, 11(3):1002–1008, 2011. 91

[44] J. Gao, C. L. Perkins, J. M. Luther, M. C. Hanna, H. Y. Chen, O. E. Semonin, A. J. Nozik, R. J. Ellingson, and M. C. Beard. N-type transition metal oxide as a hole extraction layer in PbS quantum dot solar cells. *Nano Letters*, 11(8):3263–3266, 2011. 91

[45] G. Garcia-Belmonte, P. P. Boix, J. Bisquert, M. Lenes, H. J. Bolink, A. La Rosa, S. Filippone, and N. Martín. Influence of the Intermediate Density-of-States Occupancy on Open-Circuit Voltage of Bulk Heterojunction Solar Cells with Different Fullerene Acceptors. *The Journal of Physical Chemistry Letters*, 1(17):2566–2571, sep 2010. 108, 112

[46] C. Giansante and I. Infante. Surface Traps in Colloidal Quantum Dots: A Combined Experimental and Theoretical Perspective. *The Journal of Physical Chemistry Letters*, pages 5209–5215, 2017. 8

[47] E. D. Goodwin, D. B. Straus, E. A. Gaulding, C. B. Murray, and C. R. Kagan. The effects of inorganic surface treatments on photogenerated carrier mobility and lifetime in PbSe quantum dot thin films. *Chemical Physics*, 471:81–88, 2016. 31

[48] D. D. W. Grinolds, P. R. Brown, D. K. Harris, V. Bulovic, and M. G. Bawendi. Quantum-dot size and thin-film dielectric constant: Precision measurement and disparity with simple models. *Nano Letters*, 15(1):21–26, 2015. 150, 157

[49] P. Guyot-sionnest. Electrical Transport in Colloidal Quantum Dot Films. *J Phys Chem Lett*, 3:1169–1175, 2012. 22, 31, 59

[50] A. Hagfeldt and M. Grätzel. Molecular Photovoltaics. *Accounts of Chemical Research*, 33(5):269–277, may 2000. 58

[51] R. H. Harada and H. T. Minden. Photosensitization of PbS films. *Physical Review*, 102(5):1258–1262, 1956. 83, 126

[52] J. T. Heath, J. D. Cohen, and W. N. Shafarman. Bulk and metastable defects in CuIn1-xGaxSe2thin films using drive-level capacitance profiling. *Journal of Applied Physics*, 95(3):1000–1010, 2004. 49, 50, 52, 54, 75, 76, 77, 102, 103, 129

[53] S. S. Hegedus and E. A. Fagen. Midgap states in a-Si:H and a-SiGe:H p-i-n solar cells and Schottky junctions by capacitance techniques. *Journal of Applied Physics*, 71(12):5941–5951, 1992. 59, 76

[54] S. S. Hegedus and W. N. Shafarman. Thin-film solar cells: device measurements and analysis. *Progress in Photovoltaics: Research and Applications*, 12(23):155–176, 2004. 76, 103, 158

[55] R. M. Hill and A. K. Jonscher. DC and AC conductivity in hopping electronic systems. *Journal of Non-Crystalline Solids*, 32(1-3):53–69, 1979. 152

[56] B. Hirschorn, M. E. Orazem, B. Tribollet, V. Vivier, I. Frateur, and M. Musiani. Determination of effective capacitance and film thickness from constant-phase-element parameters. *Electrochimica Acta*, 55(21):6218–6227, 2010. 39, 113, 134

[57] A. J. Houtepen, D. Kockmann, and D. Vanmaekelbergh. Reappraisal of variable-range hopping in quantum dot solids. *Nano Lett.*, 8:3516, 2008. 22

[58] R. L. Hoye, B. Ehrler, M. L. Böhm, D. Muñoz-Rojas, R. M. Altamimi, A. Y. Alyamani, Y. Vaynzof, A. Sadhanala, G. Ercolano, N. C. Greenham, R. H. Friend, J. L. MacManus-Driscoll, and K. P. Musselman. Improved open-circuit voltage in ZnO-PbSe quantum dot solar cells by understanding and reducing losses arising from the ZnO conduction band tail. *Advanced Energy Materials*, 4(8), 2014. 63, 92, 101, 108, 110, 141, 143, 144

[59] L. Hu, A. Mandelis, X. Lan, A. Melnikov, S. Hoogland, and E. H. Sargent. Imbalanced charge carrier mobility and Schottky junction induced anomalous current-voltage characteristics of excitonic PbS colloidal quantum dot solar cells. *Solar Energy Materials and Solar Cells*, 155:155–165, 2016. 81

[60] B. K. Hughes, D. A. Ruddy, J. L. Blackburn, D. K. Smith, M. R. Bergren, A. J. Nozik, J. C. Johnson, and M. C. Beard. Control of PbSe quantum dot surface chemistry and photophysics using an alkylselenide ligand. *ACS Nano*, 6(6):5498–5506, 2012. 8

[61] M. Igalson and H. W. Schock. The metastable changes of the trap spectra of CuInSe2-based photovoltaic devices. *Journal of Applied Physics*, 80(10):5765–5769, 1996. 43, 59, 98, 99, 123

[62] A. H. Ip, S. M. Thon, S. Hoogland, O. Voznyy, D. Zhitomirsky, R. Debnath, L. Levina, L. R. Rollny, G. H. Carey, A. Fischer, K. W. Kemp, I. J. Kramer, Z. Ning, A. J. Labelle,

K. W. Chou, A. Amassian, and E. H. Sargent. Hybrid passivated colloidal quantum dot solids. *Nature Nanotechnology*, 7(9):577–582, 2012. 7, 58, 91, 119, 141

[63] A. N. Jansen, P. T. Wojcik, P. Agarwal, and M. E. Orazem. Thermally Stimulated Deep-Level Impedance Spectroscopy. *Journal of The Electrochemical Society*, 143(12):4066, 1996. xii, 37, 39, 67

[64] K. S. Jeong, J. Tang, H. Liu, J. Kim, A. W. Schaefer, K. Kemp, L. Levina, X. Wang, S. Hoogland, R. Debnath, L. Brzozowski, E. H. Sargent, and J. B. Asbury. Enhanced mobility-lifetime products in PbS colloidal quantum dot photovoltaics. *ACS Nano*, 6(1):89–99, 2012. 65, 97, 106, 108

[65] M. Jiang, F. Lan, B. Zhao, Q. Tao, J. Wu, D. Gao, and G. Li. Observation of lower defect density in CH3NH3Pb(I,Cl)3 solar cells by admittance spectroscopy. *Applied Physics Letters*, 108(24):243501, 2016. 59

[66] Z. Jin, A. Wang, Q. Zhou, Y. Wang, and J. Wang. Detecting trap states in planar PbS colloidal quantum dot solar cells. *Scientific Reports*, 6, 2016. 43, 59, 98, 125

[67] J. C. Johnson, K. P. Knutsen, H. Yan, M. Law, Y. Zhang, P. Yang, and R. J. Saykally. Ultrafast Carrier Dynamics in Single ZnO Nanowire and Nanoribbon Lasers. *Nano Letters*, 4(2):197–204, 2004. xi, 31

[68] K. W. Johnston, A. G. Pattantyus-Abraham, J. P. Clifford, S. H. Myrskog, S. Hoogland, H. Shukla, E. J. Klem, L. Levina, and E. H. Sargent. Efficient Schottky-quantum-dot photovoltaics: The roles of depletion, drift, and diffusion. *Applied Physics Letters*, 92(12):1–4, 2008. 7

[69] C. R. Kagan, E. Lifshitz, E. H. Sargent, and D. V. Talapin. Building devices from colloidal quantum dots. *Science*, 353(6302), 2016. 58

[70] Y. Kanai. Admittance Spectroscopy of ZnO Crystals. *Japanese Journal of Applied Physics*, 29(Part 1, No. 8):1426–1430, aug 1990. 92, 108, 127

[71] M. S. Kang, A. Sahu, D. J. Norris, and C. D. Frisbie. Size- and Temperature-Dependent Charge Transport in PbSe Nanocrystal Thin Films. *Nano Letters*, 11(9):3887–3892, 2011. 66, 74

[72] N. Karl. Charge carrier transport in organic semiconductors. *Synthetic Metals*, 133-134:649–657, mar 2003. 59

[73] K. W. Kemp, A. J. Labelle, S. M. Thon, A. H. Ip, I. J. Kramer, S. Hoogland, and E. H. Sargent. Interface recombination in depleted heterojunction photovoltaics based on colloidal quantum dots. *Advanced Energy Materials*, 3(7):917–922, 2013. 63, 108, 137, 141

[74] S. V. Kershaw, A. S. Susha, and A. L. Rogach. Narrow bandgap colloidal metal chalcogenide quantum dots: Synthetic methods, heterostructures, assemblies, electronic and infrared optical properties. *Chemical Society Reviews*, 42(7):3033–3087, 2013. 3

[75] S. Khelifi, K. Decock, J. Lauwaert, H. Vrielinck, D. Spoltore, F. Piersimoni, J. Manca, A. Belghachi, and M. Burgelman. Investigation of defects by admittance spectroscopy measurements in poly (3-hexylthiophene):(6,6)-phenyl C61-butyric acid methyl ester organic solar cells degraded under air exposure. *Journal of Applied Physics*, 110(9), 2011. 43, 45, 59, 64, 98

[76] E. J. D. Klem, H. Shukla, S. Hinds, D. D. MacNeil, L. Levina, and E. H. Sargent. Impact of dithiol treatment and air annealing on the conductivity, mobility, and hole density in PbS colloidal quantum dot solids. *Applied Physics Letters*, 92(21), 2008. 7

[77] D. K. Ko and C. B. Murray. Probing the Fermi Energy Level and the Density of States Distribution in PbTe Nanocrystal (Quantum Dot) Solids by Temperature-Dependent Thermopower Measurements. *ACS Nano*, 5(6):4810–4817, 2011. 22, 60

[78] G. I. Koleilat, L. Levina, H. Shukla, S. H. Myrskog, S. Hinds, A. G. Pattantyus-Abraham, and E. H. Sargent. Efficient, Stable Infrared Photovoltaics Based on Solution-Cast Colloidal Quantum Dots. *ACS Nano*, 2(5):833–840, may 2008. 7

[79] T. A. Krajewski, P. Stallinga, E. Zielony, K. Goscinski, P. Kruszewski, L. Wachnicki, T. Aschenbrenner, D. Hommel, E. Guziewicz, and M. Godlewski. Trap levels in the atomic layer deposition-ZnO/GaN heterojunctionThermal admittance spectroscopy studies. *Journal of Applied Physics*, 113(19):194504, may 2013. 92, 115

[80] D. M. Kroupa, M. Vörös, N. P. Brawand, B. W. McNichols, E. M. Miller, J. Gu, A. J. Nozik, A. Sellinger, G. Galli, and M. C. Beard. Tuning colloidal quantum dot band edge positions through solution-phase surface chemistry modification. *Nature Communications*, 8, 2017. 119

[81] G. Lakhwani, R. F. H. Roijmans, A. J. Kronemeijer, J. Gilot, R. A. J. Janssen, and S. C. J. Meskers. Probing charge carrier density in a layer of photodoped ZnO nanoparticles by spectroscopic ellipsometry. *Journal of Physical Chemistry C*, 114(35):14804–14810, 2010. 92, 100, 101, 124

[82] X. Lan, O. Voznyy, F. P. García De Arquer, M. Liu, J. Xu, A. H. Proppe, G. Walters, F. Fan, H. Tan, M. Liu, Z. Yang, S. Hoogland, and E. H. Sargent. 10.6% Certified Colloidal Quantum Dot Solar Cells Via Solvent-Polarity-Engineered Halide Passivation. *Nano Letters*, 16(7):4630–4634, 2016. 12, 61

[83] M. Law, J. M. Luther, Q. Song, B. K. Hughes, C. L. Perkins, and A. J. Nozik. Structural, optical, and electrical properties of PbSe nanocrystal solids treated thermally or with simple amines. *Journal of the American Chemical Society*, 130(18):5974–5985, 2008. 7

[84] J. Lee, J. D. Cohen, and W. N. Shafarman. The determination of carrier mobilities in CIGS

photovoltaic devices using high-frequency admittance measurements. In *Thin Solid Films*, volume 480-481, pages 336–340, 2005. 96, 123

[85] J. S. Lee, M. V. Kovalenko, J. Huang, D. S. Chung, and D. V. Talapin. Band-like transport, high electron mobility and high photoconductivity in all-inorganic nanocrystal arrays. *Nature Nanotechnology*, 6(6):348–352, 2011. 22, 31

[86] K. S. Leschkies, M. S. Kang, E. S. Aydil, and D. J. Norris. Influence of atmospheric gases on the electrical properties of PbSe quantum-dot films. *Journal of Physical Chemistry C*, 114(21):9988–9996, 2010. 83, 126

[87] G. Li, V. Shrotriya, J. Huang, Y. Yao, T. Moriarty, K. Emery, and Y. Yang. High-efficiency solution processable polymer photovoltaic cells by self-organization of polymer blends. *Nature Materials*, 4(11):864–868, nov 2005. 58

[88] J. V. Li, R. S. Crandall, I. L. Repins, A. M. Nardes, and D. H. Levi. Applications of admittance spectroscopy in photovoltaic devices beyond majority-carrier trapping defects. In *Conference Record of the IEEE Photovoltaic Specialists Conference*, pages 000075–000078, 2011. 43, 59

[89] J. V. Li and D. H. Levi. Determining the defect density of states by temperature derivative admittance spectroscopy. *Journal of Applied Physics*, 109(8):083701, apr 2011. 43, 59

[90] J. V. Li, X. Li, D. S. Albin, and D. H. Levi. A method to measure resistivity, mobility, and absorber thickness in thin-film solar cells with application to CdTe devices. *Solar Energy Materials and Solar Cells*, 94(12):2073–2077, 2010. 43, 59, 60, 65, 96

[91] H. Liu, A. Pourret, and P. Guyot-Sionnest. Mott and Efros-Shklovskii variable range hopping in CdSe quantum dots films. *ACS Nano*, 4(9):5211–5216, 2010. 7, 22, 31, 59, 65

[92] H. Liu, J. Tang, I. J. Kramer, R. Debnath, G. I. Koleilat, X. Wang, A. Fisher, R. Li,

L. Brzozowski, L. Levina, and E. H. Sargent. Electron acceptor materials engineering in colloidal quantum dot solar cells. *Advanced Materials*, 23(33):3832–3837, 2011. 63, 108, 141

[93] H. Liu, D. Zhitomirsky, S. Hoogland, J. Tang, I. J. Kramer, Z. Ning, and E. H. Sargent. Systematic optimization of quantum junction colloidal quantum dot solar cells. *Applied Physics Letters*, 101(15):2012–2015, 2012. 63, 108, 141

[94] Y. Liu, M. Gibbs, J. Puthussery, S. Gaik, R. Ihly, H. W. Hillhouse, and M. Law. Dependence of Carrier Mobility on Nanocrystal Size and Ligand Length in PbSe Nanocrystal Solids. *Nano Letters*, 10(5):1960–1969, may 2010. 22, 59

[95] A. R. Long, J. Mcmillan, N. Balkan, and S. Summerfield. The application of the extended pair approximation to hopping conduction in r.f. sputtered amorphous silicon. *Philosophical Magazine B*, 58(2):153–169, aug 1988. 23

[96] D. C. Look, J. W. Hemsky, and J. R. Sizelove. Residual Native Shallow Donor in ZnO. *Physical Review Letters*, 82(12):2552–2555, mar 1999. 115

[97] J. M. Luther, M. Law, M. C. Beard, Q. Song, M. O. Reese, R. J. Ellingson, and A. J. Nozik. Schottky solar cells based on colloidal nanocrystal films. *Nano Letters*, 8(10):3488–3492, 2008. 7, 63

[98] J. R. Macdonald. Analysis of Impedance and Admittance Data for Solids and Liquids. *Journal of The Electrochemical Society*, 124(7):1022, 1977. 39

[99] A. R. Marshall, M. C. Beard, and J. C. Johnson. Nongeminate radiative recombination of free charges in cation-exchanged PbS quantum dot films. *Chemical Physics*, 471:75–80, 2016. 31

[100] A. Miller and E. Abrahams. Impurity conduction at low concentrations. *Physical Review*, 120(3):745–755, 1960. 19

[101] H. T. Minden. Effects of oxygen on PbS films. *The Journal of Chemical Physics*, 23(10):1948–1955, oct 1955. 83, 126

[102] H. T. Minden. Space-charge formation in small PbS particles. *The Journal of Chemical Physics*, 25(2):241–248, 1956. 83, 126

[103] M. Monirul Islam, N. Miyashita, N. Ahsan, T. Sakurai, K. Akimoto, and Y. Okada. Identification of defect types in moderately Si-doped GaInNAsSb layer in p-GaAs/n- GaInNAsSb/n-GaAs solar cell structure using admittance spectroscopy. *Journal of Applied Physics*, 112(11), 2012. 99, 123

[104] S. Monticone, R. Tufeu, and A. V. Kanaev. Complex Nature of the UV and Visible Fluorescence of Colloidal ZnO Nanoparticles. *The Journal of Physical Chemistry B*, 102(16):2854–2862, 1998. 97, 123

[105] N. F. Mott and E. A. Davis. *Electronic Processes in Non-crystalline Materials.* Oxford University Press, New York, NY, second edition, 1982. x, xi, 14, 15, 16, 17, 18, 20, 21, 22, 23, 25, 59, 65, 66, 71, 73

[106] N. F. Mott and H. Massey. *Theory of Atomic Collisions.* Oxford University Press, New York, NY, third edition, 1988. 16

[107] C. B. Murray, C. R. Kagan, and M. G. Bawendi. Synthesis and Characterization of Monodisperse Nanocrystals and Close-Packed Nanocrystal Assemblies. *Annual Review of Materials Science*, 30(1):545–610, aug 2000. 3

[108] C. B. Murray, D. J. Norris, and M. G. Bawendi. Synthesis and characterization of nearly monodisperse CdE (E = sulfur, selenium, tellurium) semiconductor nanocrystallites. *Journal of the American Chemical Society*, 115(19):8706–8715, sep 1993. 3

[109] M. Musiani, M. E. Orazem, N. Pebere, B. Tribollet, and V. Vivier. Constant-Phase-Element

Behavior Caused by Coupled Resistivity and Permittivity Distributions in Films. *Journal of The Electrochemical Society*, 158(12):C424, 2011. 112

[110] J. Newman. Frequency Dispersion in Capacity Measurements at a Disk Electrode. *Journal of The Electrochemical Society*, 117(2):198, 1970. 39

[111] E. Nicollian and J. Brews. *MOS Physics and Technology.* Wiley-Interscience, Toronto, 1st edition, 1982. 27, 38, 66, 69, 132

[112] E. H. Nicollian and A. Goetzberger. MOS Conductance Technique for Measuring Surface State Parameters. *Applied Physics Letters*, 7(8):216–219, 1965. 28, 38, 67

[113] W. Nie, H. Tsai, R. Asadpour, J.-C. Blancon, A. J. Neukirch, G. Gupta, J. J. Crochet, M. Chhowalla, S. Tretiak, M. A. Alam, H.-L. Wang, and A. D. Mohite. High-efficiency solution-processed perovskite solar cells with millimeter-scale grains. *Science (New York, N.Y.)*, 347(6221):522–525, 2015. 58

[114] Z. Ning, D. Zhitomirsky, V. Adinolfi, B. Sutherland, J. Xu, O. Voznyy, P. Maraghechi, X. Lan, S. Hoogland, Y. Ren, and E. H. Sargent. Graded doping for enhanced colloidal quantum dot photovoltaics. *Advanced Materials*, 25(12):1719–1723, 2013. 119

[115] S. J. Oh, N. E. Berry, J. H. Choi, E. A. Gaulding, H. Lin, T. Paik, B. T. Diroll, S. Muramoto, C. B. Murray, and C. R. Kagan. Designing high-performance PbS and PbSe nanocrystal electronic devices through stepwise, post-synthesis, colloidal atomic layer deposition. *Nano Letters*, 14(3):1559–1566, 2014. 31

[116] S. J. Oh, D. B. Straus, T. Zhao, J. H. Choi, S. W. Lee, E. A. Gaulding, C. B. Murray, and C. R. Kagan. Engineering the surface chemistry of lead chalcogenide nanocrystal solids to enhance carrier mobility and lifetime in optoelectronic devices. *Chemical Communications*, 53(4):728–731, 2017. 31

[117] S. J. Oh, Z. Wang, N. E. Berry, J. H. Choi, T. Zhao, E. A. Gaulding, T. Paik, Y. Lai, C. B. Murray, and C. R. Kagan. Engineering charge injection and charge transport for high performance PbSe nanocrystal thin film devices and circuits. *Nano Letters*, 14(11):6210–6216, 2014. 31, 74

[118] M. E. Orazem, N. Pebere, and B. Tribollet. Enhanced Graphical Representation of Electrochemical Impedance Data. *Journal of The Electrochemical Society*, 153(4):B129, 2006. 41, 42, 112, 134

[119] M. E. Orazem and B. Tribollet. *Electrochemical Impedance Spectroscopy.* Wiley, Hoboken, New Jersey, 2nd edition, 2008. 39, 41, 42, 59, 69, 112, 114, 134, 136, 138, 139

[120] A. G. Pattantyus-Abraham, I. J. Kramer, A. R. Barkhouse, X. Wang, G. Konstantatos, R. Debnath, L. Levina, I. Raabe, M. K. Nazeeruddin, M. Grätzel, and E. H. Sargent. Depleted-Heterojunction Colloidal Quantum Dot Solar Cells. *ACS Nano*, 4(6):3374–3380, jun 2010. 91, 92

[121] T. J. Penfold, J. Szlachetko, F. G. Santomauro, A. Britz, W. Gawelda, G. Doumy, A. M. March, S. H. Southworth, J. Rittmann, R. Abela, M. Chergui, and C. J. Milne. Revealing hole trapping in zinc oxide nanoparticles by time-resolved X-ray spectroscopy. *Nature Communications*, 9(1):478, dec 2018. 92

[122] R. F. Pierret. *Field Effect Devices.* Addison-Wesley, Reading, MA, second edition, 1990. 76

[123] C. Piliego, L. Protesescu, S. Z. Bisri, M. V. Kovalenko, and M. A. Loi. 5.2% efficient PbS nanocrystal Schottky solar cells. *Energy and Environmental Science*, 6(10):3054–3059, 2013. 63

[124] Y. Y. Proskuryakov, K. Durose, B. M. Taele, and S. Oelting. Impedance spectroscopy of unetched CdTe/CdS solar cellsEquivalent Circuit Analysis. *Journal of Applied Physics*, 102(2):024504, jul 2007. 67

[125] U. Reislöhner, H. Metzner, and C. Ronning. Hopping conduction observed in thermal admittance spectroscopy. *Physical Review Letters*, 104(22), 2010. 48, 60, 65, 66

[126] P. Rekemeyer, C.-H. M. Chuang, M. G. Bawendi, and S. Gradecak. Minority Carrier Transport in Lead Sulfide Quantum Dot Photovoltaics. *Nano Letters*, page acs.nanolett.7b02916, 2017. 120, 124, 126, 130

[127] E. Rhoderick and R. Williams. *Metal-Semiconductor Contacts.* Oxford University Press, second edition, 1988. xii, 11, 32, 33, 36, 66, 69, 80, 81

[128] C. T. Sah. The Equivalent Circuit Model in Solid-State Electronics Part II: The Multiple Energy Level Impurity Centers. *Proceedings of the IEEE*, 55(5):672–684, 1967. 37

[129] M. Schmitt, U. Rau, and J. Parisi. Charge Carrier Transport via Defect States in Cu(In,Ga)Se2 Thin Films and Cu(In,Ga)Se2/CdS/ZnO Heterojunctions. *Physical Review B*, 61(23):16052–16059, jun 2000. 60

[130] B. I. Shklovskii and A. L. Efros. *Electronic properties of doped semiconductors.* Springer, first edit edition, 1984. 22

[131] J. C. Simpson and J. F. Cordaro. Characterization of deep levels in zinc oxide. *Journal of Applied Physics*, 63(5):1781–1783, mar 1988. 92, 108, 127

[132] H. J. Snaith. Perovskites: The Emergence of a New Era for Low-Cost, High-Efficiency Solar Cells. *The Journal of Physical Chemistry Letters*, 4(21):3623–3630, nov 2013. 58

[133] M. J. Speirs, D. N. Dirin, M. Abdu-Aguye, D. M. Balazs, M. V. Kovalenko, and M. A. Loi. Temperature dependent behaviour of lead sulfide quantum dot solar cells and films. *Energy Environ. Sci.*, 9(9):2916–2924, 2016. 65, 98, 104, 114, 119, 129, 137

[134] B. F. Spencer, D. M. Graham, S. J. O. Hardman, E. A. Seddon, M. J. Cliffe, K. L. Syres, A. G. Thomas, S. K. Stubbs, F. Sirotti, M. G. Silly, P. F. Kirkham, A. R. Kumarasinghe,

G. J. Hirst, A. J. Moss, S. F. Hill, D. A. Shaw, S. Chattopadhyay, and W. R. Flavell. Time-resolved surface photovoltage measurements at n-type photovoltaic surfaces: Si(111) and ZnO(1010). *Physical Review B*, 88(19):195301, nov 2013. 92, 93, 113, 136

[135] B. F. Spencer, M. A. Leontiadou, P. C. J. Clark, A. I. Williamson, M. G. Silly, F. Sirotti, S. M. Fairclough, S. C. E. Tsang, D. C. J. Neo, H. E. Assender, A. A. R. Watt, and W. R. Flavell. Charge dynamics at heterojunctions for PbS/ZnO colloidal quantum dot solar cells probed with time-resolved surface photovoltage spectroscopy. *Applied Physics Letters*, 108(9):091603, feb 2016. 92, 93, 97, 100, 109, 113, 114, 123, 136, 138, 143

[136] P. Stadler, B. R. Sutherland, Y. Ren, Z. Ning, A. Simchi, S. M. Thon, S. Hoogland, and E. H. Sargent. Joint mapping of mobility and trap density in colloidal quantum dot solids. *ACS Nano*, 7(7):5757–5762, 2013. 61, 119

[137] D. B. Straus, E. D. Goodwin, E. A. Gaulding, S. Muramoto, C. B. Murray, and C. R. Kagan. Increased Carrier Mobility and Lifetime in CdSe Quantum Dot Thin Films through Surface Trap Passivation and Doping. *Journal of Physical Chemistry Letters*, 6(22):4605–4609, 2015. 31

[138] L. Sun, J. J. Choi, D. Stachnik, A. C. Bartnik, B. R. Hyun, G. G. Malliaras, T. Hanrath, and F. W. Wise. Bright infrared quantum-dot light-emitting diodes through inter-dot spacing control. *Nature Nanotechnology*, 7(6):369–373, 2012. 7

[139] S. Sze. *Physics of Semiconductor Devices Physics of Semiconductor Devices*. Wiley-Interscience, third edit edition, 2007. x, 9, 10, 12, 13, 124

[140] D. V. Talapin, J. S. Lee, M. V. Kovalenko, and E. V. Shevchenko. Prospects of colloidal nanocrystals for electronic and optoelectronic applications. *Chemical Reviews*, 110(1):389–458, 2010. 58

[141] D. V. Talapin and C. B. Murray. Applied physics: PbSe nanocrystal solids for n- and p-channel thin film field-effect transistors. *Science*, 310(5745):86–89, 2005. 7

[142] K. H. Tam, C. K. Cheung, Y. H. Leung, A. B. Djurišić, C. C. Ling, C. D. Beling, S. Fung, W. M. Kwok, W. K. Chan, D. L. Phillips, L. Ding, and W. K. Ge. Defects in ZnO nanorods prepared by a hydrothermal method. *Journal of Physical Chemistry B*, 110(42):20865–20871, 2006. 92

[143] J. Tang, K. W. Kemp, S. Hoogland, K. S. Jeong, H. Liu, L. Levina, M. Furukawa, X. Wang, R. Debnath, D. Cha, K. W. Chou, A. Fischer, A. Amassian, J. B. Asbury, and E. H. Sargent. Colloidal-quantum-dot photovoltaics using atomic-ligand passivation. *Nature Materials*, 2011. 91, 141

[144] J. Tang, H. Liu, D. Zhitomirsky, S. Hoogland, X. Wang, M. Furukawa, L. Levina, and E. H. Sargent. Quantum junction solar cells. *Nano Letters*, 12(9):4889–4894, 2012. 91

[145] J. Tang, X. Wang, L. Brzozowski, D. A. R. Barkhouse, R. Debnath, L. Levina, and E. H. Sargent. Schottky quantum dot solar cells stable in air under solar illumination. *Advanced Materials*, 22(12):1398–1402, 2010. 63

[146] B. C. Thompson and J. M. J. Fréchet. PolymerFullerene Composite Solar Cells. *Angewandte Chemie International Edition*, 47(1):58–77, jan 2008. 58

[147] B. A. Timp and X. Y. Zhu. Electronic energy alignment at the PbSe quantum dots/ZnO(101{combining overline}0) interface. *Surface Science*, 604(17-18):1335–1341, 2010. 100

[148] M. Tomozawa. Dielectric Characteristics of Glass. In *Treatise on Materials Science & Technology*, volume 12, pages 283–345. ACADEMIC PRESS, INC., 1977. 60

[149] O. Voznyy, D. Zhitomirsky, P. Stadler, Z. Ning, S. Hoogland, and E. H. Sargent. A charge-

orbital balance picture of doping in colloidal quantum dot solids. *ACS Nano*, 6(9):8448–8455, 2012. 104, 126, 129

[150] T. Walter, R. Herberholz, C. Müller, and H. W. Schock. Determination of defect distributions from admittance measurements and application to Cu(In,Ga)Se2based heterojunctions. *Journal of Applied Physics*, 80(8):4411–4420, 1996. 28, 43, 44, 45, 59, 66, 69, 73, 76, 98, 99, 103, 105, 157

[151] S. Wang, P. Kaienburg, B. Klingebiel, D. Schillings, and T. Kirchartz. Understanding Thermal Admittance Spectroscopy in Low-Mobility Semiconductors. *The Journal of Physical Chemistry C*, 122(18):9795–9803, may 2018. 48, 60, 65, 96, 123

[152] D. D. Wanger, R. E. Correa, E. A. Dauler, and M. G. Bawendi. The dominant role of exciton quenching in PbS quantum-dot-based photovoltaic devices. *Nano Letters*, 13(12):5907–5912, 2013. 120, 126, 130, 142

[153] M. C. Weidman, M. E. Beck, R. S. Hoffman, F. Prins, and W. A. Tisdale. Monodisperse, Air-Stable PbS Nanocrystals via Precursor Stoichiometry Control. *ACS Nano*, 8(6):6363–6371, jun 2014. 63, 78, 86

[154] S. M. Willis, C. Cheng, H. E. Assender, and A. A. Watt. The transitional heterojunction behavior of PbS/ZnO colloidal quantum dot solar cells. *Nano Letters*, 12(3):1522–1526, 2012. xvi, 91, 92, 93, 100, 124

[155] G. Xing, N. Mathews, S. Sun, S. S. Lim, Y. M. Lam, M. Gratzel, S. Mhaisalkar, and T. C. Sum. Long-Range Balanced Electron- and Hole-Transport Lengths in Organic-Inorganic CH3NH3PbI3. *Science*, 342(6156):344–347, oct 2013. 58

[156] L. Xu, J. Wang, and J. W. Hsu. Transport Effects on Capacitance-Frequency Analysis for Defect Characterization in Organic Photovoltaic Devices. *Physical Review Applied*, 6(6):064020, 2016. 60

[157] J. Yang and F. W. Wise. Effects of disorder on electronic properties of nanocrystal assemblies. *Journal of Physical Chemistry C*, 119(6):3338–3347, 2015. 61

[158] W. Yoon, J. E. Boercker, M. P. Lumb, D. Placencia, E. E. Foos, and J. G. Tischler. Enhanced open-circuit voltage of PbS nanocrystal quantum dot solar cells. *Scientific Reports*, 3:1–7, 2013. 11

[159] D. Yu, C. Wang, B. L. Wehrenberg, and P. Guyot-Sionnest. Variable Range Hopping Conduction in Semiconductor Nanocrystal Solids. *Physical Review Letters*, 92(21):216802, may 2004. 31, 59

[160] J. Zhang, J. Gao, E. M. Miller, J. M. Luther, and M. C. Beard. Diffusion-controlled synthesis of PbS and PbSe quantum dots with in situ halide passivation for quantum dot solar cells. *ACS Nano*, 8(1):614–622, 2014. 15, 61, 119

[161] Y. Zhang, D. Zherebetskyy, N. D. Bronstein, S. Barja, L. Lichtenstein, A. P. Alivisatos, L. W. Wang, and M. Salmeron. Molecular Oxygen Induced in-Gap States in PbS Quantum Dots. *ACS Nano*, 9(10):10445–10452, 2015. 82, 85, 98, 157

[162] Y. Zhang, D. Zherebetskyy, N. D. Bronstein, S. Barja, L. Lichtenstein, D. Schuppisser, L. W. Wang, A. P. Alivisatos, and M. Salmeron. Charge percolation pathways guided by defects in quantum dot solids. *Nano Letters*, 15(5):3249–3253, 2015. 78, 85

[163] T. Zhao, E. D. Goodwin, J. Guo, H. Wang, B. T. Diroll, C. B. Murray, and C. R. Kagan. Advanced Architecture for Colloidal PbS Quantum Dot Solar Cells Exploiting a CdSe Quantum Dot Buffer Layer. *ACS Nano*, 10(10):9267–9273, 2016. 95, 100, 116, 122, 145

[164] D. Zhitomirsky, O. Voznyy, S. Hoogland, and E. H. Sargent. Measuring charge carrier diffusion in coupled colloidal quantum dot solids. *ACS Nano*, 7(6):5282–5290, 2013. 119

[165] D. Zhitomirsky, O. Voznyy, L. Levina, S. Hoogland, K. W. Kemp, A. H. Ip, S. M. Thon, and

E. H. Sargent. Engineering colloidal quantum dot solids within and beyond the mobility-invariant regime. *Nature Communications*, 5, 2014. 119